Fall 2013

The Mechanism and Timescales of Soil Formation in the Hyper-arid Atacama Desert, Chile

Fan Wang
Purdue University

Graduate School ETD Form 9
(Revised 12/07)

PURDUE UNIVERSITY
GRADUATE SCHOOL
Thesis/Dissertation Acceptance

This is to certify that the thesis/dissertation prepared

By Fan Wang

Entitled

The Mechanism and Timescales of Soil Formatiion in the Hyper-arid Atacama Desert, Chile

For the degree of Doctor of Philosophy

Is approved by the final examining committee:

Darryl Granger
Chair

Darrell Schulze

Greg Michalski

Brenda Beitler Bowen

Nathaniel Lifton

To the best of my knowledge and as understood by the student in the *Research Integrity and Copyright Disclaimer (Graduate School Form 20)*, this thesis/dissertation adheres to the provisions of Purdue University's "Policy on Integrity in Research" and the use of copyrighted material.

Approved by Major Professor(s): Greg Michalski

Approved by: Indrajeet Chaubey 10/08/2013
Head of the Graduate Program Date

THE MECHANISM AND TIMESCALES OF SOIL FORMATION IN THE HYPER-ARID ATACAMA DESERT, CHILE

A Dissertation

Submitted to the Faculty

of

Purdue University

by

Fan Wang

In Partial Fulfillment of the

Requirements for the Degree

of

Doctor of Philosophy

December 2013

Purdue University

West Lafayette, Indiana

To my husband and parents

ACKNOWLEDGEMENTS

First and foremost, I would like to express my deepest appreciation to my advisor, Dr. Greg Michalski, for his tremendous guidance and help all the way from when I first came to Purdue in 2009 through completion of this degree. I joined EAPS department with the opportunity offered by Dr. Michalski to work for the National Science Foundation project (EAR 0922114): A new regional paleo-precipitation proxy: Oxygen isotopes in desert nitrate. This three-year-long NSF project work turned out to be the major part of this dissertation, though I also conducted some work in Turpan-Hami Basin in western China that is not included here. During the long journey towards concluding this PhD research, I have always been grateful that Dr. Michalski was mostly around to help me through many academic difficulties, and I appreciate most for his frank suggestions, continuous encouragement, and meticulous efforts to improve my scientific writing. Dr. Michalski is not only the one who introduced me to the stable isotope geochemistry field and helped me adapt to the new field and laboratory work, but also the one who inspired me by the way he worked as a scientist and he carried himself as an academic advisor. Dr. Michalski is very focused, hard-working and dedicated, and has the personality of being easy to get excited about exploring the unknown or scientific discovery, which impressed me a lot as the essences of scientists' qualities. Dr. Michalski is not very communicative sometimes, but I can feel his care for students' academic growth all the time. He devoted

numerous hours to work closely with each student, no matter undergraduate or graduate students, for students' proposals, presentations and manuscripts. He is also very supportive for establishing collaboration and connections with other scholars and research communication during conferences or workshops. Overall, I really appreciate these years' supervision from Dr. Michalski that has led me towards my career goal and strengthened my professional skills.

Next, I would like to thank my committee members, Drs. Brenda Bowen, Darryl Granger, Nathaniel Lifton and Darrell Schulze for their unparalleled support for this dissertation work. They have been actively involved in my dissertation work and continually provided encouraging and constructive feedbacks and the freedom to use their laboratory facilities during my study at Purdue. Especially, Dr. Brenda Bowen had continuous inputs to this dissertation work either during the two Atacama trips or the later thin section petrology study. Drs. Granger and Lifton contributed tremendously to the cosmogenic isotope dating study and the discussion with them greatly broadened my thinking and enlightened my minds. Dr. Schulze helped a lot with the X-ray diffractionation mineralogical analysis. Besides, I also want to recognize my Chinese collaborators, Drs. Wensheng Ge and Xinghui Xia from China University of Geoscience (Beijing) and Beijing Normal University for their aids for my research progress and intellectual growth during the years of study towards the PhD.

I also want to express my sincere thanks to the other three current or past faculty members in the Purdue Stable Isotope (PSI) lab: Drs. Yuch-Ning Shieh for his continuous help in my research and life, Tim Filley and Gabe Bowen for their permission to access their laboratory facilities and readiness to contribute research inputs. I also want to

recognize some of my past and current lab mates: David Mase, Krystin Riha, Mike King, Wendell Walters, Tanya Katzman, Daniel McMahon and Yini Ma, and two technicians: Drs. Sergey Oleynik and Bethany Theiling, for their assistance during my laboratory work . My thanks also go to the undergrads I have mentored over the past four years: Ji-hye Seo, Rahat Choudhury, Nathianel Louden, Hao Luo and Yanqi Yu, for their help with arduous chemistry analysis.

In addition, a thank you to the fellows in the Purdue Rare Isotope Measurement (PRIME) lab for their generosity of time and technical and financial support for soil ^{36}Cl, ^{10}Be and cation concentration measurements, especially the valuable assistance and contributions from Marc Caffee, Zane Gilbert, Greg Chimel, Susan Ma, Tom Clifton and Tom Miller.

I also want to express my appreciation for the special friendship with the Moser family (Joyce, John, Lori, Joel, Maebol, Ollie, Sherman, Edith and Ruth) who hosted me for all the American traditional holidays, helped me move for many times and accompanied me during many important moments in West Lafayette. There are also many other individuals at Purdue deserving big thanks for helping me to ease the stress of student life. All this support is really important for me to successfully finish this dissertation.

Finally, I would like to thank my husband, Peng Ju, who is always believing in me and easing me with his peaceful mind and kindness, and my parents who first planted the seeds of knowledge in me and poured enormous efforts to my education! Without their constant love, this dissertation would not have been possible and I would never have the chance to get where I am now.

TABLE OF CONTENTS

Page

Page

LIST OF TABLES

LIST OF FIGURES

Figure Page

ABSTRACT

Wang, Fan. Ph.D., Purdue University, December 2013. The mechanism and timescales of soil formation in the hyper-arid Atacama Desert, Chile. Major Professor: Greg Michalski.

The planetary surfaces that evolve in the near absence of water are strikingly different from surfaces where water is abundant, but their formation is poorly documented. This research is an in-depth exemplary work in the Atacama Desert in northern Chile to understand the soil formation in hyper-arid environments, as an analog for planetary surfaces such as the Mars. In detail, the basic mechanism regarding the source material, timescale, paleo-climatic settings and the role of crypto-biotic crusts have been investigated to constrain the Atacama soil development.

The geochemical, isotopic and mineralogical composition of atmospheric dust deposited along a West-East transect in the Atacama Desert, stretching from the Pacific Ocean to the Andean Altiplano, was evaluated. Results suggested that the deposited salts are mainly sourced from marine aerosol, as well as fog, local entrainment of surface material and secondary reactions. A comparison of the deposition data with the geochemistry of a paleosol in the hyper-arid core of the Atacama showed that the total paleosol ion composition can be explained by long-term accumulation of atmospheric deposition, while post-depositional leaching and salt precipitation account for the ion segregation typically found in the Atacama soil profiles. This has led to a proposed soil formation mechanism in hyper-arid environments consisting of four stages of

development: 1) initiation of soil development on regional bedrock material induced by salt fracturing, 2) maturation of soil sequence featured by a continuous trapping of atmospheric dust and salts and the salt segregation into discrete ionic zones, 3) termination of soil accretion due to the formation of surface blocky layer, and 4) unexpected alteration of soil accumulation induced by anthropogenic disturbance.

A combination of two long-lived radioactive nuclides (^{10}Be and ^{36}Cl) was used to constrain the timescale of a 225-cm-deep soil profile from the hyper-arid core of the Atacama. Considering the differences of ^{10}Be and ^{36}Cl nuclides in the half-life and mobility in the soil, ^{10}Be could indicate the fate of insoluble silicate dust (dominant in the soil matrix) because it readily adsorbs to soil particles, while ^{36}Cl could be used to trace the transport and fate of salts considering the chlorine's solubility. Soil ^{10}Be concentrations showed a systematic decline from surface to 225 cm deep, which has been reproduced using a simple model that assumes the soil matrix, including ^{10}Be, builds up as layers over time while ^{10}Be decays *in situ*. This concurs with the essence of the soil formation mechanism proposed above, *i.e.* the net soil accumulation via atmospheric deposition. The model estimates an age of ~6.6±0.4 Ma for the total soil profile. Likewise, the ^{36}Cl/Cl ratios showed a systematic decline with depth and a simple accumulation model that chloride builds up over time via atmospheric inputs and ^{36}Cl radioactively decays *in situ* also reproduces the data remarkably well. This model suggests the atmospheric origin of soil chloride and the chloride age at 225 cm of 860 (±90) ky.

Paleo-precipitation variations, which can potentially impact soil formation, were first detected from the deviations of the observed ^{10}Be concentrations from the above model estimates that are likely mainly due to changes in ^{10}Be delivery rates impacted by

invariant precipitation rates. The ^{10}Be data suggested a drying after ~4.7 Ma, likely due to Andean uplift, and the returning to an insignificant wet period at ~1 Ma, possibly connected to global climate change. Similarly, ^{36}Cl discontinuities with depth also suggested the interruption of long-term hyper-aridity by brief wet periods that induced chloride migration. To investigate the timescale of salt accumulation (^{36}Cl age: ~860 ky), a new precipitation proxy (soil NO_3^- $\Delta^{17}O$) was calibrated using the stable oxygen isotope measurements in nitrates from four deserts with different mean annual precipitation rates. The paleo-precipitation history for the formation of the 225-cm deep trench soil profile was then reconstructed based on the soil NO_3^- $\Delta^{17}O$ proxy, indicating seven wet-dry cycles, likely corresponding to possible glacial-interglacial cycles operating on the 100 ky scale.

Crypto-biotic crusts (CBC), a consortium of pioneer species in hostile environments, may play an important role in soil evolution. Preliminary data from a CBC distribution transect indicated that CBCs can enhance dust trapping and physical protection of the dust from wind erosion, leading to the thickened loose soil profile beneath CBCs compared to at nearby sites without CBCs. Fine particle fractions in the soil under CBCs were higher beneath CBC than those in non-CBC sites, and this was probably related to the enhanced small dust particle trapping or *in situ* weathering. That the profile beneath CBCs had fewer soluble ions compared to sites without CBCs suggested an enhanced leaching at sites with CBCs, though it is still unclear whether the enhanced leaching was the cause or the reason of the presence of CBCs. The bomb spike with the ^{36}Cl/Cl ratio of 398×10^{-15} was preserved on the surface at a CBC site over the past ~60 years, while the

subsurface $^{36}Cl/Cl$ ratios were likely homogenized due to the past more significant wet events.

CHAPTER 1. INTRODUCTION

1.1 Problem Statement

Soil formation is commonly described as a mass balance between inputs and losses that are integrated over geological timescales (Jenny, 1941; Brimhall et al., 1992). In most systems, soil inputs are mainly from the degradation of biological material and decomposition of bedrock, with minor contributions from the deposition of atmospheric compounds, such as dust and salts. The major soil loss processes are via physical/chemical weathering and transport of solutes as well as wind or water erosion (Chadwick et al., 1990) (Figure 1.1). Therefore, a typical soil profile development starts from consolidated bedrock (R horizon) that progressively weather into the regolith (C horizon) via physical breakup and chemical decay of the initial rock material, and the weathering front (R-C transition zone) continually moves downward over time. Vegetation then invades and organic matter accumulates in a shallow surface layer (A horizon). Subsequently, production and downward translocation of iron oxides and clay minerals creates a B horizon, while continued losses of iron oxides and clays can lead to an E horizon above B horizon (Jenny, 1941; Simmon, 1959; Soil Survey Staff, 1975; Isbell, 2002) (Figure 1.1). Overall, these soil formation processes are strongly influenced by organisms and climate imposed on the parent material over time, which initiate the

accumulation of organic material as well as the translocation of minerals, etc (Jenny, 1941).

In hyper-arid (<50 mm yr^{-1}) regions where water and plant life is nearly absent, the soil system, however, may have become radically simplified, with biological inputs, weathering losses and aqueous erosion and leaching being negligible (Dan and Yaalon, 1982; Gerson and Amit, 1987; Quade et al., 1995; Carpo and Chadwick, 1999; Ewing et al., 2006; Amit et al., 2007). Details of soil-forming processes in these regions, however, are still poorly constrained. In this dissertation, a case study of the Atacama Desert will be conducted to explore the enigma of surface processes in hyper-arid environments. The Atacama soils are unique, with extremely low levels of organic matter and microorganisms but massive amounts of soluble salt deposits (Navarro-González et al., 2003; Quinn et al., 2005; Sutter et al., 2007). A typical soil profile in the hyper-arid core of the Atacama mainly consists of chuca (the surface powdery gypsum and anhydrite layer), costra (the firmly-cemented gypsum and anhydrite layer), caliche (the firmly-cemented nitrate and halite layer), conjelo (the saline-cemented regolith), coba (a loose unconsolidated regolith) and bedrock, namely a B-C-R horizon sequence according to the previous soil classification (Ericksen, 1981). It has been suggested that soil formation in the Atacama soils passes through a nitrogen threshold (Ewing et al., 2007) where soil nitrogen accumulation rates increases with decreasing precipitation, rather than decrease as in most soil systems. However, there remain uncertainties about the parent material, timescale, climatic settings and some other influencing factors influencing the soil formation in the Atacama.

This research will seek to understand the soil formation mechanism in hyper-arid environments with a case study in the Atacama Desert in northern Chile. Firstly, the physiography, tectonics and general climatic settings of the Atacama will be detailed in Sections 1.2 and 1.3 to provide a necessary context of the study area. Previous efforts in exploring the past climatic change in the Atacama will also be overviewed in Section 1.3 to manifest the advances in paleoclimatic research. Section 1.4 will be about the principles of isotope fractionation that are the knowledge basis of the latter nitrate isotope research in Chapters 2 and 4.

Since the hyper-aridity in the Atacama has considerably limited normal soil formation processes, it has been suggested that the parent material for the Atacama soils is mainly sourced from atmospheric deposition, leading to a net mass gain and volumetric expansion of soil profiles (Ewing et al., 2006). Indeed, recent isotopic evidence has demonstrated that thick deposits of nitrate, perchlorate, and sulfate in the Atacama are mainly due to long-term accumulation of atmospherically deposited photochemical compounds (Bao and Gu, 2004; Michalski et al., 2004). Nevertheless, the characteristics of atmospheric deposition in the Atacama remain poorly constrained, and the source of soil matrices (silicate dust) is still not evident. These questions were addressed using a west-east array of dust traps that monitored atmospheric deposition across the Atacama and the results will be discussed in Chapter 2 of this dissertation.

Previous efforts to establish the timescale of soil formation in the Atacama have focused on surface exposure dating or dating of volcanic ash layers to provide some insight into soil formation history (Ewing et al., 2006; Placzek et al., 2009, 2010; Rech et al., 2006), which are both subject to uncertainties and limitations. This requires new

dating methods to decipher the soil formation timescale under hyper-arid conditions. Based on meteoric ^{10}Be and ^{36}Cl concentration measurements, consecutive ages of soil matrix and salt accumulation have been constrained for a 225-cm-deep soil profile located in the hyper-arid core of the Atacama (Chapter 3).

It is well-documented that the hyper-aridity in the Atacama Desert has existed for millions of years (Alpers and Brimhall, 1988; Hartley and Chong, 2002; Dunai et al., 2005; Nishiizumi et al., 2005; Rech et al., 2006). However, rainfall events of 1 cm or more may occur a few times a century and fog events can occur nearly daily (Ericksen 1981; Houston, 2006; Sutter et al., 2007). Furthermore, various geological evidence (Hartley and Chong, 2002; Bissig and Riquelme, 2010) has indicated a hyper-arid climate was likely interrupted by semi-arid episodes in the past. If aqueous events are sufficiently large or intense, they can induce *in-situ* weathering, leaching, erosion and enhanced biological actitivies that can impact soil formation. However, highly-resolution paleoclimate (particularly paleo-precipitation) records from the Atacama are rare, and the potentially large influence of small amounts of paleo-precipitation on soil formation in this region is still unresolved. The potential of desert soil nitrate $\Delta^{17}O$ as a paleo-precipitation proxy and gross nitrification rates will be discussed in Chapter 4 and its promising application into studying the paleo-precipitation changes was evaluated in the above mentioned soil profile.

In the hyper-arid Atacama Desert, where extremely hostile conditions preclude vascular plants and other eukaryotic or prokaryotic life, rare crypto-biotic crust (CBC) communities may be the key photoautotrophic microorganisms and primary producers (Büdel, 2001). If CBC organisms exist in currently barren locations in the Atacama, they

may have had a large influence on the evolution of the soil, which requires a better understanding of the linkage between water, nitrogen and life in hyper-arid ecosystems. Geochemical analysis (anions, cations and oxygen isotope analysis on nitrate) have been conducted to investigate the influence of CBCs on the element cycling within the soils (Chapter 5).

1.2 Physiography and Tectonics of the Atacama Desert

The Atacama Desert, Chile, stretches more than 1,000 km along the Pacific coast of South America (20°S-30°S). The physiography of the Atacama Desert consists of three major units from west to east: the Coastal Range, the Andes and Central Depression (Stoertz and Ericksen, 1974; Ericksen, 1981) (Figure 1.2). The Coastal Range is a mountain range along the Pacific coast of South America from Morro de Arica to the Taitao Peninsula (~3,000 km in length). The maximum width of the Coastal Range is ~50 km; the altitude is generally less than 2,000 m with steep cliffs on the western sides from the coast and gentle slopes of eastern flanks towards the Central Valley. The Andes consist of a vast series of plateaus about 4,000 m in altitude surmounted by even higher volcanic peaks, and a succession of parallel Pre-Andes mountain ranges to the east (*i.e.* the Cordillera Central in the north and the Cordillera Domeyko in the south) with intervening valleys and basins. The Central Valley is an intermediate depression between the Coastal Range and the Andes, comprised of two major north-south segments. The northern segment (Pampa del Tamarugal) is between the Coastal Range and the main Andes, while the southern segment is an elongate basin centering near Aguas Blancas adjacent to the Coastal Range but separated from the Pre-Andes by Domeyko Fault

system. The Central Valley is typically at elevations between 900 and 2,500 m with the maximum width of about 80 km. In the Atacama, the Coastal Range is mantled by Jurassic volcanic sequences interbedded with marine and continental conglomerates, while the Andes are predominately underlain by Pliocene-Quaternary volcanic flow, tuffs, and breccia rocks, and the Central Valley comprises of Upper Miocene-Pliocene piedmont clastic sediments of a few hundred meters thickness (SERNAGEOMIN, 2003).

The Atacama's landscape development has mainly been driven by regiuonal tectonics, especially the subduction of the eastern edge of Nazca Plate beneath the South American Plate (Moreno and Gibbons, 2007) (Figure 1.3). The Nazca Plate, a dense oceanic tectonic plate in the eastern Pacific Ocean borders the South American Plate (a buoyant continental plate) to the west, along most of the western side of South America. The Nazca Plate is being subducted beneath the South American Plate at a rate of 43-75 mm/year (Hampel, 2002; Moreno and Gibbons, 2007). Along the subduction boundary, the Peru-Chile Trench is formed, and is the longest trench in the world (>5900 km) with a maximum depth of 8 km below sea level and mean width of 64 km (Fisher and Raitt, 1962; Hayes, 1966). Massive earthquakes have been generated because of the deformation of or slip between these two plates (Barazangi and Isacks, 1976). The convergence of these two plates is also responsible for the Andean orogeny (mountain-building) (Jordan et al., 1983), while the movement of the Nazca Plate over hotspot regions and melting of the rocks around the subducting slab have led to a volcanic belt that can be subdivided into several volcanic zones on the Andean plateau (Pilger, 1984).

1.3 Climate Settings of the Atacama Desert

The Atacama Desert is one of the driest places on Earth, with the driest parts of <1 mm rainfall annually extending from approximately 22°S to 26°S in the Central Valley (McKay et al., 2003; Houston, 2006; Rech et al., 2006). The hyper-aridity in the Central Valley mainly comes from its geographic location that creates rain shadow effects from both the Coastal Range to the west and the Andes to the east (Houston and Hartley, 2003; Hartley, 2005). In addition, the quasi-permanent southeast Pacific subtropical anticyclone maintains an extensive and persistent stratocumulus cloud deck, and the cold Peru Current generates low sea surface temperature, causing a temperature inversion and frequent cloud and fog but limited rainfall on the southeast Pacific coast off Northern Chile (Houston, 2006). Moisture in the Atacama region is mainly originated from northeasterly airflows from the Amazonia during the austral summer, or southwesterly moving frontal systems from the Pacific during the winter, which are both limited since the Atacama straddles the boundary between these two rainfall zones (Houston and Hartley, 2003). The general air movement across the Atacama Desert is from west to east. Off the northern Chile coast, the prevailing winds are from south-southeast (Muñoz, 2008). In the Central Valley, solar heating of the western slope of the Andes causes daytime upslope air flow (Andean pump) resulting in much weaker seaward air mass returns (Rutllant et al., 2013), which is consistent with the inferences from the wind erosional features near the regional salars (salt flats in Spanish) by Stoertz and Ericksen (1974). From the Pre-Andes to the Andean Altiplanos (high plains in Spanish), strong prevailing winds gradually shift from the northwest or west-northwest to the westerlies (Stoertz and Ericksen, 1974; Rutllant et al., 2013).

The intensity and duration of the Atacama Desert's extremely arid climate has sparked massive research interests, but remains a matter of controversy. Since the latitudinal position of the South American continent was nearly fixed during the last 150 Ma based on geomagnetic evidence (Beck et al., 2000) and the Humboldt current system existed at least 65 Ma ago (Keller et al.,1997), it is generally accepted that arid to hyper-arid conditions (≤400 mm precipitation per year) have prevailed over the Atacama region at least since the early Oligocene (Hartley, 2003; Dunai et al., 2005) and even since the late Cretaceous (Hartley et al., 2005). However, in the Central Valley, compared to the present day hyper-aridity (<1 mm precipitation per year), geological evidence suggested more humid conditions in the remote past. The onset of hyper-aridity (≤5 mm/year precipitation) in the Atacama Desert was widely suggested to be associated with the uplift of the Andes between 15 and 10 Ma (Houston and Hartley, 2003). However, some people suggested that the switch from a semi-arid/arid climate to hyper-aridity occurred in the middle Miocene and could not be attributed to Andean uplift occurring during the lower-middle Miocene (Alpers and Brimhall, 1988; Sillitoe and McKee, 1996; Rech et al., 2006). Other studies proposed a more recent arid-to-hyper-arid transition in the Atacama between 6 and 3 Ma also related to the Andean uplift (Hartley and Chong 2002; Hartley, 2003). Some other researchers argued that the arid climate in the Atacama is the cause rather than the result of the uplift of the high Andes (Lamb and Davis, 2003; Dunai et al., 2005). In view of the considerable spatial variabilities in climate across the Atacama and the insufficient and even contradicting information according to different sources, previous paleoclimate studies in the Atacama are hereby briefly reviewed, and a new precipitation proxy in desert regions will be proposed to augment these existing

precipitation proxies and deduce the high-resolution paleoclimatic change in the Atacama Desert for comparison (Chapter 2).

Geomorphology-based paleoclimate inference. Pedimentation is usually occuring under semi-arid climates, while its termination of pedimentation may indicate a shift to hyper-arid conditions. Extensive Paleogene to late Miocene pediment surfaces have been found in southern Peru and northern Chile, suggesting the onset of hyper-aridity during the middle Miocene (Mortimer et al., 1974). However, many pediment plains may have been subject to some geological displacement, which requires additional attention to paleoclimatic inference from them. For example, pediment surfaces in the Central Valley between 20°-23°S were displaced by a north-trending fault associated with Andean uplift (Galli-Oliver, 1967), making the constraint of climate change difficult.

Supergene enrichment-based paleoclimate inference. Supergene enrichment of ore deposits is the oxidation and leaching of the metallic ore in the upper part of ore deposits and their re-deposits at depths to form a reducing zone, which usually occurs near near the surface and is linked to water availability. Therefore, the cession of supergene enrichment can signal the onset of hyper-aridity in the Atacama. Supergene enrichment has been found to be active during 23-14 Ma in the Atacama by dating the supergene alunites from several mineral deposits (Sillitoe and McKee, 1996; Alpers and Brimhall, 1988). However, tectonics and sea level variations may also account for the water availability variations and then exert important influences on supergene enrichment in addition to climate. Therefore, many thick supergene-enriched horizons in the Atacama can be due to a rapidly descending water table induced by a drier climate (Titley and

Marozas, 1995; Sillitoe and McKee, 1996), but may also be attributed to the surface uplift, and/or sea level droping (Brimhall and Mote, 1997).

Sedimentological record-based paleoclimate inferences. Sediments in arid closed-basins may have preserved paleoclimatic records that can be indicated by the sediment rock texture and mineralogy (Lowenstein et al., 2003; Hartely, 2003). The fluviolacustrine and alluvial sedimentation can be associated with a semi-arid climate while the cessation of fluviolacustrine and alluvial fan sedimentation may indicate the beginning of hyper-aridity. The Central Valley and the Pre-Andean Depression (between the Pre-Andes mountain range and the Andes are mainly mantled by Miocene to Pliocene sedimentary rocks (SERNAGEOMIN, 2003), and Hartley and Chong (2002) investigated four successions in these two basins and suggested the beginning of hyper-aridity during 4-3 Ma when fluviolacustrine and alluvial fan sedimentation ceased. However, this sedimentation change may be induced by faulting or the wind erosion rather than climate (Lowenstein and Hardie 1985; Talbot and Allen, 1996; Colman et al., 1998). Nalpas et al. (2008) then conducted both sedimentological and tectonic studies on the Atacama gravels at 26.5°S to eliminate the tectonic impact, showing the cession of sediment gravels in the Miocene (9-16 Ma) that could be connected to the shift from a semi-arid to hyper-arid climate. However, much care should be taken when extracting regional paleoclimatic information from the stratigraphic deposits in arid closed-basins.

Surface erosion evidence. The discharge from the Andes into the Central Valley occurs either as sheet flows on vast alluvial fans or via perennial rivers, and the surface erosion rates can be sensitive indicators for the variance of ephemeral sheet flows and thus be used to demonstrate the climatic change associated with it. For example, Alpers

and Brimhall (1988) found a decline of the erosion rates of the La Escondida porphyry-copper deposits from high values to the modern hyper-arid levels occurring around 15 Ma, consistent with their concurrent supergene enrichment studies. Several erosion-sensitive landforms in the Coastal Range were dated by cosmogenic ^{21}Ne in surface clasts to be 25 Ma, suggesting the cessation of erosion at hyper-aridity to preserve the continuously exposed exposed surfaces (Dunai et al., 2005). Jordan et al. (2011) also showed wetter climate in the Atacama occurring around 1 Ma, around 4 Ma between 5-7 Ma based on the erosional landscapes and the sediment transport. However, to separate the effects of possible surface uplift, long-term landscape evolution and climate change has been proved difficult in interpreting the changes in erosion rates.

Paleosol record-based paleoclimate inference. Stratigraphic, chemical, mineralogical and isotopic signatures in paleosols (ancient buried soils) have been extensively used to infer paleoclimate change. Massive evaporite deposits have preserved over much of the Andean Altiplano since the mid-Miocene, suggesting a mid-Miocene climatic regime similar to the modern hyper-aridity (Alonso et al., 1991). However, this conclusion could be challenged because evaporite salars can also occur in cold semi-arid regions (Stoertz and Ericksen, 1974). Besides, the transition from calcic vertisols to salic gypsisols has also been interpreted to reflect the initiation of hyper-aridity. The formation of >3 m thick salic gypsisols in the Central Valley at 23°S was suggested to indicate the onset of hyper-aridity at 10-8 Ma by Schlunegger et al. (2010), while Rech et al. (2006) observed the transition in the Pre-Andean Calama Basin Miocene paleosols (23°S) occurring between 19 and 13 Ma. Paleosol nitrate concentration and the novel signature of mass independent isotopic fractionation (i.e. Δ^{17}O) have also been found useful to constrain the timing of

the arid to hyper-arid transition (Rech et al., 2006). Nitrate deposits within the upper few meters of soils are geologically rare, only known to occur in the world's driest deserts today, like the Atacama, the dry valleys of Antarctica, and parts of the Turpan-Hami basin in northern China. On Earth, nitrate is mainly added to soils via atmospheric deposition and soil nitrification by bacteria ($2NH_4^+ + 4O_2 \rightarrow 2NO_3^- + 2H_2O + 4H^+$), and the rate of the latter is a function of soil moisture and NH_4^+ availability. $\Delta^{17}O$ (discussed below) is a powerful new technique for measuring the relative contribution of the two sources of nitrate. The development of nitrate deposits and their high $\Delta^{17}O$ values (small nitrification contributions probably related to little water availability) were then suggested to mark the commencement of hyper-aridity in a *ca.* 19-13 Ma geosol in the Calama Basin (Rech et al., 2006). Other stable isotopes in the paleosols from the central Andes may also be potential indicators of climatic change. The carbonate $\delta^{18}O$ and $\delta^{13}C$ values were also used to delineate the climatic change in that the carbonate $\delta^{18}O$ values may reflect the intensity of evaporation and carbonate $\delta^{13}C$ is likely related to the vegetation coverage. Rech et al. (2010) analyzed some lower Miocene-Quaternary palustrine and lacustrine carbonates in the Calama Basin to find significant increases in the carbonate $\delta^{18}O$ and $\delta^{13}C$ values during the Miocene, which may correspond to the enhanced evaporation and the lack of vegetation at the onset of hyper-aridity. However, this paleosol method always contains the uncertainties regarding the intervining effects of climatic change and other factors, like tectonic processes.

1.4 Mass-independent Oxygen Isotope Fractionation

In this study, the oxygen isotope fractionation in nitrate is of interest. Naturally occurring oxygen is composed of three stable isotopes: ^{16}O (99.762%), ^{17}O (0.038%) and ^{18}O (0.200%). In view of the small differences in absolute abundances between stable isotopes, stable isotope compositions are usually quantified in terms of delta (δ) values that are the isotope ratios relative to an accepted standard (in units of per mil):

$$\delta\ ‰ = [(R_{sample}/R_{standard}) - 1] \times 10^3 \qquad \text{Eq. 1.1}$$

where R is the ratio of the minor to major isotopes (*i.e.* $^{18}O/^{16}O$ or $^{17}O/^{16}O$). Vienna standard mean ocean water (VSMOW) ($^{18}O/^{16}O$ = 2005.20 ±0.43 ppm, $^{17}O/^{16}O$ = 379.9 ±1.6 ppm) (Craig, 1961) is one of the currently accepted oxygen isotope standards. For the majority of material or processes on the Earth, isotopic abundances vary approximately in proportion with the differences in the masses of isotopes, which is referred as mass-dependent isotopic fractionations due to both kinetic and equilibrium processes (Sharp, 2007). The mass-dependent isotope effect for oxygen can be approximately expressed in delta notation as $\delta^{17}O \sim 0.52 \cdot \delta^{18}O$, and the isotopic compositions of most terrestrial samples should follow the terrestrial fractionation line of slope 0.52 (Figure 1.4) (see review in Thiemens et al., 2006). However, notable deviations from the mass-dependent fractionations, *i.e.* "anomalous" ^{17}O excesses, have been observed during the photochemistry of oxygen in nature and can be quantified by $\Delta^{17}O = \delta^{17}O - 0.52\ \delta^{18}O$ (Figure 1.4) (Thiemens, 1999; Miller 2002). For example, it has been shown that stratospheric ozone has a positive $\Delta^{17}O$ value of 20~50‰ (Thiemens and Heidenreich 1983; Mauersberger, 1987; Michalski et al., 2003) and the formation of ozone is the most studied mass-independent fractionation (MIF) system. Despite many

disputes, the most dominant assertive theory explaining the MIF in ozone is the longer lifetime of the excited ozone (O_3*) molecule for the asymmetric isotopomers (like $^{16}O^{16}O^{17}O$ or $^{16}O^{16}O^{18}O$) when compared to the symmetric isotopomers (like $^{16}O^{16}O^{16}O$, $^{16}O^{17}O^{16}O$ or $^{16}O^{18}O^{16}O$). This is mainly attributed to the differences in rotational, vibrational and electronic couplings influenced by the molecular symmetry, which can lead to the equal enrichment in ^{17}O and ^{18}O in the produced ozone and thus positive $\Delta^{17}O$ values (Gao and Marcus, 2001; Michalski and Bhattacharya, 2009). The $\Delta^{17}O$ anomalies of ozone can further be transferred to other compounds, such as atmospheric nitrate, resulting in products with positive $\Delta^{17}O$ values (Lyons, 2001; Savarino et al., 2008). After atmospheric deposition, some of the MIF signatures can even be preserved in terrestrial systems, such as the $\Delta^{17}O$ anomalies in nitrate and sulfate minerals in the ice cores, rocks or varnishes (Bao et al., 2000, 2001; Farquhar et al., 2000; Michalski et al., 2004). Therefore, $\Delta^{17}O$ anomalies can be a potential tracer for atmospheric chemistry and the subsequent atmospheric deposition processes.

The oxidation of nitrogen compounds into nitrate has important implications for air quality and the transport of this biogeochemically important element. Oxides of nitrogen (NO_x=NO+NO_2) are naturally sourced from lightning, biomass burning and soil emissions, whereas anthropogenic NO_x emissions from fossil fuel burning and automobiles are dominating the global NO_x inventory in modern times (Galloway 1998; Galloway et al. 2004). Nitric acid can be formed via the following multiple reactions (Seinfeld and Pandis, 2006):

$NO + O_3 \rightarrow NO_2 + O_2$ (R1)

$H(\text{or } R\bullet) + O_2 \rightarrow HO_2 \text{ (or ROO)}$ (R2)

$NO + HO_2$ (or ROO•) → NO_2 + OH (or RO•) (R3)

$NO_2 + O_3 \rightarrow NO_3 + O_2$ (R4)

$NO_2 + NO_3 \leftrightarrow N_2O_5$ (R5)

$NO_2 + OH + M \rightarrow HNO_3 + M$ (R6)

NO_3 + VOC → HNO_3 + R• (R7)

$N_2O_5 + H_2O$ + surface → $2HNO_3$ (R8)

where R represents a hydrocarbon chain, and R•, RO• and ROO• are hydrocarbon radicals. Atmospheric nitric acid is an important oxidizer and a major component causing acid rain pollution. The further reaction of nitric acid with NH_3 or alkaline dust generates aerosol nitrates that can be wet or dry deposited to various terrestrial ecosystems as important nutrient inputs (Matson et al., 2002; Bobbink et al., 2010). However, the understanding of the nitrate production mechanism is insufficient, and but critically crucial.

The $\Delta^{17}O$ values of atmospheric nitrate have been observed to vary spatially and temporally, which can be attributed to the impacts of a wide range of atmospheric parameters, shifts in nitrate formation chemistry and transport effects. A marked seasonal trend with higher atmospheric nitrate $\Delta^{17}O$ values during colder months and low values during warm months has been widely found in the tropical to polar regions ranging from 22-44 ‰ (Michalski et al., 2003; Savarino et al., 2007; Morin et al., 2008, 2009). Besides, atmospheric nitrate $\Delta^{17}O$ values also show significant spatial variations. For example, the high-latitude regions typically have higher atmospheric nitrate $\Delta^{17}O$ values than the mid-latitude sites (Michalski et al., 2011). Assuming that ozone is the only oxidizer with non-

zero $\Delta^{17}O$ value and the careful inspection of three HNO_3 production pathways (R6-R8), the $\Delta^{17}O$ mass balance equations were derived (Michalski et al., 2003) as follows:

$$^{\Delta}HNO_3(\gamma) = {}^{\Delta}O_3 \bullet (2\phi/3) \quad \text{Eq. 1.2}$$

$$^{\Delta}HNO_3(\eta) = {}^{\Delta}O_3 \bullet (2\phi+1)/3 \quad \text{Eq. 1.3}$$

$$^{\Delta}HNO_3(\varphi) = {}^{\Delta}O_3 \bullet (4\phi+1)/6 \quad \text{Eq. 1.4}$$

where $^{\Delta}HNO_3$ and $^{\Delta}O_3$ are the $\Delta^{17}O$ values for HNO_3 and O_3, γ, η and φ are the mole fractions of the three major HNO_3 production reactions ($\gamma+\eta+\varphi=1$), and ϕ is the oxidation parameter for NO reflecting the mole fraction of NO oxidation by ozone (R1) relative to the total NO oxidation via ozone, HO_2 and ROO (R1+ΣR3). The η pathway (R7) can produce the largest $^{\Delta}HNO_3$, φ pathway (R8) next and finally the γ pathway (R6). Therefore, the $^{\Delta}HNO_3$ fluctuations over space and time can be attributed to the changes in $^{\Delta}O_3$, the oxidation parameter for NO and the mole fractions of different pathways (Michalski et al., 2011), which are together a function of the abundances of ozone, NO_x and VOCs, temperature, pressure, relative humidity, solar radiation and some other factors. High levels of ozone can typically induce high $^{\Delta}HNO_3$ values, and the abundances of O_3 are dependent on the temperature and pressure, while the abundances of VOCs and OH can also impact $^{\Delta}HNO_3$ by shifting the nitrate production pathways. Increased sunlight tends to lower the ϕ but increase the γ, leading to lower $^{\Delta}HNO_3$ and *vice versa*, accounting for the atmospheric nitrate $\Delta^{17}O$ seasonal trends.

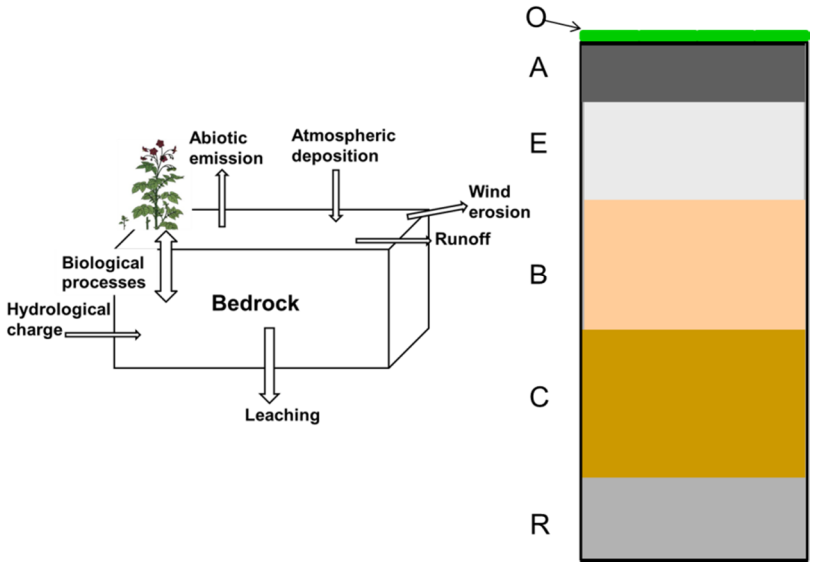

Figure 1.1 The soil formation balance and a typical soil profile in most regions on Earth

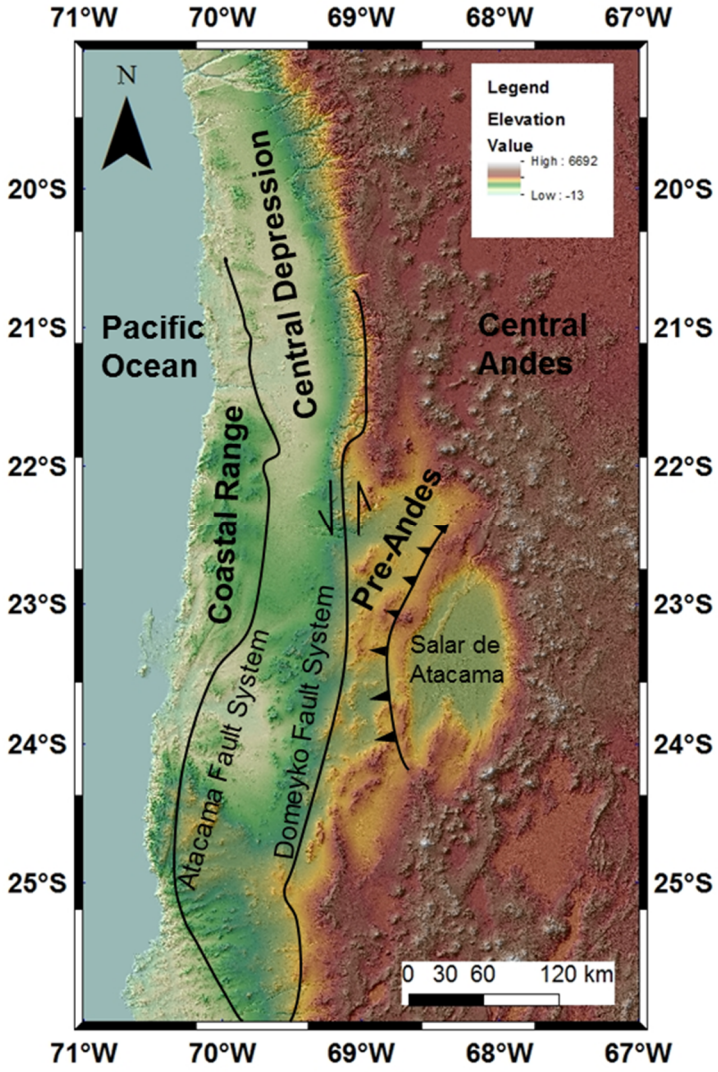

Figure 1.2 Map of the Central Atacama Desert

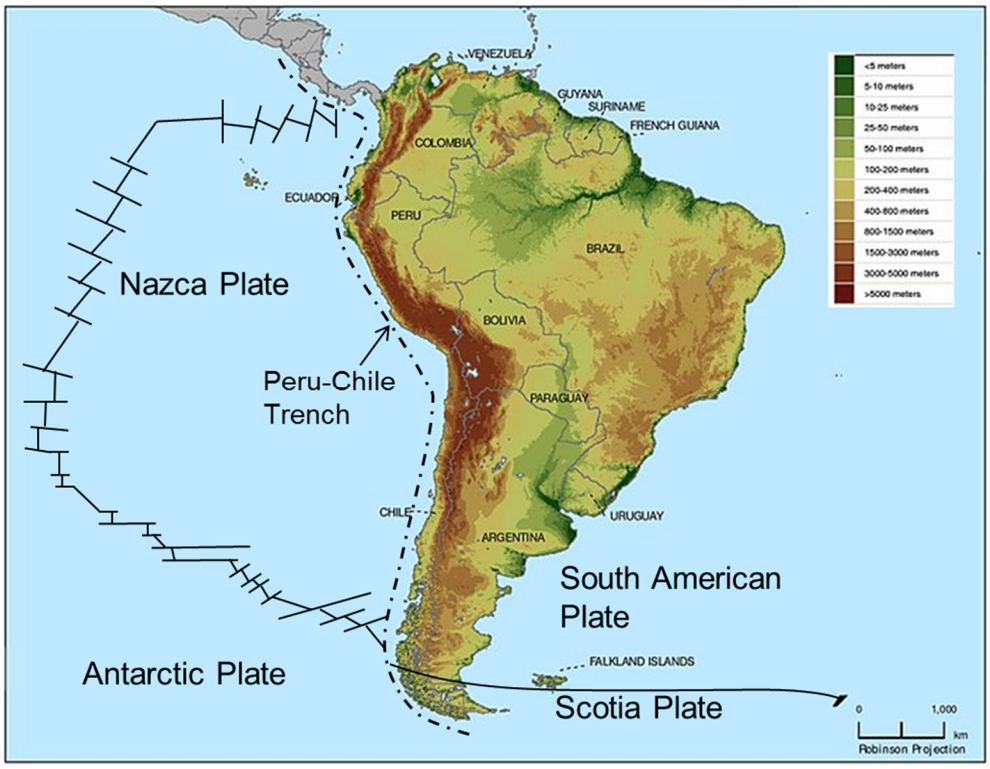

Figure 1.3 Tectonic setting of Chile (The base elevation map of the South America is sourced from http://sedac.ciesin.columbia.edu/place/)

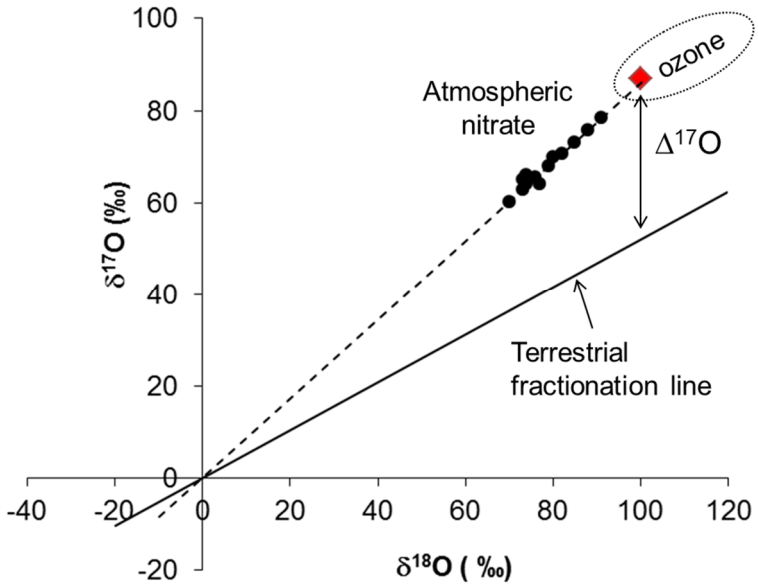

Figure 1.4 The terrestrial fractionation line (TFL) of oxygen and the mass-independent fractionation signatures in ozone (diamond- the median value, oval-the range) and atmospheric nitrates (Michalski et al., 2003 unpublished data)

CHAPTER 2. GEOCHEMICAL, ISOTOPIC AND MINERALOGICAL CONSTRAINTS ON THE ROLE OF ATMOSPHERIC DEPOSITION IN SOIL DEVELOPMENT IN THE HYPER-ARID ATACAMA DESERT, CHILE

2.1 Abstract

Modern atmospheric deposition across the Atacama was collected by an array of dust traps that stretched from the Pacific coast to the Andean Altiplano, and the material was analyzed for its geochemical, mass and isotopic composition, and depositional mechanism. The coastal trap had the second-highest insoluble mineral particle and highest soluble salt deposition rates due to significant inputs from the Morro Mejillones Range and the Pacific Ocean, respectively. The Andean trap had the highest insoluble mineral particle deposition owing to transport of weathered material, but the lowest deposition rate of soluble salts due to its distance from the ocean and anthropogenic sources. The removal of oceanic material was effective by the coastal mountains, while the westward transport of the Andean material was determined to be nominal. The atmospheric deposition in the inland traps was mainly from the local entrainment of surface material, inland anthropogenic emissions, and transport of marine aerosols. The nitrate isotopes ($\delta^{15}N$ and $\Delta^{17}O$) suggested that NO_x sources and NO_3^- chemistry shifted along the west-east transect, and were greatly impacted by anthropogenic emissions with soil NO_3^- being a minor source of deposited nitrogen. By comparing the salt composition

of the atmospheric deposition with that in an Atacama hyper-arid soil profile, the soil salts were suggested to have atmospheric origins, but had undergone post-depositional processes. The atmospheric deposition measurements were used to propose a hyper-arid soil formation mechanism and assess the potential and limitations of ion mass-balance methods for estimating soil ages in the Atacama.

2.2 Introduction

The influence of atmospheric deposition on soil development can be enhanced in arid environments and may be the dominant soil formation mechanism in hyper-arid regions such as the Atacama Desert. The Atacama Desert in northern Chile is one of the driest places on Earth, where the water limitation results in extremely low levels of organic matter and microorganisms in the soils, and little or no plant life across much of the desert (Ericksen, 1981; Navarro-González et al., 2003; Quinn et al., 2005). These conditions restrict normal soil formation processes such as weathering, leaching, mass/chemical transport, and biological transformations. As a result, net mass gains from the atmospheric deposition of dust, including water-insoluble mineral particles and associated water-soluble salts, become a more important aspect of soil development (Dan and Yaalon, 1982; Gerson and Amit, 1987; Quade et al., 1995; Capo and Chadwick, 1999; Ewing et al., 2006; Amit et al., 2007).

Atmospheric deposition can also aid in the development of desert pavements, a ubiquitous geomorphic feature in arid environments. Desert pavements are characterized by a layer of closely packed, interlocking angular or rounded pebble- and cobble-sized clasts that protect the surface from wind erosion (Cooke, 1970). Insoluble mineral

particles and soluble salts deposited from the atmosphere can fill between and beneath the surface rock fragments, promoting the development and uplift of the pavement (McFadden et al., 1987; Anderson et al., 2002). In addition to dense desert pavements, gypsum crusts have widely developed in the Atacama (Ericksen, 1981; Rech et al., 2003). These gypsum crusts could potentially allow fine dust to migrate below the crust surface, trapping atmospherically deposited material in a fashion similar to desert pavements. This desert pavement/gypsum crust theory also suggests that atmospheric deposition is a key mechanism for soil formation in arid systems. Therefore, assessing the rates at which different types of material are deposited from the atmosphere is important for understanding soil formation in arid environments in general, and in the Atacama Desert in particular (McFadden et al., 1987; Reheis and Kihl, 1995).

Atacama soils also contain the largest known nitrate deposits in the world, as well as substantial amounts of other exotic salts whose origins are not fully known. Massive nitrate deposits are unique to the Atacama as well as rare iodate and perchlorate salts, which are rarely found above trace levels in most soils. More common chloride, sulfate, and borate salts are also ubiquitous (Ericksen, 1981). A wide range of theories have speculated on the origins of the salt deposits. Charles Darwin proposed that the salt deposits were formed from "an inland arm of the sea, as may be inferred from the presence of iodic salts in the saline stratum" (Darwin, 1909). Later, the decomposition of organic material in ancient saline lakes and bird guano was proposed as the major source of the salts (Ericksen, 1981), while others argued that direct volcanic emissions (Berger and Cooke, 1997; Oyarzun and Oyarzun, 2007) or the weathering of volcanic rocks (Ericksen, 1961; Chong, 1994) may account for the salt deposits. Atmospheric deposition

of marine or extra-local aerosols (Claridge and Campbell 1968; Van Moort, 1985; Chong 1988) has also been considered an important source of many different types of salts in arid soils. Recent stable isotope evidence has indicated that a significant portion of the Atacama's nitrate, sulfate, and perchlorate salts are photochemically produced and deposited to the soil from the atmosphere (Böhlke et al., 1997; Bao et al., 2004; Michalski et al., 2004). This new evidence highlighted the important role that atmospheric deposition plays in soil formation process in the Atacama.

While it is clear that atmospheric deposition plays a major role in the Atacama's soil formation process, uncertainties still remain about the rates, ionic composition, and sources of salt deposited in the Atacama. Rech et al. (2003) used strontium and sulfur isotopes to indicate that the Atacama gypsum/anhydrite development is mainly impacted by marine aerosols in a coastal site and the eolian reworking of Andean salar salts at inland sites, but the deposition of other material was not investigated. Ewing et al. (2006) analyzed the atmospheric deposition collected at three sites, but focused on evaluating atmospheric element flux along a north-south rainfall gradient without quantitative constraints of the relative importance of various origins of the atmospheric deposition and their importance as a function of distance inland from the coast. Also, the effect of aerosol size and composition on dry deposition rates and the role of fog in wet deposition in the Atacama have not been systematically discussed. Moreover, the extent of surface material that is recycled and the net dust flux across the Atacama remain unknown. In addition, the impact of modern human activities (*e.g.* mining, fossil fuel burning) on atmospheric deposition in modern Atacama has received little attention. Addressing these uncertainties is important for understanding how atmosphere-soil interactions influence

soil formation in hyper-arid regions such as the Atacama. This may have implications for understanding surface processes on other planets such as Mars where soil development in the absence of water has occurred for the past 600 million years (Pike et al., 2011).

In this study, we assessed the composition, rates and potential sources of atmospheric deposition along a west-east transect in the Atacama Desert. The objective was to investigate the spatial variations in modern atmospheric deposition characteristics such as mineralogy, ionic content and accumulation rates in order to explore atmospheric deposition of material from different sources and their influence on soil development. Previous studies indicated that there are two categories of material in atmospheric deposition in the Atacama (Rech et al., 2003; Michalski et al., 2004; Ewing et al., 2006). The first is primary aerosols (*i.e.* eolian material) consisting of marine aerosols from the adjacent Pacific Ocean, weathering of mountainous material, local entrainment of surface material (*e.g.* surface soil, crust, and playas), long-distance dust transport, and direct volcanic emissions (Rech et al., 2003; Mather et al., 2004; Stuut et al., 2007). The second category is secondary aerosols such as nitrates and sulfates, produced from reactive atmospheric gases (Michalski, et al., 2004; Ewing et al., 2006). I hypothesize that eolian material can be carried from different source regions by winds and deposited to the west-east collection array, and the relative importance of each source will be a function of its proximity to a given collector under a relatively constant wind regime. For example, marine aerosols are likely an important source at the coastal sites because sea-salts and other oceanic emissions are enhanced by the regional marine upwelling system off the Atacama's coast as well as the dominant onshore flows of wind (Parungo et al., 1987; Rutllant et al., 2013). These oceanic salts can be transported across the Atacama, and its

importance in the central Atacama should decrease with distance from the ocean. Likewise, aerosols generated during the alteration of the Andean rocks by geothermal fluids or ground water and the denudation of barren mountain slopes of the Andes can be vital for the traps placed in proximity to the Andean Altiplano. The denudation of the Coastal Range and other small mountain ranges and volcanic emissions can also play an important role in material cycles in the surrounding region. Further, local entrainment of surface material is typically high in desert regions as a function of wind patterns, surface coverage, and surface disturbance (Zhang et al., 1997), which can be evaluated by the comparison of the trap material with the surface samples between sites of different surface types. Similarly, secondary aerosols can be deposited locally or transported globally via atmospheric circulation after production. We speculate that the distribution of secondary aerosols in the atmosphere is determined by the regional emissions of precursor gases, the residence time for converting the gases into aerosols, and the removal efficiencies of the resulting aerosols along their transport paths. In modern times, human activities are hypothesized to exert a significant enhancement in the production and deposition of secondary aerosols in the Atacama Desert.

2.3 Sampling and Analysis Method

The physiography of the Atacama Desert consists of three major geologic units going from west to east: the Coastal Range, the Central Valley and the Andes (Figures 2.1 and 2.2). The Coastal Range is a mountain range running north and south that abuts the Pacific Ocean, has altitudes generally less than 2,000 m, and is mantled by Jurassic volcanic sequences interbedded with marine and continental conglomerates

(SERNAGEOMIN, 2003). The Central Valley is a longitudinal depression typically with altitudes between 900 and 2,500 m, comprising a few hundred meters thick layers of Upper Miocene-Pliocene piedmont clastic sediments (SERNAGEOMIN, 2003). The Andes consist of a high plateau known as the Altiplano, at a mean altitude of about 4,000 m surrounded by hundreds of volcanic peaks (~5000 m), and a succession of parallel Pre-Andes mountain ranges (*i.e.* the Cordillera Central in the north and the Cordillera Domeyko in the south) with intervening valleys and basins. The Andes are predominately underlain by Pliocene-Quaternary volcanic flow, tuffs, and breccia rocks (SERNAGEOMIN, 2003).

An array of ten dust traps (T1-T10) were installed along a west-east transect across the Atacama to investigate the spatial variations of atmospheric deposition in the desert (Figures 2.1 and 2.2). The selection of the dust trap locations was based on the accessibility, absence of dirt roads or other artificially disturbed areas upwind, and inconspicuousness. The traps were mostly placed in flat, relatively open areas every 10~50 km inland from the western Pacific coast (see Figure 2.3 for site pictures). Each trap consisted of a single-piece Bundt cake pan (outer ring diameter: 25 cm, surface area: 477 cm^2) fitted with a circular piece of 0.25-inch mesh galvanized screen on which a layer of pre-washed glass marbles were placed to mimic desert pavements (Reheis and Kihl, 1995). The traps were mounted on ~1 m high poles above the ground to eliminate most saltating particles and left exposed from 7/10/2007-1/1/2010 (915 days). Trap 9 was destroyed during this period and is thus excluded from this study.

Atmospheric deposition collected in the traps during this period was retrieved and analyzed. All insoluble and soluble material was removed from the traps by washing the

pans, marbles and screen with deionized water into 1 L plastic bottles. The washed solutions were kept frozen and shipped to Purdue University overnight and gradually freeze-dried in lab. The dried solids, considered as the bulk atmospheric deposition, were weighed to calculate deposition rates and their mineralogical composition was determined using X-ray diffraction. The bulk dust was then washed, filtered to separate the insoluble mineral particles and soluble salts, and the filtrate was measured for pH value using pH meter (Fisher Science). The insoluble mineral particles were air-dried in evaporating dishes and reweighed to measure the soluble salt mass by difference. Two 3 mL aliquots of the filtrate containing soluble salts for each sample were used to analyze cations (Ca^{2+}, K^{+}, Mg^{2+} and Na^{+}) by inductively coupled plasma-optical emission spectroscopy (ICP-OES Thermo Scientific iCAP 6500), ammonium NH_4^{+} by an automated discrete analyzer (Seal Analytical AQ2), and anions (Cl^{-}, NO_3^{-} and SO_4^{2-}) by ion chromatography (Dionex DX-500). Finally, another split was withdrawn from the filtrate and $\delta^{15}N$, $\delta^{17}O$ and $\delta^{18}O$ values of nitrate were analyzed using a bacterial reduction, gold redox method (Kaiser et al., 2007; Riha et al., submitted).

To investigate the impact of atmospheric deposition on the Atacama soil formation, a comparison of the ionic composition between in the trap samples and in the soil was performed. A 225 cm deep soil trench (22.88°S, 69.64°W, 1500 m a.s.l) located in the Baquedano region in the Central Valley near Trap 4 (7 km to the southeast) were sampled at ~5 cm resolution from 15-225 cm. The upper 0-15 cm layer, comprised of blocks of loosely cemented gypsum and sand with vertical cracks at spatial intervals of 10-30 cm, was disturbed during excavation and thus not sampled. The 24-year mean annual precipitation was 0.4 mm 50 km to the north of the Baquedano soil site (Houston, 2006).

The collected soil samples were vesicular and dusky yellow (Munsell color system: 5Y 6/4) containing loosely-cemented sands and fragile aggregates. The size of soil aggregates marginally increased and soil became slightly more compacted with depth. The soil samples were analyzed for the major ion geochemistry by ICP-OES and ion chromatography.

Fog, lake water, and snow samples were also collected and analyzed. A single fog sample was collected overnight (December 2011) at Salar de Grande (21.20°S, 70.01°W, elevation: 847 m) using a 2 m × 2 m polyethylene sheet (termed as "Grande fog" for later discussion). This location is 8 km away from the ocean, ~230 km north of the T1 site. Lake water was collected from the Salar de Tara (23.10°S, 67.43°W, 4260 m, 1.5 km south of the T10 site, termed as "Tara lake water" for later discussion) in January of 2010, while one sample was collected from a remnant snow drift in the Salar de Tara (9 km northwest of the T10 site, termed as "Tara snow" for later discussion) in July of 2007. These samples were analyzed for cation and anion concentrations by ICP-OES and ion chromatography, respectively.

2.4 Results

2.4.1 General Characterization of Dust Deposition

The deposition rate and composition of atmospheric dust varied greatly from the coast to the Andean site (Figure 2.4). The bulk dust deposition rates were highest at the Andean site T10 (35.1 g m^{-2} yr^{-1}) and at the coastal site T1 (16.2 g m^{-2} yr^{-1}), while the lowest was at T7 site (5.0 g m^{-2} yr^{-1}), and was relatively consistent at T2-T6 and T8 sites (6.0-9.7 g m^{-2} yr^{-1}). Similarly, the highest insoluble mineral particle deposition rates occurred at T10

and T1 sites, 32.6 g m^{-2} yr^{-1} and 12.3 g m^{-2} yr^{-1}, respectively, and the T7 site had the lowest insoluble mineral deposition rate of 3.2 g m^{-2} yr^{-1}. The deposition rate of soluble material (*i.e.* soluble salts and other soluble material) significantly decreased from 4.0 g m^{-2} yr^{-1} at T1 site to 2.5 g m^{-2} yr^{-1} at T2 site ~65 km inland, and stayed relatively consistent from T2-T10 (2.7 ± 0.3 g m^{-2} yr^{-1}). For all traps, the soluble salts accounted for 1.4-16.6% of the bulk dust and 19-58% of the total soluble material (Figure 2.4).

2.4.2 Mineralogical and Geochemical Compositions

The major mineral (>5% by mass) assemblage in atmospheric bulk deposition for T1-10 sites was anorthite-quartz-albite-gypsum (Table 2.1). In general, the X-ray diffraction patterns of atmospheric deposition were similar but those at T2-T8 sites were slightly different from those at T1 and T10 sites. For example, T1 site has a significant amount of halite, while T10 site is mainly composed of anorthite with minor amounts of albite (<5%).

Ion analysis of the soluble salts showed that all these sites were rich in Cl^-, NO_3^-, SO_4^{2-}, Na^+, and Ca^{2+}, which totaled over 90 % of the dissolvable salt mass, with small amounts of NH_4^+, Mg^{2+} and K^+ cations also being present (Table 2.2). T1 site had the highest or second-highest deposition rates of those five major ions among all the nine sites. There was a sharp decrease in Na^+, Cl^- or SO_4^{2-} amount going from T1 to T2 site, where the soluble ion deposition rates were relatively consistent from T2-T8 sites. The lowest deposition rates of the major ions occurred at the Andean site (T10). The molar ratio of $Na^+/(NO_3^-+Cl^-)$ was approximately 1 (<10 % deviations) at all sites except T1, T6 and T10, while the Ca^{2+}/SO_4^{2-} molar ratios were close to 1 at T2-T8 sites. There were relatively low NH_4^+ deposition rates at all sites, but the highest were at T10 (0.19 mmol

m^{-2} yr^{-1}) and T1 (0.18 mmol m^{-2} yr^{-1}) sites with the lowest at T2-T8 sites ranging from 0.02-0.10 mmol m^{-2} yr^{-1}. Mg^{2+} deposition decreased continuously from the rate of 1.25 mmol m^{-2} yr^{-1} at T1 site to 0.31 mmol m^{-2} yr^{-1} at T10 site. A similar sharp decrease was observed in the K^+ deposition from T1 coastal site to T2 inland site, but it fluctuated at T2-T10 sites. The ionic charge was almost balanced (<15% deviations) at all sites other than T10.

2.4.3 Variations in Isotopic Composition of Nitrate

The isotopic composition of the nitrate salt (NO_3^-) also showed spatial differences from the coast to the Andes (Figure 2.5). The NO_3^- $\delta^{15}N$ ranged from +1.5 to +10.6 ‰, and while the NO_3^- $\delta^{15}N$ value generally decreased from the coast (+8.5 ‰) to the inland sites with the lowest value at T8 site, an abrupt increase to the highest value was observed at T10 site. The NO_3^- $\Delta^{17}O$ values were in a relatively narrow range of 24.0-27.8 ‰ with the highest value occurring at T1 site and the lowest value at T10 site. Sample replicates had mean standard deviations of 0.5 ‰ for $\delta^{15}N$ and 0.5 ‰ for $\Delta^{17}O$ (n = 3 for each sample set).

2.5 Discussion

The mass, mineralogical, ionic and isotopic composition of atmospheric dust deposited along the Atacama transect from the coast to the Andes can provide insight to the characteristics of atmospheric deposition at a detailed scale and allows us to investigate possible shifts in sources of atmospheric deposition along the Atacama transect. Therefore, we will individually discuss the T1 site, the T10 site and T2-T8 sites in order to investigate the influence of oceanic inputs, Andean inputs, local entrainment of surface

material, and anthropogenic emissions on the deposition of atmospheric compounds to the Atacama's surface.

2.5.1 The Coastal Site T1

T1 site had the second-largest bulk dust deposition rate (16.2 g m^{-2} yr^{-1}) among the nine sites, which could be mainly accounted for by the high deposition rate of insoluble mineral particles (12.3 g m^{-2} yr^{-1}). This may have been due to T1 being located on a western hillslope of the Morro Mejillones and the influence of weathering of silicate material and a significant down-slope dust flux. The area near T1 site may also have been subject to dust from some small surface mining operations during the collection period. The major mineral assemblage of the Morro Mejillones surface soil was anorthite-quartz-albite, similar to that of the atmospheric bulk deposition. Therefore, weathering material from the Morro Mejillones Range was a significant source of insoluble mineral particles deposited at T1 site. The average ionic composition in the surface soil (0-10 cm) in the Morro Mejillones was: Ca^{2+} 0.006 mmol g^{-1}, K^{+} 0.006 mmol g^{-1}, Mg^{2+} 0.004 mmol g^{-1}, Na^{+} 0.05 mmol g^{-1}, Cl^{-} 0.08 mmol g^{-1}, NO_3^{-} 0.002 mmol g^{-1} and SO_4^{2-} 0.01 mmol g^{-1}. The contribution of salts from the entrainment of surface soil material into the T1 trap would then be the multiplication of soil ion concentration by the insoluble dust deposition rate (12.3 g m^{-2} yr^{-1}). The fractions of the soil ions relative to the corresponding trap ions were 2%, 7%, 4%, 3%, 9%, 1% and 2% for Ca^{2+}, K^{+}, Mg^{2+}, Na^{+}, Cl^{-}, NO_3^{-} and SO_4^{2-}, respectively. It was evident that local soil entrainment accounts for only a small part of the other ions in the T1 trap except K^{+} and Cl^{-}. Therefore, the soil contributions of Ca^{2+}, Mg^{2+}, Na^{+}, NO_3^{-} and SO_4^{2-} ions to the T1 trap were neglected. The contribution of soil Cl^{-} was subtracted from the observed Cl^{-} deposition in T1 trap, and the resulting Cl^{-}

deposition rate of 10.02 mmol m^{-2} yr^{-1} was used as the non-soil Cl^- in the remainder of the discussion in this section. The soil K^+ contribution was not taken into account because of its small absolute amount, which would not affect the major conclusions discussed below.

The soluble fraction of material deposited at T1 site was predominately attributed to ocean salts. Amongst all sites, T1 site had the highest soluble salt deposition rate (4.0 g m^{-2} yr^{-1}), roughly five times higher than the other sites. The salts were primarily composed of Na^+ and Cl^- (Table 2.2), the main salt components of seawater, suggesting major oceanic salt inputs at T1 site. This was not surprising given that the T1 site was located on the windward side of the Morro Mejillones range on the Mejillones Peninsula approximately 6 km away from the ocean and that sea-salt aerosols usually dominate aerosol loadings in coastal regions (Fitzgerald, 1991; O'Dowd and Leeuw, 2007). Further, there were no salt playas on the Mejillones Peninsula or the nearby coast (Stoertz and Ericksen, 1974) and the entrainment of material from salt playas located east of the Coastal Range to T1 site was likely trivial because of the isolation of T1 site from the mainland by the Morro Mejillones and the Coastal Range.

Marine aerosols are comprised of primary and secondary aerosols, both of which appear to be important to ion deposition at T1 site. Primary marine aerosols are sea-salt aerosols (SSA) consisting of seawater droplets that are entrained into the atmosphere, forming particles that are mainly NaCl. The droplets originate from the bursting of air bubbles or tearing of drops off wave crests induced by the action of winds on the ocean, with the supermicron-sized (>1μm) particles typically dominating the aerosol volume (mass) concentration (O'Dowd and Leeuw, 2007). These large sea-salt particles can

quickly gravitationally settle (Lewis and Schwartz, 2004), explaining the high rate of NaCl deposition at T1 site. Secondary marine aerosols are mostly submicron-sized particles formed from the chemical and/or physical transformations of oceanic precursor gases in the atmosphere (O'Dowd and Leeuw, 2007). For example, sulfuric acid derived from the oxidation of marine dimethyl sulfide (DMS, a biogenic gas produced by certain species of marine phytoplanktons) can react on sea salts to form SO_4^{2-} aerosols explaining part of SO_4^{2-} in the T1 trap (Charlson et al., 1987). Also, $NH_{3(g)}$ emitted by the ocean can react with H_2SO_4 to form submicron sized ammonium salts (O'Dowd and Leeuw, 2007). Thus, the presence of NH_4^+ in the T1 trap was also indicative of the existence of secondary marine aerosols at this site. Therefore, the T1 trap may have accumulated marine aerosols, mainly supermicron sea-salt-aerosols and submicron secondary aerosols. This hypothesis was supported by the ionic ratios of the T1 trap salts.

To investigate the contribution of SSA to the ionic load, enrichment factors (EF_{Na}) were calculated for each ion (X) relative to the seawater using $EF_{Na} = (X/Na)_{dust}/(X/Na)_{seawater}$, where $(X/Na)_{dust}$ and $(X/Na)_{seawater}$ are the ratios of the ion X to Na^+ concentration in atmospheric dust or seawater, respectively. Here, Na^+ was used as the reference trace element to calculate the enrichment factors at T1 site because Na^+ is derived predominantly from seawater, is easily determined using the ICP-OES technique, and has a high concentration in sea-salt aerosols that is insensitive to perturbation by outside sources (Keene et al., 1986). The average composition of ions in seawater was taken as: 0.546M Cl^-, 0.468M Na^+, 0.0103M Ca^{2+}, 0.0102M K^+, 0.0532M Mg^{2+}; 0.0282M SO_4^{2-} (Millero, 1974). All of the ions showed some enrichments ($EF_{Na}>1$), except non-soil Cl^- and Mg^{2+}, that were depleted, and Na^+ (by definition = 1.0) (Table

2.3). This indicated that at T1 site there was a loss of Cl^- and Mg^{2+} whilst there were sources of Ca^{2+}, K^+, and SO_4^{2-} other than that derived from dissolved ions in seawater.

The non-soil Cl^-/Na^+ of 0.42 at T1 site was much lower than the typical seawater equivalent ratio of 1.17, likely related to the reaction of NaCl aerosols with atmospheric acids. Acids such as HNO_3 and H_2SO_4 produced photochemically in the atmosphere can displace Cl^- by liberating the more volatile acid $HCl_{(g)}$ (Ayers et al., 1999; Newberg et al., 2005), resulting in the loss of Cl^- from aerosols to the air column. This is consistent with the observations of Cl^- deficits in marine aerosols, and especially, smaller aerosols are more depleted in Cl^- owing to their higher surface to volume ratios (Harkel, 1997). During my rainless collection period with typical wind speeds of 3-10 m s^{-1}, these Cl^- depleted aerosols could have rapidly dry deposited to the land surface (including T1 trap) with the dry deposition velocity of 1~6.5 cm s^{-1} (McDonald et al., 1982). Some dry deposition of volatilized $HCl_{(g)}$ may have also occurred in the trap by interacting with its surface material but it was unlikely retained because of its high volatility and inertness of the glass marbles. Assuming Cl^- was mainly lost by the displacement reaction with HNO_3 and H_2SO_4, then $[Cl^-]_{loss} = 1.17 \times R[Na^+] - R[Cl^-]$, where R[X] was the deposition rate for the X ion, and 1.17 was the Cl^-/Na^+ molar ratio in the seawater. This yielded a $[Cl^-]_{loss}$ of 17.94 mmol m^{-2} yr^{-1}, a 60% Cl^- deficit when referenced to Na^+. This deficit at T1 site was comparable to the Cl^- deficits of ~50% in aerosols over northern Chilean coastal waters observed during the VAMOS Ocean-Cloud-Atmosphere-Land Study field campaign (Chand et al., 2010) or the 83% Cl^- deficit in bulk atmospheric deposition ~120 km southeast of T1 calculated based on the data reported by Ewing et al. (2006). This

chloride deficit should have been equivalent to the sum of secondary NO_3^- and SO_4^{2-} acids (excluding the SO_4^{2-} from seawater).

The EF_{Na} for SO_4^{2-} was 6.6 showing that sources other than seawater contributed to the bulk of SO_4^{2-} at T1 site. Besides its existence in seawater, SO_4^{2-} can be produced within the atmosphere mainly by oxidation of SO_2 into sulfate by OH radicals, H_2O_2 and ozone via heterogeneous and homogeneous pathways (Khoder, 2002; Seinfeld and Pandis, 2006). These sulfates are distinguished from the sea-salt sulfate and often termed as non-sea-salt (NSS) sulfate. A substantial fraction of NSS sulfates are associated with sea-salt aerosols because the high pH of sea-salt water promotes a rapid oxidation of reduced sulfur species into NSS sulfates via ozone (Sievering et al., 1990; Song and Carmichael, 2001). However, once the sea-salt aerosol alkalinity is consumed, the H_2O_2 and halogen oxidation pathways become significant (Vogt et al., 1996; Keene et al., 1998). The NSS sulfate amount can be calculated based on: $R[NSS\ SO_4^{2-}]=(EF_{Na}(SO_4^{2-})-1)\times R[SO_4^{2-}]/EF_{Na}(SO_4^{2-})$. This resulted in a NSS SO_4^{2-} deposition rate of 8.1 mmol m^{-2} yr^{-1}, and a corresponding seawater sulfate deposition rate of 1.4 mmol m^{-2} yr^{-1}. Considering one H_2SO_4 molecule could displace two NaCl molecules during the reaction $2NaCl + H_2SO_4 \rightarrow Na_2SO_4 + 2HCl$, assuming this NSS sulfate was previously in the form of H_2SO_4, then it could account for most of the Cl^- loss with a remaining Cl^- deficit of 1.7 mmol m^{-2} yr^{-1}.

Natural sources of the NSS SO_4^{2-} at T1 site could be volcanic and oceanic reduced sulfur emissions (*i.e.* DMS) as well as the entrainment of gypsum from salt playas. Volcanic emissions can be important over long timescales that encompass volcanic activity (Andres et al., 1991), but these were absent over the time scale of my sample

collection (Source: National Geophysical Data Center/World Data Service). Gypsum from several small playas (Salar de Carmen, Salar de Navidad and Salar Mar Muerto) within 150 km southeast of T1 site (east of the Coastal Range) (Rech et al., 2003; Stoertz and Ericksen, 1974) were probably transport limited because of the mountain barriers and predominant westward air flow (see detailed discussion below) and was thus likely a trivial source of SO_4^{2-}. This suggested that DMS oxidation may account for a significant fraction of NSS at T1 site. The average ocean/atmosphere DMS flux was estimated to be 1.4±0.1 mmol m^{-2} yr^{-1} for the coastal regions near Antofagasta (Yang et al., 2011); slightly lower than the estimated 2.1±2.4 mmol m^{-2} yr^{-1} for the gyre regions in Southeastern Pacific (Marandino et al., 2009). The latter flux was observed away from the Atacama's coast in a region with relatively higher wind speeds and during the Southern Hemisphere's summer months when there was higher primary productivity. Both wind-speed and primary productivity enhance ocean-atmosphere DMS fluxes, likely explaining the higher DMS flux in the open ocean relative to the coastal region. Based on these studies, a DMS deposition flux range of 1.3-4.5 mmol m^{-2} yr^{-1} was adopted, and by assuming all DMS was converted to an equimolar amount of NSS sulfate and deposited to the surface, this estimated DMS-derived sulfate flux could account for 16-56 % of NSS sulfate observed at T1 site. It showed that the deposition of DMS-derived sulfate could be at least equal to, or as much as three times higher than, the deposition of sea-salt sulfate along the coastal Atacama.

A check of the estimated sea-salt SO_4^{2-} and NSS deposition rates can be carried out using sulfur isotope mass balance. Rech et al. (2003) measured the $\delta^{34}S$ values of surface gypsum deposits in several Atacama coastal soils, which can be considered sulfate in the

absence of human impacts and surface disturbance. The two natural sources of oceanic sulfate have distinguishable $\delta^{34}S$ values: +21.1 ±1.9‰ for seawater SO_4^{2-} and +15.6 ±3.1‰ for DMS-derived SO_4^{2-} (Calhoun et al., 1991). The isotopic mass balance equation is therefore: $\delta^{34}S_{NDEP} \bullet R_{NDEP}[SO_4^{2-}] = \delta^{34}S_{sw} \bullet R_{sw}[SO_4^{2-}] + \delta^{34}S_{DMS} \bullet R_{DMS}[SO_4^{2-}]$, where the subscripts NDEP, SW, and DMS stand for natural rates (R) of atmospheric deposition, seawater, and DMS emission, respectively, and $R_{NDEP}[SO_4^{2-}] = R_{sw}[SO_4^{2-}] + R_{DMS}[SO_4^{2-}]$. Based on the delineation between seawater and DMS SO_4^{2-} fluxes and assuming these fluxes have remained constant prior to human sulfur sources in the region, the pre-anthropogenic sulfate $\delta^{34}S_{DEP}$ value would range from +16.9 ± 2.5 to +18.4 ± 2.8‰. This was close to the $\delta^{34}S$ values (+16.6 to +18.3‰) of soil sulfate located 4-8 km away from the coast and ~60 km south of the T1 site (Rech et al., 2003). This demonstrated that the sulfate $\delta^{34}S$ values near the coast were slightly lower than the seawater sulfate $\delta^{34}S$, likely due to the DMS flux rather than any imprint from the Andean weathering material as indicated by Rech et al. (2003). Thus, ignoring the importance of DMS flux has likely resulted in an overestimation of the importance of Andean weathering SO_4^{2-} inputs to the Atacama (Rech et al., 2003).

Anthropogenic reduced sulfur emissions could account for the remaining NSS sulfate. Important local anthropogenic sources of sulfur include regional power plants and copper smelters (Table 2.4). However, there were several lines of evidence suggesting that large amounts of anthropogenic sulfur emitted were not effectively transported to or deposited at T1 site. Firstly, most of the anthropogenic sources were inland, separated from T1 site by the Morro Mejillones and Coastal Ranges. These fog-laden mountain ranges were

effective barriers for boundary layer transport of soluble compounds (discussed below). Further inland, solar heating of the western slope of the Andes caused daytime upslope air flow (Andean pump) resulting in much weaker seaward air mass returns (Rutllant et al., 2013). This limited the number of easterly-wind events that could potentially pollute the coastal stratocumulus cloud deck with inland anthropogenic or natural sulfur aerosols to only four to eight times per year (Huneeus et al., 2006; Rutllant et al., 2013). Therefore, the inland Noranda and Chuquicamata smelters were unlikely able to significantly impact SO_4^{2-} deposition at T1 site. Moreover, the prevailing wind on the coast was the onshore southwesterly, which further limited possible anthropogenic SO_4^{2-} deposition from inland sites as well as minimizing the impact of sulfur emissions in the city of Tocopilla located 130 km northeast. Hence, the Mejillones Peninsula and the city of Antofagasta (mainly the Edelnor power plant) together emitted 10,970 metric tons of SO_2 per year (1.7×10^8 mol yr^{-1}) (Table 2.4), likely accounting for the remaining NSS sulfate. Given an average wind speed of ~5m s^{-1} (Muñoz, 2008) and a SO_2 lifetime of 10-12 hours in power plant plumes (Ryerson et al., 1998), the SO_2 could potentially spread over a circle area with the radius of 180-216 km area. Thus, the anthropogenic SO_2 emission rate in the T1 surrounding region could account for 4.6-6.7 mmol m^{-2} yr^{-1}. To sum up, all together suggested that the SO_4^{2-} deposition at T1 site was comprised of 28-62% oceanic SO_4^{2-} derived from DMS (1.3-4.5 mmol m^{-2} yr^{-1}) and seawater (1.4 mmol m^{-2} yr^{-1}), and 38-72% anthropogenic SO_4^{2-} (3.6-6.8 mmol m^{-2} yr^{-1}).

The NO_3^- found in the T1 trap, similar to NSS SO_4^{2-}, was produced in the atmosphere by the oxidation of nitrogen (N) compounds and may have accounted for the remainder of the chloride deficit. NO_3^- was deposited at a rate of 3.47 mmol m^{-2} yr^{-1} but was from

secondary, not primary aerosol production. NO_3^- in the deep ocean can exceed 30 ppm, but it is consumed as a nutrient by phytoplanktons in the euphotic zone, leading to surface water concentrations that are usually below detection limits (Whitney and Freeland, 1999). Therefore, primary sea-salt aerosols sourced from the ocean surface do not contain appreciable NO_3^-. Instead, nitrogen oxides (NO_x=NO+NO_2) can be emitted from the ground (discussed below) to the atmosphere, where the majority of NO_x is then oxidized to HNO_3 (Steinfeld and Pandis, 2006). HNO_3 can then react on aerosols, including sea-salt particles containing Cl^-, forming particulate NO_3^-, which is ultimately deposited via dry and wet deposition (Mamane and Gottlieb, 1992; Zhuang et al., 1999). The secondary NO_3^- produced should account for the remainder of the NSS sulfate corrected Cl^- deficit. The equivalent sum of the NSS SO_4^{2-} and NO_3^-, called "acid equivalent" below for convenience, was: $2\times R[\text{NSS } SO_4^{2-}]+R[NO_3^-] = 19.7$ mmol m^{-2} yr^{-1}. This actually exceeded the equivalent of the Cl^- loss by 1.8 mmol m^{-2} yr^{-1} and meant that atmospheric H_2SO_4 and HNO_3 had the potential to displace more sea-salt Cl^- than what was observed. This did not occur, probably due to the presence of NH_3 and $CaCO_3$, which can buffer mineral acids (discussed below) in the atmosphere (Ziereis and Arnold; 1986; Evans et al., 2004).

Sources of NO_x that produce NO_3^- include several anthropogenic and natural sources. Anthropogenic NO_x sources include fossil fuel combustion via electric generating units (EGUs), automobiles, and port activities. Natural sources of NO_x include nitrification, denitrification, stratospheric mixing and lightening (Holland et al., 1999; Galloway et al., 2004). The estimated preindustrial inorganic nitrogen deposition in the Atacama region was ~2.9 mmol m^{-2} yr^{-1} (Holland et al., 1999), roughly half of it in the form of nitrate, *i.e.*

~1.4 mmol NO_3^- m^{-2} yr^{-1}. This was in agreement with the estimate for remote ocean islands and south Pacific surface waters by Duce et al. (1991) and Warneck (2000). This suggested that the remaining 2.1 mmol m^{-2} yr^{-1} of atmospheric nitrate deposited at T1 site was of anthropogenic origin, which was supported by nitrate nitrogen and oxygen isotope evidence (discussed below). The anthropogenic nitrate was likely derived mainly from the nearby urban NO_x emissions from the Mejillones Peninsula and the Antofagasta city amounting to 15,200 metric tons NO_x per year (4.0×10^8 mol yr^{-1}) (Table 2.4). The anthropogenic NO_x emissions were 2.3 times the coastal anthropogenic SO_2 emissions, but the anthropogenic NO_3^- deposition was only 0.3-0.6 of anthropogenic SO_4^{2-} deposition. This could be due to an overestimation of natural NO_3^- deposition, an overestimation of anthropogenic SO_4^{2-} in the trap, or long-distance transport of inland SO_2 or SO_4^{2-} to the T1 site, or a combination of all three.

The NH_4^+ deposition rate at T1 site was second highest among the nine sites and provided a buffering capacity that partially explained the excess acid equivalents over the Cl^- loss. After release from the land surface to the atmosphere, NH_3 has a short residence time of only a few hours and mostly deposits to the source region within 50 km (Ferm, 1998). Because of its high solubility, some NH_3 is hydrated to ammonium hydroxide that can be deposited back to the surface with wet deposition (Renard et al., 2004). More importantly, as the dominant atmospheric gaseous base, NH_3 rapidly reacts with atmospheric acids (*e.g.* nitric or sulfuric acids) forming hygroscopic ammonium salts (Ziereis and Arnold, 1986; ApSimon et al., 1987); typically, the $(NH_4)_2SO_4$, with a low NH_3 vapor pressure, is preferably formed compared to the NH_4NO_3. At T1 site, the NH_4^+ deposition rate was 0.18 mmol m^{-2} yr^{-1}, which would indicate that only a small amount of

NH_3 had reacted with atmospheric acids and accounted for only a small portion of the imbalance between the potential acidity and Cl^- loss. Given the estimated imbalance of 1.8 mmol m^{-2} yr^{-1} and a base equivalent from NH_3 of 0.18 mmol m^{-2} yr^{-1}, there would still be a 1.6 mmol m^{-2} yr^{-1} of the acid equivalent unbalanced.

The source of the NH_4^+ at T1 site could be related to both natural system emissions and anthropogenic activities. It is well accepted that modern agricultural systems, especially animal farming and fertilizer application, may have given rise to large emissions of NH_3/NH_4 (NH_x) to the atmosphere (Bouwman et al., 1997). Considering the Atacama is generally barren, these land based natural sources cannot be a significant contributor. Power plants in coastal cities (Mejillones, Antofagasta and Tocopilla) can also emit significant amounts of NH_3, while other industrial processes and on-road automobile emissions are relatively minor. The NH_3 emissions from power plants were ~1/9 of the NO_x emissions in the Antofagasta region (MMA, 2011), suggesting a significant fraction of NH_3 was from anthropogenic emissions. One potential natural NH_3 source is the upper ocean where NH_3 is produced during biological decomposition of organic matter by free-living bacteria or zooplankton (Kirchman, 2000), which can then exchange across the ocean/atmosphere surface (Quinn et al., 1996). The magnitude of this emission depends on the differences in NH_3 concentrations between in the atmosphere and ocean. Quinn et al. (1988, 1990) estimated a net flux of ammonia from the ocean to the atmosphere ranging between 0.7 and 5.8 mmol m^{-2} yr^{-1} in the central and Northeastern (NE) Pacific Ocean based on the measurements of NH_3 concentrations in the seawater and atmosphere. Clarke and Porter (1993) found that ammonium concentrations in aerosols were associated with seawater chlorophyll and had a similar

net ocean to atmosphere flux of 3.6 mmol m^{-2} yr^{-1} over the equatorial Pacific. Despite T1 site being located along coastal Chile's highly productive upwelling zone, which has high ammonium regeneration rates (Probyn, 1987; Farías et al., 1996), my observed NH_4^+ deposition rate (0.18 mmol m^{-2} yr^{-1}) was surprisingly low. Liss and Galloway (1993) indicated that the oceanic ammonia fluxes should be similar to DMS fluxes, but my NH_4^+ deposition rate was at least seven times lower than the DMS-derived NSS SO_4^{2-} at T1 site. The NH_4^+/(NSS SO_4^{2-}) was 0.02, considerably lower than the NH_4^+/SO_4^{2-} molar ratios of 0.2-0.8 in remote marine aerosols in the equatorial Pacific measured by Clarke and Porter (1993). However, the observed NH_4^+ deposition at T1 site was consistent with an estimated dry deposition NH_4^+ flux of 0.18 mmol m^{-2} yr^{-1} in the NE Pacific Ocean (Quinn et al., 1988) and the bulk deposition NH_4^+ rate of 0.16 ± 0.07 mmol m^{-2} yr^{-1} ~120 km southeast of T1 site in the Atacama (Ewing et al., 2006). I consider it unlikely that the observed low NH_4^+ deposition rate was due to post-depositional nitrification of NH_4^+ in the trap based on the nitrate isotopes discussed below. The low rate was probably because free gaseous NH_3 accounted for ~70% of the total NH_3/NH_4 in the coastal atmosphere (Tsunogai, 1971; Yamamoto et al., 1995) and it was not efficiently retained by the inert surface of the dust trap. We conclude that only a small fraction of atmospheric NH_3 has neutralized atmospheric acids to form NH_4^+, suggesting the preferable uptake of atmospheric acids by other atmospheric bases at T1 site.

The large EF_{Na} for soil Ca^{2+} of 7.8 in the T1 trap suggested that there are other calcium sources in addition to dissolved seawater Ca^{2+}. The Ca^{2+} excess (*e.g.* non-sea-salt Ca^{2+} = NSS Ca^{2+}) could come from other major calcium sources that include marine aerosols, weathering of parent material, and surface material. Silicate weathering has

been considered a minor calcium source in the Atacama (Rech et al., 2003). Since there are no salt playas within 80 km of the T1 site, the NSS Ca^{2+} in atmospheric dust at T1 site likely originated from oceanic inputs, including microorganisms with calcified shells, such as Coccolithophorids. Coccolithophorids are a characteristic group of mostly unicellular algae with delicate calcified scales and significant contributors to the phytoplankton community in the South America coastal upwelling regions (Klaveness and Paasche, 1979; Chavez and Barber, 1987). The $CaCO_3$ scales can continually slough off as the Coccolithophorids grow or are released during viral infection or predation. These scales may mainly accumulate in the ocean's surface microlayer (upper 0-1 mm) (Hardy, 1982) and then readily inject into the atmosphere to form marine aerosols (MacIntyre, 1974; Fitzgerald, 1991), which may have led to the observed NSS Ca^{2+} in the T1 trap. Similar observations of marine aerosol NSS Ca^{2+} sourced off coastal New Zealand were attributed to biological surface Ca^{2+} fluxes (Sievering et al., 2004), and my observed Ca^{2+} EF_{Na} of 7.8 is in line with the EF_{Na} for NSS Ca^{2+} (4.6-27.0) in that study. Therefore, it can be concluded that all of the Ca^{2+} deposited at T1 site could be attributed to the ocean, *i.e.* the seawater and phytoplankton. This gave a sea-salt Ca^{2+} deposition rate of 0.53 mmol m^{-2} yr^{-1} and a NSS Ca^{2+} deposition rate of 3.57 mmol m^{-2} yr^{-1} (R[NSS Ca^{2+}] = $(EF_{Na}(Ca^{2+})-1) \times R[Ca^{2+}]/EF_{Na}(Ca^{2+})$).

If all the NSS Ca^{2+} originated from biogenic derived $CaCO_3$, this could account for the slightly positive charge surplus and could further resolve the potential acidity-$[Cl^-]_{loss}$ disparity at T1 site. Generally, the seawater-derived alkalinity could be determined by $0.005 \times R[Na^+]$ (Millero, 1974) of 0.12 mmol m^{-2} yr^{-1}. This alkalinity could be rapidly consumed during the oxidation of SO_2 or NO_x occurring on the sea-salt aerosols

(Chameides and Stelson, 1992). However, the presence of other alkaline species, such as NH_3 or $CaCO_3$, could help neutralize atmospheric acids. If assuming all NSS Ca^{2+} in the form of $CaCO_3$, the alkalinity equivalent of NSS Ca^{2+} was 7.14 mmol m^{-2} yr^{-1}, which far exceeded the unbalanced acid equivalent of 1.8 mmol m^{-2} yr^{-1} remaining after removing chloride displacement reactions. This was in line with the near-neutral pH value of the dust at T1 site despite the high amounts of acidic NSS and NO_3^- (Table 2.2). The reactions of atmospheric acids with $CaCO_3$ or NaCl aerosols may have accounted for the low NH_4^+ deposition rate at T1 site. The Ca^{2+} deposition rate (4.10 mmol m^{-2} yr^{-1}) was comparable to the natural sulfate (seawater SO_4^{2-} + natural NSS SO_4^{2-}) of 2.7-5.9 mmol m^{-2} yr^{-1}. This suggested that, in the absence of human sulfur emissions, sea-salt aerosols sourced off northern Chile would contain high amounts of $CaSO_4$, but little $CaCO_3$ because of the NSS SO_4^{2-} reactions. Transport of these aerosols inland and their deposition may have contributed to widespread $CaSO_4$ (anhydrite) or $CaSO_4 \cdot 2H_2O$ (gypsum) mineral crusts observed in surface soils across the hyper-arid core of the Atacama (Ericksen, 1981; Rech et al., 2003). Any sulfur excess, either from natural volcanic or anthropogenic SO_2 emissions or increased DMS, would result in Ca^{2+}/SO_4^{2-} variations and a shift towards the production of other sulfate minerals, such as thenardite (Na_2SO_4), typically found in the subsurface of the Atacama soils.

The depletion of Mg^{2+} (EF_{Na}: 0.5) was difficult to explain with any natural Mg^{2+} losses or anthropogenic processes. Mg^{2+} can randomly substitute Ca^{2+} to form Mg-calcite ($CaCO_3$) (Gattuso and Buddemeier, 2000; Andersson et al., 2008), and thus a Mg^{2+} excess was expected, but my observation contradicted this. We are arguing that the Mg^{2+} depletion is not a result of Na^+ enrichment by soil entrainment, since by assuming Mg^{2+}

was representative of seawater, half of the Na^+ (12.9 mmol m^{-2} yr^{-1}) would have to come from soil. However, this assumption was unreasonable due to the negligible Na^+ concentration in the surrounding soil profiles (see discussion above). Instead, one possible interpretation was Mg^{2+}-involved unknown reactions inside the collecting pan. There was some hard white material that could not be dissolved or washed from the trap screen and may have formed insoluble $MgCO_3$ or $Mg(OH)_2$. The highly saline environments and moisture (fog) in the T1 trap may have promoted this reaction since the same material was not observed in the other traps where fog incursions are rare. However, Sievering et al. (2004) also reported a similar Mg^{2+} deficit relative to Na^+, but it was attributed to additional Na^+ inputs from the soil and glass fiber filters. We could not rule out some other unknown natural Mg^{2+} loss processes.

There was an EF_{Na} of K^+ (1.8) that must also have had origins other than seawater K^+. The slight enrichment of K^+ in the T1 trap compared to seawater was not likely from natural biomass fuel use, or open burning of vegetation, since this did not occur in the arid, non-vegetative environment near T1 site (Didyk et al., 2000). Also, the K^+ excess was not likely due to the contribution from local soil K^+ because of the low content of K^+ in the soil as discussed above. Therefore, the K^+ excess may have been of anthropogenic origins, such as the fossil fuel burning or industry activities.

Wet deposition is the removal of atmospheric gases and particles by precipitation consisting of in-cloud and below-cloud scavenging and this may have been important at T1 site. While there was nearly no rainfall at T1 site (Houston, 2006), high-altitude terrains (>500m elevation) can intercept low clouds to produce fogs, locally called “camanchaca”. These camanchaca may form every day in the winter and twice a day

during the summer at some places because of high humidity, cold ocean surface waters, and widespread nuclei from salts and kelp (Schemenauer et al., 1988). Fog deposition rates along the Atacama's coast have been reported (8.26 and 1.43 L m^{-2} day^{-1} at two sites 80 and 350 km south of T1 site, respectively) (Kidron, 1999; Larrain et al., 2002), but they were much higher than that predicted by surface deposition rates because of the fog collector design. These collectors were oriented vertically and collect fog proportionally to the horizontal wind component (Schemenauer and Cereceda, 1994). Surface fog deposition, on the other hand, was mainly a function of the fog droplet fall velocities that were typically 1-5 cm s^{-1} (Fuzzi et al., 1985; Garreaud and Muñoz, 2005), considerably lower than the horizontal wind speeds. If the fog liquid water content at T1 site was assumed to be 0.1 g m^{-3}, a typical water content for stratocumulus (Schemenauer and Isaac, 1984; Schemenauer and Joe, 1989), then the flux of fog water to the ground would be the product of fog droplet fall velocity and the liquid water content, giving a fog deposition rate of 1-5 mg m^{-2} s^{-1}. This rate was similar to an observed fog deposition rate of 2.2 mg m^{-2} s^{-1} measured using a flat-funnel device (Fuzzi et al., 1985), similar to my collection trap orientation. With a foggy day frequency of ~70% (256 days per year) (Schemenauer, 1988; Cereceda and Schemenauer, 1991; Cereceda et al., 2008) and lasting for 8 hours a day, the annual fog deposition at T1 site could then range from 7-37 L m^{-2} yr^{-1} (equivalent to 0.7-3.7 cm annual precipitation), in line with the fog deposition rate of 25 L m^{-2} yr^{-1} estimated using the eddy covariance method at Cerro Guanaco (300 km to the north of T1 site) (Westbeld et al., 2009). Given this volume, the ion deposition rates at T1 site may have been greatly impacted by the fog deposition.

Estimates of the fog ion deposition rates at T1 could be derived if the ion concentrations of the fog were known. Multiplication of the median fog deposition rate (22 L m^{-2} yr^{-1}) and the average ion concentrations in two coastal fogs (El Tofo and Grande fogs) (Table 2.5) gave conflicting rates. The ion deposition rates based on the Grande fog ion concentrations were 13-30 times higher than those measured by the T1 trap. In particular, the Grande fog was considerably more enriched in Ca^{2+} than El Tofo fog (67 fold), and had a Ca^{2+}/SO_4^{2-} molar ratio of ~1 similar to gypsum minerals found on the Salar de Grande's surface, near where the fog was collected. The NO_3^- concentration in Grande fog was 25.4 times in El Tofo fog, and six times higher compared to the T1 Trap, suggesting the Grande fog may have been subject to anthropogenic NO_x emissions from the nearby Tocopilla city and Tarapacá power plants (Table 2.4). This indicated that Grande fog ion content was considerably impacted by the dust from Salar de Grande and anthropogenic emissions and it would not be suitable for the comparison with the T1 trap sample. The El Tofo fog had a similar ionic composition to the T1 trap as shown by EF_{Na} (Table 2.3) despite small discrepancies in Ca^{2+}, Mg^{2+} and Cl^-. Using the El Tofo fog ion content as the basis, the fog Na^+ deposition rate at T1 site was 4.6 mmol m^{-2} yr^{-1}, which was 20% of the total Na^+ deposition rate (23.9 mmol m^{-2} yr^{-1}). The Cl^-/Na^+ molar ratio of 1.06 in the El Tofo fog (EF_{Na}: 0.9, Tables 2.3 and 2.5) indicated that there was nearly no Cl^- deficit in the El Tofo fog (the same EF_{Na} of 0.9 for the Grande fog). This was likely because displaced $HCl_{(g)}$ in the air column could be scavenged by the fog. This scavenging would not be apparent in the T1 trap because the dissolved HCl would volatilize upon evaporation of the fog water. The fog Ca^{2+} deposition rate at El Tofo was estimated of 0.5 mmol m^{-2} yr^{-1}, 10% of that in T1 trap sample, and its EF_{Na} of 5.2 was

also lower than the EF_{Na} of 7.8 for Ca^{2+} for T1 trap sample, which was probably related to the smaller number of the Coccolithophorids at the latitude of El Tafo site compared to the T1 site in South Pacific (Saavedra-Pellitero et al., 2010). The EF_{Na} for SO_4^{2-} in El Tofo fog of 7.5 was slightly higher than that of 6.6 for T1 trap sample. The significantly larger EF_{Na} for K^+ and Mg^{2+} of the El Tofo fog as well as the Grande fog suggested that K^+ and Mg^{2+} in fogs were more enriched than in the T1 trap sample, possibly because of K^+ and Mg^{2+} minerals in local land surface material entrained and captured by the fog at these two fog sites. While the two fog samples were both subject to local entrainment and geographic influence, the estimated El Tofo fog ion deposition rates were likely more similar to the fog ion deposition rate at T1 site. This suggested that fog could be an important pathway of atmospheric deposition and even more efficient in scavenging gaseous species. However, given the uncertainties in estimating fog ion deposition using data from sites other than T1, future monitoring of T1 site fog deposition rates and fog water composition is warranted.

The fogs may enhance coastal deposition of large marine aerosols but may not significantly impact small particles' transport inland (sea salts, NSS Ca^{2+}, and secondary NO_3^- and SO_4^{2-}). Two mechanisms for marine aerosol removal are possible. The first is simply that the fogs are nucleated on aerosols that would predominately be large sea-salts along the coast, and the high frequency of fog events would result in high removal rates (Noone et al., 1992; Seinfeld and Pandis, 2006). The second mechanism is cloud processing, where small sea-salt particles accumulate in fog droplets as solutes but the droplets are not deposited. Upon evaporation, the salts crystallize forming larger aerosols relative to their initial state that can then be more effectively removed by gravitational

settling (O'Dowd et al., 1998). The fogs, however, are typically occurring at low elevations (500-1000 m) (Cereceda et al., 2002, 2008) and these two mechanisms would not be effective in removing particles high in the boundary layer and free troposphere. Small particles and gases, such as SO_2 derived from DMS and HNO_3, are more effectively mixed above the sea surface in the free troposphere (Ferek et al., 1986) and would therefore be more efficiently transported inland. This would suggest that deposition of secondary aerosols generated over the ocean, particularly NSS SO_4^{2-}, would be proportionately more important inland relative to the coast and that a significant faction of the Atacama's sulfate deposits are a result of biogenic sulfur emissions (in the absence of human sulfur emissions).

2.5.2 The Andean Site T10

The T10 site was located in a closed basin surrounded by rolling hills and a high-altitude lake (4260 m) on the Andean Altiplano. The bulk dust deposition rate of 35.1 g m^{-2} yr^{-1} at T10 site was more than two times the rate at the other sites, and 92.7% of it was ascribed to sand-sized insoluble mineral particles. These were likely due to mineral particles blowing in from the surrounding hills during frequent high winds. The ionic contents in the local surface soil (0-10 cm) at T10 site were low, 0.0005 mmol g^{-1} Cl^-, undetectable NO_3^- and 0.0004 mmol g^{-1} SO_4^{2-} (preliminary data), yielding a potential deposition flux of 0.02 and 0.015 mmol m^{-2} yr^{-1} Cl^- and SO_4^{2-}, respectively. This indicated that the local soil deposition contributed less than ~1% of Cl^-, NO_3^- and SO_4^{2-} to Trap 10, suggesting that local soil surfaces exerted a negligible influence in the deposition of Cl^-, NO_3^-, SO_4^{2-}, and other ions. Therefore, soil contribution to ionic deposition was not considered in the remainder of the discussion. The total salt deposition rate (2.6 g m^{-2} yr^{-1}) was relatively

low compared to T1, probably due to its distance from the ocean and the lack of anthropogenic pollution in this remote, high-elevation region. However, the Andean weathering and long-distance transport from the easterly source could be unique material sources on the Andean Altiplano that may have provided significant inputs to the atmospheric deposition at T10 site (Rech et al., 2003). Therefore, a detailed study of the atmospheric deposition at T10 site can be meaningful to identify the Andean signatures for atmospheric deposition, which is potentially used to further determine the importance of Andean sources for the atmospheric deposition in the Atacama region.

The ionic charge was not balanced at T10 site (positive/negative charge ratio of 0.77), in contrast with the other sites. This indicated there may have been other positively-charged ions (iron and H^+ would be insufficient to account for the balance) or functional groups present in the soil but not detected by my measurements. Ion charge imbalance in deposition has also been observed by other studies in the Atacama (Schemenauer and Cereceda, 1992; Grosjean et al. 1995; Ewing et al., 2006). The T10 site was close to vegetation-covered soils that surrounded the Tara Lake and were likely sources of organic matter and clays. Therefore, the charge imbalance at T10 site may have been due to the presence of negatively charged organic matter or clay minerals that could exchange cations during filtration.

The T10 site was the wettest site, with the annual average precipitation of ~150 mm, thus wet deposition could account for a significant fraction of soluble ions at T10 site. However, during my 2007-2009 collection period, La Niña was in effect and precipitation was only approximately 50 mm mainly as snow (DGA, 2010). In order to constrain the importance of snow in ion deposition at T10 site, ion concentrations in three regional

snows were compared. The ion concentrations in a remnant snow drift (Tara snow) near T10 (except Cl^-) were considerably higher than in the El Tatio or Cerro Tapodo snow (two fresh snow samples) (Ginot et al., 2001; Houston, 2007) (Table 2.5). This was probably because ion concentrations in snow drifts (Tara snow) were known to increase through snow sublimation. Therefore, Tara snow was excluded from my further comparison with the T10 trap data. The ionic concentrations (except NO_3^-) in the Cerro Tapado snow were 5-47 times lower than in the El Tatio snow, which could be explained by the ion dilution effect occurring at Cerro Tapado site because of snow accumulation rates as high as ~1000 mm yr^{-1} (Ginot et al., 2001). Therefore, only snow from El Tatio, which has similar average annual precipitation to T10 site, was used to estimate wet ion deposition at T10 site (Houston, 2007). The snow deposition rates of Ca^{2+}, K^+, Mg^{2+} and SO_4^{2-} could account for 66-92% of those deposition rates detected in T10 trap, while the snow deposition rates of Na^+ and Cl^- exceeded those in the T10 trap. It was unlikely that this was due to the local entrainment of salar salt minerals at El Tatio site (personal communication with Dr. John Houston), but probably because the T10 trap did not effectively retain all snow deposition or due to uncertainties in estimating the total snow fall at T10 site. This also highlighted the uncertainties in using a composite sample collected during one season (December 1999-March 2000) to estimate the net snow deposition rates over a different 2.5-year period. However, similar ionic molar ratios in the El Tatio snow and the T10 trap indicate that the snow precipitation was likely an important contributor of ion deposition at T10 site.

Local ion sources on the Andean Altiplano could also impact the atmospheric deposition at T10 site. The Cl^- deposition rate at T10 site was 2.86 mmol m^{-2} yr^{-1}, the

third largest among the nine sites, while the Na^+ deposition (2.20 mmol m^{-2} yr^{-1}) was the lowest. This apparent contradiction was a result of there being little Cl^- displacement by HNO_3 and H_2SO_4 on NaCl aerosols at T10 site. The lack of Cl^- displacement corroborated by smaller amounts of SO_4^{2-} deposition relative to the Central Valley/coast, negligible amounts of NO_3^- deposition, and a Cl^-/Na^+ molar ratio of 1.3. This suggested that anthropogenic NO_x and SO_2 produced in the Central Valley or on the coast were not effectively entrained into the Andean Altiplano (see discussion below) and were not reacting with local NaCl particles.

The source of the NaCl deposited in the T10 trap was likely local, rather than influenced by oceanic transport as T1 Trap. Mountain ranges can greatly hinder the transport of sea-salt aerosols, which is evidenced by the pronounced attenuation of Cl^- deposition (by 87%) by the Coastal Range (Table 2.2). This suggested that the delivery of oceanic Cl^- over the Coastal Range (1-2 km in altitude), the Domeyko Range (~3 km in altitude) and the Andes front (~5 km in altitude) to the Andean Altiplano located ~320 km away from the Pacific coast was likely negligible. T10 was near the Tara Lake, part of a series of connected salt lakes in the region, whose ionic content is primarily Na^+ and Cl^- with Cl^-/Na^+ molar ratio of 1.1 (Table 2.5). Salt crusts surrounding the lake, as well as large desiccated sections, would likely be a major source of NaCl in T10 trap, espeically in view of the short distance of 1.5 km from the Tara Lake to the T10 trap. This is consistent with Cl^-/Na^+ molar ratio in T10 trap of 1.3 being similar to the ratio in Tara lake water (of 1.1) and local halite minerals (of 1.0). This is also supported by the hypothesis attributing increases in Cl^- in Andean ice cores to recycled Cl^- from salt lakes during desiccation cycles in high-altitude closed basins (Herreros et al., 2009).

Attributing NaCl to the lake system contradicts the conclusion that snow can account for most of the NaCl. However, the high Cl^- concentrations in the El Tatio snow relative to similar mountain systems suggest that local NaCl is likely incorporated into snow. For example, the Cl^- concentrations in snow collected in the Sierra Nevada range (US) average 11.3 μmol L^{-1} (Feth et al., 1964), nearly 10 times less than El Tatio snow. This is in spite of the fact that the Sierra Nevada has several geographic similarities to the Andes, including distance to the ocean, coastal ocean circulation characterized by cold water upwelling zones, the barrier of a coastal range, and high altitude (Feth et al., 1964). Indeed, one would expect the higher elevation of the Andes to result in less Cl^- deposition because of rainout and particle settling. However, salt playas are common in the Central Andes but absent in the US Sierra Nevada, which likely accounts for the difference in the Cl^- concentration in their snow. Thus, it is likely that the high amount of NaCl found in the El Tatio snow was from local dust acting as cloud condensation nuclei or washed out during precipitation events. Therefore, it is unlikely that the salt lake and snow can be considered separate sources of ion deposition in T10 trap rather they are one and the same.

While the NaCl found in the T10 trap may have originated from the Tara Lake system, the SO_4^{2-}/Cl^- molar ratio (0.8) was considerably higher than the lake (0.2), suggesting there were additional source(s) of SO_4^{2-} other than the Tara Lake. There are two copper smelters that can provide SO_2 precursor gases for H_2SO_4 production in the Atacama region (Table 2.4) and the "Andean pump" effect can induce eastward air flows (Rutllant et al., 2013). However, the SO_4^{2-} deposition rate of 2.37 mmol m^{-2} yr^{-1} at T10 site was lowest among all nine sites, suggesting limited amounts of anthropogenic

derived SO_4^{2-} have reached the high altitude site, which was also supported by apparent minimal Cl^- volatilization loss. The low anthropogenic SO_4^{2-} inputs were probably due to most SO_4^{2-} being pumped into the free troposphere and lost instead of being delivered to the Andean Altiplano. Therefore, the SO_4^{2-} in T10 trap could not be mainly attributed to anthropogenic inputs, but the local entrainment of surface, stream, lake, and salar salts (reflecting Andean weathering material) as suggested by Rech et al. (2003).

Total N deposition at T10 site was the lowest of all sites and reflected a relatively pristine environment that is not significantly impacted by Central Valley anthropogenic N emissions. The NO_3^- deposition rate at T10 site (0.54 mmol m^{-2} yr^{-1}) was a factor of 3-8 lower than at the other sites, and only 38% of model-estimated (1.4 mmol m^{-2} yr^{-1}) preindustrial nitrate deposition (Duce et al., 1991; Holland, 1999; Warneck, 2000). It was similar to wet deposition (0.36 mmol m^{-2} yr^{-1}) at a remote high-altitude site on the eastern slope of the Andes in southern Chile (Galloway et al., 1996), supporting the hypothesis that NO_3^- may be primarily due to snow deposition. The NO_3^- was unlikely from local NO_x emissions (a single low usage road) or NO_3^- minerals, since there are no reported nitrate-bearing playas or exposed nitrate minerals in the Andes region. Thus the low NO_3^- deposition rate has reflected limited regional emissions, the modern global nitrogen budget, and the high-altitude effect featured by an efficient aerosol removal along the slope (Galloway et al., 2004). This is consistent with the minor importance of anthropogenic sulfur pollution in SO_4^{2-} deposition (discussed above). The NH_4^+ deposition rate (0.19 mmol m^{-2} yr^{-1}) was the highest of all sites and was likely the result of the local high-altitude prairie ecosystems with significant animal grazing and possibly

the transport of material from the Amazon plain where there are frequent biomass-burning activities (Andreae et al., 1988).

To sum up, the T10 site featured the largest insoluble dust deposition but lowest salt deposition rates among all sites. The salt ions (except NO_3^-) at T10 site mainly originated from the entrainment of local surface material (like salt lakes) or the snow deposition with salt components incorporated, whereas the low NO_3^- and SO_4^{2-} deposition rates reflected a pristine environment with little anthropogenic influences or delivery of SO_2 and NO_x emissions from the Central Valley. Considering the small amounts of salts at T10 site and the predominant eastward air flows, the net flux of salts from the Andean Altiplano to the Central Valley should be small.

2.5.3 The Inland Sites T2-T8

The T2-T6 sites were located in the longitudinal depression (Central Valley) of the Atacama bounded by the Coastal Range to the west and the Pre-Andes (separated by Domeyko Fault system from the Andes Range) to the east. The rain shadow effects created by these two mountain ranges make this central region the driest portion of the desert (<10 mm annual average precipitation), called the hyper-arid core of the Atacama Desert (Ericksen, 1981). The T7 and T8 sites were located on the Cordillera de Domeyko, and the rim of the Atacama basin (Salar de Atacama), respectively. These Pre-Cordillera sites were slightly wetter than the valley site with ~10 mm annual average precipitation (Houston, 2006). The atmospheric deposition at these seven inland sites is hypothesized to be impacted by a mixing of the oceanic and Andean inputs, local entrainment and anthropogenic emissions with essentially no wet deposition.

There was an abrupt decrease in the salt deposition rate from the T1 to T2 site, reflecting an efficient blocking of oceanic aerosol salts by the Coastal Range. The NH_4^+, Na^+, Cl^- and SO_4^{2-} deposition rates at T2 site dropped by 73%, 87%, 83% and 61%, respectively, relative to those at T1 site. This was comparable to the 90% attenuation of sea-salt particles by the 2000 m high coastal mountain range in Alaska (Shaw, 1991), and consistent with low Cl^- deposition in the lee of the Rocky Mountains in the US (Junge et al., 1957). This efficient removal of oceanic aerosol ions was likely related to scavenging by wet deposition (fog) and dry deposition of large sea-salt particles by gravitational settling on the windward side of the mountains (McDonald et al., 1982). The deposition rate of Mg^{2+} decreased by 37% , which could be doubled to 74%, similar to the decrease in Na^+, Cl^- and SO_4^{2-}, if the missing Mg^{2+} in Trap 1 was due to aqueous reactions on the trap screen (discussed above). In contrast, the deposition rates of Ca^{2+} and NO_3^- decreased only by 14% and 17%, respectively. Since most NH_4^+, Na^+, Cl^-, SO_4^{2-}, Mg^{2+} and NO_3^- salts have similar solubility, the lower attenuation of Ca^{2+}, NO_3^-, and possibly SO_4^{2-}, indicated there may have been significant sources of these latter ions other than marine aerosols at the T2 site.

Rech et al. (2003) suggested that Andean inputs are a significant source of material in the Central Valley and Pre-Andes region (T2-T8) but this was not supported by my data. The T10 site had the lowest ion deposition rates (except Cl^-) among all the nine sites, which were specifically lower than at its nearest T8 site by 30-270%, suggesting small aerosol loadings at T10 site and scanty material that could be transported out of the Andes. This was probably because at T10 site, mineral dust from local entrainment can be quickly gravitationally settled and the Andean snow does not occur in low-altitude

regions (Seinfeld and Pandis, 2006). Moreover, considering removal by the Pre-Andes range and the predominant westerly winds in the Atacama induced by the "Andean pump" effect, ion deposition west of the Andes can be mainly regulated by local entrainment of salts rather than Andean inputs. Therefore, though Rech et al. (2003) suggested that the Atacama Ca and S are a mixture of oceanic and Andean inputs, we are arguing that the Andean inputs are relatively minor to the east of the Andes. Indeed, the inland T2-T8 sites could likely be a source region for the Andean deposition such as SO_4^{2-} because of the westerly airflow as discussed above.

The geographic location of the T2 site was similar to the Yungay site studied by Ewing et al. (2006) and a comparison of deposition characteristics between the two sites can give insights into local deposition effects. The Yungay site is located in a mountain basin to the east of the Coastal Range, 95 km to the south of the T2 site at a similar altitude (1276 m versus 1372 m for T2). The ion deposition rates at Yungay were 1.7-5.9-fold higher than those at T2 site (Table 2.2). However, the percentage of soluble/total material at the Yungay site (37 ± 22%) was similar to that at the T2 site (41.4%). This suggested that the Yungay site was subject to significantly more local dust deposition compared to the T2 site. This could not be evaluated, however, because the insoluble dust accumulation rate was not published (Ewing et al., 2006). A similar Cl^- deficit was observed at Yungay (Cl^-/Na^+ molar ratio of 0.2 calculated based on their published data) and T2 (Cl^-/Na^+ molar ratio of 0.3) sites, revealing the presence of acid displacement at both sites (discussed above). The NH_4^+ deposition rate was similarly low at Yungay and T2, while the difference in the NO_3^- deposition rate between the two sites likely reflected their dust deposition difference. The Yungay's Ca^{2+}/SO_4^{2-} molar ratio was only 0.32

compared to 0.96 at T2. Considering the ions at Yungay site were far from being charge balanced, it was difficult to infer the meaning of Ca^{2+}/SO_4^{2-}, which also limits a further comparison of the other ions between the two sites.

After an abrupt decline in the Na^+ or Cl^- deposition rate from T1 to T2 site, these rates were relatively constant at T2-T8 sites. There was no clear trend of the Na^+ deposition rate with distance from the ocean, suggesting that Na^+ at T2-T8 sites was not exclusively from the oceanic inputs, but subject to some other sources. Though the most important source of inland Cl^- deposition may have been sea-salt, there are also salt playas containing chloride deposits (Stoertz and Ericksen, 1974). For example, the relatively high Na^+ and Cl^- deposition rates at the T8 site could be explained by eolian inputs from the nearby Salar de Atacama, the largest NaCl-type salt playa in Chile, while the second-highest Na^+ deposition rates at T5 site was likely attributed to the influence of Salar de Pampa Blanca (7.5 km to the southwest) that is rich in NaCl (Stoertz and Ericksen, 1974). The Cl^-/Na^+ molar ratios at the T2-T8 sites were in the range of 0.2-0.7, indicating a chloride deficit relative to NaCl at these valley sites, which could be due to displacement by atmospheric acids and/or the enrichment of Na^+ deposition. The $Na^+/(Cl^- + NO_3^-)$ molar ratios of 0.94-1.26 approximated to 1 (Table 2.2), which supported the mechanism of Cl^- displacement by nitric acid or the enrichment of Na^+ in the form of $NaNO_3$. I argue that the displacement reactions were more important based on the common absence of $NaNO_3$ in the surface soil and isotopic evidence (see detailed discussion below).

The NO_3^- deposition rate was relatively consistent in the range of 2.0-4.8 mmol m^{-2} yr^{-1} at T2-T8 sites. This was comparable to 17 mmol m^{-2} yr^{-1} if corrected by the several-

fold higher total dust deposition at Yungay site. The NO_3^- deposition inland (T3, T5 and T6 sites) exceeded that of T1 and T2 sites (closest to the coastal urban regions), which could not be completely explained by the coastal anthropogenic inputs. Local entrainment of surface material may have also contributed to the trap NO_3^- deposition. Though there was a lack of NO_3^- in the upper 10 cm of most Atacama soil (preliminary data), there are many historic nitrate mines that have exposed subsurface nitrate minerals that could be sources of atmospheric nitrate. If true, then this would be most evident at T5 site that was located in the Sierra Gorda nitrate works (Ericksen, 1981) and near the Salar de Pampa Blanca that has surface crusts containing $NaNO_3$ (Stoertz and Ericksen, 1974). However, isotopic evidence seemed to refute this explanation.

Modern secondary atmospheric NO_3^- had $\Delta^{17}O$ values of 20-32 ‰, and the T5 site had trap NO_3^- $\Delta^{17}O$ values of 25.6 ‰, within ±0.7 ‰ of the $\Delta^{17}O$ values at the T2-T8 sites. The Atacama surface NO_3^-, on the other hand, had $\Delta^{17}O$ values between 15-21 ‰ significantly lower than the traps values (Michalski et al., 2004). The consistently high NO_3^- $\Delta^{17}O$ values in the T2-T8 trap samples and the absence of a lower $\Delta^{17}O$ values in T5 trap NO_3^- suggested that soil NO_3^- entrainment was minimal. The T3 and T5 sites, with the highest NO_3^- deposition, were ~2 km away from major roads, while T6 site was 40 km away from the city of Calama, both of which emitted significant amounts of NO_x. This suggested that although we tried to minimize the potential anthropogenic influence at my sites, there were still significant anthropogenic activities across the Atacama that impacted ion deposition. This was supported by relatively lower NO_3^- deposition at T7 and T8 sites, which are furthest from road and city NO_x sources.

The Ca^{2+} and SO_4^{2-} deposition rates were relatively consistent at T2-T8 sites (Table 2.2) with the Ca^{2+}/SO_4^{2-} molar ratio of 0.91±0.12. The comparable concentrations of Ca^{2+} and SO_4^{2-} suggested the deposition of $CaSO_4$ (anhydrite) or $CaSO_4 \cdot 2H_2O$ (gypsum) minerals as dust. These minerals may have been sourced from local soil entrainment considering they are widespread on the surface of Atacama soils and usually occur just below surface clasts forming large polygonal surface structures (chuca layer) (Ericksen, 1981; Rech et al., 2003). These surface minerals could be susceptible to wind erosion and disturbance by off-road vehicles, further enhancing regional entrainment (field observation).

That surface gypsum may have been the dominant source of SO_4^{2-} at the T2-T8 sites was somewhat surprising given the amount of anthropogenic SO_4^{2-} emissions along the trap gradient (Table 2.4). In the Antofagasta region, which encompasses most of the traps, the total SO_2 emissions were 3.8×10^9 mol yr^{-1} and dominated by the Chuquicamata copper smelter (the largest open-pit copper mine in the world) while NO_x (x=1.5) emissions were $\sim 9.4 \times 10^9$ mol yr^{-1}. Given a 1.5-fold higher SO_2 emission rate relative to NO_x in the Antofagasta region and assuming equal proportions of NO_x and SO_2 were converted to NO_3^- and SO_4^{2-}, we would expect four times as much SO_4^{2-} relative to NO_3^-. Yet the molar ratio was only 1.2±0.3. Thus it appeared that at least 75% of secondary aerosol SO_4^{2-} was not being deposited in the traps. Even this is a low estimate given that the Ca^{2+}/SO_4^{2-} molar ratio indicated much of the SO_4^{2-} was local gypsum dust.

This low anthropogenic SO_4^{2-} deposition in the Central Valley could arise from several reasons. The chemical conversion of SO_2 into SO_4^{2-} was considerably slower than the oxidization of NO_x to NO_3^- (Seinfeld and Pandis, 2006). Therefore, transport of SO_2

out of the basin may have occurred faster than SO_4^{2-} production. This could be facilitated by the "Andean pump" effect that draws SO_2 eastward into the free troposphere. SO_2 oxidation may have also been hindered by the near absence of boundary layer clouds at T2-T8 sites. In the absence of clouds, the oxidation of SO_2 via OH radical in the gas phase ($SO_2+OH+M(N_2, O_2)\rightarrow HOSO_2+M$) as the only effective pathway. The chemical lifetime (τ) of SO_2 would then be: $1/\tau=k[OH]$ where k was the effective second-order rate constant (4.1×10^{-13} cm^3 $molecule^{-1}$ s^{-1} at 300 K at 2400 m) and [OH] was assumed to be 1 $\times$ 10^6 molecules cm^{-3} (Lee et al., 1990; Seinfeld and Pandis, 2006). This yielded a chemical lifetime of τ =~28 days, sufficiently long for the transport of SO_2 out of the basin before its conversion to SO_4^{2-} and subsequent deposition. In contrast, the apparent higher fraction of anthropogenic SO_4^{2-} at T1 (T10) may have been due to aqueous SO_2 oxidation in the frequent fogs (clouds), which would decrease the chemical lifetime of SO_2 and result in more NSS SO_4^{2-} deposition along the coast.

Despite the overall relatively low SO_4^{2-} deposition rate, the importance of proximity of the anthropogenic sulfur sources for SO_4^{2-} deposition, could be detected near the Chuquicamata smelter. The T6 trap, nearest to the Chuquicamata smelter (~50 km to the north), had the highest SO_4^{2-} deposition rate among T2-T8 sites with the Ca^{2+}/SO_4^{2-} and $Na^+/(Cl^-+NO_3^-)$ molar ratios of 0.8 and 1.3, respectively. This suggested the existence of anthropogenic SO_4^{2-} that could account for the chloride deficit. However, the SO_4^{2-} deposition at T6 site exceeded that of other inland sites by only 0.31-1.35 mmol m^{-2} yr^{-1}, indicating that even at T6 site the deposition of local anthropogenic SO_4^{2-} was limited. This was probably because the Chuquicamata smelter is located to the north of my trap array and the prevailing eastward wind (Rutllant et al., 2013) may have restricted the

transport of SO_2 and SO_4^{2-} southward to my traps. Overall, the contribution of anthropogenic SO_4^{2-} inputs to the T2-T8 sites did not appear to be the main SO_4^{2-} source rather it is surface gypsum/anhydrite dust.

The Mg^{2+} deposition rate logarithmically declined with the distance from T1 to T10 site: $R[Mg^{2+}] = -0.25 \times \ln(\text{distance}) + 1.79$ (R^2=0.94). This was consistent with models and observations that showed oceanic aerosol deposition decreasing exponentially with increasing distance from the ocean (Slinn et al., 1982). This suggested that Mg^{2+} at these nine sites was of oceanic origin, mainly seawater Mg^{2+}. In contrast, the K^+ deposition rate had abruptly dropped from T1 to T2 site and then varied among T2-T8 sites (0.31±0.13%). This could probably be explained by that K^+ is more easily subject to the influences of crustal dust and biogenic sources than Mg^{2+} (Hoffman et al., 1974; Buat-Menard, 1983; Andreae, 1983).

Surface type may have been one of the key factors influencing atmospheric deposition at T2-T8 sites by impacting the local entrainment of surface material. Mineral dust from entrainment of surface material usually has a short residence time because of the rapid gravitational settlement of larger aerosols near the source, and thus the surface type is an important aspect of local dust entrainment. The development of desert pavements and/or gypsum crusts, both common in desert regions, can protect the underlying soil profile from wind erosion, and are key factors controlling the degree of local entrainment (Qu et al., 2001; Goudie and Middleton, 2006). The T8 site had the largest bulk dust deposition rate of 9.7 g m^{-2} yr^{-1} among the seven inland sites. This site had no desert pavements, but rather windy conditions and NaCl crusts. Similarly, sparse desert pavements and disturbed surfaces at T5 site may have contributed to the observed

high deposition rate of bulk dust (9.6 g m^{-2} yr^{-1}) and certain ions, like Ca^{2+} and SO_4^{2-}. Conversely, the T7 site, which contained dense stone desert pavements, had the lowest bulk dust and salt deposition rates of the sites studied: 5.0 g m^{-2} yr^{-1} and 2.2 g m^{-2} yr^{-1}, respectively. Vegetation coverage could increase the adhesive properties of soil in order to stabilize arid soils like stone pavements and interact with the atmosphere (Wolfe and Nickling, 1993). Among T2-T8 sites, T6 was the only site with seasonal shrubs, whose emissions and/or decomposition may have explained why this site had the highest ammonium deposition rates among the seven inland sites.

2.5.4 Nitrate Isotope Variations

The observed $\delta^{15}N$ of the trap NO_3^- varied from 1.5-10.6 ‰, which may have reflected shifts in the NO_x sources. Different anthropogenic and natural sources of NO_x have distinctive $\delta^{15}N$ signatures (Heaton, 1986; Elliott et al., 2007). For example, $\delta^{15}N$ values of NO_x from coal-fired EGUs range from +9.0 to +12.6 ‰ (Felix et al., 2011), while vehicle NO_x exhausts have $\delta^{15}N$ values in the range of +3.7 to +5.7 ‰ (Moore, 1977; Ammann et al., 1999; Pearson et al., 2000) with significantly lower $\delta^{15}N$ values from -13 to +2 ‰ also reported (Heaton, 1990). In comparison to natural NO_x, $\delta^{15}N$ values of NO_x produced by lightning and biogenic emissions range from 0 to +2 ‰ (Hoering, 1957), and from -20 to -49 ‰ (Li and Wang, 2008), respectively. A $\delta^{15}N$ analysis of NO_3^- in a 300 year-old Greenland ice core indicated that biomass burning can induce high $\delta^{15}N$ values of NO_x (+14.3 ‰) while fossil fuel burning is associated with negative $\delta^{15}N$ values (Hastings et al., 2009). These distinguishable $\delta^{15}N$ signatures of NO_x can then be imprinted on atmospheric NO_3^- via the transfer of N atoms during the oxidation of NO_x to NO_3^- and the small N isotopic fractionation associated with this oxidation (Freyer, 1991).

Because the trap NO_3^- was deposited over a 2.5-year period, any $\delta^{15}N$ changes arising from seasonal shifts in NO_x chemistry or sources should have been eliminated. Therefore, $\delta^{15}N$ values of NO_3^- in the traps should reflect the $\delta^{15}N$ of the NO_x sources that produced the NO_3^-.

The observed $\delta^{15}N$ values of the trap NO_3^- varied depending on the trap location, which can help resolve the sources of NO_3^- found in the dust traps. At T1 site, the NO_3^- $\delta^{15}N$ was +8.5 ‰ (Figure 2.5), slightly lower than the $\delta^{15}N$ values of coal-fired EGU-derived NO_x (Felix et al., 2011). This supported the previous prediction that T1 trap NO_3^- was mainly derived from coastal power plant NO_x emissions and port activities whose NO_x $\delta^{15}N$ signatures should be similar since they burn similar fuels (Table 2.3), but also due to natural sources (*i.e.* lightning, biogenic emissions and biomass burning) that typically possess lower $\delta^{15}N$ signatures. The NO_3^- $\delta^{15}N$ value of +7.1 ± 0.6 ‰ at T2 site was similar to that at T1 site, also indicating that the collected NO_3^- was still primarily NO_x transported inland from nearby coastal power plants. There was a decrease in the NO_3^- $\delta^{15}N$ values from T3 to T8 sites. This suggested a shift in NO_x/NO_3^- sources away from EGU's to mobile NO_x sources associated with the city of Calama and the Chilean central highway. The NO_3^- $\delta^{15}N$ of +10.6 ± 0.2 ‰ at T10 was close to the NO_3^- $\delta^{15}N$ values for preindustrial ice core NO_3^- (Hastings et al., 2009), suggesting a minor anthropogenic imprint at T10 site and possibly a significant amount of NO_x from biomass burning on the Altiplano or the Amazon Plain to the east.

The concurrent analysis of stable oxygen isotopes (^{16}O, ^{17}O and ^{18}O) can be indicative of atmospheric chemistry that transforms NO_x into NO_3^- and can help constrain sources of NO_3^- along the trap array. For the majority of the processes on Earth, the

abundances of the three different oxygen isotopes depend on the relative isotope mass differences. This is termed as "mass-dependent fractionation" and follows the rule in $\delta^{17}O \sim 0.52 \cdot \delta^{18}O$ (Thiemens et al., 2006). However, deviations from mass-dependent fractionation have been observed in photochemically produced NO_3^- that can be quantified by $\Delta^{17}O = \delta^{17}O - 0.52\ \delta^{18}O$ (Thiemens, 1999; Miller 2002). Limited measurements have indicated the $\Delta^{17}O$ of modern atmospheric NO_3^- in the range of 20-33‰ in non-polar regions (*e.g.* Michalski et al., 2003; Morin et al., 2009; Costa et al., 2011). The magnitude of the NO_3^- $\Delta^{17}O$ value is a function of the $\Delta^{17}O$ of ozone (the main NO_x oxidant), the amount of NO oxidized by O_3, and the relative importance of three major pathways of nitric acid production in the atmosphere: the third body mediated OH oxidation of NO_2, heterogeneous hydrolysis of N_2O_5 on wet aerosol surfaces, and hydrogen abstraction by NO_3 radicals (Michalski et al., 2003, 2011). Thus, changes in NO_3^- $\Delta^{17}O$ values can be related to atmospheric N chemistry regarding NO_x oxidation.

The NO_3^- $\Delta^{17}O$ values differed significantly between T1 and T10 sites (24.0 and 27.8 ‰, respectively), but were relatively consistent across the remainder sites, ranging from 25.3-26.5 ‰. The NO_3^- $\Delta^{17}O$ value (27.8‰) in the T1 trap was the highest among the nine sites. This was likely because of an increase of the heterogeneous N_2O_5 pathway ($N_2O_5 + H_2O + \text{surface} \rightarrow 2HNO_3$), which had a higher contribution of oxidation by ozone leading to higher NO_3^- $\Delta^{17}O$ values (Michalski et al., 2003, 2011). The enhanced N_2O_5 pathway was probably because of high aerosol surface area from the coastal fogs and high amount of sea-salt aerosols (evidenced by the high salt load in the T1 trap). The limited amount of sunlight caused by thick stratus cloud decks and cool temperature from

Peru Current's coastal upwelling may have also been a factor. The NO_3^- $\Delta^{17}O$ values at T2-T8 sites were significantly lower than at T1 site ($p<0.01$). This was likely the result of a decrease in the importance of the N_2O_5 pathway since the number density of sea-salt and fog particles diminished as the amount of sunlight increased, thus promoting the OH oxidation pathway. The T10 site had the lowest NO_3^- $\Delta^{17}O$ value most likely due to the small amount of NO_x and clean air at this altitude. It is improbable that the midrange $\Delta^{17}O$ values at T2-T8 sites were the result of the mixing of the high $\Delta^{17}O$ NO_3^- from the coastal regions and the low $\Delta^{17}O$ values of NO_3^- from the Andes, since that would require ~80% contribution from the Andean NO_3^- which was unlikely given the Andean site has by far the lowest NO_3^- deposition rate.

2.5.5 Perspectives into Soil Development in the Atacama

The ion content in a 225 cm deep soil profile located in the Baquedano region was compared to the T4 dust trap ion composition in order to assess possible linkages between atmospheric deposition and soil development at this site. The Baquedano soil contained abundant Na^+, Cl^-, NO_3^-, Ca^{2+} and SO_4^{2-} and also small amounts of K^+ and Mg^{2+}, similar to the nearby T4 trap (Table 2.2). When the total salt composition was integrated to 225 cm, there was a remarkable similarity between soil and deposition ion molar ratios in the Atacama (Table 2.2). The Ca^{2+}/SO_4^{2-} molar ratio was 0.81, nearly identical to the T4 trap Ca^{2+}/SO_4^{2-} molar ratio (0.86) and similar to the other inland traps. The Baquedano soil Ca^{2+} and SO_4^{2-} concentrations, however, were relatively low compared to the T4 trap when referenced to Na^+ concentrations. This was probably because the upper 0-15 cm gypsum-cemented sand layer in the soil was not sampled or counted into the soil inventory calculation, which may have caused the underestimation

of soil Ca^{2+} and SO_4^{2-} inventories. The inventories of soil K^+ and Mg^{2+} relative to Na^+ were similar to the ranges of K^+/Na^+ and Mg^{2+}/Na^+ molar ratios in the inland traps. These observations suggested that atmospheric deposition of oceanic salts and photochemical secondary aerosols are the main sources of ionic compounds incorporated into Atacama soils.

In the Baquedano soil, Na^+ was mainly coupled with NO_3^- and Cl^- suggesting two mineral forms, $NaNO_3$ and NaCl. The $Na^+/(NO_3^-+Cl^-)$ molar ratio was 1.04 in the Baquedano soil, similar to the ratios observed at different depths in Yungay soil (Ewing et al., 2006). This supported the assumption that acid displacement reactions on NaCl are natural occurrences. However, the soil NO_3^-/Cl^- molar ratio (0.7) was much lower than those in the T2-T7 traps (2.0-4.8). This was unlikely due to ion separation during the leaching migration and mineral precipitation because of the similar solubility of $NaNO_3$ and NaCl (1.0 mol and 0.6 mol in 100 g water at 20°C, respectively). Instead, the higher NO_3^-/Cl^- molar ratio in the traps was probably because the modern atmosphere over the Atacama has more NO_3^- production via NO_x oxidation relative to the preindustrial Atacama. Assuming the soil NO_3^-/Cl^- ratio reflects natural atmospheric NO_3^- production and subsequent Cl^- displacement, then the modern Atacama troposphere has 2-6 times more NO_3^- (NO_x) relative to pre-anthropogenic conditions. This is consistent with the large regional anthropogenic NO_x emissions (Table 2.4) and the much higher NO_3^- $\Delta^{17}O$ values in the traps (25.8±0.5 ‰) than in the soils (18.5±0.8 ‰) (preliminary data) (see discussion below). Such high increases in NO_3^- concentrations have not been observed in the Andean ice cores (Thompson et al., 2013), which generally showed at most a factor of two increase since the 1900s. This was probably due to the removal of atmospheric NO_3^-

at low elevations, close to the NO_x sources, which is consistent with the low NO_3^- deposition rate observed at T10 site (see discussion in section 2.4.2).

The trap (atmospheric dust) NO_3^- $\Delta^{17}O$ values were significantly higher compared to Atacama soil NO_3^- $\Delta^{17}O$ values, suggesting that humans have altered the nitrogen oxidation chemistry in the troposphere in Chile's Antofagasta region. The high trap NO_3^- $\Delta^{17}O$ values were in the same range as polluted atmospheres found at similar latitudes in Northern Hemisphere (Michalski et al., 2003) and similar to the observations of 26±2 ‰ in low-latitude regions in Southern Hemisphere (Morin et al., 2009). This would suggest that the majority of the NO_3^- in the trap was from deposition of modern NO_x oxidized to NO_3^-, not from entrainment of dust from the NO_3^- mineral deposit that were ubiquitous in the region with much lower NO_3^- $\Delta^{17}O$ values. Moreover, if the soil NO_3^- was important, the T5 site that was in closest proximity to active nitrate mines and nitratine-crusted salars (as mentioned above), would have lowest NO_3^- $\Delta^{17}O$. However, T5 trap NO_3^- $\Delta^{17}O$ was not significantly lower than those at other sites from T2 to T8 sites ($p>0.1$).

The difference between the NO_3^- $\Delta^{17}O$ values in the traps relative to the NO_3^- deposits could be explained by two mechanisms. The first is that soil NO_3^- deposits are comprised of a mixture of biotic NO_3^- ($\Delta^{17}O=0$) and atmospheric NO_3^-. Though the current hyper-aridity in the Atacama has existed for millions of years (Rech et al., 2006), rainfall events of 1 cm or more may still have occurred a few times a century, which could sustain some pioneer bacterial species with short pulses of water (Maier et al., 2004; Lester et al., 2007). These microbes may have produced NO_3^- in the soils and accounted for the lower soil NO_3^- $\Delta^{17}O$. If preindustrial atmospheric NO_3^- had the same $\Delta^{17}O$ value

as the modern dust trap NO_3^-, then matching the soil NO_3^- $\Delta^{17}O$ values observed in the driest regions of the Atacama would require nitrification rates to be (26-20/26) ~20% of the preindustrial NO_3^- input rate. Given the extremely low levels of current NH_4^+ deposition, there was simply not enough NH_4^+ deposited to allow for much nitrification to occur. In addition, bacteria are often absent from extremely hyper-arid soils such as my sites (Navarro-Gonzalez et al., 2003), which would also limit such a high level of nitrification. Rather, the second mechanism-a shift in modern relative to ancient NO_x oxidation pathways-is a more likely an explanation. The higher atmospheric NO_3^- $\Delta^{17}O$ values in modern times were probably the result of a shift in atmospheric N chemistry, *i.e.* high NO_x contents from local and global emissions, elevated levels of troposphere ozone, aerosols, and biogenic gases (Michalski et al., 2011). In contrast, hyper-arid soil NO_3^- reflects preindustrial atmospheric NO_3^- $\Delta^{17}O$ values generated in a troposphere that had trace levels of NO_x, low O_3 mixing ratios and much lower aerosol surface area.

While the total ion contents of the soil mirrors the trap ions, at any given soil depth there were differences, suggesting a mechanism other than a simple deposition is at work in the hyper-arid core of the Atacama. Ericksen (1981) has described a typical soil profile in the hyper-arid core of the Atacama Desert. It is composed of *chuca* (the surface powdery gypsum and anhydrite layer, generally 10-30 cm thick), *costra* (the firmly-cemented gypsum and anhydrite layer, 50 cm-2 m thick), *caliche* (the firmly-cemented nitratine and halite layer, 1-3 m thick), *conjelo* (the saline-cemented regolith, 0-2 m thick) and *coba* (a loose unconsolidated regolith). This is consistent with the later observations of well-developed *chuca* and *costra* layers along the Antofagasta transect (~65 km to the south of my dust trap transect) by Rech et al. (2003) or at Yungay site by Ewing et al.

(2006). At my Baquedano site, the disturbed 0-15 cm gypsum block unit is likely comparable to the *chuca* and *costra* layers, while the underlying layer consisting of loosely-cemented sand with large amounts of nitratine and halite minerals probably corresponded to the *caliche* layer that was, however, not well developed nor cemented. The shallow depths and the low degree of cementation of these *chuca*, *costar and caliche* layers at the Baquedano site suggested that the development of the Baquedano profile was not exactly the same as that of a typical profile described by Ericksen (1981), probably related to the even drier climate at my site. The segregation of salt minerals as a function of depth, whose total composition was similar to atmospheric ion deposition, suggested a post-depositional dissolution-migration mechanism. Despite the well-documented aridity in the Atacama Desert (Houston, 2006), the Atacama Desert straddles between the tropical summer rainfall zone (northeasterly airflows) and the mid-latitude winter rainfall zone (southwesterly moving frontal systems). The annual precipitation amount spans from <2-1000 mm (Houston, 2006), but is typically <10 mm annually in the hyper-arid core zone. This small amount of rainfall can dissolve the surface ions to form concentrated brines with a composition similar to the trap ions. Downward movement of ions within the soil profile and evaporation would lead to a saturated solution and the sequential precipitation of minerals based on thermodynamic equilibrium. Generally, the Ca^{2+} and SO_4^{2-} ions are the first to precipitate forming low solubility gypsum/anhydrite crusts near the surface, while other ions (K^+, Na^+, Mg^{2+}, Cl^- and NO_3^-) can travel further down in the profile depending on the water availability. While ionic compounds are mainly added into desert soils via atmospheric deposition in the Atacama,

insoluble mineral particles of atmospheric dust can also be retained to account for the development of soil profiles together with the evolution of ionic compounds.

2.6 The Influence of Atmospheric Deposition on Soil Development in the Atacama

2.6.1 Soil Development Mechanism

Here I propose a general mechanism for soil development in the Atacama's hyper-arid environment and its relationship to atmospheric deposition. While the process occurs as a continuum, we will discuss the mechanism as it relates to four stages of development. The first stage is the initiation of soil development on regional bedrock material. The second stage is the maturation of soil sequence as it begins to segregate into discrete ionic zones. The third stage is the termination phase, where accumulation has significantly slowed. The final stage is the modern stage where anthropogenic deposition has become a significant factor in soil accumulation.

In the first stage, the decomposition of basement rock plays an important role in the soil formation in the Atacama. Barren surfaces without vegetation coverage can be susceptible to wind erosion, which is evidenced by the high dust loadings in desert regions and may result in the exposure of bedrock on the surface. The deposition of atmospheric salts, an important agent of rock weathering, can enhance the break-down of bedrock material even in the presence of only trace amounts of moisture (Cooke, 1981; Goudie et al., 2002). This salt fracturing (Figure 2.6) can enable atmospheric dust to fill in the bedrock fractures to further advance the bedrock weathering and increase soil material gains. A separation of surface bedrock fragments from the bedrock would also initiate the development of a desert pavement (McFadden et al., 1987) that begins to trap atmospheric dust beneath. The desert pavements also help protect the deposited dust from

subsequent wind erosion (Anderson et al., 2002). In this early phase, the inflation of soil profiles can be slow because of the slow bedrock weathering rates and significant wind erosion.

During the second stage, the continuous influx of long-distance transported dust (trace amounts) and oceanic ions (seawater and biotic emissions), including significant amounts of Ca^{2+} and SO_4^{2-}, can mix with local sands/dust building soil and lifting desert pavements and the ions begin to segregate by leaching during periodic rainfall. The desert pavements become completely isolated from the bedrock and begin to thin as physical and salt weathering continue. Meanwhile, low solubility gypsum/anhydrite crusts are forming at the surface. Unlike the bedded and subsurface gypsum layers typical in wetter deserts (Watson, 1985), surface gypsum/anhydrite crusts in the Atacama are widespread and often found as fragile and powdery crusts just below the pavement surface (Figure 2.6). This difference is likely because, while extreme aridity provides sufficient water to induce gypsum dissolution and rapid recrystallization near the surface, there is not enough water to induce the migration of Ca^{2+} and SO_4^{2-} ion down profile (Ericksen, 1981). These gypsum crusts can now replace the desert pavement's role as the protectors of the subsurface layers from wind erosion. However, desiccation fractures in the crusts (Figure 2.6) can still allow atmospheric dust and salts to continually infill below and inflate the profile over time (Watson, 1985), especially considering the near absence of water and plant life minimizes the normal mass losses via aqueous erosion, leaching and uptake. Excess SO_4^{2-} and highly soluble K^+, Mg^{2+}, Na^+, Cl^- and NO_3^- would migrate deeper into soil profiles, precipitate out and cement the atmospheric dust, together advancing the soil development.

During the third stage of soil formation, the rate of accumulation may slow as the surface gypsum crusts accrete. Over time the surface gypsum crusts may thicken and become a firmly-cemented mixture of atmospheric insoluble mineral particles and soluble salts (Figure 2.6), which may be related to a temporary increase in precipitation. These units have been referred to as "gypcrete" and *costar* (Ericksen, 1981; Watson, 1985). Even in these cements, desiccation and thermal stresses induces fracturing still allowing downward transport of surface material (Hartley and May, 1998). However, the thickness and reduced penetrability of the cemented matrix would likely retard the atmospheric dust accumulation rate relative to the second stage. On the other hand, the gypcrete is likely more effective in protecting accumulated material from wind erosion.

The fourth stage occurs in the current environment in the Atacama. Anthropogenic activities have significantly altered the atmospheric chemistry and the landscapes in the Atacama, and exert a significant influence on the current soil development. For example, we have shown that atmospheric NO_3^- or SO_4^{2-} deposition derived from anthropogenic emissions of NO_x and SO_2 are comparable to or even exceed their natural deposition across the Atacama except the high-altitude Andean site. This will cause substantial increases in modern nitrogen and sulfur inventories but a decrease in the chloride inventory because of the chloride displacement by atmospheric acids, and thus impact the formation of gypsum crusts, an important feature for soil formation, and other salt minerals in the soil. In addition, my data indicated that widespread mining and off-road activities can lead to significant surface disturbance at most places in Central Valley and has enhanced the local entrainment of surface material as discussed above. The surface desert pavements and gypsum crusts (or gypcretes) are particularly susceptible to these

anthropogenic disturbances. The destroying of desert pavements and gypsum crust (gypcretes) will then either enhance wind erosion to slow down soil formation at places without well-developed gypsum crusts or promote the penetration of atmospheric dust to resume the soil development at sites with mature soil profiles. The influence of anthropogenic activities on soil formation can be huge, leading to rapid and irreversible changes in the soil profile development or evolution compared to that under natural conditions, and thus deserves people's immediate awareness.

2.6.2 Ion Accumulation and Soil Age

The ion deposition data presented above suggest that the ion accumulation in hyper-arid regions may be a proxy for soil age, but caution must be used when using modern ion deposition rates to infer past deposition rates. The chloride mass-balance method has been widely accepted to date ground water or soil pore water in semi-arid and arid regions (Tyler et al., 1996; Houston 2007). Similarly, the mass-balance method using other major ions can be used to develop soil ages by dividing the cumulative soil ion concentration from the surface to the depth of interest by the annual ion deposition rate. We have demonstrated that chloride deposition rates varied across the Atacama depending on the distance from the ocean and salars, and they are subject to chloride displacement by natural and anthropogenic HNO_3 and H_2SO_4, which may have varied in the past. Using modern deposition rates in chloride mass balance models would result in significant uncertainties when estimating a soil age. Likewise, compared to the past, modern deposition rates of NO_3^- or SO_4^{2-} have also been shown to be significantly altered by anthropogenic NO_x and SO_2 emissions. Again, using modern human impacted NO_3^- and SO_4^{2-} deposition rates to infer a soil age based on soil NO_3^- and SO_4^{2-} inventories is

tenuous. Conversely, the modern deposition of Na^+, Mg^{2+} and perhaps Ca^{2+} ions are likely conservative with respect to major anthropogenic alteration. Absolute net rates of Ca^{2+} and Na^+ deposition at a specific site, however, are difficult to evaluate because we have shown that local entrainment of surface material containing Ca^{2+} or Na^+ may be significant. Therefore, Mg^{2+} would be the best ion for ion mass balance to estimate the soil age.

2.7 Conclusions

A west-east array of nine dust traps (T1-T8 and T10) were analyzed to investigate the characteristics and spatial variations of modern atmospheric deposition across the Atacama. The coastal trap (T1) had the second-highest insoluble particle deposition rate, perhaps due to the surrounding mountain ranges, and the largest amount of soluble salt that was dominated by Na^+, Cl^- and SO_4^{2-} ions, mainly from oceanic inputs including seawater droplets, calcium carbonate mineral and dimethyl sulfide emissions. The T10 trap was located on the Andean Altiplano and likely susceptible to the weathering material from the Andes, leading to its highest insoluble particle deposition rate. The deposition rates of soluble salt ions at T10 site were relatively low, owing to minimal anthropogenic influence and the direct entrainment of the surrounding salars or snow deposition. There were relatively consistent insoluble mineral particle and soluble salt deposition rates among T2-T8 sites. The oceanic inputs were greatly attenuated because of the blockage of the coastal mountain ranges, and the Andes should have exerted limited importance on material inputs in the inland regions to the west of the Andes because of the little material input and the distance of the Andes as well as the prevailing

westerly winds. Therefore, local entrainment of surface material instead played an important role in determining the atmospheric dust patterns at T2-T8 sites. The NO_3^- $\delta^{15}N$ and $\Delta^{17}O$ indicated the shifts in NO_x sources from the coastal power plants to the road activity emissions at inland sites. In addition, the NO_3^- chemistry experienced decreasing contributions of the N_2O_5 pathway from west to east. Despite the variations in the characteristics of atmospheric deposition across the Atacama, the similarities between soil salt inventory ratios and the salt ratios in the nearest dust trap provided a line of evidence of the depositional mechanism of soil formation in the hyper-arid core of the Atacama. The atmospheric deposition rates can be useful for the ion mass-balance method to date the soil ages in the Atacama Desert.

2.8 Acknowledgements

This work was supported by the National Science Foundation grant (EAR 0922114), Purdue Rare Isotope Measurement (PRIME) laboratory, and Mineralogical Society of America Student Award in mineralogy and petrology. We thank Zane Gilbert, Darrell Schulze, Brenda Bowen and Raul Ochoa for assistance during sample collection and analysis. We are also grateful for Dr. John Houston's contribution about Chilean precipitation information.

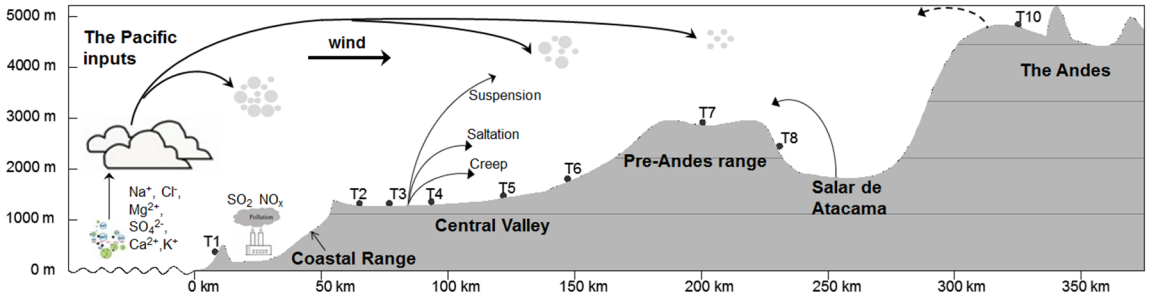

Figure 2.1 Diagram showing the origins and transport of eolian material and secondary aerosols in the Atacama Desert. Seawater droplets, anthropogenic emissions and local entrainment of surface material (mainly suspension process) can be introduced to the atmosphere before they are eventually transported and deposited across the Atacama depending on their distance to the source regions and compositions and sizes.

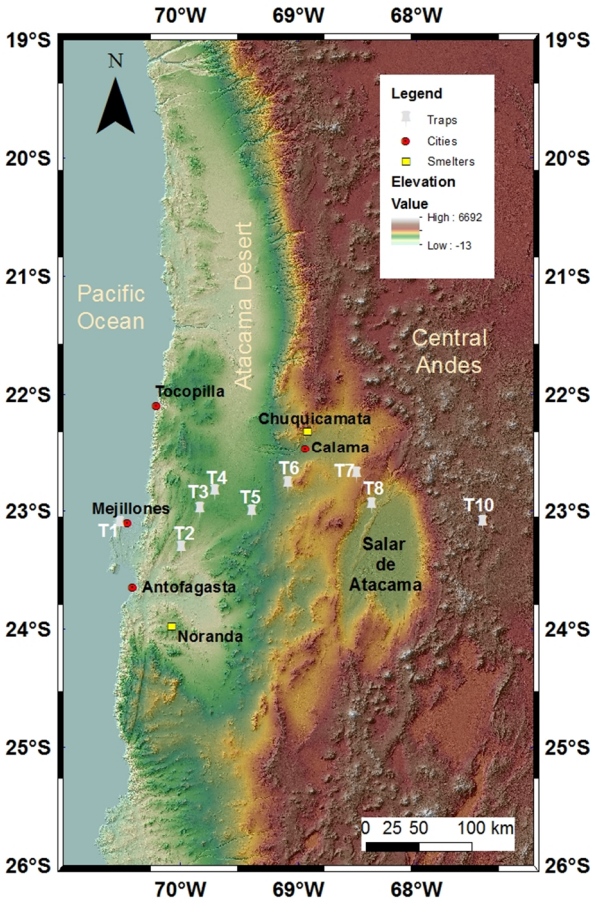

Figure 2.2 Location map of the trap array along an west-east transect across the Atacama Desert, major cities and copper smelters in the Antofagasta region (T1-a barren hillslope of the Morro Mejillones; T2-a barren mountain basin with sparse desert pavements; T3-a barren hillslope with medium desert pavements; T4-a barren mountain basin with sparse desert pavements; T5-a barren alluvial fan with disturbed surface; T6-a mountain basin with dense desert pavements and dry plant roots; T7-a barren hilltop of the Cordillera de Domeyko with dense desert pavements; T8-the Atacama basin rim with salt crusts and holes; T10-a closed mountainous basin with dense desert pavements)

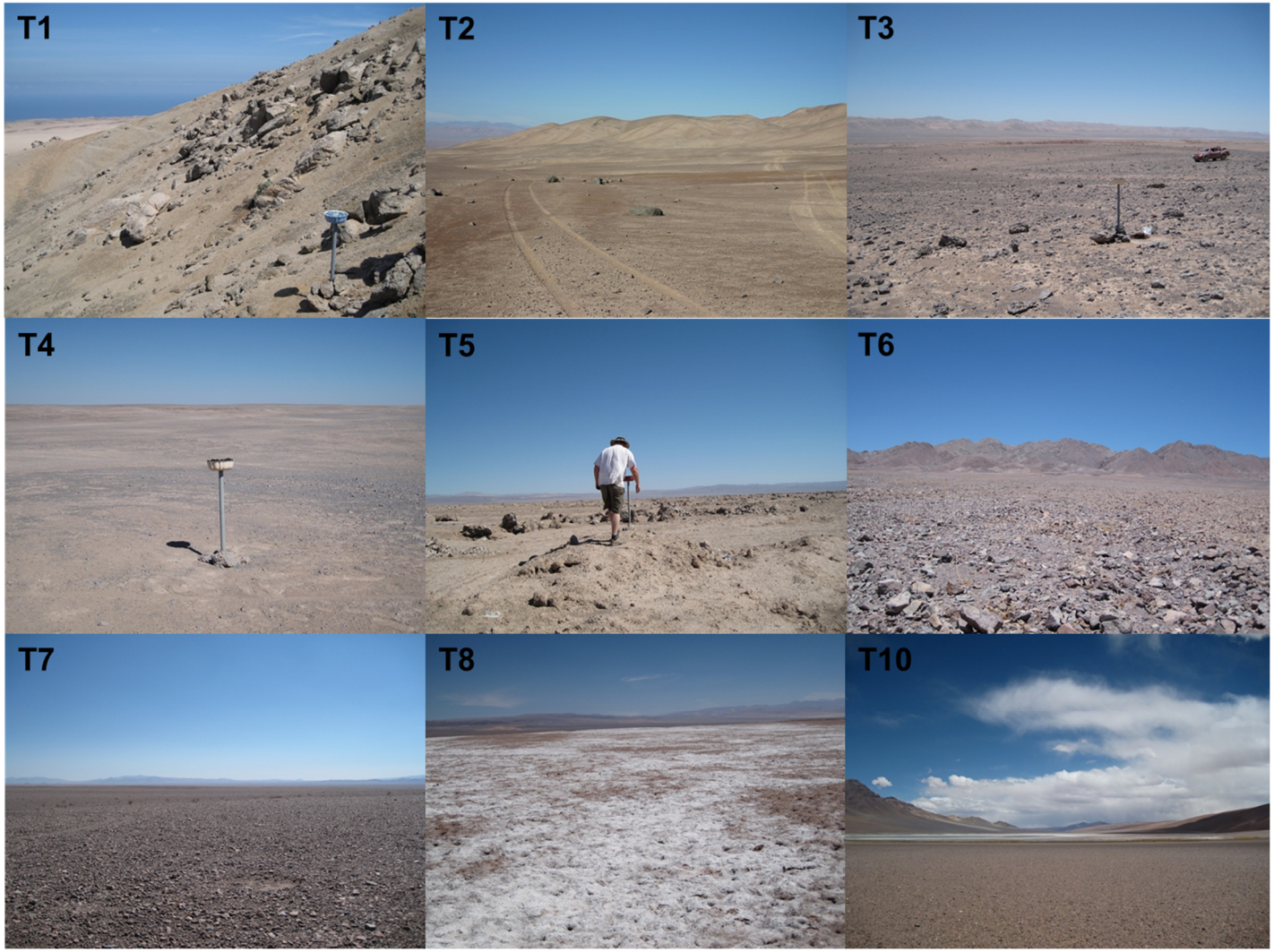

Figure 2.3 Field pictures for the dust trap site

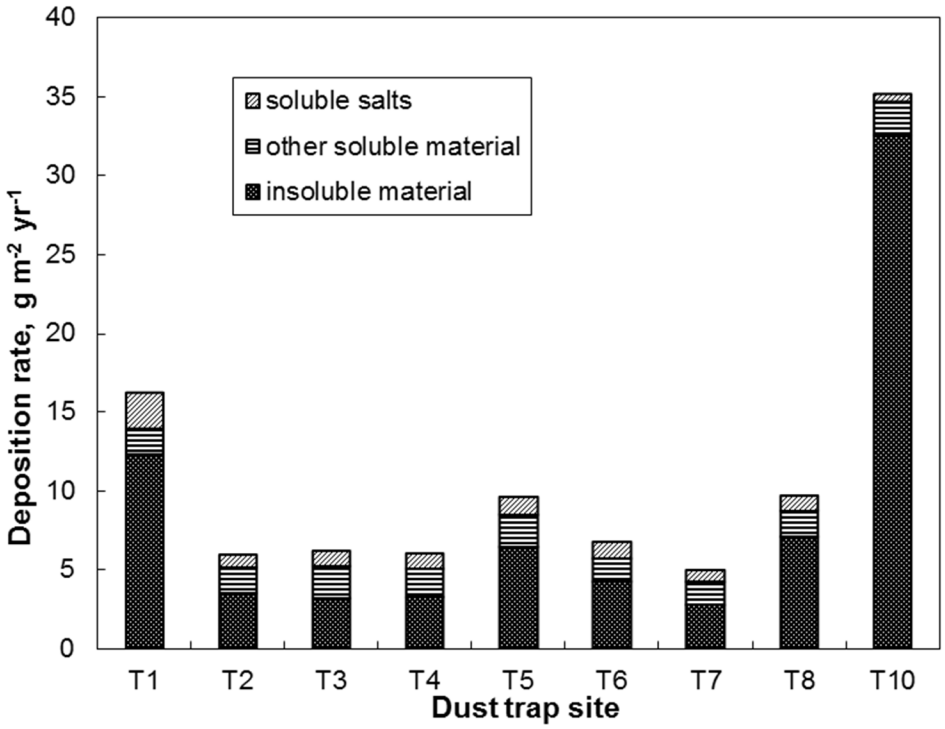

Figure 2.4 The deposition rates and general composition of atmospheric deposition

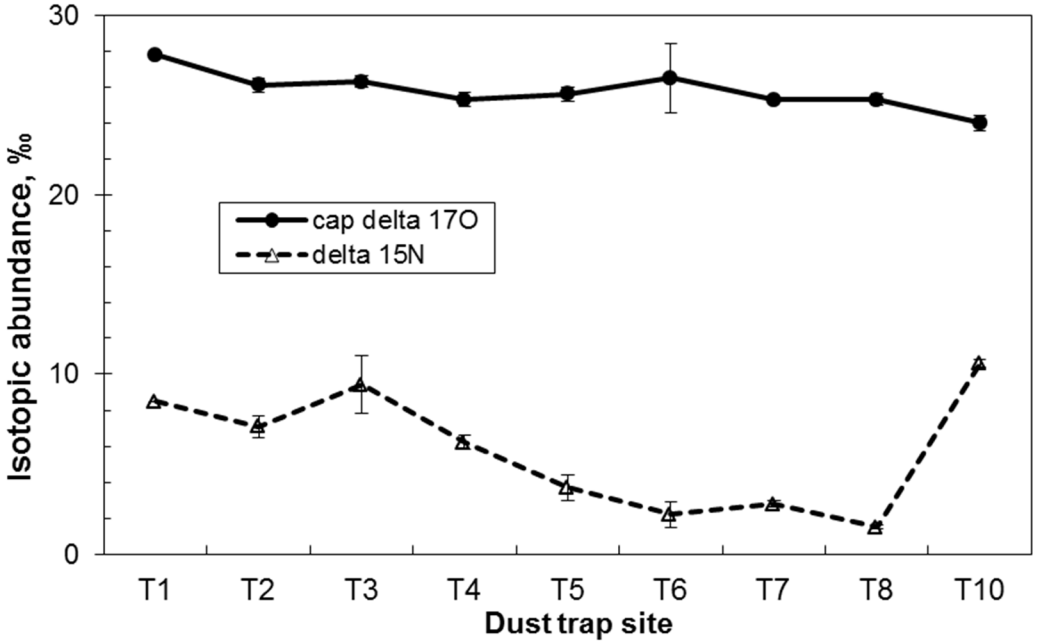

Figure 2.5 The isotopic composition of trap NO_3^-

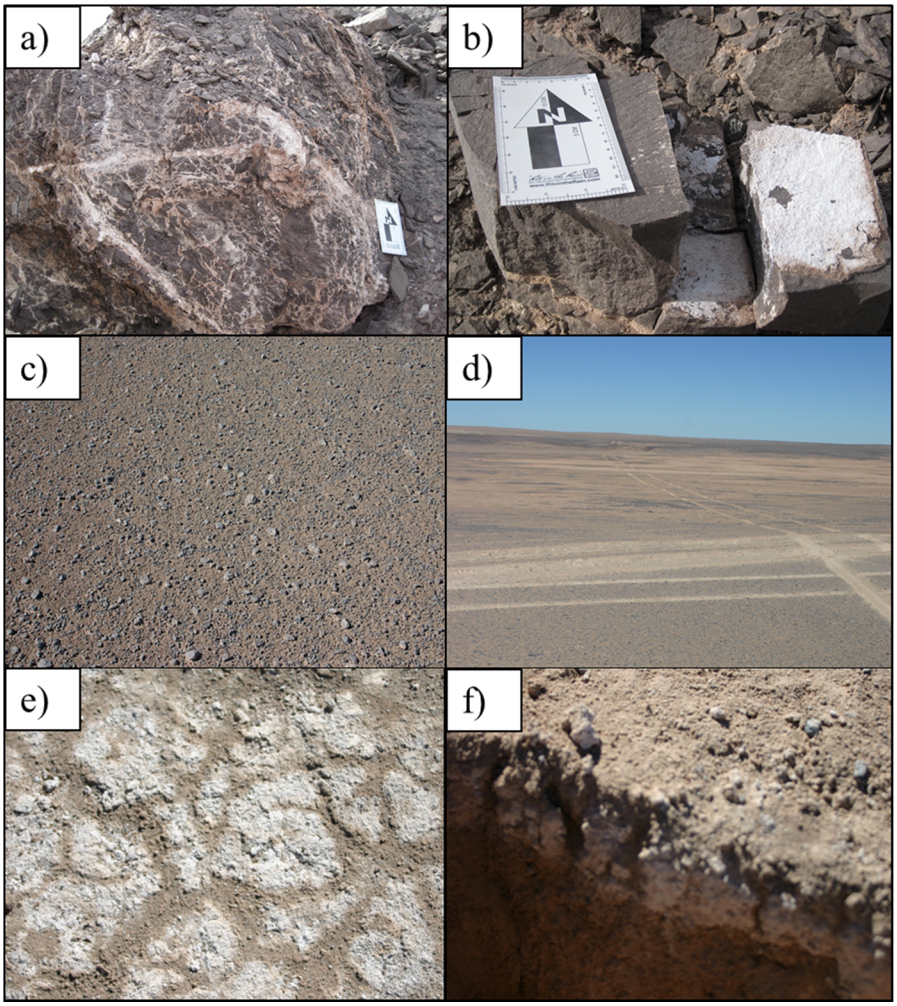

Figure 2.6 Field pictures of salt fractures (a and b), desert pavements and their susceptibility to human disturbance (c and d), and surface gypsum crusts with desiccation fractures and vertical cracks (e and f)

Table 2.1 The major mineralogy of bulk atmospheric deposition

Sampling site	XRD results
T1	An, Qz, Ab, H, Gp
T2	An, Gp, Ab, Qz
T3	An, Gp, Qz, Ab
T4	Gp, An, Qz, Ab
T5	An, Gp, Qz, Ab
T6	An, Gp, Qz, Ab
T7	An, Gp, Qz, Ab
T8	An, Gp, Qz, Ab
T10	An, Qz, Ab

Qz: quartz (SiO_2), Ab: albite ($NaAlSi_3O_8$), An: anorthite ($CaAl_2Si_2O_8$); Gp: gypsum ($CaSO_4$), H: Halite (NaCl) (listed from highest to lowest amount no less than 5%)

Table 2.2 Deposition rates of the soluble ions (mmol m^{-2} yr^{-1}) and the molar ratios and the soil salt inventory (last two rows)

Sampling site	NH_4^+	Ca^{2+}	K^+	Mg^{2+}	Na^+	Cl^-	NO_3^-	SO_4^{2-}	Ca^{2+}/SO_4^{2-}	$Na^+/(Cl^-+NO_3^-)$	Positve/ Negative charge	pH
Coastal site												
T1	0.18	4.10	0.93	1.25	23.90	11.05	3.47	9.53	0.43	1.65	1.06	7.03
Andean site												
T10	0.19	1.55	0.18	0.31	2.20	2.86	0.54	2.37	0.65	0.65	0.77	5.04
Inland sites												
T2	0.05	3.54	0.22	0.79	4.13	1.39	2.88	3.69	0.96	0.97	1.12	4.71
T3	0.04	3.19	0.35	0.75	5.24	0.96	4.62	4.01	0.79	0.94	0.99	6.03
T4	0.06	3.93	0.53	0.85	4.86	1.29	3.54	4.55	0.86	1.01	1.08	4.38
T5	0.02	4.41	0.26	0.70	6.77	1.73	4.83	4.23	1.04	1.03	1.15	6.74
T6	0.10	3.98	0.39	0.66	5.75	0.85	3.70	4.86	0.82	1.26	1.09	6.58
T7	0.03	2.89	0.16	0.37	3.48	1.11	2.74	3.51	0.82	0.91	0.94	4.64
T8	0.06	4.04	0.23	0.43	5.49	3.91	2.00	3.69	1.09	0.93	1.11	5.33
Previous study												
Yungay[a]	0.16	6	n.d.	n.d.	20	4	17	19	0.32	0.95	0.55	n.d.
Salt inventory, 10^2 mol m^{-2}												
Baquedano[b]	n.d.	6.56	0.87	1.38	18.58	10.24	7.54	8.05	0.81	1.04	1.04	n.d.

[a]From Ewing et al. (2006) except the NH_4^+ data that is from Ewing et al. (2007)
[b]For a 225-cm soil profile in the Baquedano region (preliminary data)

Table 2.3 The enrichment factors (EF_{Na}) for different ions in the trap and fog samples

Species	Coastal site		
	EF_{Na} T1	EF_{Na} El Tofo fog	EF_{Na} Grande fog
Ca^{2+}	7.8	5.2	21.7
K^{+}	1.8	2.1	3.7
Mg^{2+}	0.5	1.1	1.0
Na^{+}	1.0	1.0	1.0
Cl^{-}	0.4	0.9	0.9
SO_4^{2-}	6.6	7.5	6.9

Table 2.4 Major regional anthropogenic emissions

Sources	Emissions, metric tons per year	
	NO_x	SO_2
Mejillones Peninsula		
Edelnor power plant (341MW)[a]	7,128	10,951
On-road automobiles[b]	42	0.5
Antofagasta city		
On-road automobiles[b]	1,485	18
Port activities[c]	5,772	
Tocopilla city		
Norgener power plant (277MW)[a]	5,800	8,911
Electroandina power plant (269MW)[a]	10,146	18,357
On-road automobiles[b]	94	1
Port activities[c]	1,653	
Calama city		
On-road automobiles[b]	619	8
Inland smelters		
Chuquicamata[d]		212,000
Noranda[d]		40,000
Antofagasta region (126,049 km^2)[e]	**35,718**	**242,253**
Tarapacá bay (Tarapacá region)		
Celta power plant (158MW)[a]	3,304	5,075

[a]Norgener and Electroandina data from Jorquera (2009), the other power plant data scaled from Norgener data based on their output shown in the parentheses

[b]Antofagasta data from MMA (2011), the others scaled from Antofagasta data based on the population relative to Antofagasta population (2008 population, Mejillones: 10,108; Antofagasta: 354,372; Tocopilla: 22,464; Calama: 147,702, Lagos and Blanco, 2010)

[c]Tocopilla data from Jorquera (2009), Antofagasta data scaled from Tocopilla data based on the maximum loading ratio of 1,676 to 480 million metric tons

[d]Huneeus et al., 2006

[e]MMA et al., 2011

Table 2.5 The ion composition of fog, lake and snow water samples and the derived ion deposition rates

Samples	NH_4^+	Ca^{2+}	K^+	Mg^{2+}	Na^+	Cl^-	NO_3^-	SO_4^{2-}
Ion concentration, µmol L^{-1}								
El Tofo fog[a]	65.0	24.0	9.5	25.8	209.1	221.7	32.7	95.0
Grande fog[b]	n.d.	1621.2	272.0	392.6	3397.9	3546.7	831.1	1406.2
Tara lake water[c]	n.d.	1014.3	153.0	95.7	9935.7	10630.9	0.0	215.6
Tara snow[d]	n.d.	106.3	24.5	14.0	324.0	186.7	10.8	70.9
Cerro Tapado snow[e]	2.8	4.2	0.5	0.9	2.9	3.0	5.7	4.8
El Tatio snow	n.d.	28.5	9.5	5.0	87.0	140.8	n.d.	31.3
Fog ion flux, mmol m^{-2} yr^{-1} with the fog deposition rate of 22 L m^{-2} yr^{-1}								
El Tofo fog	1.4	0.5	0.2	0.6	4.6	4.9	0.7	2.1
Grande fog	n.d.	35.7	6.0	8.6	74.8	78.0	18.3	30.9
Snow ion flux, mmol m^{-2} yr^{-1} with the snow deposition rate of 50 mm yr^{-1}								
Tara snow	n.d.	5.3	1.2	0.7	16.2	9.3	0.5	3.5
Cerro Tapado snow	0.4	0.2	0.0	0.0	0.1	0.1	0.3	0.2
El Tatio snow	n.d.	1.4	0.5	0.3	4.3	7.0	n.d.	1.6

[a]El Tofo (29.26°S, 71.15°W, elevation: 780 m, 34 km away from the ocean) (Schemenauer and Cereceda, 1992)
[b]Cerro Tapado (30.13°S, 69.92°W, 5536 m asl, 800 km south of T10 site) (Ginot et al., 2001)
[c]El Tatio (22.37°S, 68.00°W, 4345 m asl, 100 km northwest of T10 site) (Houston, 2007)
n.d.-not determined

CHAPTER 3. THE ATACAMA SOIL FORMATION TIMESCALES

3.1 Beryllium-10 Concentrations in the Hyper-arid Soils in the Atacama Desert, Chile: Implications for Soil Formation and Paleoclimate Change

3.1.1 Abstract

Soil ^{10}Be concentrations show a systematic decline from the surface to 225 cm deep. This systematic decline of soil ^{10}Be concentrations with depth has been reproduced using a simple model that assumes the soil matrix, including ^{10}Be, builds up as layers over time while ^{10}Be decays *in situ*. This suggests a mechanism of soil accumulation via atmospheric deposition, which is in agreement with stable isotopic evidence. The model estimates an age of ~6.6±0.4 Ma for the total soil profile, while small discrepancies between the model and observations are likely mainly due to changes in ^{10}Be delivery rates that can be impacted by precipitation rates. Interpreted in this way, the ^{10}Be data suggest drying after ~4.7 Ma, which could be due to Andean uplift, and returning to an insignificant wet period at ~1 Ma, which was possibly connected to global climate change.

3.1.2 Introduction

The mechanism of soil formation in hyper-arid regions and its connection to climate have only recently been investigated (*e.g.* Ewing et al., 2006) and remain poorly understood. Soil formation is commonly driven by several key processes, *i.e.* incorporation of organic

matter, break-down of bedrock, atmospheric deposition, weathering, erosion and transportation of solutes, which are integrated over geological timescales (Chadwick et al., 1990). In hyper-arid regions, such as the driest parts of the Atacama Desert, Chile (mean annual precipitation <2 mm), biological activity and water-related processes are limited, and soil development may enter into a new paradigm: soil forms mainly by a simple long-term accumulation of atmospheric deposition ("dust"), *i.e.* eolian sediment, airborne particles and photochemical products (Ewing et al., 2006; Wang et al., submitted). This mechanism is supported by recent isotopic studies showing that deposits of oxy-anions (e.g. NO_3^- and SO_4^{2-}) in the Atacama soils are primarily derived from photochemically produced secondary aerosols (Böhlke et al., 1997; Bao et al., 2004; Michalski et al., 2004). However, details about the factors such as the timescale of soil accumulation and influence of past climate in hyper-arid regions are still uncertain.

Establishing the timescale of soil formation in the Atacama has previously proved challenging. Published efforts to establish the timescale of soil formation in the Atacama have focused on surface exposure dating or dating of volcanic ash layers (Ewing et al., 2006; Rech et al., 2006; Placzek et al., 2009), but both approaches are subject to uncertainties and limitations. The inference of soil ages from surface exposure dates using cosmogenic nuclides is based on the assumption that surficial clasts or boulders are originated from parent rocks and coevolve with soil formation giving the age of the whole soil profile starting from parent material (Anderson et al., 2002). The total soil depth, however, is not always known, and potential prior exposure or disturbance after deposition of surface boulders/clasts can result in additional or reduced cosmogenic nuclide accumulation (Gosse and Phillips, 2001), both leading to poorly constrained ages.

Volcanic ash layers are rare, often spatially discontinuous, and only provide the maximum ages of their overlying soil profile rather than continuous depth-dependent age of discreet soil layers (Placzek et al., 2009). Therefore, new techniques are warranted for constraining the soil formation timescales in the Atacama.

Hyper-aridity has likely prevailed in the Atacama for millions of years (Hartley and Chong, 2003; Rech et al., 2006), but sporadic changes in rainfall rates are believed to have occurred over time (Houston, 2006) and could have had a significant influence on soil formation. With increasing rainfall in hyper-arid regions, atmospheric inputs can increase accordingly, and possible torrential storms can exert a large influence on soil erosion (Haug, 2010); also, a part of the rainfall can percolate through the soil profile to promote the losses of dissolved materials by way of deep seepage (Jenny, 1941). Ewing et al. (2006) have demonstrated that increasing rainfall may induce a shift in the soil formation mechanism from a continuous accumulation of atmospheric solutes with a dramatic volumetric expansion to a net mass loss and volumetric collapse. Also, increased water pulses in the Atacama may induce viable soil microorganisms to become biologically active and initiate their carbon and nitrogen fixation (Azua-Bustos et al., 2012). Amit et al. (2010) also suggested that the depletion of salts in the soil profile caused by precipitation-induced leaching may enable vegetation establishment in hyper-arid regions. However, highly resolved temporal shifts in the Atacama's climate have proved difficult to assess because of the lack of highly time-resolved records.

The Atacama Desert is particularly sensitive to precipitation changes because of its extreme aridity and thus may be a key area to study extreme climatic systems and their global teleconnections. The aridity in the Atacama Desert comes from its geographic

location that creates rain shadow effects bounded by the Coastal Range to the west and the Andes to the east. In addition, the quasi-permanent southeast Pacific subtropical anticyclone and the cold Peru Current generate low sea surface temperatures causing a temperature inversion and thus limited rainfall (Houston and Hartley, 2003). However, evidence indicates that Atacama aridity can be altered by heavy rainfall episodes related to El Niño–Southern Oscillation (ENSO) characterized by a weakened subsiding branch of the Pacific Walker circulation and strong positive sea surface temperature anomalies (Garreaud et al., 2003; Houston, 2006; Vargas et al., 2000). Historical records suggested that there were persistent ENSO instabilities during the glacial–interglacial cycles, but assessing the ENSO modulation dynamics has been largely speculative and limited to model predictions or rare terrestrial climate proxies (Clement et al., 2001). These proxies, however, gave different and sometimes conflicting results about precipitation variability in arid regions over time (Joubert and Hewitson, 1997; Hulme, 2001; Covey et al., 2003; Hewitson and Crane, 2006). Therefore, new precipitation proxies from the Atacama Desert would be useful for detecting regional precipitation variations and their teleconnections to global climate oscillations.

Meteoric beryllium-10 (^{10}Be) has been used in other environments to both constrain soil ages and detect climate change (cf. Willenbring and Blanckenburg, 2010), suggesting it may be a new tool for exploring soil formation mechanisms and recognizing climate change in hyper-arid regions. Meteoric ^{10}Be is produced by spallation of nitrogen and oxygen atoms by secondary cosmic rays in the stratosphere and becomes quickly attached to aerosols (Lal, 1987). When these aerosols are delivered to soil surfaces by dry or wet deposition, ^{10}Be usually becomes bound to soil clay minerals and iron oxy-hydroxides.

The deposited ^{10}Be then decays with a radioactive half-life of 1.39 My (Chmeleff et al., 2010). Thus, concentrations of meteoric ^{10}Be in soils reflect a balance between inputs, outputs and decay over time, and can therefore be used to estimate soil ages and accumulation rates. However, there are several challenges when using ^{10}Be to date soils including ^{10}Be losses by erosion or leaching (cf. Willenbring and Blanckenburg, 2010), variations in ^{10}Be production rates over time (*e.g.* Masarik and Beer, 2009), and shifting ^{10}Be delivery rates that accompany climate change (*e.g.* Lal, 1987). In the hyper-arid core of the Atacama where erosion and leaching are minimized, we have utilized meteoric ^{10}Be concentrations to model the accumulation of a soil profile in order to assess the mechanism and timescale of soil development and to detect any evidence of climatic change.

3.1.3 Method

Soil was collected from a temporary 225 cm deep pipeline trench (22.88°S, 69.64°W, 1500 m a.s. l) located in the central longitudinal depression of the Atacama that is called the "Central Valley". The Central Valley is a result of the uplift of the coastal Range to the west and the Andes mountains to the east over the past 30 million years. The trench surface is covered with sparse desert pavements of moderately to darkly varnished gravel to cobble-sized clasts with no evidence of vegetation or water erosion. The underlying basement material is an alluvial fan of Miocene piedmont sediments (SERNAGEOMIN, 2003) that mantles rocks of Jurassic and Cretaceous age (Ericksen, 1983) (Figure 3.1). The 24-year mean annual precipitation (50 km to the north) was 0.4 mm (Houston, 2006). The soil consisted of two horizons: an upper layer (0-15 cm) comprising blocks of moderately-cemented gypsum and sand with vertical cracks at spatial intervals of 10-30

cm, and a lower layer that was vesicular and dusky yellow (Munsell color system: 5Y 6/4) containing loosely-cemented sands and fragile aggregates (Figure 3.1). This was a relatively simple structure compared to the soil profile in the nearby Yungay region (24.10°S, 70.02°W, 153 km southwest) depicted by Ewing et al. (2006). The surface gypsum block layer was disturbed during excavation and thus not sampled. Forty-three samples were collected at ~5 cm vertical resolution in the lower layer.

The salt-cemented soil aggregates were gently broken up and a dry sieve analysis was conducted to study the grain size distribution with depth. An average soil density of 1.4 g cm^{-3} was calculated by slightly compacting soil into a specific volume. The major mineral assemblage throughout the profile is quartz-anorthite-albite with intermittent existence of halite, nitratine or gypsum at depths determined by X-Ray Diffraction analysis. One gram of bulk soil (<2 mm fraction) was weighed, powdered by a ball mill, and extracted of soluble salts with 45 mL Millipore water using vortex mixing. Cation (Ca^{2+}, Na^{+}, K^{+} and Mg^{2+}) concentrations in the soil extracts were determined using Thermo Scientific iCAP 6500 inductively coupled plasma-optical emission spectroscopy (ICP-OES). Dionex DX-500 ion chromatography with suppressed conductivity detector (Alltech 626 model) was used for anion analysis (NO_3^{-}, SO_4^{2-}, Cl^{-}). The mass content of water-insoluble fractions, obtained by subtracting the cation and anion (including completely extracted gypsum) contents measured by ICP-OES and ion chromatography, was ~90% for each sample.

Atmospheric deposition was collected using two passive dust traps installed at two adjacent sites (<30 km distance), which were chosen on the basis of absence of dirt roads and inconspicuousness. The traps consisted of a single-piece Bundt cake pan fitted with a

circular piece of 1/4-inch-mesh galvanized screen on which a layer of pre-washed glass marbles suspend to mimic desert pavements on the surface (Reheis and Kihl, 1995). The traps were mounted on ~1 m high poles above the ground to eliminate most saltating particles. Atmospheric deposition during the rainless period 7/10/2007-1/1/2010 (DGA, 2011) was recovered by rinsing the pan and marbles with Millipore water. The rinse solution was kept on ice until transported to a location where they were frozen and shipped overnight to Purdue University. The frozen solution was freeze-dried, and the resulting solids weighed. The solid material was re-suspended in Millipore water and filtered to remove water soluble ions, and the insoluble fraction was dried and weighed again. The trap extract was also analyzed using ICP-OES and ion chromatography for cation and anion concentrations. Water-soluble salts comprise 39±7% of the dust mass.

The bulk soils and dust residues (water-soluble salts being removed) were analyzed for ^{10}Be concentrations. They were sieved and 0.5-1 g of the <2 mm fraction was leached using 10-20 ml 0.5 M HCl at 60°C for six hours. The leachate should contain only meteoric ^{10}Be because the samples were not subjected to physical treatment or HF decomposition, and the acid was too weak to liberate *in situ*-produced ^{10}Be that is typically incorporated inside the quartz minerals. After ^{9}Be carrier addition, the Be was separated by EDTA titration, cation exchange, and pH-specific precipitation. ^{10}Be/^{9}Be ratios were determined by accelerator mass spectrometry (AMS) at the Purdue Rare Isotope Measurement (PRIME) laboratory. The average ^{10}Be amount in blank controls of 3.88 (±1.37) × 10^5 atoms (n=7) was subtracted from all samples. All reported ^{10}Be concentrations were normalized to insoluble fractions in soils or atmospheric dust (see Table 3.1 for detailed analytical data).

3.1.4 Results

The measured soil ^{10}Be concentrations exponentially decreased with depth (Figure 3.2). The highest values (1.36-1.45 × 10^8 atoms g^{-1}) occurred near the surface, and the lowest concentrations (4.78-6.90 × 10^6 atoms g^{-1}) were at the bottom of the profile. This decreasing trend was similar to a ^{10}Be decay curve as observed in several Chinese loess and a New Zealand loess sequences (Gu et al., 1996; Graham et al., 2001). There were small but significant deviations from the exponential decrease at depths of approximately 25, 75, 100 and 175 cm. Sieving analysis has showed that the soil is composed of 4±4% gravels (>2 mm), 91±10% sands (63 μm-2 mm) and 5±2% silt and clay (<63 μm) by mass (Figure 3.3). The ^{10}Be concentration in atmospheric dust was 1.24 (±0.19) × 10^8 atoms g^{-1}, and the bulk and insoluble dust deposition rates based on dust trap analysis were 7.8 (±1.8) × 10^{-4} g cm^{-2} yr^{-1} and 3.0 (±0.2) × 10^{-4} g cm^{-2} yr^{-1} (n=2), respectively.

3.1.5 Discussion

A simple model for interpreting the observed decline of ^{10}Be concentrations with depth (Figure 3.2) is that soil matrix accumulates in layers via the deposition of atmospheric dust containing meteoric ^{10}Be and the ^{10}Be radioactively decays *in situ* over time. This hypothesized soil accumulation mechanism is consistent with the pedogenic process in the Mojave Desert proposed by McFadden et al. (1987) and Anderson et al. (2002). They suggested that weathered bedrock surface clasts begin to trap eolian dust, leading to the development of a cumulate soil over time. The soil in turn lifts the clasts, forming a "desert pavement" that continues to trap more wind-blown dust facilitating further soil development. Similar to desert pavements, the columnar, blocky gypsum layer (Figure3.1) at the surface of the study site can trap and stabilize atmospheric dust, including adhered

^{10}Be and allow it to migrate down through the vertical cracks, which would isolate it from wind erosion. This would enable the dust (and ^{10}Be) accumulation and the inflation of the soil profile over time nearly as discrete layers. The gypsum layer itself is likely formed by Ca^{2+} and SO_4^{2-} in ocean aerosols that deposit to the surface and then precipitate as gypsum during rare and small rainfall events. For this simple accumulation model, assuming a constant soil accumulation rate a (cm yr^{-1}), the age of each soil layer t (yr) can be established as a function of depth h (cm) using $t = h/a$. Considering ^{10}Be decays approximately exponentially with time according to the law of radioactive decay (Arthur et al., 1981), there is then an exponential decrease in soil ^{10}Be concentration ([^{10}Be]) with depth:

$$[^{10}\mathrm{Be}] = [^{10}\mathrm{Be}]_i \exp(-\lambda h/a) \qquad \text{Eq. 3.1}$$

where $[^{10}\mathrm{Be}]_i$ is ^{10}Be concentration in the surficial soil without decay (*i.e.* ^{10}Be concentration in atmospheric dust), and λ is the ^{10}Be decay constant (4.9975×10^{-7} yr^{-1}).

This simple accumulation-decay model reproduces the ^{10}Be data remarkably well. When the data are fitted with Eq. 3.1 using the least-squares regression coefficients, they yield a $[^{10}\mathrm{Be}]_i = 1.53(\pm 0.20) \times 10^8$ atoms g^{-1} and soil accumulation rate (a) = 3.43 ($\pm$0.22) $\times 10^{-5}$ cm yr^{-1} (uncertainties arising from the regression fittings with r^2>0.85) (Figure 3.2). Based on this soil accumulation rate, the soil age is estimated to be ~6.6 ± 0.4 Ma at a depth of 225 cm. The net insoluble soil mass accumulation rate is then derived by multiplying the corresponding soil accumulation rate (3.43×10^{-5} cm yr^{-1}) and the average soil density (1.4 g cm^{-3}), yielding 4.8×10^{-5} g cm^{-2} yr^{-1}. This is roughly 7-15 times lower than the bulk dust flux ($7.8 (\pm 1.8) \times 10^{-4}$ g cm^{-2} yr^{-1}) measured in the dust traps in this study and of ~4×10^{-4} g cm^{-2} yr^{-1} at Yungay site 150 km southwest of the

Baquedano site (Ewing et al., 2006). However, it is similar to the net bulk soil accumulation rate of ~4×10^{-5} g cm^{-2} yr^{-1} at Yungay site estimated by the total soil mass change in the 1.5 m soil profile divided by surface age (Ewing et al., 2006). The higher measured dust fluxes are likely the result of two effects. Firstly, the soil accumulation rate is the long-term net accumulation rate whereas the trap rates reflect the short-term accumulation rate, somewhere between the gross and net rates. Secondly, regional mining, off-road driving, and wind erosion of disturbed surfaces (field observations) entrain large amounts of local eolian material that enhances the modern accumulation (deposition) relative to preindustrial times. The modeled $[^{10}Be]_i$ value of 1.53×10^8 atoms g^{-1} is close to the $[^{10}Be]$ measured in sub-surface soils (1.36-1.45 $\times 10^8$ atoms g^{-1}), but slightly higher than the $[^{10}Be]$ in atmospheric dust ($1.24 \pm 0.19 \times 10^8$ atoms g^{-1}). This also suggests that common open-pit mining in the area may have entrained older subsurface material, which would have low ^{10}Be activity, and was deposited into the dust traps. Also, the rainless dust collection period may have had less ^{10}Be deposition (see discussion below) relative to the long-term total that includes wet deposition.

The modern meteoric ^{10}Be flux can be derived as:

$$F_{10Be}\,(\text{atoms cm}^{-2}\ \text{yr}^{-1}) = [^{10}Be]_{dust} \times D_{insol.dust} \qquad \text{Eq. 3.2}$$

where $[^{10}Be]_{dust}$ is 1.24 ($\pm$0.19) $\times 10^8$ atoms•(g insoluble dust)$^{-1}$ and $D_{insol.dust}$ is the insoluble dust deposition rate of 3.0 ($\pm$0.2) $\times 10^{-4}$ g (insoluble dust)•cm^{-2} •yr^{-1}. This yields a F_{10Be} of 3.7($\pm$0.6) $\times 10^4$ atoms cm^{-2} yr^{-1}. This flux is only 6% of the current estimated global average ^{10}Be deposition rate of ~5.8×10^5 atoms cm^{-2} yr^{-1} (*e.g.* Field et al., 2006) but is comparable to a low ^{10}Be flux of ~1×10^4 atoms cm^{-2} yr^{-1} observed in the Dry Valley of Antarctica, which has a similar hyper-arid climate (Bettoli et al., 1993). The

significantly lower ^{10}Be deposition rate in hyper-arid regions is because scavenging of ^{10}Be from the atmosphere occurs mostly by wet deposition, which is essentially absent in hyper-arid environments. Similarly, the ^{10}Be soil accumulation rate $R[^{10}Be]_{accum}$ (atoms cm^{-2} yr^{-1}) can be approximated as:

$$R[^{10}Be]_{accum} = [^{10}Be]_i \times \rho \times a \times f \quad \text{Eq. 3.3}$$

where ρ is the average soil bulk density (1.4 g cm^{-3}), and f is the average fraction of soil insoluble material (0.92). This yields the $R[^{10}Be]_{accum}$ of 6.8×10^3 atoms cm^{-2} yr^{-1}. The soil $R[^{10}Be]_{accum}$ is only 18% of the observed trap F_{10Be}. This difference suggests two possible mechanisms. Either there was only partial retention of ^{10}Be deposition and more than 82% was lost to wind erosion. Or anthropogenic entrainment of old material with low ^{10}Be activity by subsurface open-pit mining that was deposited into the dust traps accounted for >82% of dust deposition. However, it is more likely that both mechanisms were important, and the $R[^{10}Be]_{accum}$ represents the average net ^{10}Be accumulation rate in the soil over the past 6.6 My.

The total soil profile age of ~6.6 Ma is striking since soils in other regions rarely date older than the Pleistocene, but it is consistent with other studies in the Atacama. For example, roughly 70 km southwest of my site, a tuff layer overlain by ~4 m thick coarse alluvial sediment has a comparable age of 6.67 ± 0.13 Ma (Placzek et al., 2009). Rech et al. (2006) reported *ca.* 19-13 Ma salic gypsisols at the depths of 2-31 m located ~90 km east of my site, which does not contradict my study given the limited depth of my trench. Many stable landforms in central Atacama have younger surface exposure ages (1.5-2.6 Ma) (Ewing et al., 2006; Placzek et al., 2010), but these differences could be due to different landform development history and dissimilar geographic conditions (*e.g.*

exhumation, weathering or mobilization of surface clasts/boulders). While there is an excellent agreement in the model-data fit, there exist some small deviations at some depths that may be meaningful (Figure 3.2). The small deviations are likely due to the uncertainties in the model assumptions of (1) no post-depositional ^{10}Be movement or mixing, (2) constant meteoric ^{10}Be production rates, (3) constant dust production, and (4) a constant ^{10}Be delivery rate that is not impacted by climate change.

Discrepancies between the model-predicted and observed ^{10}Be concentrations could arise if assumption (1) is not true, and there has been post-depositional ^{10}Be movement and mixing during pedogenesis. After being deposited onto the soil, ^{10}Be is usually strongly held by the solid particles with the distribution coefficient K_d (the ratio of ^{10}Be amounts in particulate and dissolved phases) of 10^5-10^6 (Balistrieri and Murray, 1986; You et al., 1989) and can be as higher as 10^7 (Li, 1982) at neutral pH. The binding of ^{10}Be and soil particles is, however, strongly pH dependent and decreases rapidly by four orders of magnitude between pH 6 and 2 (You et al., 1989). But my soils were neutral to alkaline (pH=7~9) (preliminary data), and therefore, the ^{10}Be likely bound tightly to soil particles, *e.g.* silicate minerals and trivial amounts of clay and iron minerals, and was unlikely to migrate freely alone. Moreover, at the observed soil pH, most Be was likely present as $Be(OH)_2$ or its hydrolyzed species that are relatively water-insoluble (K_{sp}= 6.92×10^{-22} mol^2 L^{-2} at 25°C for $Be(OH)_2$) (Willenbring et al., 2010). In addition, downward migration of ^{10}Be would have been limited by small amounts of rainfall at the Baquedano site (0.4 mm MAP) and their shallow wetting depths. Therefore, we conclude that ^{10}Be mixing via dissolution and downward migration is trivial, and cannot explain the observed deviations from the decay trend with depth.

Given the limited precipitation at the Baquedano site, it is likely that soil particle movement should also have been minimal, which can be inferred from the profile's grain size data. The grain size distribution with depth was relatively consistent with no abrupt textural transition observed (Figure 3.3). This suggests that particle movement was certainly not freely available. This is in contrast to soluble salt (chloride, nitrate, and sulfate) concentration profiles that varied with depth and had peak concentrations at ~200 cm (Figure 3.3). These anions can typically form NaCl, $NaNO_3$ Na_2SO_4 and $CaSO_4$ minerals which have solubility product constants (K_{sp}) of 3.14×10^{-5}-1.12×10^{3} mol^2 L^{-2} at 25°C. With these solubilities, these minerals would be free to migrate during sporadic small water flows, yet they have only migrated 200 cm (Figure 3.3). Therefore, like free ^{10}Be, particle bound ^{10}Be migration was also probably negligible and had minimal impacts on the scatter in the ^{10}Be data relative to the model estimates. This is consistent with the inference that ^{10}Be mobility has been negligible in a New Zealand loess-paleosol profiles that are significantly wetter (annual precipitation: ~900 mm) and more acidic than my Baquedano site by Graham et al. (2001). The overall limited migration behavior of ^{10}Be within the soil profile is also supportive of my soil accumulation model that soil matrix including ^{10}Be is building up as layers over time, rather than that meteoric ^{10}Be migrates through a pre-existing soil profile to the depth of 225 cm in the context of the long-term Atacama hyper-arid climate settings.

The accumulation-decay model assumes meteoric ^{10}Be production is constant, but it is well established that variations in solar modulation, interplanetary magnetic field and geomagnetic field can alter meteoric ^{10}Be production (*e.g.* Christl et al., 2007), thus changing $[^{10}Be]_i$ in Eq. 3.1 and the model's soil age estimates. Meteoric ^{10}Be production

variations are caused by the fairly regular 11-year solar cycle or stochastic solar activities (Usoskin et al., 2007), which likely average out over my temporal resolution (~150 ky). Further, the long-term mean interplanetary magnetic field is commonly assumed relatively constant over 10^5-10^9 yrs (*e.g.* Wieler et al., 2011). Therefore, only variations in ^{10}Be production induced by changes in geomagnetic intensity were modeled to explore potential impact on the $[^{10}Be]_i$ value. The global absolute paleointensity (PINT) database, which catalogues all absolute palaeointensity data with ages >50 ka (Biggin et al., 2010), was used to select high-quality virtual dipole moment (VDM) data in the past 7 Ma. The selected VDMs were averaged over 100 ky, and then used to derive dipolar latitudinal geomagnetic cutoff rigidities (Lifton et al., 2008). These rigidities and the long-term average solar modulation potential (550 MV) were used to estimate the globally-averaged scaling factors for ^{10}Be production rates relative to the global mean production rate in 1950 (Kovaltsov and Usoskin, 2010). The production scaling factors were also derived from the latest PADM2M model, which is based upon globally distributed paleointensity records spanning 0-2 Ma, and were compared with those from PINT database (Ziegler et al., 2011). Time-varying $[^{10}Be]_{i(t)}$ were then calculated using the production scaling factors and the model-estimated $[^{10}Be]_i$ of 1.53×10^8 atoms g^{-1} (Tables 3.2 and 3.3). Each observed soil $[^{10}Be]$ value was corrected for decay to yield $[^{10}Be]_{i(h)}$ as a function of depth (h) following Eq. 3.1 using $a = 3.43 \times 10^{-5}$ cm yr^{-1}. Assuming temporal variations in the global mean production rate are representative of geomagnetic effects at my Baquedano site, the comparison between $[^{10}Be]_{i(h)}$ and $[^{10}Be]_{i(t)}$ shows that VDM changes alter $[^{10}Be]_{i(t)}$ by less than a factor of 1.5 and are out of phase with $[^{10}Be]_{i(h)}$ variations. This indicates that the VDM variations could not account for significant discrepancies in

$[^{10}Be]_{i(h)}$, especially around 1, 2.5, 3.5, 5 Ma, suggesting other processes besides geomagnetic field change were affecting $[^{10}Be]$ over time (depth) in my soils.

The soil layer ages predicted by the accumulation-decay model could also be impacted if the assumption (3), a constant atmospheric dust production rate, is violated. The dust flux is mostly impacted by climate variations, atmospheric circulation, and surface wind. However, the Atacama dust is mainly of local origins rather than originating from dust transport (Tanaka and Chiba, 2006), which has likely been stable for millions of years in view of the consistent sand-sized particles in the soil. Dust production variations due to climate fluctuations also tend to average out over ~100 ky and the change can be especially small when compared to a relatively large and constant dust input rate. Model estimates by Mahowald et al. (1999) suggested that the Atacama region would experience from almost no change to at most a two-fold change in annual dust deposition (production) during glacial-interglacial periods. Moreover, for a fixed amount of ^{10}Be in the atmosphere, an increase in the amount of atmospheric dust will lead to a dilution effect in $[^{10}Be]_i$ but an increase in soil accrual rate of dust and *vice versa*. The inverse correlation between $[^{10}Be]_i$ and soil accrual rate would tend to counteract each other and minimize the impact of atmospheric dust production variations on soil $[^{10}Be]$. Hence, regional dust production variations are not likely to have considerably impacted the model's age estimates or to account for the deviations between the model and observations.

Climate change is thus the most likely cause of the deviations between the data and the modeled $[^{10}Be]$ (Figure 3.4). The climate effect would be via a change in the ^{10}Be delivery efficiencies of different sized aerosols via dry and wet deposition. Dry

deposition is dominated by gravitational settling of 10-100μm diameter particles, which account for most of the aerosol mass. In the hyper-arid core of the Atacama, reworking of local sands and deposition of 10-100μm diameter particle are the main contributors to deposition mass. ^{10}Be uptake, on the other hand, occurs mostly on sub-micron sized aerosols in the stratosphere where ^{10}Be is produced (Gaffney et al., 2004). This results in that large particles (>1μm), with low ^{10}Be activities because of their small number densities, low surface areas in a given volume and short residence in the atmospheric boundary layer (Papastefanou, 2010), may contribute a relatively stable but small amount of meteoric ^{10}Be flux to the ground via dry deposition.

In contrast, wet deposition scavenges particles of all sizes in the air column (Seinfeld and Pandis, 2006), which would include those sub-micron particles with high ^{10}Be activity. In humid regions where frequent rainfall events efficiently scavenge particulate ^{10}Be, the ^{10}Be deposition rate is likely only dependent on the abundance of meteoric ^{10}Be. In contrast, dry deposition and rare rainfall in the hyper-arid regions are likely unable to scavenge all the meteoric ^{10}Be in the boundary layer, resulting in significantly lower ^{10}Be deposition fluxes. This is evident at my Baquedano site where ^{10}Be deposition is only 6% of the present global average ^{10}Be flux (discussed above) and is similar to the ^{10}Be flux in Antarctic Dry Valleys where wet deposition is also minimal (Bettoli et al., 1993; Field et al., 2006). Therefore, even a small increase in wet deposition would increase ^{10}Be deposition by facilitating the delivery of sub-micron sized particles with high^{10}Be contents to the soil, but without significantly altering the total deposited dust mass. Thus, the positive ^{10}Be excursions (Figure 3.4) can be explained by an increase in precipitation, while the negative excursions suggest decreased precipitation, relative to the long-term

average precipitation. This is consistent with the observation of the increased ^{10}Be inputs and the thus elevated $^{10}Be/^{9}Be$ in paleosols during warmer, wetter interglacial times by Graham et al. (2001). The minimum decay-corrected $[^{10}Be]_{i(h)}$ of 5.59×10^{7} atoms g^{-1} at ~3.2 Ma may represent the $[^{10}Be]_i$ in dry deposition, while the maximum decay-corrected $[^{10}Be]_{i(h)}$ of 3.30×10^{8} atoms g^{-1} around 5.4 Ma may indicate a significant wetter climate than the long-term average climate.

Paleoprecipitation during the wettest period around 5.4 Ma can be roughly inferred based on some assumptions and calculations. The scheme is to estimate 1) the large (>1 μm) and small (<1 μm) aerosol dry deposition rates, 2) the large and small aerosol wet deposition rates, 3) the ratios of ^{10}Be flux during wet relative to dry periods, and 4) the historic precipitation amounts. Firstly, the large to small aerosol mass concentrations are assumed to be 3.5×10^{-12} g cm^{-3} and 1.5×10^{-12} g cm^{-3}, respectively, which are based on the median values for aerosols in remote continents from Seinfeld and Pandis (2006). Assuming all particles are spheres, the average gravitational settling velocities for the large to small aerosols can be calculated using:

$$v_s = D_p^2 \rho_p g C_c / (18\mu) \qquad \text{Eq. 3.4}$$

where D_p is the particle diameter (1×10^{-4} cm and 1×10^{-5} cm for large and small particles, respectively), ρ_p is the particle density (2.6 g cm^{-3} for typical desert dust particles from Nickovic et al. (2001)), g is the gravitational acceleration (9.8 m s^{-2}), C_c is the slip correction factor (Cunninghan correction factor) of 1.08 and 2.86 for large and small particles, respectively (calculated based on the equation $C_c = 1 + 2\lambda/d_p[1.257 + 0.4\exp(-1.1d_p/2\lambda)]$, where λ is the mean free path of gas molecules in air of 0.065×10^{-6} m), and μ is air dynamic viscosity of 1.8×10^{-2} g m^{-1} s^{-1} (Seinfeld and

Pandis, 2006). This gives the large and small aerosol gravitational settling velocities of 9.4×10^{-3} and 2.3×10^{-4} cm s^{-1}, respectively. The dry flux of large and small particles to the ground would be the product of the gravitational settling velocity and the aerosol mass concentrations, giving the dry deposition rates of large and small particles of 3.3×10^{-14} g cm^{-2} s^{-1} and 3.4×10^{-16} g cm^{-2} s^{-1}, respectively.

Secondly, assuming an air column 3000 m high, the large and small aerosol amounts are 1.0×10^{-6} g cm^{-2} and 4.5×10^{-7} g m^{-2}, respectively. The aerosol wet removal efficiencies for large and small aerosols are assumed to be 0.6 and 0.5, respectively for <2 cm rainfall events or be the same of 0.8 for ≥2 cm rainfall events (Radke et al., 1980; Schumann, 1991). Then, for a <2 cm rainfall event, the large and small aerosol wet deposition rates can then be 6.3×10^{-7} g cm^{-2} and 2.2×10^{-7} g cm^{-2}, respectively, whereas for a >2 cm rainfall event, the large and small aerosol wet deposition rates would be 8.4×10^{-7} g cm^{-2} and 3.6×10^{-7} g cm^{-2} , respectively.

Thirdly, adopting the modern rainfall regime of one 0.5 cm rainfall event per decade, 2 cm rainfall event per century and 5 cm rainfall event per millennium (Dr. Ronald Amundson, personal communication), there would be 15,000 <2 cm rainfall events and 1500 rainfall events (≥2 cm) over the 150 ky timescale (corresponding to 5 cm accumulation based on the previously derived accumulation rate). The dry to wet mass deposition rate ratio over 150 ky would be 10.6, and the dry deposition is accounting for 91% of the bulk deposition. Based on the ^{10}Be activity in a small particle to a large particle of 70 (Gaffney et al., 2004), the ratio of ^{10}Be via modern wet and dry deposition to ^{10}Be via only dry deposition of 2.1, similar to the ratio of 2.2 of the measured [^{10}Be] in

the dust of 1.24×10^8 atoms g^{-1} to the lowest decay-corrected $[Be]_{i(h)}$ of 5.59×10^7 atoms g^{-1}.

Finally, assuming 5.59×10^7 atoms representing only dry deposition, my regression-derived $[Be]_i$ of 1.53×10^8 atoms g^{-1} corresponding to long-term average climate and the decay-corrected $[Be]_{i(h)}$ maximum of 3.30×10^8 atoms g^{-1} corresponding to wettest climate, the long-term average precipitation can be reversely estimated to be 1.6 times the modern precipitation, while the wettest period may have 4.6 times the number of modern wet events. This climatic variations may impact dust production, but high dust-flux and low $[^{10}Be]_i$ tend to counteract with each other and not impact the accumulation rate and *vice versa* as discussed. Meanwhile, the climatic shift can also affect the dust deposition, but probably just induce minor dust flux variations compared to the persistently large dust input rates in the Atacama region, different from in the Antarctic region where multiple-fold change in dust flux was observed maybe because the low dust flux rate was subject to disturbance. Based on the calculation above, the dust flux may vary only by ~20% from a 5-6 Ma wet period to the modern hyper-arid period.

The climatic variations in the Atacama inferred from the ^{10}Be data are consistent with, but more highly resolved than, other million-year timescale paleoclimate proxies. My data suggest that the Atacama's climate was wetter during 5.6-4.7 Ma and possibly 1.3-0.6 Ma (to a lesser degree), and drier between 4.5-2.0 Ma and possibly 6.3-5.6 Ma, compared to the long-term average. The wettest period 5.6-4.7 Ma is consistent with evidence from supergene enriched alunite-group minerals of semi-arid episodes during late Miocene (Bissig and Riquelme, 2010). The estimated drying during 6.3-5.6 Ma and after ~4.7 Ma may correspond to increased desiccation at *ca.* 6 Ma and after 3 Ma

inferred from evaporite precipitation and salt crust formation (Hartley and Chong, 2002). My ^{10}Be-based climatic inferences also concur with a recent surface erosion study that showed wetter climates in the Atacama occurring around 1 Ma and between 5-7 Ma, though a wet period near 4 Ma does not appear in my ^{10}Be signals (Jordan, et al., 2011). However, it must be acknowledged that there are some uncertainties associated with these interpretations. The magnitude and duration of dryness and wetness in this study rely on the regression-derived long-term average $[Be]_i$ and may vary slightly when compared to the modern hyper-arid climate. Also, the conclusion of a drier period during 6.3-5.7 Ma is tentative because of the lack of extensive paleointensity data at ~6 Ma.

The potential climatic variations detected in my soil ^{10}Be profile might reflect a combination of global and regional climate change. The termination of an extended period of heavy precipitation at ~4.7 Ma could be explained by the central Andes attaining their modern elevation (~3700 m) at *ca.* 5 Ma thus blocking moisture from the Amazon basin. This is consistent with the inference of the Andes uplift to >2 km during 19-13 Ma (Rech et al., 2006) and on the order of 2300-3400 m since the late Miocene (Gregory-Wodzicki, 2000). The alternating wet/dry periods before ~4.7 Ma, on the other hand, may be connected to global climate change, such as El Nino-Southern Oscillation (ENSO) instabilities in frequency and amplitude on million-year scale (Houston, 2006).

3.1.6 Conclusions

Meteoric ^{10}Be dating has proved successful in establishing a depth-dependent soil chronology and providing perspectives on soil formation mechanism and paleoclimate change over the past millions of years in the hyper-arid Atacama. An exponential decline of soil ^{10}Be concentrations with depth was well reproduced by a simple accumulation-

decay model that soil matrix, including ^{10}Be, builds up as layers over time while ^{10}Be decays *in situ*, suggesting the soil is primarily formed by the slow accumulation of atmospheric dust. The model-estimated soil age of ~6.6 Ma at 225 cm is comparable with soil age estimates at several other sites in the Atacama. Changes in paleo-precipitation may account for the model-data misfit, suggesting wetter climates during 5.6-4.7 Ma and possibly 1.3-0.6 Ma, and drier climates during 4.5-2.0 Ma and possibly 6.3-5.6 Ma, compared to the long-term average. The transition to a drier climate at ~4.7 Ma may have been associated with Andean uplift, and the alternating wet/dry periods after 4.7 Ma may be connected to global climate change. The wettest climate at ~5.6 Ma is comparable to 4.6 times modern precipitation.

3.1.7 Acknowledgments

This work was supported by the National Science Foundation (EAR 0922114). I thank Ji-hye Seo, Raul Ochoa, Susan Ma, and Mike Bourgeois for assistance in the lab and field. I am also grateful for several reviewers' comments and inputs.

3.2 Meteoric ^{36}Cl Dating: A Salt Accumulation Chronology

3.2.1 Abstract

Meteoric ^{36}Cl has been used to understand the mechanism and timescale of salt accumulation in the hyper-arid soils of the Atacama Desert, Chile. The observed ^{36}Cl/Cl ratios range from 394 to 70 × 10^{-15}, showing a systematic decline from the surface to 225 cm deep. A simple model that chloride builds up over time via atmospheric inputs and ^{36}Cl radioactively decays *in situ* reproduces the data remarkably well. This model suggests the chloride age at 225 cm of 860 (±90) ky and yields a chloride accumulation

rate of 0.26 cm ky^{-1} (*i.e.* 1.3 mmol m^{-2} y^{-1}). This shows that hyper-aridity characterized by chloride accumulation has persisted in the Atacama at least since the early Pleistocene. Chloride concentration variations and ^{36}Cl discontinuities with depth suggest the hyper-aridity may have been interrupted by brief wet periods that induced chloride migration, which may be a way of extracting past climatic variations.

3.2.2 Introduction

The Atacama Desert, Chile has highly saline soils containing chloride, nitrate, sulfate and perchlorate (Ericksen, 1981). Salt accumulation is a mass balance between inputs and losses that is integrated over geological timescales. Inputs mainly include hydrological inflow and atmospheric deposition, while the major losses are due to biological uptake and water transport of solutes. In the hyper-arid core of the Atacama (mean annual precipitation <2 mm), however, biological processes and aqueous flow are both small (Ericksen, 1981). As a result, it has been suggested that atmospheric salt inputs are efficiently retained leading to a net mass gain and volumetric expansion of soils (Ewing et al., 2006). This accumulation model is supported by recent isotopic studies in which the Atacama's thick salt deposits are mainly due to long-term accumulation of atmospheric photochemical compounds (Bao and Gu, 2004; Michalski et al., 2004). Yet, the timescale of this depositional accumulation remains poorly constrained.

It is likely that significant salt accumulation in the Atacama has occurred throughout the period of hyper-aridity (Ewing et al., 2006), but there is little consensus on when hyper-aridity was initiated. Extremely low weathering rates suggest that a hyper-arid climate may have persisted since 25 Ma (Dunai et al., 2005), yet the cessation of supergene mineralization and the development of gypsic paleosols indicate that the

transition from an arid to a hyper-arid climate took place during 23-14 Ma (Alpers and Brimhall, 1988; Rech et al., 2006). Alternatively, a hyper-arid transition occurring between 6 and 3 Ma has been inferred from the cessation of fluviolacustrine and alluvial fan sedimentation in Atacama's central depression (Hartley and Chong, 2002; Nishiizumi et al., 2005). Given the wide range of estimates for the onset of hyper-aridity in the Atacama, a new salt chronology may help constrain these uncertainties.

We present a new approach for assessing the timescale of soil chloride accumulation under hyper-arid conditions in the Atacama using meteoric ^{36}Cl. Meteoric ^{36}Cl (301 ky half-life) is produced by spallation of Ar by secondary cosmic rays in the atmosphere (Lal et al., 1958) and is then deposited by dry and wet deposition. Meteoric ^{36}Cl has been used to constrain the ages of ground water, soils, and evaporites (Phillips et al., 1986; Jannik et al., 1991; Tyler et al., 1996). There are, however, limitations when using meteoric ^{36}Cl as a dating proxy, including ^{36}Cl production variations (Lal et al., 1958), unstable chloride inputs (Thompson et al., 2003), changes in the depositional conditions (Jannik et al., 1991) and the possible disturbance from *in situ* ^{36}Cl contribution. But the main limitation is chloride's high solubility, which can lead to mixing of chloride of different ages (Phillips et al., 1986). Tyler et al. (1996) attempted to use ^{36}Cl to date arid soils in the southwestern U.S., but found that limited precipitation still caused the mixing of chloride at different depths, leading to ambiguous ^{36}Cl ages. In the hyper-arid Atacama, these limitations are likely minimized and ^{36}Cl dating of a soil profile sampled at a fine scale may provide a precise depth-dependent age constraint on salt accumulation. In addition, discontinuities in ^{36}Cl ages and chloride abundance variations with depth may provide perspectives into regional precipitation change over time. This study is the first

attempt to establish a chronology of chloride accumulation in the hyper-arid region by means of meteoric ^{36}Cl.

3.2.3 Method

The study site (22.88°S, 69.64°W) is located in the Baquedano Valley region in the hyper-arid core of the Atacama with mean annual precipitation of 0.4 mm recorded by a rainfall gauge 50 km north from my site during 1977-2000 (Houston, 2006). Soil samples were collected from a 225 cm deep trench (~ 5 cm vertical resolution) from the bottom of the trench up to 10 cm below the surface where polygonal gypsum blocks covered the surface; these blocks were disturbed by the excavation process and were not sampled. Instead, two surface samples (0-1 cm) were collected near the study site to estimate $^{36}Cl/Cl$ ratios in modern dust fallout. More details about the site and sample description were in Section 3.1. All samples were carefully homogenized and ground by hand, sieved to remove gravels (diameter >2 mm) and one gram of soil was extracted in 50 mL of Millipore water. The soil extract was filtered through a 0.45 μm polytetrafluoroethylene filter and a one milliliter aliquot was withdrawn for anion analysis (Alltech 620 Ion Chromatography system). $Ba(NO_3)_2$ was added to the remaining solution to eliminate soluble SO_4^{2-} as $BaSO_{4(s)}$, and $AgCl_{(s)}$ was precipitated using excess $AgNO_3$. $AgCl_{(s)}$ was isolated by centrifuging and filtration, washed 5 times in Millipore water, and freeze dried. The purified $AgCl_{(s)}$ was loaded into a copper target and analyzed by accelerator mass spectrometry (AMS) at the Purdue Rare Isotope Measurement (PRIME) laboratory.

3.2.4 Results

The measured $^{36}Cl/Cl$ ratios and soil chloride concentrations are presented in Figure 3.5. The $^{36}Cl/Cl$ ratios systematically decrease with depth; the highest values (354-394 × 10^{-15}) occurring near the subsurface are close to the $^{36}Cl/Cl$ ratios for the two surface samples near the study site (341 (±14) × 10^{-15} and 324 (±9) × 10^{-15}), and the lowest ratios (70-74 × 10^{-15}) are at the bottom of the profile. Significant deviations from the systematic decline exist at depths of 25, 50, 125 and 150 cm where $^{36}Cl/Cl$ ratios are larger than those in overlying horizons. The chloride concentration (averaging 0.35 mmol (g soil)$^{-1}$) varies greatly with depth; chloride decreases with depth in the upper 15-100 cm, stays depleted at 100-150 cm, and becomes enriched below 150 cm.

3.2.5 Discussion

The simplest model for interpreting the observed systematic decline of $^{36}Cl/Cl$ ratios with depth (Figure 3.5) is that chloride builds up as layers over time via atmospheric deposition and ^{36}Cl radioactively decays *in situ*. The accumulation of chloride as layers that can reproduce the decline of $^{36}Cl/Cl$ ratios with depth is possible under a gradual drying climatic scheme (see Appendix A), which is not contradicting the recent hyper-arid climate in the Atacama indicated by previous studies (Alpers and Brimhall, 1988; Rech et al., 2006). This is also not conceptually different from the depositional layers moving down profile at a constant rate or through a piston flow, without incurring a mixing between layers.

This simple accumulation-decay model has five assumptions: (1) *in situ* ^{36}Cl is minor relative to meteoric ^{36}Cl; (2) meteoric ^{36}Cl production rate is constant over time; (3) there

is no significant temporal change in atmospheric chloride production, *i.e.* there are constant $^{36}Cl/Cl$ inputs; (4) the rate of chloride accumulation after deposition is constant with depth/time; (5) chloride is immobile and no mixing of differently aged chloride layers occurs. *In situ* ^{36}Cl production from spallation of potassium (K) and calcium (Ca) target and thermal neutron activation of ^{35}Cl was evaluated based on Liu et al. (1994) (see Appendix B). Due to low Ca and K elemental content and the shielding of thermal neutron flux by boron (~1,000 ppm, Ericksen, 1981) in my soils, *in situ* ^{36}Cl production is minor in the upper profile but becomes increasingly important with depth causing an offset between meteoric input estimates and the observation in the lower profile (Appendix B). However, to incorporate the variations of *in situ* ^{36}Cl input with depth/time with meteoric ^{36}Cl inputs is far too complicated to be practicable. Also, since meteoric net input is one order of magnitude higher at most depths, for the sake of simplicity, a constant *in situ* ^{36}Cl input of 5×10^6 atoms $(g\ soil)^{-1}$, close to the estimates in the bottom profile (see Appendix B), *i.e.* $(^{36}Cl/Cl)_{in\ situ} = 23.7\times10^{-15}$, is assumed and removed from the data. The model predicts an increase in chloride age with depth corresponding to the observed systematic decrease in $(^{36}Cl/Cl)_{obs}$ according to the law of radioactive decay:

$$(^{36}Cl/Cl)_{obs} - (^{36}Cl/Cl)_{in\ situ} = (^{36}Cl/Cl)_i \exp(-\lambda t) \quad (t\neq0) \qquad \text{Eq. 3.5}$$

where $(^{36}Cl/Cl)_i$ is the initial ratio in meteoric chloride, λ is the ^{36}Cl decay constant $(2.25\times10^{-3}\ ky^{-1})$, and t is the ^{36}Cl residence time in the soil (ky). If $(^{36}Cl/Cl)_i$ is taken to be $350\ (\pm20) \times 10^{-15}$ based on the $^{36}Cl/Cl$ ratios on the modern surface near my study site (see discussion below), the age of the deepest chloride at 225 cm can be determined to be 860 (±90) ka. Assuming a constant chloride accumulation rate (a), dividing the maximum depth (225 cm) by total age gives an approximate chloride depth accumulation rate of

0.26 cm ky^{-1}. This can be used to establish the age of each chloride layer as a function of depth (h) using $t = h/a$, and derive the modeled $^{36}Cl/Cl$ ratios ($(^{36}Cl/Cl)_{mod}$) as:

$$(^{36}Cl/Cl)_{mod} = (^{36}Cl/Cl)_i \exp(-\lambda h/a) + (^{36}Cl/Cl)_{in\ situ} \ (h \neq 0). \quad \text{Eq. 3.6}$$

This simple accumulation-decay model reproduces the observations remarkably well (Figure 3.5). There is a significant model-observation correlation with a Pearson coefficient of 0.95 ($p<0.0001$) (SAS 9.0, SAS Institute Inc., USA). The model misfit is evaluated using the reduced chi-squared statistic (χ_r^2):

$$\chi_r^2 = \Sigma \ \{[(^{36}Cl/Cl)_{obs} - (^{36}Cl/Cl)_{mod})]/\sigma\}^2/(N-1), \quad \text{Eq. 3.7}$$

where σ is the standard error for $(^{36}Cl/Cl)_{obs}$ measurement, and N is the number of data points with N-1 representing the degrees of freedom. While a χ_r^2 in the range of 0~1 represents a perfect fit between the model and the measurement, the χ_r^2 of my simple accumulation-decay model is 13, indicating the model is fitting the data very well but not capturing all $^{36}Cl/Cl$ ratio variations.

The misfit χ_r^2 can be decreased to 10 when a $(^{36}Cl/Cl)_i$ of 370×10^{-15} is used. However, 370×10^{-15} is substantially higher than the $^{36}Cl/Cl$ ratios for two surface samples near the study site, although these two measurements may slightly underestimate $(^{36}Cl/Cl)_i$ because of decreased ^{36}Cl production rate during the last millennia (Ziegler et al., 2011) and possible chloride mixing with older chloride from nearby micro-channels but minor *in situ* production in the ~4 ky time frame. In addition, when magnetic field strength variations are considered in the model (discussed below), there is no improvement in χ_r^2 with 370 ($\times 10^{-15}$). Therefore, a $(^{36}Cl/Cl)_i$ value of 350 with a standard deviation of 20×10^{-15} that is the sum of the average instrumental measurement error and the standard deviation between replicate surface samples was adopted. However, there

still exists significant underestimation of $^{36}Cl/Cl$ ratios, especially in the middle of the profile (Figure 3.5). The residual model-observation deviations are likely due to some degree of the invalidity of the other four assumptions of the model.

The simple accumulation-decay model assumes meteoric ^{36}Cl production is constant, but the interplanetary magnetic field, solar activity and Earth's magnetic field have changed over geologic time. This results in variations in the $(^{36}Cl/Cl)_i$ ratio in Eq. 3.6 and impacts the model's ages (Lal et al., 1958). The ^{36}Cl production variations from a fairly regular 11-year solar cycle or possibly stochastic solar activities likely average out over the ~19 ky-timescale (based on the accumulation rate) being considered here (Usoskin et al., 2007) and interplanetary magnetic field is commonly assumed to remain relatively constant over millions of years (Wieler et al., 2011). Therefore, the model was adjusted to account for the variations in ^{36}Cl production induced by changes in the Earth's palaeomagnetic axial dipole moment (PADM). The PADM2M database, which incorporates globally distributed paleointensity records (76 records and 81,446 data) for the past 2 My (Ziegler et al., 2011), was used to estimate the PADM change over my timescale of ~860 ky. The PADM variation was then used to estimate ^{36}Cl production rates relative to the present level using the fifth-degree polynomial fitting equation given by Wagner et al. (2000). The meteoric $^{36}Cl/Cl$ ratios and *in situ* offset term $(^{36}Cl/Cl)_{in\ situ}$ at each depth were adjusted using the relative ^{36}Cl production rates and Eq. 3.6 was reevaluated to produce a new curve of $^{36}Cl/Cl$ ratios versus depth (Figure 3.5). By including ^{36}Cl production variations in the model, the predicted $^{36}Cl/Cl$ ratios are closer to the observations with the minimized χ_r^2 of 8 when the modern $^{36}Cl/Cl$ ratio is $350 \times 10^{-}$

^{15} and a = 0.26 cm ky^{-1}. However, there are still several points that fall outside the 1σ error of my ^{36}Cl/Cl measurements, especially beginning at 150 cm depth.

The model-observed outliers may be because the third assumption of no temporal chloride deposition change to impact the atmospheric ^{36}Cl/Cl ratio is not valid. Chloride deposition is primarily a function of the surface's proximity to the ocean or major evaporites. Over the 860 ky age of the chloride at my study site, the latitudinal translocation of the Atacama by tectonic movement is negligible based on paleomagnetic data (Jesinkey et al., 1987), and therefore, variations in chloride input due to shifting geographic location can be ignored. Salt loading from nearby salt flats can be strongly modulated by wind speed and climate conditions. However, the main source of chloride at my site is oceanic sea-salt (Chapter 2) and the Southern Hemisphere mid-latitude westerly winds would likely show no difference from the last glacial maximum to Holocene (Hesse and McTainsh, 1999), which is consistent with the global model prediction that the Atacama would experience from almost no change to a two-fold increase in annual chloride deposition from the last glacial to current interglacial period (Mahowald et al., 2006). Chloride content in an Andean ice core has varied by a factor of 10, but this reflects the entrainment of chloride from nearby periodically desiccated salt lakes and is impacted by temporal precipitation variations (Thompson et al., 2003). My observed chloride content change in soils by up to 500% are therefore unlikely to be due to changes in chloride deposition rates alone. In addition, if changes in chloride concentrations are due to increased sea-salt loading, we would expect to find high ^{36}Cl/Cl ratios where there are low chloride concentrations or low ^{36}Cl/Cl ratios with high chloride

concentrations; instead, we find the opposite. I would conclude that chloride deposition variations cannot wholly explain the model-data discrepancies.

The modeled $^{36}Cl/Cl$ ratios would be impacted if the fourth model assumption, constant chloride depth accumulation rate after deposition, is violated. There may have been climatic variations that would impact the delivery efficiency of chloride (and ^{36}Cl) via dry and wet deposition (without significantly altering the input $^{36}Cl/Cl$ ratios), and inconsistent compaction degrees of chloride layers after deposition. If true, there would be a change of chloride depth accumulation rate and chloride layer's age, and a divergence between the modeled and observed $^{36}Cl/Cl$ ratios. Considering large deviations of the model prediction from the observations, a possible transition in the chloride depth accumulation rate may exist around 150 cm (Figure 3.5). Using two different accumulation rates, 0.30 cm ky^{-1} for the upper 0-145 cm and 0.16 cm ky^{-1} for the lower 150-225 cm, has further improved the model fit with χ_r^2 minimized to 6 (Figure 3.6). However, the high $^{36}Cl/Cl$ ratio at 150 cm relative to the adjacent upper layers still cannot be interpreted.

The fifth assumption in my accumulation-decay model is that there is no chloride mixing within the profile. Figure 3.5 indicates low soil chloride content at 100-160 cm and high chloride content at 160-220 cm. Since this chloride concentration difference is not mainly due to different rates of chloride input (see discussion for assumption 3), the most likely interpretation is that chloride migrated from 100-160 cm to 160-220 cm. A rough estimation shows that the chloride excess at 160-220 cm can balance the chloride deficit at 100-160 cm from the average concentration of 0.35 mmol $(g\ soil)^{-1}$. Clearly, the chloride could not be completely mobilized and mixed, because this would destroy the

^{36}Cl near-exponential decay trend that we observe. The possible scenario is that sporadic rainfall dissolves most of the shallow chloride layers, and displaces them at deeper depths by diffusion as discrete layers without complete homogenization over the traveling course. Assuming 80% chloride from 100-160 cm migrates 60 cm down, the ^{36}Cl/Cl ratios will be intact at 100-160 cm but elevated by ~25% at 160-220 cm due to chloride mixing (Figure 3.6). This is the only mechanism that could lead to the observed higher ^{36}Cl/Cl at 150 cm relative to at 145 cm (see discussion above). However, the actual conditions are certainly more complicated than my simulation of a single chloride migration, considering temporal variations in rainfall amounts and evaporation rates that would influence the amount and distance of salt transport.

The Atacama soil chloride age of 860 ka at 225 cm is striking because it is radically older than soil chloride ages in other deserts. In semi-arid southwest U.S., the ages of 10-46 m deep chloride deposits range 10-16 ka, which are indicative of the onset of arid Holocene climate conditions that led to the retention of soil chloride (Walvoord et al., 2003). While the Pre-Holocene (>20 ka) climate was wet enough to leach chloride to the water table in North America, chloride has been stable in the Atacama at least since the early Pleistocene considering the high chloride concentrations near the surface. This suggests prevailing hyper-aridity over the past ~900 ky in the Atacama, despite the interruption of wet periods with significant chloride migration mentioned above. The final depth/time of chloride accumulation will be important to know to indicate the onset of hyper-aridity.

The chloride concentration and ^{36}Cl age constraint allow us to estimate the chloride inventory and chloride molar accumulation rate that are comparable to previous studies.

The average chloride concentration of 0.35 mmol (g soil)$^{-1}$ together with the soil density of 1.4 g cm^{-3} (Wang et al., submitted) and the age of 860 ka for the 225 cm deep chloride profile gives a soil chloride inventory of 1102 mol m^{-2} and an average chloride molar accumulation rate of 1.3 mmol m^{-2} y^{-1}. This chloride molar accumulation rate is close to that of 1.2 mmol m^{-2} y^{-1} in the Yungay region in the Atacama (Ewing et al., 2006), but roughly six times higher than the estimate of 0.20 mmol m^{-2} y^{-1} based on crude estimates of nitrate inventories from mining records and the rough assumption of a constant ratio of depositional chloride to nitrate (Michalski et al., 2004). Passive deposition samplers measured the chloride deposition rate of ~4 mmol m^{-2} y^{-1} in the Yungay (Ewing et al., 2006), while chemistry-climate models predict a current climatic chloride deposition rate of ~3 mmol m^{-2} y^{-1} (~55% of sea-salt mass) in the Atacama (Mahowald et al., 2006). These are about two times higher than my chloride accumulation rate, suggesting chloride may have been subject to post-depositional losses by wind erosion (field observation).

There is no evidence in the Atacama soils of the ^{36}Cl bomb spike that was found in other soils and groundwaters. Starting in 1955, a 100 fold increase in ^{36}Cl fallout from nuclear testing was detected in the Huascarán ice core (1,760 km northwest of my site) before decreasing over 25 years to natural levels (Heikkilä et al., 2009). Considering my surface soil layer (0-1 cm) spans ~4 ky, the contribution of bomb ^{36}Cl to the surface layer may elevate its ^{36}Cl/Cl ratio by ~62%, suggesting the actual natural level of $(^{36}Cl/Cl)_i$ is ~ 216×10^{-15}. This seems unreasonably low given the ^{36}Cl/Cl ratios in the upper profile and that the meteoric ^{36}Cl/Cl ratios in North America at locations that are comparable in distance to the ocean and have similar orographic barriers are 300~500$\times 10^{-15}$ (Moysey et

al., 2003). Therefore, I would argue that since the surface is susceptible to wind erosion, the bomb ^{36}Cl may have been deposited to the pediment but was not preserved on the relatively unstable surface, especially considering the 25 year accumulation only approximates to a 6.5×10^{-3} cm thick depositional layer.

There are discrepancies between the ^{36}Cl dates and my previous ^{10}Be dates (Section 3.1) on the same soil profile, which may be due to the solubility differences between the two radionuclides. The previous ^{10}Be dating suggested the insoluble soil matrix age at 225 cm of ~7 My, one order of magnitude higher than my ^{36}Cl date (~860 ka). This may be attributed to the fact that ^{36}Cl (chloride) is subject to aqueous leaching and ancient chloride (low $^{36}Cl/Cl$ ratios) may have been lost to the deeper profile. Instead, the less soluble meteoric ^{10}Be is likely locked in insoluble soil particles (Section 3.1). Therefore, there is obviously an asynchrony between the soil matrix (including ^{10}Be) accumulation and chloride accumulation. I propose that the chloride in my profile reflects a recent salt accumulation and migration through the relatively stable and old soil matrix. The chloride migration is necessarily conducted also as layers to preserve the exponential decay trend in the $^{36}Cl/Cl$ ratios, which is likely by piston flow but limited to my unique hyper-arid conditions (Tyler et al., 2002). I argue that meteoric ^{36}Cl dating may be a way to produce an accurate salt accumulation chronology, while meteoric ^{10}Be can be an accurate, high resolution dating method for soils in hyper-arid regions, which can both be meaningful for developing novel paleoclimate proxies from the unique soil and salt accumulation under hyper-arid conditions.

3.2.6 Conclusions

Meteoric ^{36}Cl dating has proved successful in providing a depth-dependent chronology for salt accumulation in the hyper-arid Atacama. A systematic decline of $^{36}Cl/Cl$ ratios with depth was well reproduced by a simple accumulation-decay model that chloride builds up as layers over time and ^{36}Cl decays *in situ*. This model demonstrates the antiquity of chloride (860 ± 90 ka at 225 cm), suggesting the prevailing hyper-aridity at least since the early Pleistocene in the Atacama. However, deviations of the modeled $^{36}Cl/Cl$ ratios from the observations and chloride concentration variations with depth suggest that short-term wet periods may have induced downward migration of chloride but as discrete layers without complete mixing. The accumulation rate of 1.3 mmol m^{-2} y^{-1}, significantly smaller than the dust deposition rate, indicating that chloride via atmospheric deposition is not completely retained in the Atacama soils, which explains the absence of a ^{36}Cl bomb spike. Since the salt accumulation and migration have been widely used to reflect paleoclimate change, my prospective depth-dependent chronology of chloride can give best age constraints for these paleoclimate proxies.

3.2.7 Acknowledgments

This work was supported by the National Science Foundation (EAR 0922114). We thank Ji-hye Seo, Raul Ochoa, Susan Ma, and Mike Bourgeois for assistance in the lab and field. We are also grateful for several reviewers' comments and inputs.

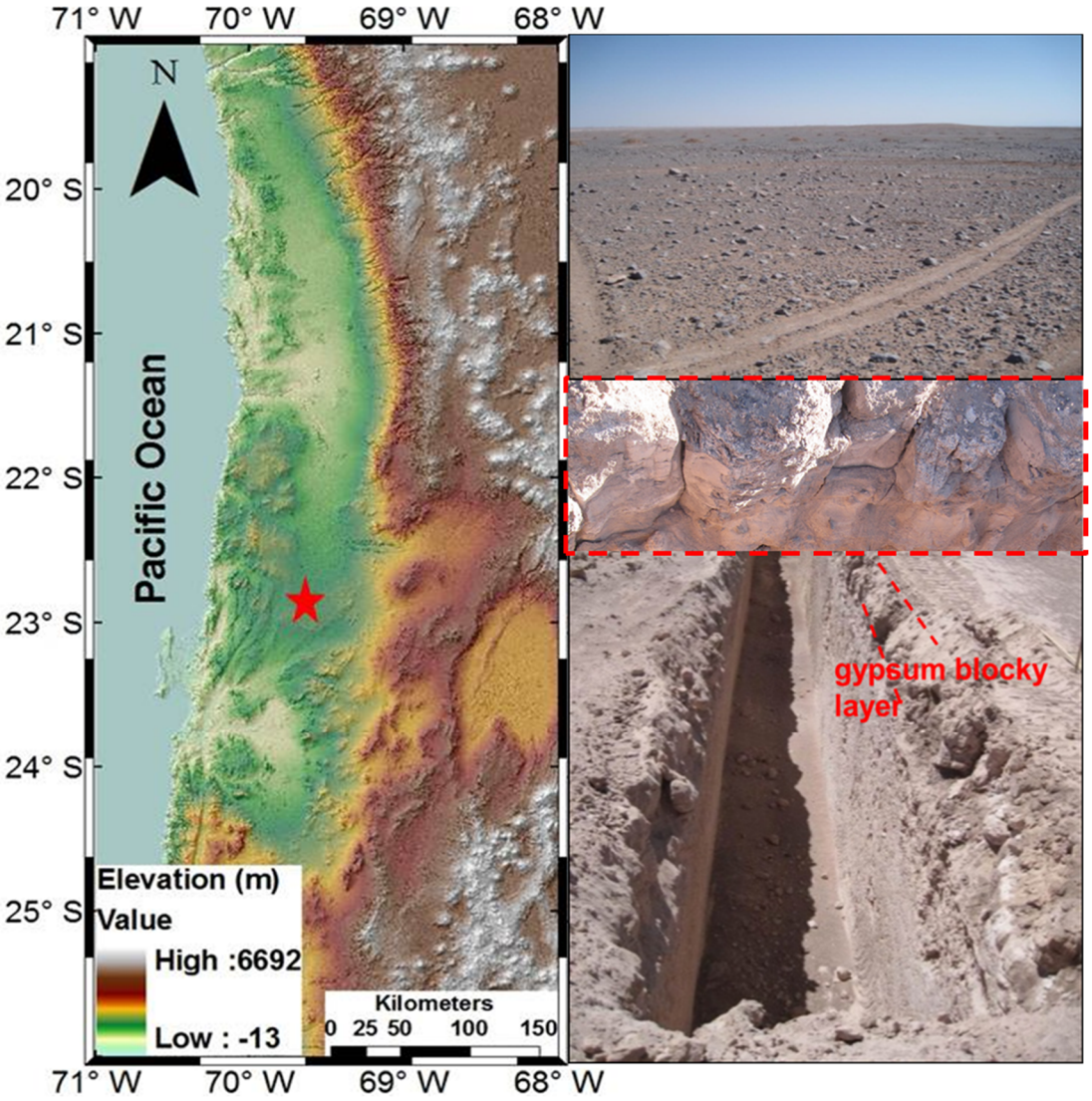

Figure 3.1 Site location (red star) and field pictures of the surface (between dash lines: gypsum blocky layer)

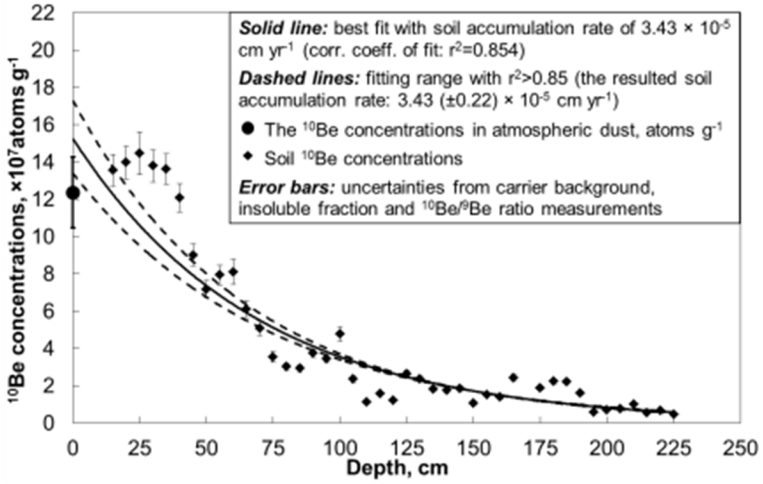

Figure 3.2 The soil [^{10}Be] depth profile in the Atacama Desert and the exponential fittings of the data according to Eq. 3.1.

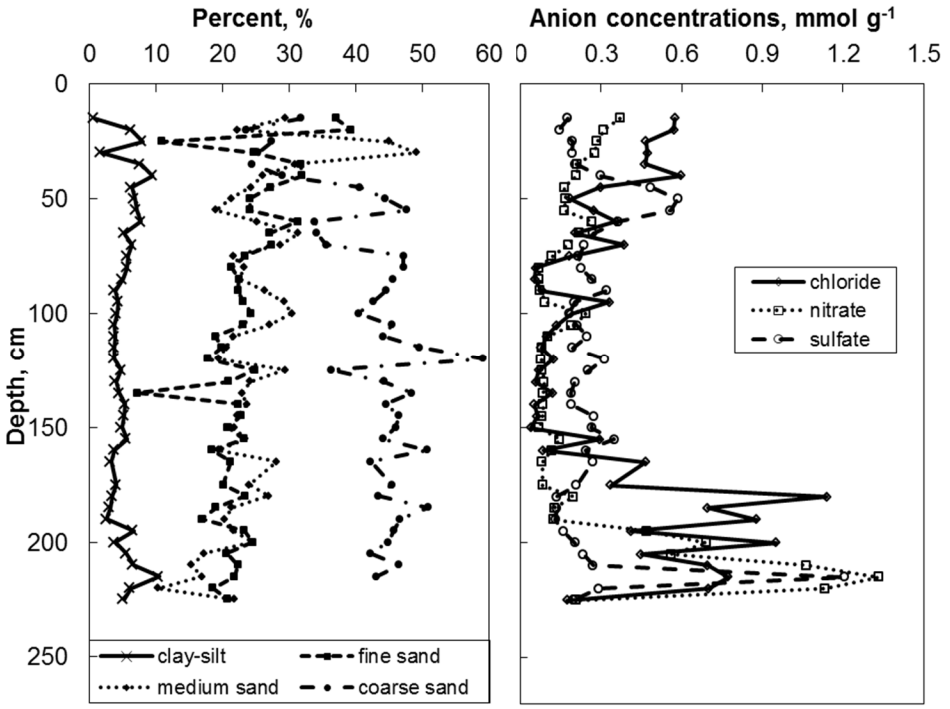

Figure 3.3 The comparison of grain size distribution and anion depth profiles

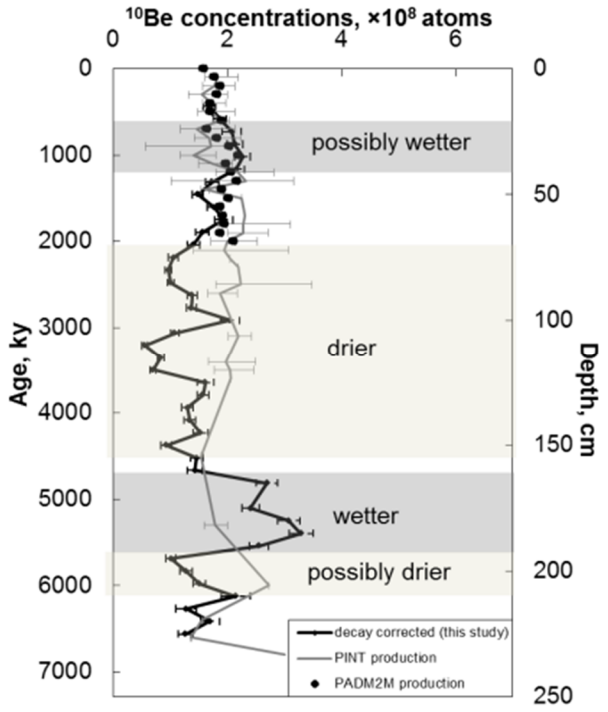

Figure 3.4 Decay corrected soil ^{10}Be concentrations ($[^{10}Be]_{i(h)}$) were compared to time-varying $[^{10}Be]_{i(t)}$ that was corrected by the PINT database-derived and PADM2M model-derived production scaling factors based on the regression-derived $[^{10}Be]_i$ of 1.53×10^8 atoms g^{-1}. Error bars for PINT production reflect the scattering of data from different sources.

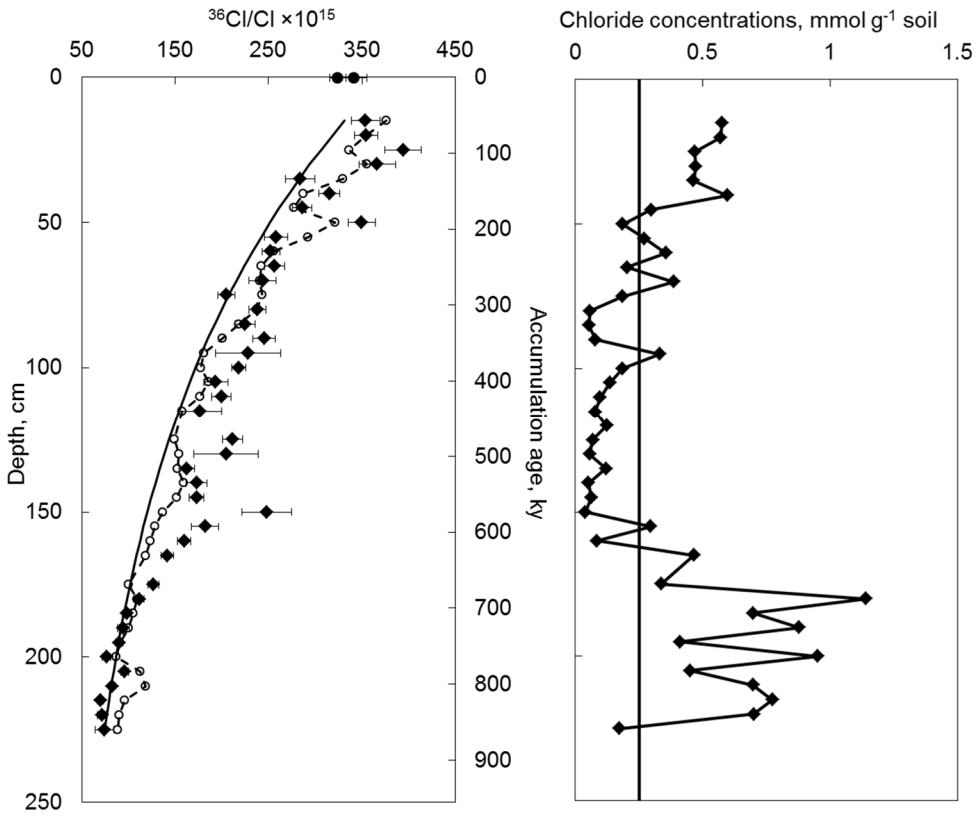

Figure 3.5 Left: the surface ^{36}Cl/Cl ratios (solid circles) and the measured ^{36}Cl/Cl ratios in the Atacama soils with depth (solid diamonds); the estimated ^{36}Cl/Cl ratios using the simple accumulation-decay model (Eq. 3.6) with the initial of 350×10^{-15} are shown in the solid line, while open circles and dashed line indicate the model estimates with the initial ^{36}Cl/Cl ratio altered by Earth's magnetic field; the depth axis is lined up with the accumulation age axis based on the chloride depth accumulation rate of 0.26 cm ky^{-1}. Right: chloride concentrations in the Atacama soils versus depth.

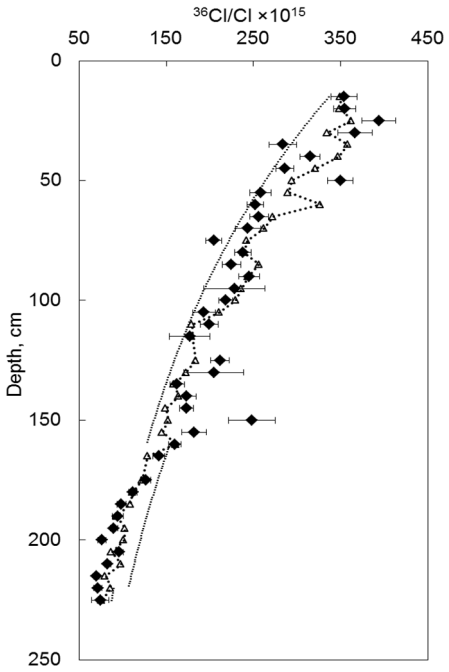

Figure 3.6 The modeled ^{36}Cl/Cl ratios using the modified accumulation-decay model with two chloride accumulation rates: 0.30 cm ky^{-1} for 0-145 cm and 0.16 cm ky^{-1} for 150-225 cm and initial ^{36}Cl production rates corrected by Earth's magnetic field variations (open triangles and dot line) are compared to the measurement (solid diamonds). Assuming 80% chloride at 100-160 cm is migrated 60 cm down, the left-behind chloride still preserves the original ^{36}Cl/Cl signature while the ^{36}Cl/Cl ratios in the lower layers are elevated due to the mixing with the upper younger chloride without change in decay curve curvature (solid line), which may explain the model outliers.

Table 3.1 Analytical results of meteoric ^{10}Be profile

Sample[a, b]	Depth (cm)	Soil mass (g)	Be carrier (mg)	^{10}Be/Be[c, d] ($\times 10^{-15}$)	^{10}Be concentrations[e, f] (10^7 atoms g^{-1} bulk soil)	Insolube fraction[g] (%)	^{10}Be concentrations[h, i] (10^7 atoms g^{-1} insoluble frac.)
Atmospheric deposition	0	0.5009	0.3770	2224.16±338.54		62.33	12.36±1.90
LT1	15	0.5057	0.3762	2252.62±64.84	12.38±0.36	91.20±4.56	13.57±0.84
LT2	20	0.5074	0.3755	2340.00±80.00	12.89±0.44	92.21±4.61	13.98±0.90
LT3	25	0.5064	0.3760	2443.43±139.80	13.35±0.77	92.29±4.61	14.47±1.14
LT4	30	0.5054	0.3766	2312.66±69.30	12.75±0.39	92.39±4.62	13.80±0.86
LT5	35	0.5043	0.3777	2285.24±60.43	12.65±0.34	92.86±4.64	13.63±0.82
LT6	40	0.5033	0.3773	1982.34±56.39	10.97±0.32	90.74±4.54	12.09±0.75
LT7	45	0.5047	0.3773	1476.02±50.52	8.15±0.28	90.30±4.52	9.02±0.59
LT8	50	0.5024	0.3807	1150.00±40.00	6.41±0.23	89.30±4.47	7.18±0.48
LT9	55	0.5053	0.3779	1300.00±50.00	7.10±0.28	89.50±4.48	7.93±0.54
LT10	60	0.5046	0.3786	1330.00±80.00	7.34±0.45	90.46±4.52	8.11±0.67
LT11	65	0.502	0.3692	1058.20±53.05	5.69±0.29	93.29±4.66	6.09±0.45
LT12	70	1.0053	0.4974	1286.98±74.45	4.73±0.28	93.04±4.65	5.08±0.40
LT13	75	1.0072	0.5121	885.53±52.81	3.37±0.20	94.89±4.74	3.55±0.29
LT14	80	1.0074	0.5078	773.00±18.84	2.91±0.07	95.90±4.80	3.03±0.18
LT15	85	1.0054	0.5208	699.70±18.90	2.80±0.08	95.43±4.77	2.94±0.17
LT16	90	1.0066	0.5152	901.99±27.98	3.53±0.11	94.23±4.71	3.74±0.23
LT17	95	1.0057	0.5145	855.45±25.98	3.26±0.10	94.56±4.73	3.45±0.21
LT18	100	0.5086	0.3747	840.75±48.88	4.51±0.27	94.34±4.72	4.78±0.38
LT19	105	0.5049	0.3733	420.48±18.55	2.23±0.11	94.76±4.75	2.35±0.17
LT20	110	0.5033	0.3736	219.91±15.57	1.07±0.09	95.02±4.75	1.13±0.11
LT21	115	0.5087	0.3744	292.32±13.02	1.51±0.08	96.11±4.81	1.57±0.11
LT22	120	1.0339	0.5129	325.33±11.81	1.15±0.05	94.16±4.71	1.23±0.08
LT23	125	0.5094	0.3751	473.36±33.41	2.50±0.19	95.34±4.77	2.63±0.24
LT24	130	0.503	0.3769	444.35±14.33	2.27±0.08	96.04±4.80	2.37±0.15
LT25	135	0.5053	0.3763	330.64±15.80	1.75±0.09	95.89±4.79	1.82±0.14
LT26	140	0.5055	0.3762	320.28±14.85	1.68±0.09	96.30±4.81	1.75±0.13
LT27	145	0.5046	0.3774	332.23±19.87	1.76±0.11	95.08±4.75	1.85±0.15
LT28	150	0.5034	0.3774	196.98±14.66	1.01±0.09	95.41±4.77	1.06±0.11
LT29	155	0.502	0.3759	270.49±12.34	1.42±0.07	92.22±4.61	1.54±0.12
LT30	160	0.5075	0.3799	249.37±15.35	1.30±0.09	93.25±4.66	1.39±0.12
LT31	165	0.5049	0.3759	423.17±16.11	2.26±0.09	92.86±4.64	2.44±0.17
LT33	175	1.0252	0.5130	490.09±15.45	1.78±0.06	94.39±4.72	1.88±0.12
LT34	180	1.0282	0.5212	542.22±17.50	2.00±0.07	89.74±4.49	2.23±0.15
LT35	185	0.504	0.3722	391.92±10.78	2.07±0.07	92.98±4.65	2.22±0.14
LT36	190	1.0255	0.5130	407.38±11.63	1.48±0.05	92.06±4.60	1.61±0.10
LT37	195	1.0268	0.5130	157.66±9.36	0.54±0.04	91.47±4.57	0.59±0.05
LT38	200	1.0245	0.5139	171.32±8.36	0.59±0.03	85.55±4.28	0.69±0.06
LT39	205	1.0252	0.5144	194.96±7.58	0.68±0.03	89.45±4.47	0.77±0.06
LT40	210	0.5046	0.3721	167.73±14.64	0.84±0.08	82.98±4.15	1.01±0.12
LT41	215	0.5053	0.3730	85.22±6.15	0.38±0.05	67.83±3.39	0.56±0.08
LT42	220	0.5043	0.3728	119.15±5.86	0.57±0.04	82.16±4.11	0.69±0.07
LT43	225	0.5068	0.3758	97.47±4.78	0.45±0.04	94.67±4.73	0.48±0.05

[a]Sample LT1-43 were from a trench (22.88°S, 69.64°W, elevation: 1497 m)

[b]Atmospheric deposition sample was the combined sample collected by two dust collectors from two adjacent sites (22.84°S, 69.70°W, 1486 m and 23.01°S, 69.39°W, 1480 m)

[c] Isotope ratios were normalized to the ICN standard Be-01-5-2 with a ratio of 8.558×10^{-12}

[d]Uncertainties are reported at the 1σ confidence level

[e]A mean blank value of 388,184 ±137,435 ^{10}Be atoms (^{10}Be/^{9}Be = 14.29 (± 5.91) $\times 10^{-15}$) was used to correct for carrier background

[f]Propagated uncertainties from uncertainties in blank and AMS analytical errors

[g]the insoluble soil fractions were obtained by subtracting cation and anion contents measured by inductively coupled plasma optical emission spectroscopy (ICP-OES) and ion chromatography with propagated uncertainty of 5%, while the insoluble fraction in atmospheric dust was the mass difference between before and after removing soluble salts.

[h]Propagated uncertainties from uncertainties in blank, insoluble fraction and AMS analytical errors

Table 3.2 Production rates derived from PINT paleointensity variations

Age_ka	VDM_avg[b] (× E+22)	VDM_std	VDM_n	VDM/M_{1950}	Production rate[d], atoms s^{-1} cm^{-2}	Production scaling factor	$[Be]_{i(t)}$
1950[a]	8.0648[c]			1.00	3.05E-02	1.00	1.53E+08[e]
100	5.7062	3.39	21	0.71	3.66E-02	1.20	1.83E+08
200	6.0573	2.16	32	0.75	3.54E-02	1.16	1.78E+08
300	7.7666	2.94	15	0.96	3.11E-02	1.02	1.56E+08
400	6.3406	2.72	5	0.79	3.46E-02	1.13	1.73E+08
500	6.3746	1.66	15	0.79	3.45E-02	1.13	1.73E+08
600	5.5026	2.22	9	0.68	3.73E-02	1.22	1.87E+08
700	8.6144	1.92	5	1.07	2.94E-02	0.96	1.48E+08
800	6.6481	3.75	29	0.82	3.37E-02	1.11	1.69E+08
900	6.4647	3.22	13	0.80	3.42E-02	1.12	1.72E+08
1000	9.4145	3.64	12	1.17	2.80E-02	0.92	1.41E+08
1100	6.2702	2.48	2	0.78	3.48E-02	1.14	1.74E+08
1200	4.0317	1.40	3	0.50	4.34E-02	1.42	2.18E+08
1300	3.4746	2.03	2	0.43	4.64E-02	1.52	2.33E+08
1400	7.2412	4.72	2	0.90	3.23E-02	1.06	1.62E+08
1500	3.7411	0.34	2	0.46	4.49E-02	1.47	2.25E+08
1600	3.6075	0.00	1	0.45	4.56E-02	1.50	2.29E+08
1700	3.5397	0.00	1	0.44	4.60E-02	1.51	2.31E+08
1800	3.6231	0.00	1	0.45	4.55E-02	1.49	2.28E+08
1900	3.6372	2.62	2	0.45	4.55E-02	1.49	2.28E+08
2000	4.7743	1.98	5	0.59	4.01E-02	1.31	2.01E+08
2100	5.0997	2.43	31	0.63	3.88E-02	1.27	1.95E+08
2200	4.5689	4.99	2	0.57	4.10E-02	1.34	2.06E+08
2300	3.9656	0.00	1	0.49	4.38E-02	1.43	2.20E+08
2500	3.7850	0.00	1	0.47	4.47E-02	1.47	2.24E+08
2600	5.4875	4.79	8	0.68	3.73E-02	1.22	1.87E+08
3100	3.9444	1.23	5	0.49	4.39E-02	1.44	2.20E+08
3400	4.9405	1.20	2	0.61	3.94E-02	1.29	1.98E+08
3500	4.5990	2.19	2	0.57	4.08E-02	1.34	2.05E+08
3600	4.5400	1.86	15	0.56	4.11E-02	1.35	2.06E+08
4000	11.1200	1.99	10	1.38			
4500	7.9397	0.00	1	0.98	3.07E-02	1.01	1.54E+08
5300	6.0006	0.00	1	0.74	3.56E-02	1.17	1.78E+08
6000	2.3038	0.60	12	0.29	5.45E-02	1.79	2.73E+08
6400	7.8000	0.00	1	0.97	3.10E-02	1.02	1.56E+08
6600	9.9000	0.00	1	1.23	2.73E-02	0.89	1.37E+08
6800	1.6820	0.03	2	0.21	6.00E-02	1.97	3.01E+08
6900	11.5401	1.61	2	1.43			

[a] The year of 1950

[b] VDM (virtual dipole moment) from the global absolute paleointensity (PINT) database (Biggin et al., 2010) were averaged over 100 ky intervals. To select high-quality data, the PINT database was trimmed by: (1) removing all data during polarity transitions because of the likelihood of abnormal low fields associated with transitions; (2) removing all data with a standard deviation ≥ 25%; (3) extracting all data using the latest Thellier or Microwave technique with pTRM checks with replicates ≥ 3.

[c] Dipole field of moment in1950 (IGRF-10, http://www.ngdc.noaa.gov/IAGA/vmod/igrf.html)

[d] Interpolation between a set of pre-computed production as a grid of geomagnetic cutoff rigidity and the solar modulation potential by Kovaltsov and Usoskin (2010)

[e] The regression-derived long term average $[^{10}Be]_i$ of 1.53 × 10^8 atoms g^{-1}

Table 3.3 Production rates derived from PADM2M paleointensity variations

Age_ka	PADM_avg[a] (× E+22)	VDM/M_{1950}	Production rate, atoms s^{-1} cm^{-2}	Production scaling factor	$[Be]_{i(t)}$
1950	8.0648	1.00	3.05E-02	1.00	1.53E+08[d]
0.0	7.5567	0.94	3.16E-02	1.03	1.58E+08
0.1	6.0292	0.75	3.54E-02	1.16	1.78E+08
0.2	5.4840	0.68	3.74E-02	1.23	1.87E+08
0.3	5.7657	0.71	3.63E-02	1.19	1.82E+08
0.4	6.5812	0.82	3.39E-02	1.11	1.70E+08
0.5	6.6342	0.82	3.38E-02	1.11	1.70E+08
0.6	5.3037	0.66	3.80E-02	1.25	1.91E+08
0.7	6.9906	0.87	3.29E-02	1.08	1.65E+08
0.8	5.8090	0.72	3.62E-02	1.19	1.82E+08
0.9	4.7095	0.58	4.05E-02	1.33	2.03E+08
1.0	3.9786	0.49	4.36E-02	1.43	2.19E+08
1.1	4.9176	0.61	3.95E-02	1.30	1.98E+08
1.2	4.5075	0.56	4.13E-02	1.35	2.07E+08
1.3	4.1304	0.51	4.31E-02	1.41	2.16E+08
1.4	5.2896	0.66	3.81E-02	1.25	1.91E+08
1.5	4.6958	0.58	4.04E-02	1.32	2.03E+08
1.6	5.4476	0.68	3.75E-02	1.23	1.88E+08
1.7	5.2684	0.65	3.82E-02	1.25	1.91E+08
1.8	5.0455	0.63	3.90E-02	1.28	1.96E+08
1.9	5.5209	0.68	3.73E-02	1.22	1.87E+08
2.0	4.3018	0.53	4.21E-02	1.38	2.11E+08

[a] PADM from the PADM2M (0-2 Ma palaeomagnetic axial dipole moment) model (Ziegler et al., 2011) were averaged over 100 ky intervals.

CHAPTER 4. PALEOCLIMATE SETTINGS OF SOIL FORMATION

4.1 Abstract

We have performed stable oxygen isotope measurements in nitrate salts from the Atacama (Chile), Kumtag (China), Mojave (US), and Thar (India) deserts. The detected ^{17}O anomalies in desert soil nitrate were quantified by $\Delta^{17}O_{soil}$ which were observed to vary between different desert sites. The varied $\Delta^{17}O_{soil}$ values in the four deserts indicate that atmospheric nitrate is the primary origin of nitrate in the hyper-arid core of the Atacama and Kumtag deserts, while the Mojave and Thar deserts as well as some parts of the Atacama have substantial amounts of nitrate from nitrification. There is a negative correlation between $\Delta^{17}O_{soil}$ and the mean annual precipitation (MAP) of the studied desert sites, suggesting the potential of $\Delta^{17}O_{soil}$ as a precipitation proxy in arid landscapes. Further discussion revealed $\Delta^{17}O_{soil}$ together with careful geological site inspections can be used to explore the past precipitation history, specifically in the precipitation range of 0-200 mm, despite some uncertainties associated with the correlation equation. Gross nitrification rates were derived based on the relative molar fractions of these two sources and the documented atmospheric nitrate deposition rates for the studied sites, ranging from 0.7 mg N m^{-2} yr^{-1} in the hyper-arid core of the Atacama to 885 mg N m^{-2} yr^{-1} in the wettest Thar Desert. The fluctuations of soil NO_3^- $\Delta^{17}O$ in a 225-cm deep soil profile in the hyper-arid core of the Atcama likely reflected seven wet-dry cycles over the ^{36}Cl ages,

maybe corresponding to possible glacial-interglacial cycles operated on the 100 ky scale or induced by historic volcanic eruptions.

4.2 Introduction

Nitrate is an integral component of the N cycle in desert environments, but a quantitative understanding of input rates and their linkage to the availability of liquid water remain uncertain. Nitrate is naturally added to desert soils through atmospheric deposition or produced *in situ* via biological nitrification (Boring et al., 1988). Generally, nitrification, the oxidation of ammonium via nitrifying bacteria, is considered the dominant mechanism of nitrate accumulation in desert soils (Ericksen 1981; Walvoord et al., 2003; Graham et al., 2008), but it is often limited by the availability of liquid water in desert environments (West and Skujins, 1978; Grimm and Fisher, 1986). Atmospheric nitrate is produced in small quantities by photochemical oxidation of reduced nitrogen (Galloway et al., 2004), but it can account for a significant fraction of soil NO_3^- when nitrification diminishes with the decreasing water availability in desert regions (Michalski et al., 2003; Qin et al., 2012). The relative importance of these two sources, and the environmental factors that influence rates of nitrate addition into desert soils, such as precipitation rates, however, are poorly constrained over space and time (West and Skujins, 1978; Boring et al., 1988).

Oxygen isotope abundances have recently proven useful for distinguishing these two nitrate sources (Michalski et al., 2004). In nitrate produced by bacterial nitrification (biotic nitrate), approximately two oxygen atoms are derived from water and the one from air (Amberger and Schmidt, 1987; Kendall et al., 1995; Mayer et al., 2001). The

oxygen isotopic compositions of water (Meijer and Li, 1998) and air (Luz and Barkan, 2005) are both mass dependent, and the oxygen transfer during nitrification is a mass-dependent process, leading to $\delta^{17}O \approx 0.52 \cdot \delta^{18}O$ for the biotic nitrate (Miller, 2002). Atmospheric nitrate, on the other hand, contains an "anomalous" ^{17}O excess over what is expected based on ^{18}O abundances (Michalski et al., 2011). The deviation from mass-dependent fractionation is quantified by $\Delta^{17}O = \delta^{17}O - 0.52 \cdot \delta^{18}O$ (Thiemens, 1999; Miller 2002). In atmospheric nitrate the observed $\Delta^{17}O$ values ($\Delta^{17}O_{atm}$) range from 20-35‰ (Michalski et al., 2003; Alexander et al., 2009; Morin et al., 2009; Costa et al., 2011). This arises because NO_3^- is mainly derived from the transfer of oxygen atoms from ozone, which has large $\Delta^{17}O$ values (Johnston and Thiemens, 1997; Krankowsky et al., 2000), to nitrogen oxides that then form NO_3^-.

The soil NO_3^- $\Delta^{17}O$ ($\Delta^{17}O_{soil}$) can then be used to apportion the two nitrate sources by applying a two-component $\Delta^{17}O$ mixing model:

$$1 \bullet \Delta^{17}O_{soil} = f_{atm} \bullet \Delta^{17}O_{atm} + f_{nitrif} \bullet \Delta^{17}O_{nitrif} \qquad \text{Eq. 4.1}$$

where f_{atm} is the mole fraction of atmospheric NO_3^- contributing to the soil nitrate pool, f_{nitrif} is the mole fraction of soil NO_3^- from nitrification ($f_{atm} + f_{nitrif} = 1$), $\Delta^{17}O_{atm}$ is the $\Delta^{17}O$ value in atmospheric NO_3^- and $\Delta^{17}O_{nitrif}$ is the $\Delta^{17}O$ value in soil NO_3^- produced from nitrification. While a mixing of nitrate derived from nitrification and atmospheric deposition at specific sites can be distinguished using the multiple stable oxygen isotopes, there is a lack of in-depth comparison of the relative importance of the two sources between similar landscape positions in different desert systems.

My hypothesis is that in desert regions, rare precipitation events can alter nitrification (Gleeson et al., 2008) and atmospheric NO_3^- deposition (Seinfeld and Pandis,

2006) in different proportions, making soil NO_3^- $\Delta^{17}O$ values a proxy for precipitation and nitrification rates. Nitrification rates in deserts are controlled by precipitation since low soil water content inhibits the activity of nitrifying bacteria by lowering intracellular water and reducing substrate supply (Stark and Firestone, 1995; Gleeson et al., 2008). An increase in nitrification induced by elevated precipitation amount would lower soil NO_3^- $\Delta^{17}O$ values if atmospheric deposition of NO_3^- remained constant. Increases in precipitation amount, frequency and intensity, however, can also increase NO_3^- deposition rates by controlling NO_3^- scavenging efficiency (Seinfeld and Pandis, 2006). Nevertheless, the influences of increased precipitation on soil nitrification and atmospheric NO_3^- deposition rates are likely not equal and thus changes in precipitation would alter soil NO_3^- $\Delta^{17}O$ values. Therefore, soil NO_3^- $\Delta^{17}O$ values could be used to assess mean annual precipitation over time or local nitrification over wide spatial-temporal scales.

Three studies have attempted to make some link between soil NO_3^- $\Delta^{17}O$ values and the competing processes of nitrification and atmospheric NO_3^- deposition. Michalski et al. (2004) first analyzed several soil samples from southern California to find variations in soil NO_3^- $\Delta^{17}O$ between nearby soil samples and proposed the potential of soil NO_3^- $\Delta^{17}O$ for understanding the soil N cycle, such as the nitrification rates. Rech et al. (2006) used $\Delta^{17}O$ values in paleosols NO_3^- to infer shifts in past climate. They found that NO_3^- $\Delta^{17}O$ values (4.6-14.4‰) in a salic gypsisol from the Atacama's Calama Basin were significantly lower than soil NO_3^- $\Delta^{17}O$ values (13.7-21.6‰) from the hyper-arid core (MAP <3 mm) in the Atacama. This difference was attributed to an increase in

nitrification that was a response to an increased regional mean annual precipitation (MAP) of 5-10 mm. However, their estimation neglected the significant heterogeneity within the profile or over space and was not based on a robust relationship between observed soil NO_3^- $\Delta^{17}O$ and known MAP, likely resulting in some uncertainties in their climatic inference. Ewing et al. (2006) also discovered a decreasing trend of the soil NO_3^- $\Delta^{17}O$ values with increasing MAP along a north-to-south precipitation transect in the Atacama Desert.

While it is widely believed that hyper-aridity (<50 mm yr^{-1} precipitation) in the Atacama Desert has existed for millions of years (Alpers and Brimhall, 1988; Hartley and Chong, 2002; Dunai et al., 2005; Nishiizumi et al., 2005; Rech et al., 2006), temporal shifts in annual precipitation rates have also been inferred. Rainfall events of 1 cm or more may occur a few times a century and fog events can occur nearly daily along the Atacama's coastal zone (Ericksen 1981; Houston, 2006; Sutter et al., 2007). Furthermore, supergene alunite-group minerals (Bissig and Riquelme, 2010), sedimentological (Hartley and Chong, 2002) or surface alteration records (Dr. Teresa Jordan, personal communication) all indicated that a hyper-arid climate was likely interrupted by semi-arid episodes. There are, however, no highly-resolved paleoclimate records in the Atacama, particularly for paleo-precipitation. If wet events (rainfall or fog) are sufficiently large or intense, they can induce *in-situ* weathering, leaching, erosion and enhancement of biological actitivity that can impact soil formation mechanism. Therefore, understanding how small amounts of precipitation may have varied in the past and how this rainfall may have influenced soil formation in the Atacama are crucial but still unresolved questions.

Here we present data and discuss two aspects of this hypothesis. First, an empirical determination of soil NO_3^- $\Delta^{17}O$ values in deserts with different mean annual precipitation rates to calibrate them as a precipitation proxy. Second, we discuss the linkage between precipitation and gross nitrification rates as the driving mechanism for the soil NO_3^- $\Delta^{17}O$ variations observed in desert systems. Finally, the paleo-precipitation history for the formation of the 225-cm deep trench soil profile is reconstructed to reveal the paleoclimatic settings for the hyper-arid soil formation in the Atacama Desert.

4.3 Methods

Undisturbed surface soils were collected from 22 sites in four hot deserts that spanned a range of MAP rates. The four deserts are the Atacama (Chile), Mojave (United States), Thar (India) and Kumtag (China) deserts; the former three are near the coast and the latter is inland (Figure 4.1). The Atacama Desert, located between the coastal range to the west and the Andes to the east in northern Chile, is one of the driest places on Earth with MAP<2 mm in its hyper-arid core (Houston, 2006). It is well known to contain the most massive nitrate deposits in the world that have been extensively mined since early 1800's (Ericksen, 1981). The Kumtag Desert is located in the Turpan-Hami basin in western China, which is second-driest among the four deserts with MAP of 30~50 mm in most areas (Dong et al., 2008; Li et al., 2011). 2.5 billion ton nitrate deposits, rivaling those in the Atacama, have recently been identified in the Kumtag and generated research interests in the region (Qin et al., 2012). The Mojave Desert is situated between the Great Basin Desert to the north and the Sonoran Desert to the south in the southwestern US with MAP of 30-300 mm (Hereford et al., 2006). Sporadic subsurface (~ 2 meters) nitrate

deposits have been found in the Mojave (Walvoord et al., 2003; Graham et al., 2008). The Thar desert is located in Northwestern India forming a natural boundary running along the border between India and Pakistan, which is the wettest among the four deserts with MAP of 100~500 mm (Parmanik, 1952). Nitrate deposits in the Thar have not been documented. Soils were hand sampled from the surface to a depth of ~50 cm at sites with available precipitation data in the four deserts. Most of the sites were mantled by desert pavements, a common land-surface feature in arid regions, and some of them were covered by patchy brushes (see detailed site description in Table 4.1). At the sites where sufficient precipitation existed for brushes to flourish, only the open space between brushes was sampled. The samples were stored in air-tight plastic bags at 20°C until analysis.

In addition, 43 subsurface soil samples were collected from a temporary 225 cm deep trench in the Baquedano region of the Atacama Desert. Site descriptions and sampling strategies were detailed in Chapter 2. This trench soil profile was for the later paleo-precipitation history construction study.

All bulk soils were sieved to <2 mm fractions, 1-10 g of soil was added to 30-40 ml of Millipore water and the mixture was vortex-extracted of soluble salts. Nitrate concentrations were measured by Dionex DX-500 ion chromatography. Soils with high NO_3^- concentrations and low organic loads (majority of samples) were converted into $AgNO_3$ and thermally decomposed (Michalski et al., 2004). The resulting O_2 was purified and analyzed by isotope ratio mass spectrometer with a $\Delta^{17}O$ precision of ±0.2‰. Samples with low NO_3^- concentrations were analyzed using a recent bacterial reduction, gold redox method (Kaiser et al., 2006) that has a $\Delta^{17}O$ precision of ±0.5‰ and is

calibrated using several working standards of $\Delta^{17}O$ values ranging from 0-32‰ as developed by Riha et al. (submitted).

4.4 Results and Discussion

Surficial soil NO_3^- $\Delta^{17}O$ values varied from 0.3-21.3‰ at different sites in the four deserts (Table 4.2). The largest $\Delta^{17}O$ values (19.1-21.3‰) were observed in soil NO_3^- from four sites in the Atacama, *i.e.* Chiu Chiu, Coya Sur, Huatacondo and Quillagua. Surficial soil NO_3^- samples from the Kumtag also had large $\Delta^{17}O$ values ranging from 12.3-17.6‰. In the Mojave, as well as some high-altitude sites in the Atacama, the soil NO_3^- $\Delta^{17}O$ values were significantly lower (5.1-11.1‰), while the lowest $\Delta^{17}O$ values of 0-1‰ in soil nitrate occurred in the Thar Desert. A significant negative correlation between soil NO_3^- $\Delta^{17}O$ values and MAP (0-305 mm) at these studied sites (Figure 4.2) was also observed: $MAP = 0.5 \times (\Delta^{17}O_{soil})^2 - 21.1 \times \Delta^{17}O_{soil} + 248.1$ (r^2=0.89). The Baquedano site subsurface soil NO_3^- $\Delta^{17}O$ varied from 17.1-20.0 ‰ with depth (Figure 4.3).

4.4.1 The Precipitation Proxy Calibration

The negative correlation between soil NO_3^- $\Delta^{17}O$ and MAP shown in Figure 4.2 indicated that the increase of MAP was promoting the nitrification to a greater degree than any increase in atmospheric NO_3^- deposition by wet deposition. This suggests that soil NO_3^- $\Delta^{17}O$ may be useful as a new precipitation proxy in desert regions. To ascertain the actual paleoclimate applications of soil $NO_3^-\Delta^{17}O$ values, it was a prerequisite to constrain the applicable range of the proxy. When nitrification rates exceed atmospheric nitrate

deposition rates by >95%, Eq. 4.1 predicts that soil NO_3^- $\Delta^{17}O$ values would be at the analytical detection limit of 1‰. This limit was reached in the Thar Desert when MAP exceeded 212 mm (Table 4.1). This was likely because as MAP increases, soil nitrification rates increase much more quickly than atmospheric nitrate deposition. Conversely, at the arid extreme, nitrification was assumed to be completely excluded and atmospheric deposition is the only nitrate input source in the soil. We observed that the highest soil NO_3^- $\Delta^{17}O$ value (21.3‰) occurred at the Coya Sur site with MAP=0.4, and was close to the atmospheric NO_3^- $\Delta^{17}O$ value of 23±0.9‰ observed in the Atacama by Ewing et al. (2007). This was likely due to that Coya Sur had extremely low soil water availability (Houston, 2006) and nearly absent microorganisms (Navarro-Gonzalez et al., 2003), which have likely excluded any significant soil nitrification, leaving atmospheric deposition as the dominant source of soil NO_3^-. Therefore, the NO_3^- $\Delta^{17}O$ data points in soils were narrowed to the MAP range between 0 and 212 mm for the use of estimating the correlation between soil NO_3^- $\Delta^{17}O$ ($\Delta^{17}O_{soil}$) and MAP as follows:

$$MAP = 0.3 \times (\Delta^{17}O_{soil})^2 - 15.9 \times \Delta^{17}O_{soil} + 215.8 \ (r^2=0.88) \qquad \text{Eq. 4.2}$$

However, the sites with MAP≤11.5 mm (except the Ojos and Calama) had soil NO_3^- $\Delta^{17}O$ clustered in the range of 19.1-21.3‰, with the soil NO_3^- $\Delta^{17}O$ at Huatacondo (MAP=11.5 mm) of 20.6(±1.5)‰ being close to that at Coya Sur (MAP=0.4 mm) of 21.3(±1.4)‰. This suggested that the relationship between soil NO_3^- $\Delta^{17}O$ values and MAP in Eq. 4.2 may have had a plateau effect (soil NO_3^- $\Delta^{17}O$>~19‰) at the limit of microbial life, corresponding to MAP ≤11.5 mm.

This new precipitation proxy calibration can be used to reevaluate Rech et al. (2006) $\Delta^{17}O$ values in NO_3^- extracted from a ~9 Ma gypsisol strata on the margin of the Calama Basin in the Atacama Desert. The desert soil NO_3^- $\Delta^{17}O$ values from well-developed salic gypsisols ranged from 4.6-14.4‰ (mean 9.9‰), corresponding to 43.3-148.3 mm MAP based on Eq. 4.2. These precipitation estimates are much larger than that of 5-10 mm estimated by Rech et al. (2003). This disagreement may be due to that the estimates by Rech et al. (2003) were based on a rough comparison rather than an in-depth quantitative relationship between soil NO_3^- $\Delta^{17}O$ values and precipitation amount as presented here. Also, it can be ascribed to the scattering of soil NO_3^- $\Delta^{17}O$ values in the gypsisol soil profile.

Ewing et al. (2006) reported the soil NO_3^- $\Delta^{17}O$ values of 17.9±0.6‰ (n=10), 13.8±0.2‰ (n=2) and 9.3±0.1‰ (n=2) along a north-to-south precipitation transect in the Atacama desert, which correspond to MAP of 18.6, 43.3 and 52.5 mm based on Eq. 4.2. This contradictes the modern rainfall rates along the transect spanning the hyper-arid to arid climates (MAP: <2 mm, ~10 mm, ~20 mm). This discrepancy may be because the nitrates collected by Ewing et al. (2006) were mostly from subsurface samples (>50 cm deep) that may have included nitrates formed under wetter climates compared to the modern rainfall regimes. Two soil samples from the surface 1-3 cm layer of the hyper-arid site (<2 mm MAP) had soil NO_3^- $\Delta^{17}O$ values of 19.4±0.1 ‰ (n=2) (Ewing et al., 2006), which corresponds to MAP=~10.0 mm according to Eq. 4.2 and can be considered a reasonable estimate in view of the plateau effect. This overestimation by Eq. 4.2 was, however, in line with the soil NO_3^- $\Delta^{17}O$ plateau effect in Eq. 4.2 when MAP<11.5 mm as

discussed above. This suggests that desert soil NO_3^- $\Delta^{17}O$ values are sensitive to MAP variations but the application of Eq. 4.2 should be cautiously limited to the surface nitrate and ideally within a MAP range of 11.5-212 mm.

Despite the great potential to use soil NO_3^- $\Delta^{17}O$ to infer the past precipitation change, as mentioned above, we acknowledge that there may be some other systematic deviations than the plateau effect associated with the established Eq. 4.2. The first deviation arises from using the modern precipitation data to represent the precipitation information over the timescales of NO_3^- accumulation in the surface soil samples at specific sites. The accumulation of the surface 0-50 cm NO_3^- may span hundreds to thousands of years that vary between sites. There are likely some deviations in precipitation amount between in modern times and over the past hundreds to thousands of years, resulting in uncertainties in estimating the long-term mean precipitation by using the modern data. However, using modern precipitation data was required because precipitation records before 1900 A.D., especially in desert regions, are rarely available. The use of modern precipitation data was also based on the consideration that the nitrate at shallow depths (<50 cm for my sampling) is relatively young, while ancient nitrate is likely leached to deeper depths during a wetter climate (Walvoord et al., 2003). As a result, the modern precipitation data are likely to yield the most suitable guess of the precipitation regimes for the surface or near-surface soil NO_3^- accumulation among the limited available data. Therefore, the existing modern annual precipitation data (Table 4.1) were used to derive the relationship between soil NO_3^- $\Delta^{17}O$ and MAP shown in Eq.4.2.

The second uncertainty in Eq. 4.2 is the assumption of a fixed $\Delta^{17}O_{atm}$ value over the timescales of NO_3^- accumulation in the surface soil samples between different desert sites.

Significant seasonal oscillations in $\Delta^{17}O_{atm}$ values have been observed (*e.g.* Michalski et al., 2003; Morin et al., 2008) and modeled (Alexander et al., 2009) and they have been attributed to shifts in atmospheric chemistry that produces atmospheric NO_3^-. These shifts in chemistry are driven by variables such as the relative abundance of ozone and peroxy oxides, temperature, relative humidity, and hours of sunlight (*e.g.* Alexander et al., 2009; Michalski et al., 2011). However, the observed seasonal variations in $\Delta^{17}O_{atm}$ would average out for atmospheric NO_3^- collected over the course of one or several years. Indeed, the longer the deposition period, the more homogeneous the $\Delta^{17}O_{atm}$ should be, assuming the average local to regional photochemistry has remained constant over time. Nevertheless, this assumption may not be valid over the longer timescale of the nitrate accumulation (hundred to thousand years). Long-term variations in $\Delta^{17}O_{atm}$ are also primarily driven by NO_x concentrations, surface solar radiation, aerosol density and temperature. These potential long-term $\Delta^{17}O_{atm}$ variations could be related to some global events, such as solar activity cycle and volcanic emissions, which would have likely affected all the studied sites and are thus not further discussed. There may also have existed spatial variations in $\Delta^{17}O_{atm}$ values among different sites in the four deserts. However, the factors influencing $\Delta^{17}O_{atm}$ between different desert sites should be comparable considering their remoteness from human disturbance, since the modern anthropogenic activities are a major cause of elevated $\Delta^{17}O_{atm}$ (Michalski et al., 2003, 2011). For example, the $\Delta^{17}O_{atm}$ values (two and a half year average) of NO_3^- collected across a west-east transect in the Atacama Desert (Central Valley and the Pre-Andes region) were 25.8±0.5‰ (n=7) (Chapter 2). Therefore, though neglecting the spatial and temporal variations in $\Delta^{17}O_{atm}$ may cause deviations from the real conditions and

uncertainties in exploring the relationship between $\Delta^{17}O_{soil}$ and MAP, the assumption of a uniform $\Delta^{17}O_{atm}$ endmember value can still be justified, especially in view of the lack of widespread $\Delta^{17}O_{atm}$ measurements.

The third deviation from the relationship between soil NO_3^- $\Delta^{17}O$ and MAP in Eq. 4.2 may come from heterogeneous soil NO_3^- $\Delta^{17}O$ values. There were some differences (>1‰) in soil NO_3^- $\Delta^{17}O$ between different depths or sites with similar MAP (Table 4.2), significantly exceeding the analytical precisions. This is probably owing to the heterogeneous distribution of NH_4^+ or organic N and/or the distribution of soil water, required for the nitrification process (Schmit, 1982; Stark et al., 1995). However, multiple samples were typically taken from different locations or depths at a site, and several sites with relatively similar landscapes (see discussion below) and environmental factors were selected for one precipitation regime in order to reduce the bias derived from spatial heterogeneity. Therefore, potential spatial heterogeneity between different locations at one site or sites cannot be a major factor to disturb the Eq. 4.2 relationship.

Among the 22 sites utilized in this study, two sites showing significant $\Delta^{17}O_{soil}$ differences with different locations or depths were both in the Atacama region. The El Tatio site was a hilly location in the Altiplno region of the Andes with an average elevation>4000 m. Both a hill top and hill slope were sampled. The $\Delta^{17}O_{soil}$ value from the hill top (0-30 cm integrated sample) was 12‰ larger than the $\Delta^{17}O_{soil}$ from the hill slope (0-20 cm integrated sample). This was probably because water was unevenly distributed over the hill with the hill slope receiving and holding a significant amount of water drained from the hill top. This may have explained the shrub coverage on the hill

slope and barren surface with desert pavements on the hill top (see site descriptions in Table 4.1). The $\Delta^{17}O_{soil}$ values from these two locations at one site were then averaged to estimate the actual $\Delta^{17}O_{soil}$.

The second significant difference in $\Delta^{17}O_{soil}$ between two different depths was detected at Copaquire. Copaquire was a mountain valley part of the central Andes with elevation of 3384 m. It was covered with dense desert pavements and 20% brush. The brush was likely sustained by water draining from the surrounding mountains or from the rains. There was a ~6‰ shift in the $\Delta^{17}O_{soil}$ value between the surface (0-2 cm) and the subsurface (10-20 cm). The considerably lower $\Delta^{17}O_{soil}$ at 10-20 cm may result from that depth range being the rooting depth of the brush, and high organic matter around the roots may have enabled soil bacteria to overcome the extremely low C/N barrier for NH_4^+ nitrification (Kuroiwa et al., 2011) that was common in desert regions and promote the nitrification. The low subsurface $\Delta^{17}O_{soil}$ may also be due to a wetter climate in ancient times when possible surface runoff brought in nitrate from other sources featured by low $\Delta^{17}O_{soil}$ values (maybe beneath the brushes in the surrounding grids) and/or more water availability could sustain more *in situ* nitrification but lower $\Delta^{17}O_{soil}$ (Schlesinger and Pilmanis, 1998). To correspond to the modern likely drier climate, the $\Delta^{17}O_{soil}$ of the surface 0-2 cm nitrate at Copaquire was adopted to explore the relationship between $\Delta^{17}O_{soil}$ and precipitation. However, the 9.6‰ was probably still an underestimation of the $\Delta^{17}O_{soil}$ when MAP=54.1 mm, due to that the Copaquire site is located in a mountain basin and subject to surface water drainage from the surrounding mountains, different from the other sites with precipitation as the major water source. Likewise, we suspect

that Quillagua, Ojos and Tocene sites in different mountain basins that are also subject to drainage water from the mountains as well as the Calama site nearby the Loa River may imply underestimations of $\Delta^{17}O_{soil}$ with the corresponding MAP. If $\Delta^{17}O_{soil}$ values at these sites are elevated, the correlation should get significantly improved (Figure 4.2). This suggests that the application of $\Delta^{17}O_{soil}$ into paleoclimate studies has some demanding requirements of sampling, which should avoid the sites subject to stream runoff, drainage, and biology disturbance and the profiles beneath the brushes. The ideal sampling sites allow the precipitation as the major local water source without complicated hydrological and biological processes.

Despite these uncertainties, the good correlation between $\Delta^{17}O_{soil}$ and precipitation indicates that $\Delta^{17}O_{soil}$ is a robust precipitation proxy in desert regions that have a precipitation range of 0-212 mm. This proxy can be particularly beneficial with the advantage of recent breakthroughs in soil NO_3^- $\Delta^{17}O$ measurements using a convenient and economic bacteria reduction method (Kaiser et al., 2006; Riha et al., submitted), though geological inspections and sampling site selection should be cautioned during the application of the proxy. The $\Delta^{17}O$ of desert soil nitrate derived in climate-sensitive systems has practical implications for paleoclimate studies and can potentially overcome some of the limitations of other continental precipitation proxies.

Nearly one third of the Earth's land surface is comprised of deserts, the landscapes with MAP<400 mm (Middleton and Thomas, 1997). The expansion, contraction, and intensification of these deserts are linked to global climate phenomena (e.g. Hillel and Rosenzweig, 2002). Desert soil ecosystems are particularly sensitive to changes in

precipitation, even of relatively small magnitude and short duration, because they are already under water stress (Veron et al., 2006). This suggests that geochemical or isotopic variations in desert paleosols that were evidence of small variations in continental precipitation may have preserved long-term paleo-precipitation records to provide valuable information connected to global events (*e.g.* Andrews et al., 1998; Prochnow et al., 2006; Rech et al., 2006). However, the most often-used continental paleo-precipitation proxies, *e.g.* fossil leaves, pollen, glacial advances and retreats, tree-line migration, tree-rings, ice-core and lake level changes, are unavailable or only occasionally exist because they are limited by geographic position in desert regions (Bradley, 1985; Cronin, 2010; Pachur et al., 1995; Francis and Hill, 1996; Herzschuh et al., 2004). Recent paleoclimate reconstruction in deserts are mainly based on assemblages of pack rat middens (Wells and Jorgensen, 1964), depth or properties of carbonate (Royer, 1999; Wang et al., 2005), depth to gypsic soils (Retallack and Huang, 2010), iron-magnesium nodules (Stiles et al., 2001), surface erosion features (Jordan et al., 2011), which become rare with increasing aridity and are difficult for time constraints. Therefore, a new precipitation proxy, such as $\Delta^{17}O$ in desert soil nitrate, can be a meaningful supplement to these existing precipitation proxies in desert regions, and even across the globe. This proxy can help constrain the accuracy of regional climate model simulations, and advance understandings of how rainfall patterns have evolved in the past and will be altered by future climate change.

4.4.2 Gross Nitrification Rate Estimations

Desert soil NO_3^- $\Delta^{17}O$ that can apportion NO_3^- sources between nitrification and atmospheric deposition can potentially be a novel natural proxy of soil gross nitrification

rates (GNR) in desert ecosystems. GNR is the rate of conversion of ammonium/ammonia to nitrate regardless of consumption via microbial assimilation, plant uptake, or denitrification (Sumner, 2000). The knowledge of soil GNRs is important because they can control the bioavailability of nitrogen and affect the potentials for N loss via denitrification and soil emissions in desert regions. The ^{15}N-pool dilution technique has been used to determine soil GNRs by adding $^{15}NO_3^-$ to the soil and observing the dilution in abundance of heavy ^{15}N in soil NO_3^- pool as natural $^{14}NH_4^+$ is oxidized to $^{14}NO_3^-$ (Davidson et al., 1991; Hoyle et al., 2006; Verchot et al., 2006). The ^{15}N-pool dilution method has been considered applicable because of its small disturbance of the soil and direct measurement of nitrification process without the confounding influence of immobilization (Murphy et al., 2003). Soil NO_3^- $\Delta^{17}O$ values are the result of a natural isotope dilution experiment. The $\Delta^{17}O_{atm}$ is diluted by NO_3^- produced by nitrification and thus can also be used to predict soil GNRs if the atmospheric NO_3^- deposition rate is known. Similar to the ^{15}N dilution, the soil NO_3^- $\Delta^{17}O$ values are not altered by microbial assimilation, plant uptake, or denitrification processes that fractionate isotopes in a mass dependent manner. This allows soil $\Delta^{17}O$ values to independently predict soil GNRs, and therefore, will be useful for understanding nitrification potentials in desert N cycles.

4.4.2.1 The Relation between Gross Nitrification and Atmospheric Deposition Rates

Knowing the mole fractions of atmospheric nitrate and biotic nitrate as well as the rates of atmospheric nitrate deposition, the soil GNRs can be derived. The soil nitrate inventory is a mass balance between inputs (*i.e.* atmospheric deposition, *in-situ* nitrification, and stream inflow of either atmospheric or biotic nitrate) and losses mainly

through plant assimilation, denitrification, deep seepage, and surface hydrological outflow. The study sites are typically in remote deserts with no evidence of stream channels, stream inflow and outflow (Schlesinger and Jones, 1984), and the inputs are mainly from atmospheric deposition and *in-situ* nitrification. In addition, when these inputs exceed the losses, they result in the accumulation of significant nitrate deposits (Walvoord et al., 2003; Michalski et al., 2004; Qin et al., 2012). The desert soil nitrate inventory mass balance is then:

$$dQ/dt = R_{dep} + R_{nitrif} - R_{loss} \quad \text{Eq. 4.3}$$

where Q is the desert soil nitrate inventory at the time t, and R_{dep}, R_{nitrif} and R_{loss} are the rates of atmospheric nitrate deposition, gross soil nitrification, and soil nitrate loss (denitrification, assimilation, uptake, and leaching), respectively. Assuming the isotopic composition in the soil nitrate pool is always homogeneous, the $\Delta^{17}O$ mixing model can be subsequently derived as:

$$(Q_{i+1} \bullet \Delta^{17}O_{i+1} - Q_i \bullet \Delta^{17}O_i)/dt = \Delta^{17}O_{atm} \bullet R_{dep} + \Delta^{17}O_{nitrif} \bullet R_{nitrif} - \Delta^{17}O_i \bullet R_{loss} \quad \text{Eq. 4.4}$$

where i is the time step (i=0 the initial time), Q_0 is the inventory (mass) of soil "legacy" nitrate that is formed prior to time zero, and $\Delta^{17}O_0$ is the $\Delta^{17}O$ value of the initial pool Q_0. Though R_{dep}, R_{nitrif} and R_{loss} may vary slightly with time, they can be assumed relatively time-invariant during a given geologically stable period with modern climate setting for each desert. If Q_0=0, then atmospheric nitrate is always proportional to biotic nitrate during both the input and loss processes, and the $\Delta^{17}O$ of the remaining soil nitrate pool ($\Delta^{17}O_{soil}$) is $\frac{\Delta^{17}O_{atm} \bullet R_{dep}}{R_{dep}+R_{nitrif}}$. Otherwise, if Q_0 is not zero, then

$$\Delta^{17}O_{soil} = \frac{\Delta^{17}O_{atm}\bullet R_{dep}+[\Delta^{17}O_0(R_{dep}+R_{nitrif})-\Delta^{17}O_{atm}\bullet R_{dep})\bullet\left[1+(R_{dep}+R_{nitrif}-R_{loss})\bullet\frac{t}{Q_0}\right]^{-\frac{R_{dep}+R_{nitrif}}{R_{dep}+R_{nitrif}-R_{loss}}}}{R_{dep}+R_{nitrif}}$$

Eq. 4.5

The $\Delta^{17}O_{soil}$ values are then determined by the size and $\Delta^{17}O$ value of the original soil nitrate pool, R_{dep}, R_{nitrif} and R_{loss}, as well as the timescale. There are two timescale extremes for applying the model that are limiting.

The first timescale extreme is when the integration time is short and on the same scale of N turnover (assimilation, mineralization and nitrification), which is typical in relatively wet desert sites, such as the Mojave and Thar deserts. For these sites, the initial nitrate inventory Q_0 may be periodically flushed to a subsoil reservoir by infrequent large storm events, which was evidenced by the nitrate pools at depths >2 m in several southwestern US deserts (Walvoord et al., 2003). This can be considered to be resetting the initial nitrate inventory Q_0 to zero. The surface and near-surface nitrate is thus relatively young and the $\Delta^{17}O_{soil} = \frac{\Delta^{17}O_{atm}\bullet R_{dep}}{R_{dep}+R_{nitrif}}$, where R_{dep} and R_{nitrif} are the modern nitrate deposition and nitrification rates.

The second extreme is when the integration time is long (thousand to million years) and N turnover is negligible. Over geological timescales with the term $\left(R_{dep} + R_{nitrif} - R_{loss}\right) \bullet \frac{t}{Q_0}$ in Eq. 4.5 (the accumulation amount relative to the original inventory Q_0) becoming large enough, the soil nitrate will also achieve an isotopic steady state with $\Delta^{17}O_{soil} = \frac{\Delta^{17}O_{atm}\bullet R_{dep}}{R_{dep}+R_{nitrif}}$. Under this limit, nitrate accumulation begins within the time

integral, all previous nitrate having been removed by leaching, runoff or utilization. In the driest parts of the Atacama and Kumtag deserts where hyper-aridity has persisted for millions of years (e.g. Rech et al., 2006; Qin et al., 2012), the near absence of water and biology results in a long-term stable accumulation of atmospheric deposition and nitrification with the soil nitrate legacy Q_0 relatively becoming minor (Michalski et al., 2004; Ewing et al., 2006). The build-up of nitrate at these sites can occur at shallow depths because leaching loss is also minimal and be operated over long timescales to finally form massive nitrate deposits (Ericksen, 1981), which can also initiate a isotopic steady state in these ancient surface nitrate.

Therefore, for the nitrate sampled <50 cm deep in this study, the impact of the original soil pool Q_0 on the isotopic signature of soil nitrate should be minor in all the four deserts. Then, the ratio of R_{nitrif} and R_{dep} should be proportional to that of the mole fractions of atmospheric nitrate (f_{atm}) and biotic nitrate (f_{nitrif}) in Eq. 4.1 and R_{nitrif} can be deduced from:

$$R_{nitrif} = f_{nitrif}/f_{atm} \bullet R_{dep} \qquad \text{Eq. 4.6}$$

4.4.2.2 The NO_3^- Source Apportionment

The relative contributions of the two NO_3^- sources can be obtained based on the two-component $\Delta^{17}O$ mixing model as stated in the introduction section (Eq. 4.1). Atmospheric NO_3^- $\Delta^{17}O$ values modeled by Alexander et al. (2009) over each desert have had too coarse a spatial resolution and used anthropogenic conditions and were therefore not considered. A uniform $\Delta^{17}O_{atm}$ value of 23‰ was hereby used for different sites (Michalski et al., 2003; Ewing et al., 2007). This adopted value is slightly lower than the

NO_3^- $\Delta^{17}O$ values in the 2003-2006 Greenland snowpit ranging from 24.7‰ to 33.0‰, which is due to the nonzero $\Delta^{17}O$ of oxidant, the nitrate production pathway with high $\Delta^{17}O$ value favored by cold temperature in polar regions (Kunasek et al., 2008; Michalski et al., 2011). In this way, Eq. 4.1 can be simplified as: $f_{atm} = \Delta^{17}O_{soil}/23$. The molar fractions of gross nitrification production are then calculated ($f_{nitrif} = 1 - f_{atm} = 1 - \Delta^{17}O_{soil}/23$) and shown in Table 4.2. In some parts of the Atacama and the Kumtag, atmospheric deposition is the primary source of these nitrates while minor biotic sources of nitrate are evident. In the Mojave and some high-altitude Atacama sites, soil nitrate is partially derived from atmospherically deposited N with a substantial fraction from nitrification, whereas most of soil nitrate in the Thar is derived from nitrification. This shift in nitrate source between these desert sites is a function of water availability, in line with the negative correlation between soil NO_3^- $\Delta^{17}O$ and MAP.

4.4.2.3 Atmospheric Deposition Rates

Estimating R_{dep} has been roughly attempted in three ways: by measurements, using large scale N deposition models, and applying a simple column N removal model (*e.g.* Young, 1988; Holland, 1999; Galloway et al., 2004; Báez et al., 2007). There are only a few measurements of the rates and patterns of modern N deposition in deserts, and these are mainly near large urban cities (Báez et al., 2007; Baker et al., 2001; Fenn et al., 2003). This is because of technical difficulties and expenses associated with the station set-up and maintenance, as well as the subsequent sample recovery in remote areas (Fenn et al., 2003). The pre-human rates of N deposition in pristine desert cannot be directly derived

from the limited number of modern measurements because of the significant influence of modern anthropogenic N emissions (Galloway et al., 2004).

Preindustrial N deposition rates have been estimated using global transport-chemistry models (Holland et al., 1999; Galloway et al., 2004). These are useful tools for understanding the entire N cycle at the global scale, but the pre-industrial N species emission estimates can have large uncertainties. This is because evaluating the magnitude of NO_x produced by different quantities and types of biomass burning, spatial/temporal variations in lightning NO_x and the local effectiveness of stratospheric NO_x fluxes, is often difficult (Holland et al. 1999). Also, the spatial resolution of these global models is usually coarse (>230,000 km^2). This further limits the precision of estimating the spatial variations of N deposition between different desert sites (Holland et al., 1999; Galloway et al., 2004; Liao and Seinfeld, 2005).

An alternate approach to assess desert N deposition rates is to explore N-species removal from a column of air by the way of dry and wet deposition, respectively (Seinfeld and Pandis, 2006). To estimate nitrate deposition in the Atacama, Michalski et al. (2004) assumed that the dry removal is mainly influenced by air mass origins and the mixing of different air masses with different nitrate deposition fluxes, while the wet removal can be derived from the size and amount of forming droplets and the nitrate concentrations in fog/rainfall droplets. In view of the complexity and variability of the processes involved in nitrate deposition, this method mainly focused on atmospheric output (deposition) characteristics and their influencing factors, which was simple and appropriate at a regional scale. In this study, a strategy of combining the column removal mechanisms and the global transport-chemistry model results has been used to estimate

nitrate deposition rates across the four studied deserts: the total nitrate deposition (R_{dep}) is considered as a sum of dry deposition ($R_{dry\text{-}dep}$), and wet deposition ($R_{wet\text{-}dep}$) that consists of two distinct removal processes: in cloud (ic) and below cloud (bc) nitrate removal: $R_{dep} = R_{wet\text{-}dep}$ (ic, bc) + $R_{dry\text{-}dep}$, where $R_{dry\text{-}dep}$ and $R_{wet\text{-}dep}$ can be obtained based on the global model results.

Wet deposition of nitrate is first estimated by lumping the effects of in-cloud and below-cloud scavenging of the local air column into a few parameters. Because of its high solubility, in-cloud nitrate can be rapidly dissolved into cloud droplets and is assumed to be contained wholly within cloud water droplets before being removed (Chang, 1984). Therefore, the in-cloud nitrate removal rate is determined by the collection of cloud droplets by raindrops. In the air column, below-cloud nitrate mainly exists as nitric acid vapor $HNO_{3(g)}$ and nitrate particles. Among these, aerosol nitrate is always associated with ammonium at fine mode (diameter <2.5μm), while coarse mode aerosol (diameter>2.5μm) nitrate is mainly formed via heterogeneous reactions of gaseous HNO_3 and N_2O_5 with coarse sea-salt aerosols or mineral dust (Wall et al., 1988). The amount of fine nitrate aerosols can be trivial due to the absence of base as NH_3 in pristine clean atmosphere, but coarse nitrate aerosols can be substantial along the coasts with sea-salt sprays or in desert regions featured by local mineral dust cycling (Wolff, 1984; Hwang et al., 2006). Hence, below-cloud nitrate scavenging can be considered consisting of the nearly irreversible transfer of $HNO_{3(g)}$ to the rain drops and the entrainment of coarse aerosols coated with nitrate by raindrops (Seinfeld and Pandis, 2006). Based on some simple assumptions and integration of the existing research results, two removal coefficients of Λ_c and Λ_g (s^{-1}) were used to quantify the entrainment of

cloud drops (in-cloud nitrate removal) and below-cloud gaseous HNO_3 in a homogeneous atmosphere, respectively: $\Lambda_c = 4.0\times10^{-4}I^{0.74}$ and $\Lambda_g = 0.34\times10^{-4}I^{0.65} + 1.1\times10^{-4}I^{0.76}$, where I is the precipitation intensity (mm h^{-1}) (Chang, 1984). The removal of below-cloud aerosol nitrate, however, was not in scope. If assuming the aerosol equivalent diameter is 10μm, the same as the assumed cloud droplet diameter by Chang (1984), and the aerosol nitrate swept by precipitation follows the same raindrop collision mechanism as for cloud droplets, the scavenging of below-cloud aerosol nitrate coefficient (Λ_a) should be the same as Λ_c of $4.0\times10^{-4}I^{0.74}$. This near-linear correlation between wet deposition rate and precipitation rate is consistent with observations in the Chihuahuan Desert in Western US that the total nitrate deposition is positively correlated with precipitation amount (Báez et al., 2007), though dry and wet deposition were not separated in their research.

These scavenging coefficients can be used to investigate the detailed impact of the intensity and frequency of precipitation on nitrate removal. Assuming constant scavenging coefficients with time and negligible chemical losses during a rain event, the content of nitrate in each phase varies along the trend with time: $C=C_0e^{-\Lambda t}$ (Seinfeld and Pandis, 2006). Then, for a 5 mm h^{-1} rainfall event lasting for 30 minutes, 91% of in-cloud nitrate can be considered to have washed out, while 43% and 91% of the below-cloud aerosol nitrate and $HNO_{3(g)}$ are removed, respectively. Instead, for a one-hour 10 mm h^{-1} event, most of atmospheric nitrate (>90%) should have been removed. This suggests that a light or moderate rain (2.5-10 mm) can efficiently deplete most of the atmospheric nitrate, and after raining for a while, the latter-stage rainfall contains very little nitrate since the atmosphere is nearly depleted. Therefore, atmospheric nitrate deposition is determined by the frequency of storms (sequences of rain occurring on successive days

separated by gaps of rain-free days) rather than individual events. This is an important point at some relatively wet desert sites because the majority of storms may be strongly clustered with gaps of less than 10 days and even less than 5 days (Reynolds et al., 2004). Yet, for the hyper-arid core of the Atacama, only a single 30-min recording period of 2.3 mm rainfall was observed during September 1994-October 1998 (McKay et al., 2003), and it would be reasonable to assume the rainfall events are rare and more scattered at relatively dry sites in the Atacama and in the Kumtag.

Holland et al. (1999) estimated global preindustrial NO_x and NH_3 emissions and then used them in a global troposphere model, MOGUNTIA, to estimate N deposition rates in continental regions based on land and plant types, local emission inventories, and global circulation and precipitation. They suggested that the average rates of pre-industrial total N deposition for deserts located in the tropics and northern-hemisphere (NH) temperate regions were 43 and 26 mg N m^{-2} yr^{-1}, respectively. These pre-industrial N deposition rates are 3~6 times lower than the modern deposition rates (Holland et al., 1999), consistent with the model results by Galloway et al. (2004). If assuming the dry deposition components accounts for 30% of the average total N deposition rates of 43 and 26 mg N m^{-2} yr^{-1} (Báez et al., 2007) and nitrate is the dominant N species in atmospheric deposition, the average nitrate inputs from wet deposition are then 18 mg N m^{-2} yr^{-1} for the NH temperate deserts and 30 mg N m^{-2} yr^{-1} for the tropic deserts. For simplicity, the equations by Chang et al. (1984) can be approximated to the linear relationships between scavenging coefficients and the rainfall intensity. The total R_{wet_dep} can then depend on the rainfall intensity and rainfall events. Though clustered rainfall events may reduce the efficiency in nitrate removal, the rainfall amount P (the multiplication of rainfall intensity,

duration and frequency) is treated as the best index for rainfall characteristics without accurate storm event frequencies for the four deserts. Therefore, assuming R_{wet_dep} is linearly correlated to rainfall amount P in the range of 0-500 mm (desert rainfall range), then for the NH deserts, $R_{wet\_dep} = 0.072 \times P$ and for the Atacama, $R_{wet\_dep} = 0.12 \times P$, where the coefficients of 0.072 and 0.12 were derived by dividing the average wet deposition rates of 18 and 30 mg N m^{-2} yr^{-1} by the supposed average rainfall amount of 250 mm, respectively.

The nitrate dry deposition rate is estimated based on the nitrate deposition fluxes from different air masses that contribute to the studied regions. Nitrate deposition rate is mainly governed by atmospheric turbulence, the chemical properties of nitrate species and the nature of the surface (Seinfeld and Pandis, 2006). The chemical properties of nitrate species and the nature of the surface should be similar across the four studied deserts, while the dry deposition rate of nitrate depends on the degree of atmospheric turbulence that can greatly vary with different air mass origins (Michalski et al., 2004). Among the four deserts, the Mojave, Atacama and Thar likely receive a mixture of oceanic and continental air masses, while the Kumtag is an inland desert. The differences in dry deposition rate of nitrate among the four studied deserts may arise from the differences in continental and oceanic fluxes. In detail, equal proportions of oceanic and continental nitrate deposition will be assumed for the three coastal deserts, while only continental nitrate deposition exists in the Kumtag. The global oceanic deposition model of Duce et al. (1991) yielded dry deposition fluxes of nitrate of 9, 4 and 11 mg N m^{-2} yr^{-1} for North Pacific, South Pacific and North Indian surface waters, in agreement with results given in Warneck (2000) for pristine oceanic atmospheres. The continental nitrate

inputs from dry deposition are 8 mg N m^{-2} yr^{-1} for the NH temperate deserts and 13 mg N m^{-2} yr^{-1} for the tropic desert as discussed above (Holland et al., 1999). The half-and-half mixing of North Pacific and NH temperate continental fluxes would imply a dry deposition nitrate flux to the Mojave of 8.5 mg N m^{-2} yr^{-1}. Similarly, South Pacific and tropic continental fluxes are approximately equally represented in the Atacama leading to the nitrate dry deposition rate of 8.5 mg N m^{-2} yr^{-1}, and the homogenization of North Indian oceanic and NH temperate continental fluxes makes the dry deposition rate of nitrate of 9.5 mg N m^{-2} yr^{-1} for the Thar, while the Kumtag nitrate dry deposition is only derived from continental air flux at the rate of 8 mg N m^{-2} yr^{-1}.

Total nitrate deposition can be obtained by summing the constant dry deposition and variable wet deposition components as shown in Table 4.2. The smallest nitrate deposition of 8.5 mg N m^{-2} yr^{-1} is for the hyper-arid site in the Atacama, which is four times lower than the measured 46.2 mg N m^{-2} yr^{-1} in modern times for a similarly hyper-arid site (Yungay site) in the Atacama by Ewing et al. (2007). This is probably because the nitrate deposition rate at Yungay site has been overestimated due to the local mining and road activities and the imprint of global anthropogenic N emissions in modern times. The nitrate deposition rates in the Kumtag, Mojave and Thar are more than 10-20 times lower than those measured in modern times by Zhang et al. (2008) in northwestern China, Young et al., (1988) in the southwestern USA and Bhattacharya et al. (2004) in the Arga region in India, respectively, which can also be attributed to the increased N emissions since industrial evolution as well as the distribution of monitoring stations nearby the urban regions.

4.4.2.4 Gross Nitrification Rates

The soil GNRs for each desert can be derived based on the deposition rates discussed above according to Eq. 4.6 (Table 4.2). The soil GNRs in four deserts concur with the wide range of GNRs (0-150 kg N ha^{-1} yr^{-1}) in natural non-desert systems (Hart and Gunther, 1989; McClaugherty et al., 1985; Aber et al., 1985; Castro et al., 1992). The lowest gross nitrification rate at the site Coya Sur in the Atacama (P=0.4 mm) of 0.7 mg N m^{-2} yr^{-1} is approximately twice the net nitrification rate of 0.36 mg N m^{-2} yr^{-1} estimated based on the $\Delta^{17}O_{soil}$ value and soil nitrate inventory, suggesting the reliability of my estimates (Ewing et al., 2007). The gross nitrification rate beneath annual grass stands at a Great Basin desert site in Northern Utah in the USA (annual precipitation: 315 mm) was determined in intact soil cores using the ^{15}N isotope dilution technique to be 22,535 mg N m^{-2} yr^{-1} (Booth et al., 2003), ~20 times higher than that at my Bikaner site with 305 mm of precipitation per year. This is likely due to the increased soil microbial mass beneath desert brushes compared to that under brush interspaces, which may significantly elevate the nitrification rate causing "islands of fertility" (Schlesinger and Pilmanis, 1998). Some nitrification rates derived from lab incubation experiments in the Mojave are also one or two order of magnitude higher than my estimates (Schaeffer et al., 2002), because soil water content is always elevated to maintain microbial activity in the lab compared to the natural soils. However, there are only a few measurements of nitrification rates in desert soils. In addition, most of these measured nitrification rates were derived from laboratory incubation or field addition experiments with soil water or nutrient content elevated to maintain microbial activities (Schaeffer et al., 2003; Nejidat, 2005). Those rates often overestimate nitrification compared to natural desert

environments where microbial communities are acclimated to rainfall pulses or nutrient limitation (Austin et al., 2004). Therefore, a new proxy for GNRs in natural desert regions is desired.

4.4.3 Paleo-climate Inference

The Baquedano trench soil NO_3^- $\Delta^{17}O$ varied from 17.1-20.0 ‰, far exceeding the analytical precision of ±0.2‰, suggesting significant variations of soil NO_3^- $\Delta^{17}O$ with depth (Figure 4.3). According to Eq. 4.1, these soil NO_3^- $\Delta^{17}O$ variations can be ascribed to three factors: 1) atmospheric NO_3^- $\Delta^{17}O$ variations; 2) atmospheric NO_3^- deposition rate variations (possibly post-depositional processes); 3) nitrification rate variations.

The weight percents of chloride and nitrate in soil correlate with each other (Pearson correlation coefficient $r=0.565$, $p<0.01$) (Figure 4.4), indicating their behaviors in soil may be controlled by the same mechanism. The dominant mineral forms of chloride and nitrate are $NaNO_3$ (nitratine) and NaCl (halite), which are both soluble with solubilities of 87.4 g (1.03 mol) and 35.7 g (0.61 mol) in 100 g water at 20°C, respectively. Small amounts of rainfall events in the Atacama still occur in the hyper-arid core zone of the Atacama, which can dissolve surface ions from atmospheric deposition forming concentrated brines. During the downward movement of the brines, salt minerals would sequentially precipitate out based on thermodynamic equilibrium (Chapter 2). This can probably explain the segregation of chloride and nitrate salts at similar depths because of their similar solubilities. Therefore, the ages of soil chloride as a function of depth (Chapter 3) estimated by the ^{36}Cl dating technique can also provide rough constraints for soil nitrate in the Baquedano trench profile (spanning ~860 ky and at the time resolution of ~20 ky for each sample). Then, the significant variations in Baquedano trench soil

NO_3^- $\Delta^{17}O$ with depth would reflect temporal variations in soil NO_3^- $\Delta^{17}O$. Further observations indicated roughly six periodic cycles over the past 860 ky (Figure 4.3). Therefore, I will focus on possible driving force mechanisms for soil NO_3^- $\Delta^{17}O$ on the ~150 ky scale.

As discussed in Chapter 1, there are seasonal and spatial variations in atmospheric NO_3^- $\Delta^{17}O$ derived from the NO_x oxidation pathways (Michalski et al., 2011), which may partly account for the soil NO_3^- $\Delta^{17}O$ variations in the Baquedano trench. For the Baquedano trench site, the spatial variations in atmospheric NO_3^- $\Delta^{17}O$ should be trivial since the geographic position of the South America continent was nearly fixed during the last 150 Ma based on geomagnetic research (Beck et al., 2000). The seasonal variations in atmospheric NO_3^- $\Delta^{17}O$ may mostly average out over the timescale of thousand years (the time resolution of my sampling according to ^{36}Cl dating results). However, there should exist secular variations in atmospheric NO_3^- chemistry that can impact atmospheric NO_3^- $\Delta^{17}O$. Several box model systems have been used to simulate atmospheric NO_3^- $\Delta^{17}O$ (Michalski et al., 2003; Kunasek et al., 2008; Morin et al., 2008; Michalski and Xu, 2010), while global variations in atmospheric NO_3^- $\Delta^{17}O$ were further estimated by a 3D global chemical transport model by Alexander et al. (2009). These model results all pointed to one factor that atmospheric NO_3^- $\Delta^{17}O$ values are most sensitive to the abundance of O_3 relative to other atmospheric oxidants (Kunasek et al., 2008; Michalski and Xu, 2010). The 30-year running average of the $\Delta^{17}O$ of NO_3^- from the Site A, Greenland ice core showed a 1.5 ‰ difference between the minimum and maximum values during the preindustrial period 1680-1830 (Alexander et al., 2004). The

high NO_3^- $\Delta^{17}O$ values were mainly owing to an elevation of O_3 and decrease of OH in the atmosphere as well as the gained importance of the $N_2O_5+H_2O+surface \rightarrow 2HNO_3$ pathway induced by the intense biomass burning recorded in North America during this period (Alexander et al., 2004). There have been no terrestrial or atmospheric NO_3^- $\Delta^{17}O$ records extended to thousands of years ago yet, but several ice core non-seasalt (nss) SO_4^{2-} $\Delta^{17}O$ measurements were dated back over the past ~100 ky. The $\Delta^{17}O$ of nss-SO_4^{2-} from Vostok site, Antarctic ice core peaked with 4.8 ‰ during the Eemian period (~130 ka) compared to the lowest value of 1.3 ‰ during the last glacial period (~60 ka), while the nss-SO_4^{2-} $\Delta^{17}O$ spanned from 4.1-2.2 ‰ for the Dome C ice core (another Antarctic site) over the preindustrial Holocene to the last glacial period (2~37 ka) (Alexander et al., 2003). These nss-SO_4^{2-} $\Delta^{17}O$ differences are likely attributed to the higher OH concentrations in the last glacial period than in the Eemian or preindustrial Holocene periods (Thompson, 1992). Similarly, I argue the oxidation capacity (the interaction of three principal oxidants in the lower atmosphere O_3, OH and H_2O_2) can also significantly influence atmospheric NO_3^- $\Delta^{17}O$. The atmospheric oxidation capacity variations over long timescales, such as the glacial-interglacial cycles, may then have partly accounted for soil NO_3^- $\Delta^{17}O$ variations with depth in the Baquedano trench, but the extent of the influence is difficult to resolve because of the challenge of reconstructing oxidation chemistry in the past (Thompson, 1992).

Also, there may be some temporal variations in atmospheric NO_3^- deposition that may cause soil NO_3^- $\Delta^{17}O$ variations with depth, which depend on the NO_y (the sum of oxidized nitrogen species) inventory and the subsequent production, deposition and the

perseverance of NO_3^- in my soil profile (Galloway et al., 2004). Lightning, biomass burning and soil emissions of NO_x ($NO+NO_2$) are the major sources of NO_y in the preindustrial atmosphere, especially at my site near the tropical region (Holland, 1999). For an individual measurement site, lightning variations tend to be small over long timescales (Williams, 2005). Global biomass burning, however, may vary significantly over time related to the frequency and intensity of fire activities. Fire activities in preindustrial periods have been assumed to be a function of vegetation density, ambient meteorological conditions (relative humidity, temperature and precipitation) and availability of ignition sources (*e.g.* lightening) (Marlon et al., 2008; Pechony and Shindeli, 2010). Vegetation density was shown to be relatively consistent over the past 10,000 years when imprinted by small anthropogenic influences (Goldewijk et al., 2011) but may still change through glacial-interglacial cycles (Tzedakis, 1994). Interglacial periods would likely induce larger vegetation coverage in response to their warmer temperature and less ice coverage compared to glacial period. In addition, warm and dry periods are more liable to incur wildfires than cold and wet periods (Marlon et al., 2008; Pechony and Shindeli, 2010). Therefore, interglacial periods should tend to have more NO_x emissions from biomass burning. Soil emissions in hot deserts (such as my site) have been predicted to experience negligible change in response to temperature or precipitation change using a coupled ecosystem production and soil carbon-nitrogen model (Carnegie-Ames-Stanford biosphere model) by Potter et al. (1996), and would unlikely vary significantly over the glacial-interglacial cycles. The production of atmospheric NO_3^- from NO_x is related to some meteorological conditions besides the amount of NO_x. The influence of abundant volcanic sulfur emissions that can lead to high

concentrations of H_2SO_4, the consumption of atmospheric oxidants and a less formation of NO_y have been found in both Antarctica and Greenland ice cores (Legrand and Kirchner, 1990; Wolff, 1995). Variations of the Antarctic and Greenland ice core NO_3^- deposition were also partly attributed to the variations in solar activities that can impact the amount of energy particles to break N_2 and O_2 and form N_2O and then NO_3^- in the stratosphere that can be transported to the troposphere (McCracken et al., 2001; Zeller and Dreschhoff, 1995; Zeller et al., 1986). However, the contribution of stratospheric NO_3^- is probably unimportant in tropic regions because of the relative lack of low-energy particles at low latitudes compared to those in polar region. The deposition processes may also cause variations in atmospheric NO_3^- deposition at my site. Since the site is hyper-arid and should be dominated by dry deposition, the scavenging of NO_3^- in the atmosphere column cannot be sufficient and small change in wet deposition may thus influence NO_3^- deposition significantly. In the polar ice cores, post-depositional processes, like the photolysis and transport of NO_3^-, may impact the perseverance of NO_3^-. In the soil core, downward migration induced by wet events probably plays a role in the NO_3^- distribution though the hyper-arid climate may have minimized the leaching processes compared to those at most other sites on earth. Therefore, climate change that can impact the regional NO_x inventory and the scavenging of atmospheric NO_3^- from the atmosphere column as well as potential volcanic emission can both cause variations in atmospheric NO_3^- deposition, leading to the soil NO_3^- $\Delta^{17}O$ variations.

Lastly, nitrification rates may vary over time with increasing or decreasing water availability to account for the soil NO_3^- $\Delta^{17}O$ variations. Some pioneer soil microorganisms in the Atacama can become biologically active in response to short

pulses of water with high instantaneous rates of nitrogen fixation and NO_3^- production, contributing significantly to desert ecosystem nitrogen inventory (Chapter 5). This suggests that larger nitrification rates, corresponding to wetter climate, may elevate the contribution of biotic nitrate relative to atmospheric nitrate and then lower soil NO_3^- $\Delta^{17}O$. Therefore, paleoprecipitation variations can also be an important reason for the soil NO_3^- $\Delta^{17}O$ variations in the Baquedano trench profile.

From the three aspects, interglacial periods with warmer and drier climates and smaller ice coverage compared to glacial periods tend to have higher atmospheric NO_3^- $\Delta^{17}O$, more NO_x emissions from biomass burning, smaller nitrification contribution, and thus higher soil NO_3^- $\Delta^{17}O$. Therefore, the periodic fluctuations of soil NO_3^- $\Delta^{17}O$ are likely reflecting the glacial-interglacial cycles controlled by orbital change (Figure 4.3). Historic volcanic eruptions may have further caused the soil NO_3^- $\Delta^{17}O$ variations with depth and disturbed the glacial-interglacial trend.

4.5 Conclusions

Soil NO_3^- $\Delta^{17}O$ values ($\Delta^{17}O_{soil}$) were observed to significantly vary between different desert sites from the Atacama (Chile), Kumtag (China), Mojave (US), and Thar (India) deserts due to different contributions of atmospheric nitrate to soil nitrate pool. The negative correlation between $\Delta^{17}O_{soil}$ and the mean annual precipitation (MAP) of the corresponding desert soil sites demonstrated the potential of $\Delta^{17}O_{soil}$ as a precipitation proxy in arid landscapes. This quantitative relation ($MAP = 0.3 \times (\Delta^{17}O_{soil})^2 - 16.0 \times \Delta^{17}O_{soil} + 214.9$) can be used to explore the past precipitation history together with

careful geological site inspections, specifically in the precipitation range of 0-212 mm. Moreover, $\Delta^{17}O_{soil}$, coupled with the documented atmospheric nitrate deposition rates, can be used to estimate soil GNRs by delineating the relative molar fractions of the two sources (i.e. atmospheric deposition and nitrification). The resulted soil GNRs ranged from 0.7 mg N m^{-2} yr^{-1} in the hyper-arid core of the Atacama to 885 mg N m^{-2} yr^{-1} in the wettest Thar Desert among the four deserts. The $\Delta^{17}O_{soil}$ variations in the 225 cm deep Baquedano long trench profile constrained by the ^{36}Cl date-defined ages likely reflected seven periodic cycles, corresponding to possible glacial-interglacial cycles operated on the 100 ky scale induced by that orbital change and volcanic emissions.

4.6 Acknowledgments

This work was supported by the US National Science Foundation (EAR 0922114). We thank Wensheng Ge, Brenda Bowen, S.K. Bhattacharya, Raul Ochoa, Ritesh Purohit and Hao Luo for assistance during sample collection.

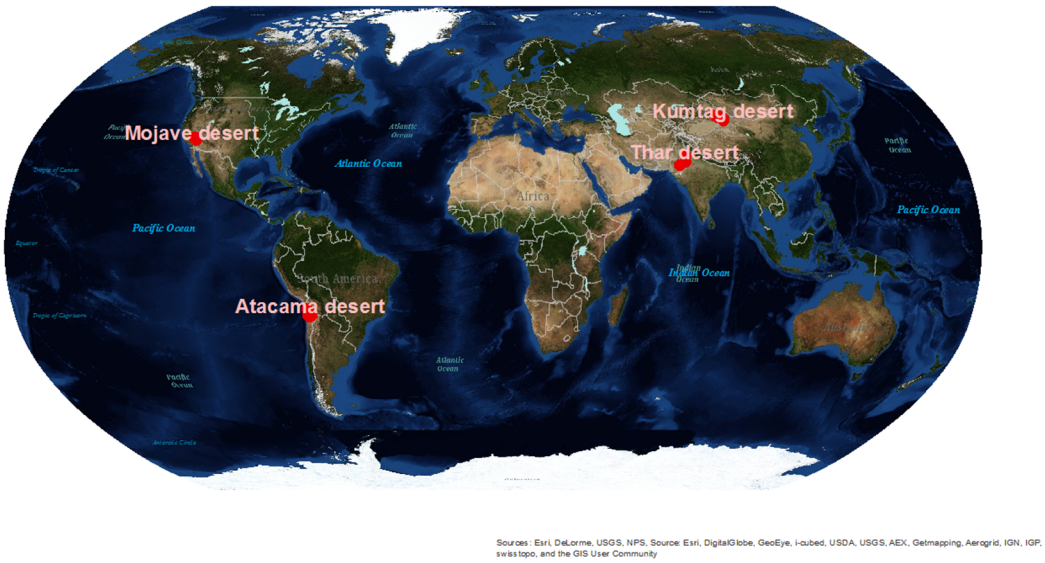

Figure 4.1 The location of sampling sites from the four deserts around the world

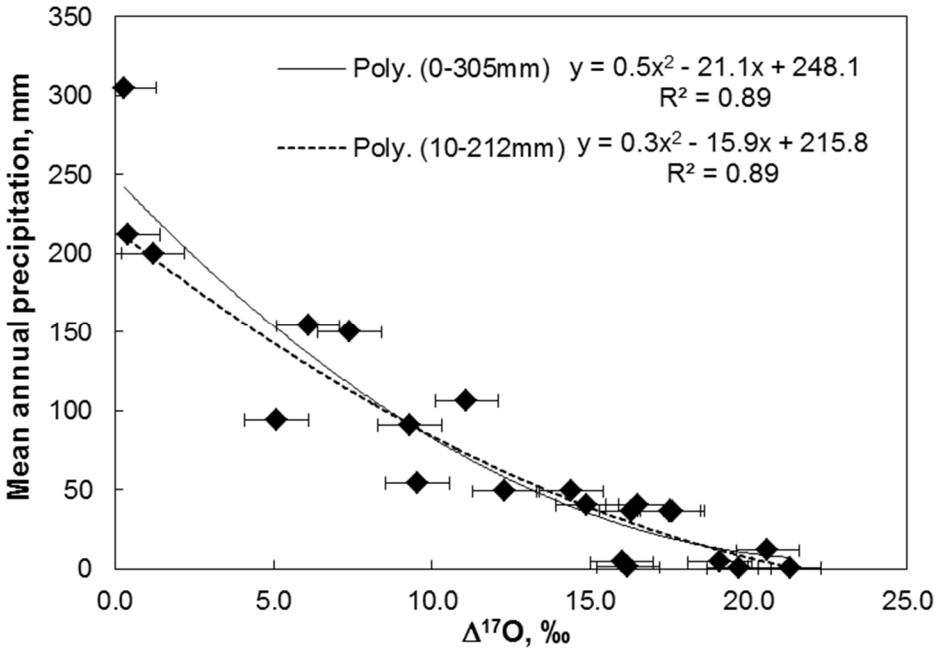

Figure 4.2 The relationship between soil NO_3^- $\Delta^{17}O$ and annual precipitation amount

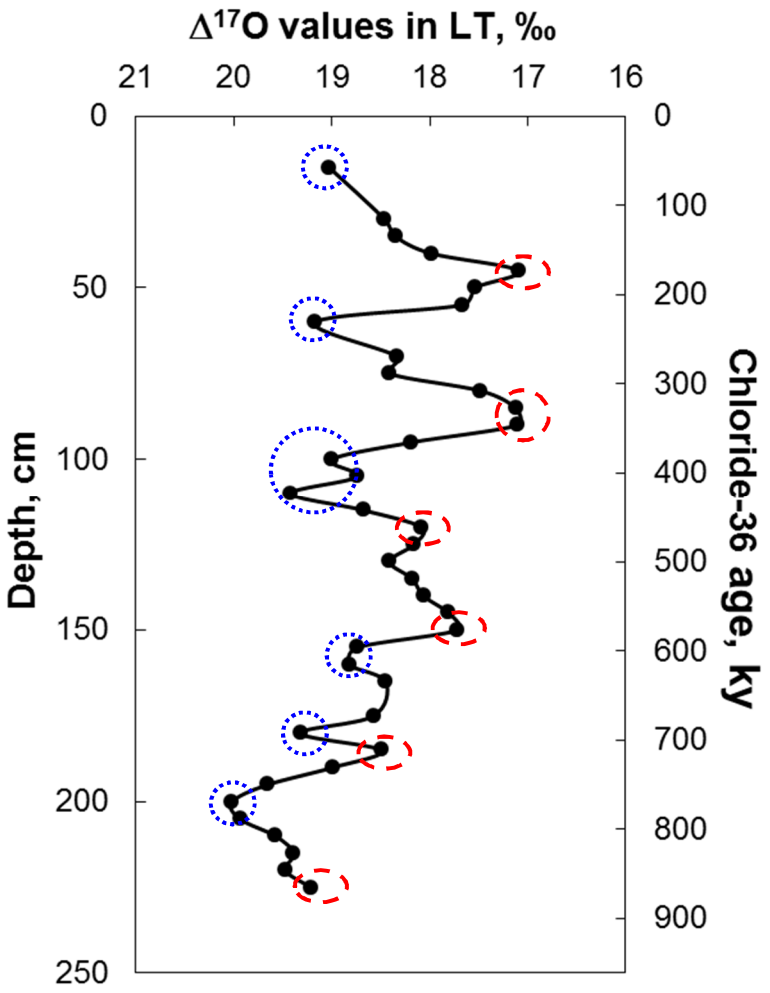

Figure 4.3 The soil NO_3^- $\Delta^{17}O$ variations with depth constrained by the chloride-36 age for the Baquedano soil profile (the blue circles and red ovals suggesting periodic cycles)

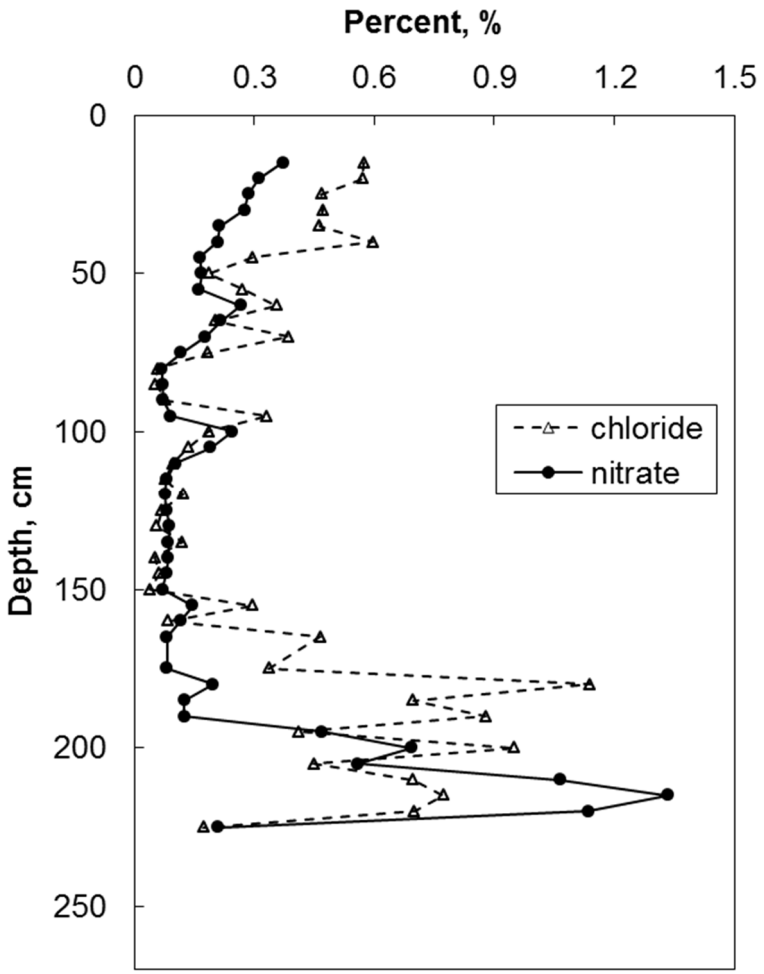

Figure 4.4 Percent distribution of chloride and nitrate (by mass) in the soil with depth

Table 4.1 Descriptions of the selected precipitation sites

Sites	Coordinates (elevation, m)	Rainfall, mm[a]	Site descriptions
Atacama Desert, Chile			
Calama	22.53°S 68.97°W (4374)	4.2	Alluvial fan, dense desert pavement with light-colored 1-5cm clasts
Chiu Chiu	22.34°S 68.66°W (2555)	4.4	Alluvial fan, dense desert pavement with light-colored 1-5cm clasts
Copaquire	20.94°S 69.07°W (3384)	54.1	Mountain valley, dense desert pavement with moderately varnished 1-5cm clasts and 20% coverage of brushes
Coya Sur	22.40°S 69.58°W (1220)	0.4	Alluvial fan, moderate desert pavement with varnished 2-5 cm clasts
El Tatio	22.38°S 68.02°W (4374)	153.9	Small hill, dense desert pavement with light-colored 1-5 cm clasts on the top and 30% coverage of brushes on the slope
Huatacondo	20.92°S 69.04°W (2219)	11.5	Fluvial terrace at hill foots, moderate desert pavements with light-colored 5-20 cm cobbles
Ojos	19.96°S 69.54°W (1336)	0.9	Mountain basin, sparse desert pavements with moderately varnished 1-5 cm clasts and 5-20 cm cobbles
Quillagua	21.68°S 69.54°W (906)	0.2	Alluvial fan, sparse desert pavement with light-colored 1-5 cm clasts
Tocene	22.26°S 68.19°W (3237)	94.1	Alluvial fan, rugged surface with light-colored 5-20 cm cobbles and dead brushes occupying 40% of the surface
Kumtag Desert, China			
Dananhu	42.37°N 92.82°E (543)	40.5	Alluvial fan, moderate desert pavement with moderately varnished 1-5cm clasts
Dawadi	41.45°N 92.65°E (1028)	49.1	Mountain basin, rugged surface with light-colored 5-10 cm cobbles, no brushes
Kumtag mine	42.69°N 91.17°E (312)	36.5	Alluvial fan, dense desert pavement with varnished 1-5cm clasts
Kuzishan	41.45°N 92.80°E (1079)	49.1	Mountain valley, compensated by brine spring creek, and brushes occupying 30% of the surface
Qiketai	42.92°N 90.88°E (408)	36.5	Small hill, exposed profile (road cut) in a layer-like fashion (the top 20cm: well-cemented sand layer)
Xiaocaohu	43.10°N 90.30°E (713)	36.5	Alluvial fan, rugged surface with heavy-colored 5-10 cm cobbles, and brushes occupying 15% of the surface
Xigebi	42.05°N 92.95°E (767)	40.5	Alluvial fan, dense desert pavement with varnished 1-5cm clasts
Mojave Desert, USA			
Cima	35.20°N 115.87°W (1106)	149.9	Alluvial fan, fully covered dense pavements with dark 5-10 cm clasts with brush roots
Lower canyon	35.71°N 116.23°W (217)	90.7	Fully covered pavements with brush roots
Pannemint	36.03°N 117.30°W (469)	106.2	Alluvial fan, rugged surface with mostly dark-colored 2-5 cm clasts and dead brushes occupying 40% of the surface
Thar Desert, India			
Bikaner	28.05°N 73.24°E (215)	305.0	Desert terrain with low relief and sand dune topography
Ganganagar	29.87°N 73.89°E (176)	200.0	Sand surface with >50% brush coverage
Jaisalmer	26.92°N 70.91°E	212.0	Desert terrain with low relief and sand dune topography

[a]Detailed rainfall data are from Houston (2006) for the Atacama sites, from Li et al. (2011) for the Kumtag sites, from http://www.prism.oregonstate.edu/ for the Mojave sites, and from Indian National Data Centre for the Thar sites

Table 4.2 The soil NO_3^- $\Delta^{17}O$ values and calculated N input rates

Sampling site	Sampling depth, cm	$\Delta^{17}O$ (‰) ± SD (sample number)	Mole fraction of nitrification	Atmospheric deposition, mg N m^{-2} yr^{-1}	GNR, mg N m^{-2} yr^{-1}
Atacama Desert, Chile					
Calama	0-20	16.0±1.9(2)[a]	0.30	8.8	3.8
Chiu Chiu	0-25	19.1±0.6(3)[a]	0.17	8.8	1.8
Copaquire	1-3	9.55±0.0(1)[a]	0.58	11.7	16.5
Coya Sur	0-30	21.3±1.4(4)[a]	0.07	8.5	0.7
El Tatio	0-30	6.1±6.0(4)[a]	1.00	17.7	
Huatacondo	0-50	20.6±1.5(2)[a]	0.10	9.2	1.1
Ojos	0-20	16.2±0.5(2)[a]	0.30	8.6	3.6
Quillagua	0-10	19.7±0.4(2)[a]	0.14	8.5	1.4
Tocene	0-40	5.1±0.0(1)[a]	0.78	14.1	49.6
Kumtag Desert, China					
Dananhu	0-30	16.5±0.5(7)[b]	0.28	9.5	3.7
Dawadi	20-30	14.4±0.0(1)[b]	0.37	9.8	5.8
Kumtag mine	5-30	16.3±0.0(2)[b]	0.29	9.3	3.8
Kuzishan	10	12.3±0.2(2)[b]	0.47	9.8	8.5
Qiketai	20	17.5±0.0(1)[b]	0.24	9.3	2.9
Xiaocaohu	30-50	17.6±0.0(1)[b]	0.23	9.3	2.9
Xigebi	0-30	14.9±0.5(2)[b]	0.35	9.5	5.1
Mojave Desert, USA					
Cima	2-30	7.4±0.4(4)[a]	0.68	9.0	19.1
Lower canyon	0-30	9.3±0.0(1)[a]	0.60	8.8	13.0
Pannemint	13-43	11.1±0.6(3)[a]	0.52	8.9	9.5
Thar Desert, India					0.0
Bikaner	0-50	0.3±0.0(1)[b]	0.99	10.6	801.9
Ganganagar	0-50	1.2±0.0(1)[b]	0.95	10.2	185.7
Jaisalmer	0-50	0.4±0.0 (2)[b]	0.98	10.3	579.9

[a]Measured by bacterial reduction method
[b]Measured by bacterial reduction method

CHAPTER 5. THE ROLE OF CRYPTO-BIOTIC CRUSTS ON SOIL FORMATION

5.1 Introduction

While water is often the limiting resource in desert environments, nitrogen deficiency can also cause a low biological productivity, a limitations that is often overcome by crypto-biotic crusts (CBCs) (Belnap, 2006; Lalley et al., 2006). CBCs are living consortia of cyanobacteria, green algae, lichens, and mosses that are capable of surviving in extremes of cold, heat, and aridity, and colonize soil surfaces in deserts across the Earth (Belnap, 2003). They become biologically active, with high instantaneous rates of C and N fixation, by absorbing brief pulses of water, contributing significantly to desert ecosystem fertility and aiding the evolution and spread of other terrestrial life forms. In the hyper-arid Atacama Desert, where extremely hostile conditions preclude vascular plants and other eukaryotic or prokaryotic life, CBC communities are often the key photoautotrophic microorganisms and primary producers (Büdel, 2001).

As part of the N cycling, CBCs are known to exude nitrate into soil (Austin et al., 2004; Johnson et al., 2007), yet how much soil nitrate is produced by CBC versus deposited from the atmosphere, which is significant in deserts, is an open question. CBCs are also found to be able to reduce wind erodibility of soil surfaces (Williams, et al., 1995; Leys and Eldridge, 1998) by exuding extracellular sheath material that binds soil

particles together (Belnap and Gardner, 1993). Fine particle fractions in the soil are typically higher in the crust or the upper few-cm of surface soils beneath CBC than those in non-CBC sites (Belnap, 2001; Li et al., 2005; Zhao et al., 2010), but the explanation of the reason for more fine particles is still not complete. CBCs may also have the potential to alter the soil's water infiltration and ability to retain water by retarding evaporation (Belnap, 2006). However, previous studies showed little agreement on the roles of CBC crusts in affecting water filtration, and advanced knowledge is needed. On the whole, the detailed impact mechanisms of CBCs on desert ecosystem evolution are still insufficiently studied, especially for the hyper-arid regions, and require more research attention.

5.2 Method

Massive CBC communities were identified in a remote valley in the Atacama's Coastal Range near Salar de Grande during field work in December of 2011 (Figure 5.1) and soil samples were collected. The landscape contained three major features: barren grounds, CBC patchy grounds and depression pits. On barren grounds, there were typically no CBC communities, and the surface was covered with 0.5-1 cm reddish to tannish pebbles. CBC communities were widespread on the CBC patchy grounds except in the shallow depression pits that were scattered across the ground surface. The pits were filled with large white salt crystals (mainly NaCl) (Figure 5.2). There are likely frequent occurrences of fog in the valley based on field observation and its geographic similarities to some other foggy sites along the coastal Atacama (Cereceda and Schemenauer, 1991). Eight soil pits were dug along two approximately north-west transects in the CBC area. Sites 2,

3, 5 and 6 had CBCs while the other sites 1, 4, 7 and 8 had no CBC coverage. Pits were excavated to depths in the range of 15-70 cm at which a hard salt layer was encountered. Four to eight samples were obtained from each representative soil horizon in each soil pit. Detailed site descriptions and sampling depths are shown in Table 5.1.

The soils were analyzed for grain size, ions, and stable isotopes. The soil aggregates were gently broken up and a dry sieve analysis was conducted to study the grain size distribution with depth. A split of each soil sample was homogenized and ground by ball mill or hand. Soluble salts were extracted with Millipore water and a series of geochemical and isotopic analysis was subsequently performed on the soil extracts. Cation (Ca^{2+}, Na^{+}, Mg^{2+} and K^{+}) concentrations were determined using inductively coupled plasma-optical emission spectroscopy (ICP-OES Thermo Scientific iCAP 6500), while anions (Cl^{-}, NO_3^{-} and SO_4^{2-}) were analyzed using ion chromatography (IC) with suppressed conductivity detector (Alltech 626 model). Based on the ion concentrations, one split of the soil extract was completely removed of SO_4^{2-} with excess $Ba(NO_3)_2$, converted to $AgCl_{(s)}$ and analyzed for $^{36}Cl/Cl$ ratios by accelerator mass spectrometry (AMS) at Purdue Rare Isotope Measurement (PRIME) Laboratory (Chapter 2), while another split was analyzed for $\delta^{15}N$, $\delta^{17}O$ and $\delta^{18}O$ values of nitrate using a recent bacterial reduction, gold redox method (Riha et al., submitted).

5.3 Results and Discussion

5.3.1 Soil Profile Depth

The loose soil layer above the hard salt basement material was significantly thicker underneath CBCs compared to soils without CBC coverage (Table 5.1). For example, the

loosely-cemented powdery soil extended to 70 cm and 60 cm depths underneath the CBCs at Site 2 and Site 5, respectively, but was only 15-20 cm deep at the barren ground and depression pit sites without CBC coverage only a few meters away. Two profiles located in the transition zones (Sites 3 and 6) had loose soil depths in between ranging from 25-40 cm.

The increase in the loose soil thickness beneath CBC coverage compared to those without CBC coverage suggests that the CBC coverage may be facilitating soil stabilization by trapping more soil particle and isolating them from wind erosion. Wind erosion should be significant at the study site because of frequent high winds (field observation in summer and winter seasons). Fractures and upturned edges in the CBC coverage (Figure 5.2) may allow atmospheric dust to migrate beneath the crust resulting in the accretion of soil over time (Belnap, 2003). This accretion-protection mechanism is similar to soil accumulation under desert pavements, a surface layer of closely packed, interlocking angular or rounded pebble- and cobble-sized clasts, that protect the desert surfaces from wind erosion (McFadden et al., 1987; Anderson et al., 2002). The significant increase in soil depth underneath CBC is thus attributed to enhanced particle trapping and physical protection of the particles from wind erosion.

5.3.2 Size Distribution

The hypothesis of CBC enhancement of soil accretion-protection was tested using grain size analysis. The soil particles consist of mostly sand (63-2000 μm) and only 1-39% silt or clay (<63 μm) fractions (Figure 5.3). General Linear Model-Multivariate Analysis of Variance (GLM-MANOVA) was performed by IBM® SPSS 20.0 using the existence of CBC coverage (*i.e.* with CBCs and without CBCs) as the fixed factor and the percentages

of the five grain size fractions (<63 μm, 63-125 μm, 125-250 μm, 250-500 μm, 500-2000 μm) were the dependents. The GLM-MANOVA analysis showed that there was a statistical difference ($p=0.071<0.1$) in the particle size distribution between soils beneath CBCs and those without CBCs. The two smallest size fractions (63-125 μm and <63 μm) were particularly different between CBC soils and non-CBC soils at the 0.05 significant level ($p<0.05$). This is consistent with the previous studies that indicated CBCs enhanced the fine particle fractions in their underlying soils (Li et al., 2005; Zhao et al., 2010). Two possible mechanisms may account for the greater amount of small particles beneath the CBCs. The first is that CBCs can trap more small particles in wind-blown dust from atmospheric deposition and then protects them from subsequent wind erosion. This does not contradict the discussion in section 5.3.2 of the physical protection. Alternatively, the CBC may facilitate *in situ* weathering, by breaking large particles into small particles due to soil amelioration (Schwartzman and Volk, 1989; Li et al., 2005). I argue that both mechanisms may be important, though the second mechanism requires more study (see discussion below).

5.3.3 Ion Concentrations

The hypothesis of CBC enhancement of soil accretion-protection was also tested by comparing soil ion distribution profiles observed at different sites (Figures 5.4 and 5.5). Generally, for all the sites, soil Na^+, K^+, Mg^{2+}, Cl^- and NO_3^- contents were almost nil on the surface, while Ca^{2+} and SO_4^{2-} were widespread throughout the soil profiles. The Ca^{2+}/SO_4^{2-} molar ratios were 0.75-1.09 in the upper 10 cm of the soil profiles suggesting the presence of gypsum ($CaSO_4 \cdot 2H_2O$) or anhydrite ($CaSO_4$) minerals near the surface. In the subsurface, the soluble ions were dominated by Na^+ and Cl^-, and the Na^+/Cl^- molar

ratios approximated to 1, signaling the existence of halite (NaCl) minerals. There were also significant amounts of K^+, Mg^{2+}, Cl^-, NO_3^-, SO_4^{2-} and Ca^{2+} in the subsurface, and SO_4^{2-} was in excess of Ca^{2+} unlike the coupling of Ca^{2+} and SO_4^{2-} near the surface.

The ion distribution in soil below CBC was statistically different from those without CBC coverage indicating CBCs may be altering ion accumulation rates. The GLM-MANOVA analysis revealed that at CBC sites, all soil ion concentrations (g/g), except Ca^{2+} and SO_4^{2-}, were significantly lower than those at sites without CBCs ($p<0.1$ for K^+, Mg^{2+}, Na^+ and Cl^- and $p=0.000$ for NO_3^-) (Figures 5.5 and 5.6). This suggests that the distribution of soil ions except Ca^{2+} and SO_4^{2-} appears to be related to the CBC coverage. The similar soil K^+, Na^+, NO_3^- and Cl^- concentrations as a function of depth could be explained by three mechanisms related to the presence of CBCs: 1) biological consumption, 2) soil dilution, and 3) hydrological leaching, which are detailed as follows.

Firstly, CBCs may have consumed some ions accounting for the lower ion concentrations below CBCs compared to without CBC coverage. However, this is contrary to most previous studies that CBCs can export fixed carbon and nitrogen (such as nitrate as a by-product of the N cycle) to the soil below (*e.g.* Belnap, 2001; Austin et al., 2004; Johnson et al., 2007). In addition, Na^+ and Cl^- ions typically do not undergo biological consumptions or transformation (Biggar and Nielsen, 1962), but also have relatively lower concentrations in soils beneath CBCs, indicating that biological consumption cannot explain soil ion concentration differences associated with CBC coverage. Indeed, the inputs of biotic nitrate were also nominal in this, according to the nitrate oxygen isotope data that showed large $\Delta^{17}O$ values, an indicator of the importance of biotic nitrate relative to atmospheric nitrate (see discussion in Chapter 1 section 1.4),

but no significant differences between the sites with CBCs and without CBCs (Figure 5.6). This may have been because the particular CBC species did not nitrify given that NO_3^- was readily available from atmospheric deposition in the Atacama soil.

Secondly, the depths of loose soil beneath the CBCs were larger than those without CBC coverage, which may have induced a diluted ion concentration by the soil. In other words, the certain amounts of ion influx are associated with a larger soil mass, leading to smaller soil ion concentrations. However, when the salts masses are integrated over the entire sampling depth, the salt inventory of the soil profile with CBC coverage is generally higher than that without CBC coverage. This is consistent with the previous study that the enhanced dust trapping by CBCs could also increase the retention of atmospheric salts, and indeed result in the increased nitrogen, phosphorus and potassium concentrations in the soil by up to four fold (Reynolds et al., 2001). This suggests that soil dilution cannot be possible to account for the different soil ion depth distributions related to the CBC coverage.

Thirdly, if downward movement of water in the loose soil below CBCs is enhanced, it would have the tendency to leach more salts from the upper layers and transport them to the deeper sections. This would be in line with the observed salt depletion at sites with CBCs compared to sites without CBCs. However, the impact of the CBCs on the vadose zone hydrology and then soil ion distribution cannot be accurately constrained because of the debates on the roles of CBC crusts in affecting water filtration (Belnap, 2006). Or, the distribution of salts at deeper depths on the CBC patchy ground may instead be the reason for, rather than the result of, the CBC establishment (Amit et al., 2010).

To sum up, the profile beneath CBCs could be expected to have more ions considering the excretion of fixed nitrogen from CBCs that can be oxidized to nitrate and greater dust and salt trapping by CBCs, but actuallyhad less ions, compared to sites without CBCs. This could only be due to enhanced leaching at sites with CBCs. However, it is still unclear whether the enhanced leaching was induced by the presence of CBCs or indeed, accounted for the establishment of CBCs on the surface.

5.3.4 The $^{36}Cl/Cl$ Data

The $^{36}Cl/Cl$ ratio was analyzed in order to try and constrain the age of soils with and without CBCs. The largest $^{36}Cl/Cl$ ratio of 398×10^{-15} occurred in the surface crust at Site 1. This is significantly larger than the $^{36}Cl/Cl$ ratios of $31.5\text{-}233.6 \times 10^{-15}$ measured by dust traps installed within 60 km from the Pacific Ocean (Chapter 2). The higher value may be ascribed to the ^{36}Cl bomb spike (Phillips et al., 1988). If so, the detection of bomb-spike ^{36}Cl in the surface crust suggests that the downward movement of salts was nominal over the past 50 years. Frequent fog may induce salt deliquescence and downward leaching, but the $^{36}Cl/Cl$ data suggests the fog water was unable to move the salts into the lower depths of the soil profile, indicating evaporation is higher than the downward water flux. Another possible explanation for the high $^{36}Cl/Cl$ ratio in the surface crust would be that there is a mixing of meteoric ^{36}Cl and *in situ* ^{36}Cl produced via the spallation of calcium (Ca) and potassium (K) and thermal neutron absorption (Appendix A). However, the *in situ* ^{36}Cl production rate calculated based on Appendix A is not comparable to the meteoric ^{36}Cl fallout rate of $\sim 2.0 \times 10^{8}$ atoms m^{-2} yr^{-1} in the Atacama at a site with a similar latitude and distance from the ocean (T2 site) (dust trap preliminary data). Therefore, the *in situ* ^{36}Cl production cannot completely explain the

high surface $^{36}Cl/Cl$ ratios. Also, the high surface $^{36}Cl/Cl$ ratio cannot be attributed to a possible low Cl^- concentration in the surface crust. However, Site 1 is actually close to the Salar de Grande, a basin filled with massive halite minerals (Stoertz and Ericksen, 1974), and should be expected to have more Cl^- deposition compared to the T2 site with similar distance from the ocean along the transect of my dust trap measurements in Chapter 2. This is consistent with the observation of 14.3 μmol Cl^- (g soil)$^{-1}$ in the surface crust at Site 1 and 4.7 μmol Cl^- (g dust)$^{-1}$ at T2 site. The large $^{36}Cl/Cl$ ratio of 398×10^{-15} at Site 1, 1.7 times the $^{36}Cl/Cl$ ratio of 233.6×10^{-15} measured by the T2 trap (Chapter 2) can thus not be ascribed to lower Cl^- concentration. Therefore, it is plausible to attributehe $^{36}Cl/Cl$ ratio of 398×10^{-15} in the surface crust in Site 1 to the bomb spike.

The soil $^{36}Cl/Cl$ ratios vary greatly from $37\text{-}125\times10^{-15}$ in the subsurface of the two sites (Table 5.3). The $^{36}Cl/Cl$ ratios at Site 1 are larger than those at similar depths at Site 2, probably related to the extremely high concentrations of Cl^- (Figure 5.5) that likely initiate significant *in situ* ^{36}Cl production via thermal neutron absorption (Liu et al., 1994). The fluctuations of the $^{36}Cl/Cl$ ratios with depth, different from an exponential decline of the $^{36}Cl/Cl$ ratios with depth (a decay trend) observed for a 225 cm deep trench in the hyper-arid core of the Atacama in Chapter 3, suggests complicated mechanisms behind the $^{36}Cl/Cl$ depth profiles in the CBC region compared to the simplified soil system in the Atacama core zone. This is perhaps due to the presence of some significant water events or capillary migration of ground water in the past that have led to the free movement of Cl^- in the profile and thus relatively homogenized $^{36}Cl/Cl$ signatures. Therefore, it is unlikely to establish a ^{36}Cl age for the CBC sites hereby.

5.4 Conclusions

The thickened loose soil profile beneath CBCs compared to nearby areas without CBCs could be ascribed to the enhanced dust trapping and physical protection of the dust from wind erosion. Fine particle fractions in the soil under CBCs were higher beneath CBC than those in non-CBC sites, probably also related to the enhanced dust trapping, especially small dust particles, and/or the greater *in situ* weathering. The profile beneath CBCs had less soluble ions compared to sites without CBCs, which could only be explained by leaching that has depleted salts to a deeper depth at sites with CBCs. However, it is not clear whether the enhanced leaching was the result or the cause of the presence of CBCs. The bomb spike with the $^{36}Cl/Cl$ ratio of 398×10^{-15} was preserved on the surface at a CBC site over the past ~60 years, while the subsurface $^{36}Cl/Cl$ signals were likely homogenized due to the past wet events.

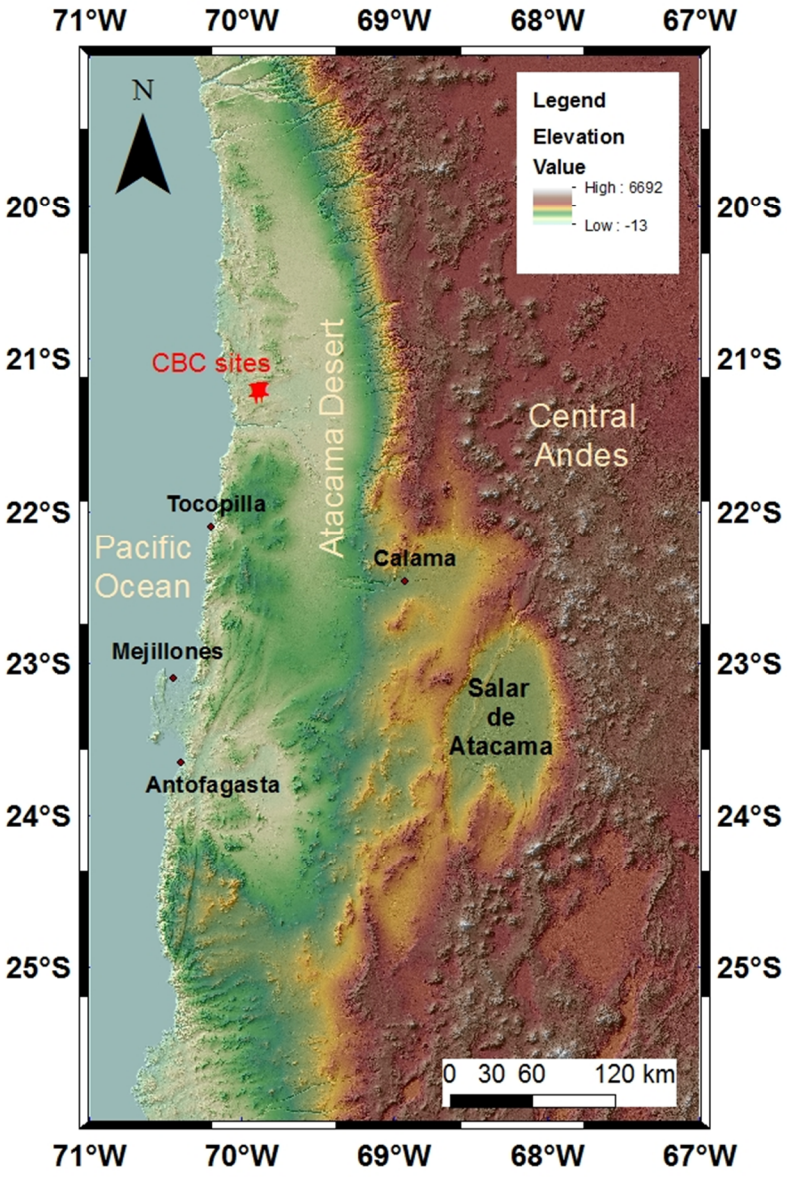

Figure 5.1 The location of the overlapping CBC sampling sites

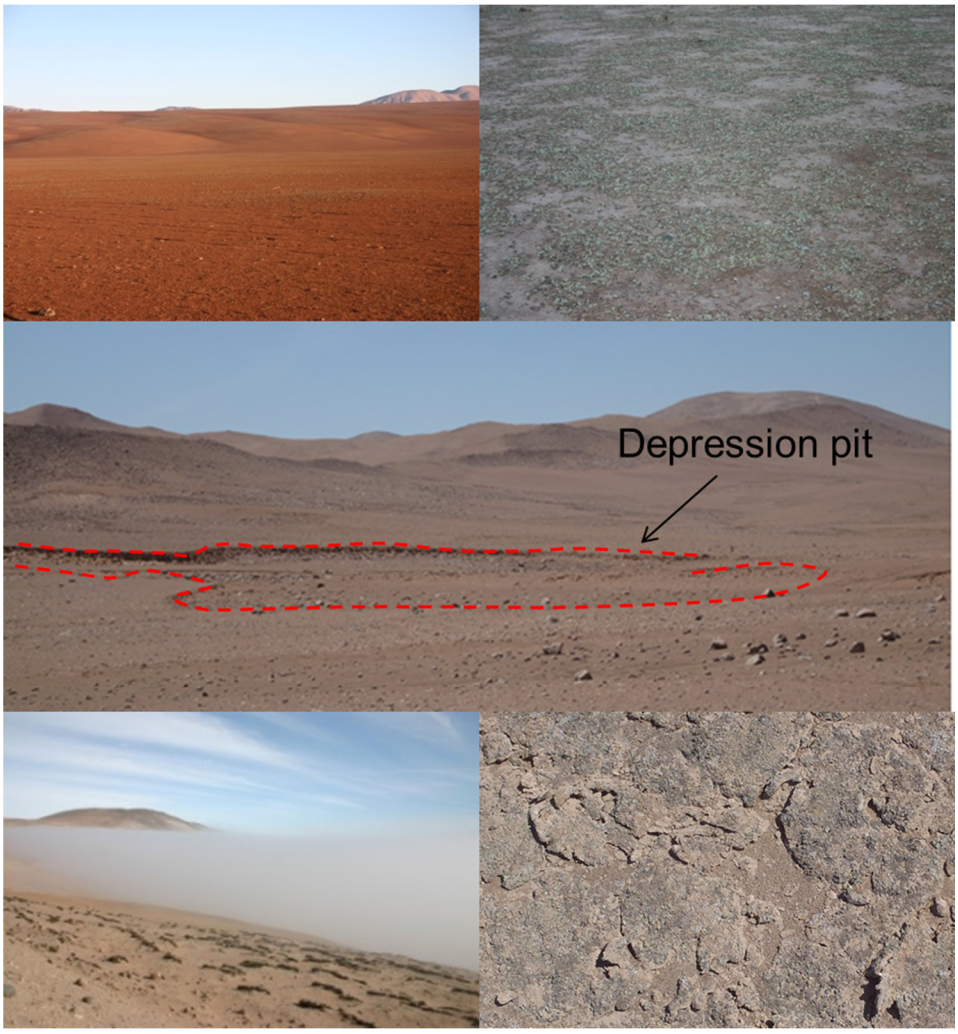

Figure 5.2 There is an abrupt transition from barren soils (left upper-barren ground) or depression pits (middle) to blankets of Crypto-Biotic Crust (right upper-CBC patchy ground). This transition occurs over a narrow distance (10-100s of meters). The bottom pictures are showing fog filling in the remote valley (left) and the close-up look of the fractured and upturned crust (right) in dry seasons.

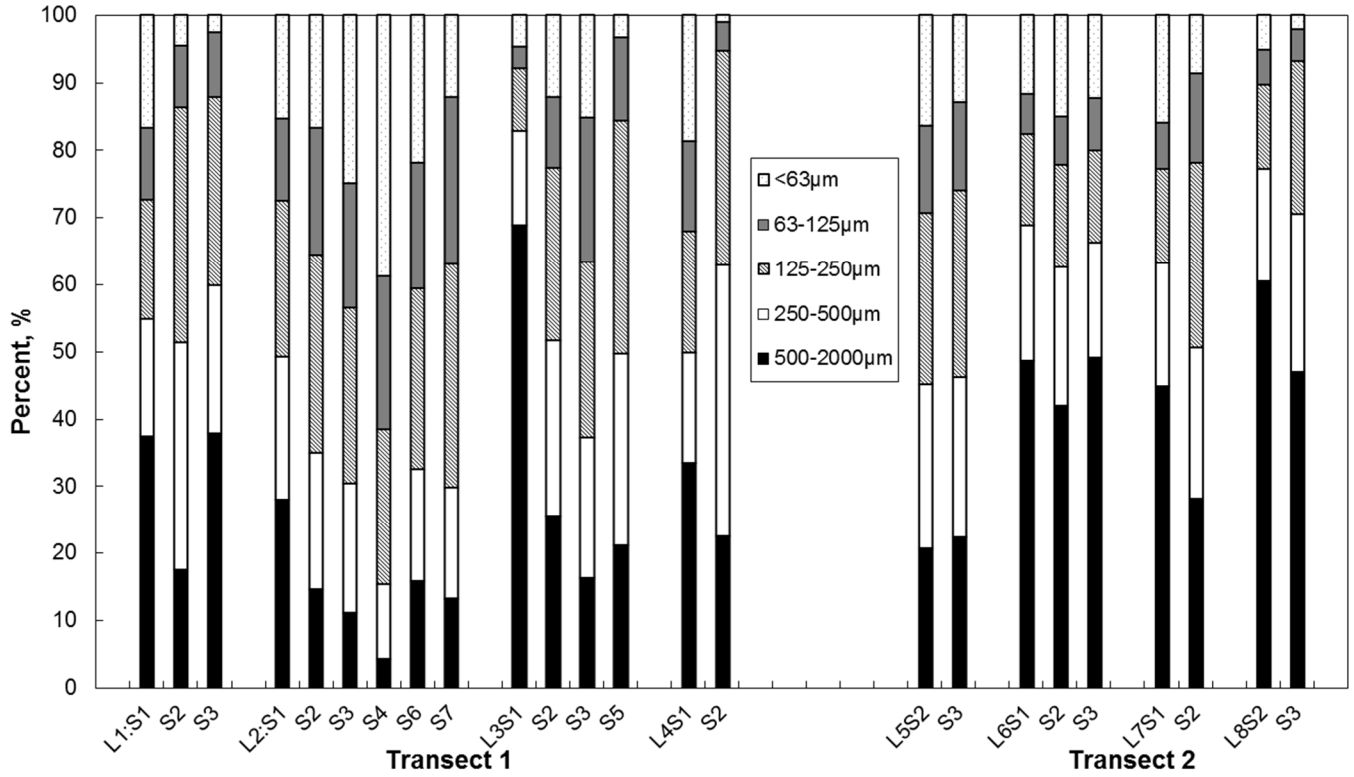

Figure 5.3 The grain size distribution of the soils of Transect 1 and Transect 2

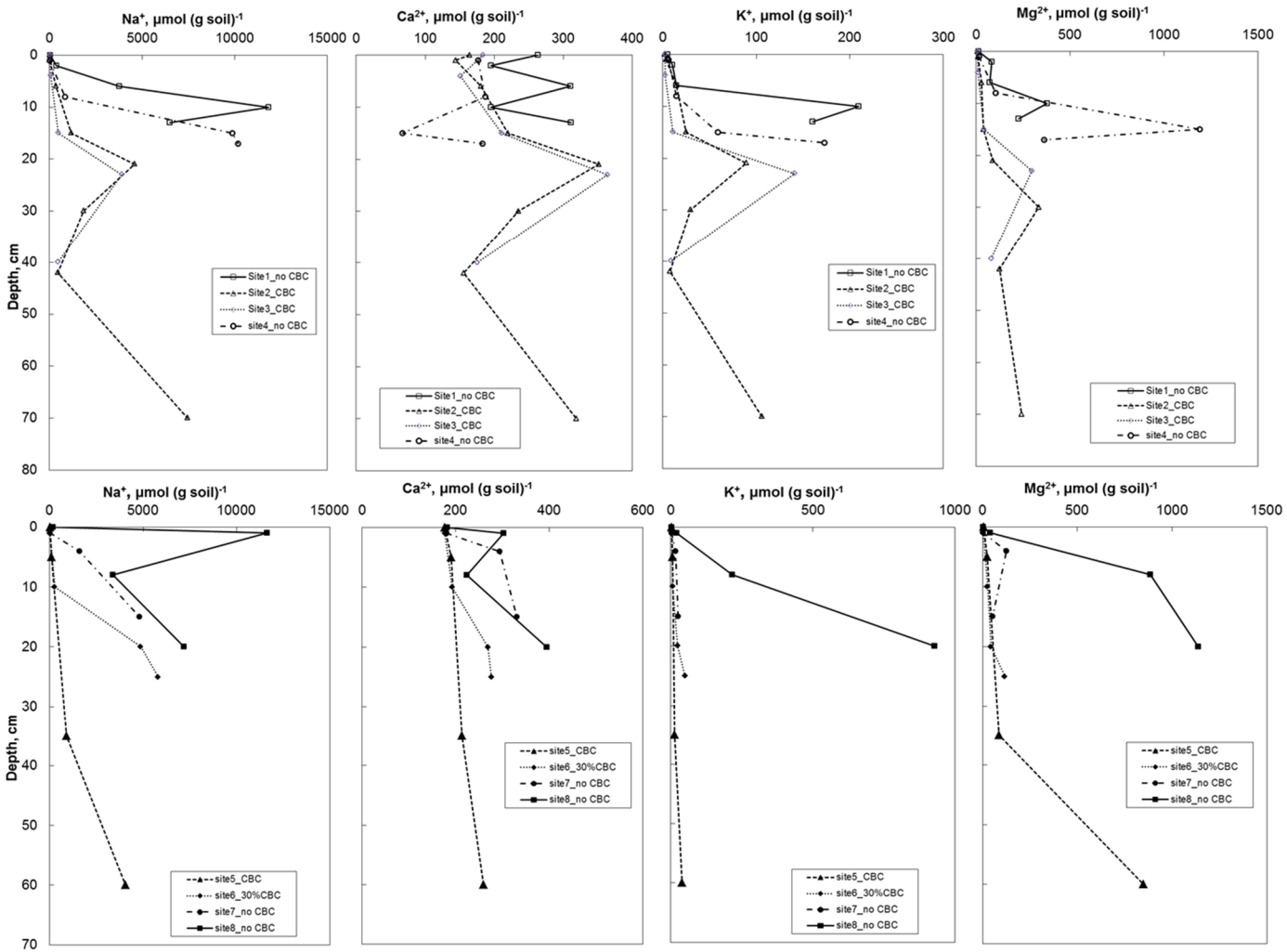

Figure 5.4 Cation distribution with depth for different sites along Transect 1 (upper panel) and Transect 2 (lower panel)

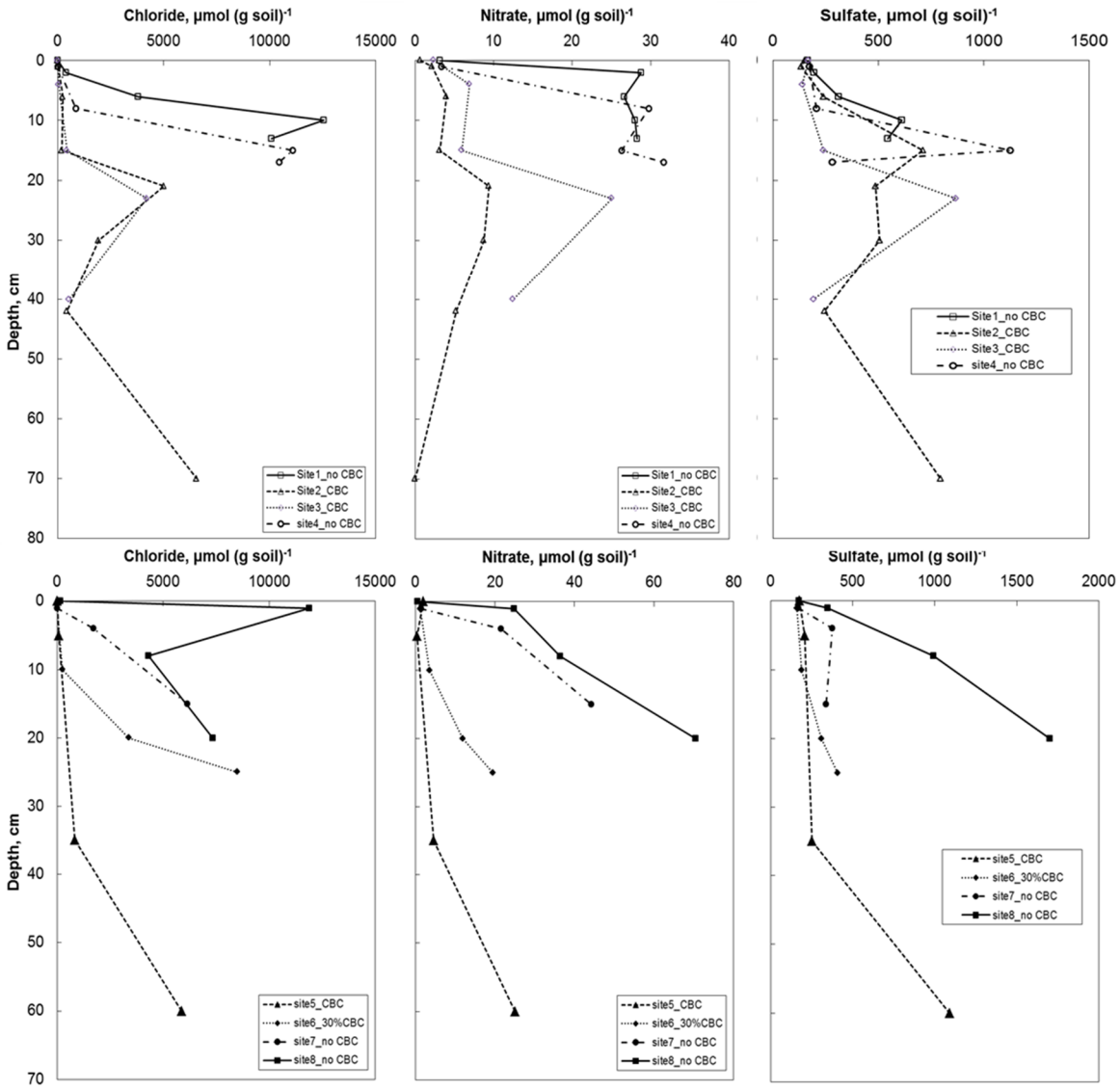

Figure 5.5 Anion distribution with depth for different sites along Transect 1 (upper panel) and Transect 2 (lower panel)

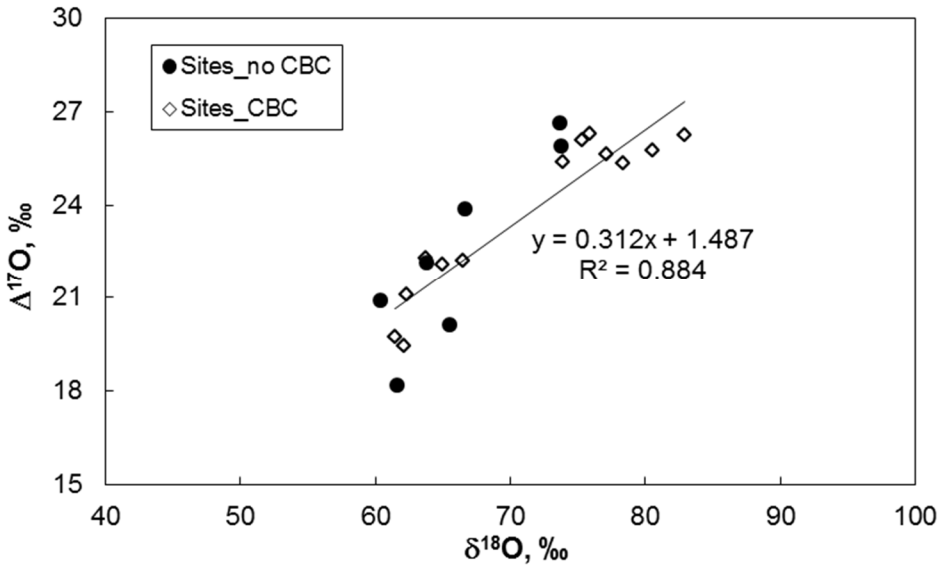

Figure 5.6 Nitrate oxygen isotopic variations ($\Delta^{17}O$ vs. $\delta^{18}O$)

Table 5.1 Detailed site descriptions

Sampling site	Geomophological unit	CBC coverage	Sampling depth
Transect 1			
Site 1	Barren ground	No	15 cm
Site 2	CBC patchy ground	Yes	70 cm
Site 3	On the edge of the depression pit	Yes	40 cm
Site 4	Barren ground	No	20 cm
Transect 2			
Site 5	On the edge of the CBC patchy ground	Yes	60 cm
Site 6	The foot of the CBC patchy ground	Yes (30%)	25 cm
Site 7	Barren ground	No	15 cm
Site 8	In the depression pit	No	20 cm

Table 5.2 The comparison in the average ion composition between in seawater and soil

Element	**Concentration in seawater[a], mmol L^{-1}**	**Soil, µmol (g soil)$^{-1}$**	**X/Na seawater**	**X/Na soil**
Ca^{2+}	10.3	223.1	0.022	0.070
K^{+}	10.2	63	0.022	0.020
Mg^{2+}	53.2	183.3	0.114	0.057
Na^{+}	468.3	3195.9	1.000	1.000
Cl^{-}	545.9	3474.6	1.166	1.087
SO_4^{2-}	28.2	401.7	0.060	0.126

[a]From Millero (1974)

Table 5.3 $^{36}Cl/Cl$ ratios between two sites with CBC and without CBCs

Sample ID	**Depth, cm**	**$^{36}Cl/Cl$, $\times 10^{-15}$**
Site 1_no CBC		
L1S1	surface	398±25
L1S2	0-4cm	78±5
L1S3	4-8cm	125±10
L1S4	8-12cm	81±5
L1S5	12-15cm	97±13
Site 2_CBC		
L2S3	2-10cm	45±3
L2S4	10-20cm	37.4±2
L2S5	20-22cm	55±6
L2S7	36-48cm	78±3
L2S8	70cm	67±3

REFERENCES

REFERENCES

Aber J. D., Melillo J. M., Nadelhoffer K. J., McClaugherty C. A. and Pastor J. (1985) Fine root turnover in forest ecosystems in relation to quantity and form of nitrogen availability: A comparison of two methods. *Oecologia* **66**, 317-321.

Alexander B., Hastings M., Allman D., Dachs J., Thornton J. and Kunasek S. (2009) Quantifying atmospheric nitrate formation pathways based on a global model of the oxygen isotopic composition ($\Delta^{17}O$) of atmospheric nitrate. *Atmos. Chem. Phys.* **9**, 5043-5056.

Alexander B., Savarino J., Kreutz K. J. and Thiemens M. (2004) Impact of preindustrial biomass-burning emissions on the oxidation pathways of tropospheric sulfur and nitrogen. *J. Geophys. Res.* **109**, D08303.

Alexander B., Thiemens M., Farquhar J., Kaufman A., Savarino J. and Delmas R. (2003) East Antarctic ice core sulfur isotope measurements over a complete glacial-interglacial cycle. *J. Geophys. Res.* **108**, 4786.

Alonso R., Jordan T., Tabbutt K. and Vandervoort D. (1991) Giant evaporite belts of the Neogene central Andes. *Geology* **19**, 401.

Alpers C. N. and Brimhall G. H. (1988) Middle Miocene climatic change in the Atacama Desert, northern Chile: Evidence from supergene mineralization at La Escondida. *Geol. Soc. Am. Bull.* **100**, 1640.

Amberger A. and Schmidt H. L. (1987) Natürliche isotopengehalte von Nitrat als Indikatoren für dessen Herkunft. *Geochim. Cosmochim. Acta* **51**, 2699-2705.

Amit R., Enzel Y., Grodek T., Crouvi O., Porat N. and Ayalon A. (2010) The role of rare rainstorms in the formation of calcic soil horizons on alluvial surfaces in extreme deserts. *Quatern. Res.* **74**, 177-187.

Amit R., Lekach, J., Ayalon A., Porat N. and Grodek T. (2007) New insight into pedogenic processes in extremely arid environments and their paleoclimatic implications—the Negev Desert, Israel. *Quatern. Int.* **162**, 61-75.

Ammann M., Siegwolf R., Pichlmayer F., Suter M., Saurer M. and Brunold C. (1999) Estimating the uptake of traffic-derived NO_2 from ^{15}N abundance in Norway spruce needles. *Oecologia* **118**, 124-131.

Anderson K., Wells S. and Graham R. (2002) Pedogenesis of vesicular horizons, Cima volcanic field, Mojave Desert, California. *Soil Sci. Soc. Am. J.* **66**, 878-887.

Andersson A. J., Mackenzie F. T. and Bates N.R. (2008) Life on the margin: Implications of ocean acidification on Mg-calcite, high latitude and cold-water marine calcifiers. *Mar. Ecol. Prog. Ser.* **373**, 265-273.

Andreae M. O. (1983) Soot carbon and excess fine potassium: Long-range transport of combustion-derived aerosols. *Science* **220**, 1148-1151.

Andreae M. O., Browell E. V., Garstang M., Gregory G., Harriss R., Hill G., Jacob D., Pereira M., Sachse G. and Setzer A. (1988) Biomass-burning emissions and associated haze layers over Amazonia. *J. Geophys. Res.* **93**, 1509-1527.

Andres R. J., Rose W. I., Kyle P. R., DeSilva S., Francis P., Gardeweg M. and Moreno-Roa H. (1991) Excessive sulfur dioxide emissions from Chilean volcanoes. *J. Volcanol. Geoth. Res.* **46**, 323-329.

Andrews J. E., Singhvi A. K., Kailath A. J., Kuhn R., Dennis P. F., Tandon S. K. and Dhir R. P. (1998) Do stable isotope data from calcrete record late Pleistocene monsoonal climate variation in the Thar Desert of India? *Quatern. Res.* **50**, 240-251.

ApSimon H., Kruse M. and Bell J. (1987) Ammonia emissions and their role in acid deposition. *Atmos. Environ.* **21**, 1939-1946.

Arthur M., Brysk H., Paveri-Fontana S. and Zweifel P. (1981) The law of radioactive decay. *II Nuovo Cimento B* **63**, 565-587.

Austin A. T., Yahdjian L., Stark J. M., Belnap J., Porporato A., Norton U., Ravetta D. A. and Schaeffer S. M. (2004) Water pulses and biogeochemical cycles in arid and semiarid ecosystems. *Oecologia* **141**, 221-235.

Ayers G., Gillett R., Cainey J. and Dick A. (1999) Chloride and bromide loss from sea-salt particles in Southern Ocean air. *J. Atmos. Chem.* **33**, 299-319.

Azua-Bustos A., Urrejola C. and Vicuña R. (2012) Life at the dry edge: Microorganisms of the Atacama Desert. *FEBS Lett.* **586**, 2939-2945.

Báez S., Fargione J., Moore D., Collins S. and Gosz J. (2007) Atmospheric nitrogen deposition in the northern Chihuahuan desert: Temporal trends and potential consequences. *J. Arid Environ.* **68**, 640-651.

Baker L. A., Hope D., Xu Y., Edmonds J. and Lauver L. (2001) Nitrogen balance for the Central Arizona–Phoenix (CAP) ecosystem. *Ecosystems* **4**, 582-602.

Balistrieri L. S. and Murray J. W. (1986) The surface chemistry of sediments from the Panama Basin: The influence of Mn oxides on metal adsorption. *Geochim. Cosmochim. Acta* **50**, 2235-2243.

Bao H. and Gu B. (2004) Natural perchlorate has a unique oxygen isotope signature: *Environ. Sci. Technol.* **38**, 5073-5077.

Bao H., Jenkins K. A., Khachaturyan M. and Dí az, G. C. (2004) Different sulfate sources and their post-depositional migration in Atacama soils. *Earth Planet. Sci. Lett.* **224**, 577-587.

Bao H., Michalski G. M. and Thiemens M. H. (2001) Sulfate oxygen-17 anomalies in desert varnishes. *Geochim. Cosmochim. Acta* 65, 2029-2036.

Bao H., Thiemens M. H., Farquhar J., Campbell D. A., Lee C. C. W., Heine K. and Loope D. B. (2000) Anomalous ^{17}O compositions in massive sulphate deposits on the Earth. *Nature* **406**, 176-178.

Barazangi M. and Isacks B. L. (1976) Spatial distribution of earthquakes and subduction of the Nazca plate beneath South America. *Geology* **4**, 686-692.

Battan L. J. and Reitan C. H. (1957) Droplet size measurements in convective clouds, Artificial stimulation of rain, Pergamon Press, New York, USA.

Beck M., Burmester R., Cembrano J., Drake R., García A., Hervé F. and Munizaga F. (2000) Paleomagnetism of the North Patagonian Batholith, southern Chile. An exercise in shape analysis. *Tectonophysics* **326**, 185-202.

Belnap J. (2003) The world at your feet: Desert biological soil crusts. *Front. Ecol. Environ.* **1**, 181-189.

Belnap J. (2006) The potential roles of biological soil crusts in dryland hydrologic cycles. *Hydrol. Process.* **20**, 3159-3178.

Belnap J. and Gardner J. S. (1993) Soil microstructure in soils of the Colorado Plateau: the role of the cyanobacterium Microcoleus vaginatus. *West. N. Am. Naturalist* **53**, 40-47.

Berger I. and Cooke R. (1997) The origin and distribution of salts on alluvial fans in the Atacama Desert, northern Chile. *Earth Surf. Proc. Land.* **22**, 581-600.

Bettoli M. G., Cantelli L., Tositti L., Tubertini O. and Valcher S. (1993) Activity of Be-7 and Pb-210 in snow samples at Terra Nova Bay--Antarctica: Preliminary results. In: *Environmental Radioactivity in the Arctic and Antarctic* (eds Strand P. and Holm E.). Scientific Committee of the Environmental Radioactivity in the Arctic and Antarctic, Osteras, Norway, pp. 229-232.

Bhattacharya A., Mudgal R. and Taneja A. (2004) Acid deposition and critical load analysis in Agra, India. *J. Hazard. Mater.* **106**, 157-160.

Biggar J. and Nielsen D. (1962) Miscible displacement: II. Behavior of tracers. *Soil Sci. Soc. Am. J.* **26**, 125-128.

Biggin A., McCormack, A. and Roberts A. (2010) Palaeointensity database updated and upgraded. *EOS Trans. Amer. Geophys. Union* **91**, 15.

Bissig T. and Riquelme R. (2010) Andean uplift and climate evolution in the southern Atacama Desert deduced from geomorphology and supergene alunite-group minerals: *Earth Planet. Sci. Lett.* **299**, 447-457.

Bobbink R., Hicks K., Galloway J., Spranger T., Alkemade R., Ashmore M., Bustamante M., Cinderby S., Davidson E. and Dentener F. (2010) Global assessment of nitrogen deposition effects on terrestrial plant diversity: A synthesis. *Ecol. Appl.* **20**, 30-59.

Böhlke J. K., Ericksen G. E. and Revesz K. (1997) Stable isotope evidence for an atmospheric origin of desert nitrate deposits in northern Chile and southern California, USA. *Chem. Geol.* **136**, 135-152.

Booth M. S., Stark J. M. and Caldwell M. M. (2003) Inorganic N turnover and availability in annual-and perennial-dominated soils in a northern Utah shrub-steppe ecosystem. *Biogeochemistry* **66**, 311-330.

Boring L. R., Swank W. T., Waide J. B. and Henderson G. S. (1988) Sources, fates, and impacts of nitrogen inputs to terrestrial ecosystems: Review and synthesis. *Biogeochemistry* **6**, 119-159.

Bouwman A., Lee D., Asman W., Dentener F., Van Der Hoek K. and Olivier J. (1997) A global high-resolution emission inventory for ammonia. *Global Biogeochem. Cy.* **11**, 561-587.

Bradley R. S. (1985) Quaternary paleoclimatology: Methods of paleoclimatic reconstruction. Allen & Unwin, Crows Nest, N.S.W., Austrialia.

Brimhall G. and Mote T. (1997) Optimal secondary mineralization in the Andes: Vadose response to global Cenozoic cooling events, glaciation, eustasy, and desiccation. *GSA Abstr. with Programs* **29**, 17.

Brimhall G. H., Chadwick O. A., Lewis C. J., Compston W., Williams I. S., Danti K. J., Dietrich W. E., Power M. E., Hendricks D. and Bratt J. (1992) Deformational mass transport and invasive processes in soil evolution. *Science* **255**, 695-702.

Buat-Ménard P. (1983) Particle geochemistry in the atmosphere and oceans. In: *Air-sea exchange of gases and particles* (eds Liss P. S. and Slinn W. G. N.). D. Reidel Publishing Company, Dordrecht. pp. 455-532.

Büdel B. (2001) Biological soil crusts of South America. In: *Biological soil crusts: Structure, function, and management* (eds. Belnap J. and Lange O. L.). Springer, Berlin, pp. 51-55.

Calhoun J. A., Bates T. S. and Charlson R. J. (1991) Sulfur isotope measurements of submicrometer sulfate aerosol particles over the Pacific Ocean. *Geophys. Res. Lett.* **18**, 1877-1880.

Capo R. C. and Chadwick O. A. (1999) Sources of strontium and calcium in desert soil and calcrete. *Earth Planet. Sci. Lett.* **170**, 61-72.

Castro M. S., Steudler P. A., Melillo J. M., Aber J. D. and Millham S. (1992) Exchange of N_2O and CH_4 between the atmosphere and soils in spruce-fir forests in the northeastern United States. *Biogeochemistry* **18**, 119-135.

Cereceda P. and Schemenauer R. S. (1991) The occurrence of fog in Chile. *J. Appl. Meteorol.* **30**, 1097-1105.

Cereceda P., Larrain H., Osses P., Farías M. and Egaña I. (2008) The spatial and temporal variability of fog and its relation to fog oases in the Atacama Desert, Chile. *Atmos. Res.* **87**, 312-323.

Cereceda P., Osses P., Larrain H., Farıas M., Lagos M., Pinto R. and Schemenauer R. (2002) Advective, orographic and radiation fog in the Tarapacá region, Chile. *Atmos. Res.* **64**, 261-271.

Chadwick O. A., Brimhall G. H. and Hendricks D. M. (1990) From a black to a gray box—A mass balance interpretation of pedogenesis. *Geomorphology* **3**, 369-390.

Chameides W. and Stelson A. (1992) Aqueous-phase chemical processes in deliquescent sea-salt aerosols: A mechanism that couples the atmospheric cycles of S and sea salt. *J. Geophys. Res.* **97**, 20565-20580.

Chand D., Hegg D., Wood R., Shaw G., Wallace D. and Covert D. (2010) Source attribution of climatically important aerosol properties measured at Paposo (Chile) during VOCALS. *Atmos. Chem. Phys.* **10**, 10789-10801.

Chang T. (1984) Rain and snow scavenging of HNO_3 vapor in the atmosphere. *Atmos. Environ.* 18, 191-197.

Charlson R. J., Lovelock J. E., Andreae M. O. and Warren S. G. (1987) Oceanic phytoplankton, atmospheric sulphur, cloud albedo and climate. *Nature* **326**, 655-661.

Chavez F. P. and Barber R. T. (1987) An estimate of new production in the equatorial Pacific. *Deep Sea Res. Pt. I* **34**, 1229-1243.

Chmeleff J., von Blanckenburg F., Kossert K. and Jakob D. (2010) Determination of the ^{10}Be half-life by multicollector ICP-MS and liquid scintillation counting. *Nucl. Instrum. Methods Phys. Res. B* **268**, 192-199.

Chong G. (1988) The Cenozoic saline deposits of the Chilean Andes between 18° and 27° South. In: *The Southern Central Andes* (eds. Bahlburg H., Breitkreuz C. and Giese P.), Springer-Verlag, Berlin. pp. 135-151.

Chong G. (1994) The Nitrate Deposits of Chile. In *Tectonics of the Southern Central Andes: Structure and Evolution of an Active Continental Margin* (eds. Reutter K. J., Scheuber E. and Wigger P. J.). Springer-Verlag, Berlin. pp. 303-316.

Christl M., Mangini A. and Kubik P. (2007) Highly resolved Beryllium-10 record from ODP Site 1089—A global signal? *Earth Planet. Sci. Lett.* **257**, 245-258.

Claridge G. G. C. and Campbell I. B. (1968) Origin of nitrate deposits. *Nature* **217,** 428–430.

Clarke A. D. and Porter J. N. (1993) Pacific marine aerosol: 2. Equatorial gradients in chlorophyll, ammonium, and excess sulfate during SAGA 3. *J. Geophys. Res.* **98**, 16997-17010.

Clement, A. C., Cane M. A. and Seager R. (2001) An Orbitally Driven Tropical Source for Abrupt Climate Change, *J. Climate* **14**, 2369-2375.

Colman S. M. (1998) Water-level changes in Lake Baikal, Siberia: Tectonism versus climate. *Geology* **26**, 531-534.

Cooke R. U. (1970) Stone pavements in deserts. *Ann. Ass. Am. Geogr.* **60**, 560-577.

Cooke R. U. (1981) Salt weathering in deserts. *P.Geologist. Assoc.* **92**, 1-16.

Costa A., Michalski G., Schauer A., Alexander B., Steig E. and Shepson P. (2011) Analysis of atmospheric inputs of nitrate to a temperate forest ecosystem from $\Delta^{17}O$ isotope ratio measurements. *Geophys. Res. Lett.* **38**, L15805.

Covey C., AchutaRao K. M., Cubasch U., Jones P., Lambert S. J., Mann M. E., Phillips T. J. and Taylor K. E. (2003) An overview of results from the Coupled Model Intercomparison Project. *Global Planet. Change* **37**, 103-133.

Craig H. (1961) Standard for reporting concentrations of deuterium and oxygen-18 in natural waters. *Science* **133**, 1833-1834.

Cronin T. M. (2010) Paleoclimates: Understanding climate change past and present. Columbia University Press, New York, NY, USA.

Dan J. and Yaalon D. (1982) Automorphic saline soils in Israel. *Catena Suppl.* **1**, 103-115.

Darwin C. (1909) The Voyage of the Beagle. P. F. Collier & Son corp., New York. pp. 385.

Davidson E., Hart S., Shanks C. and Firestone M. (2006) Measuring gross nitrogen mineralization, and nitrification by ^{15}N isotopic pool dilution in intact soil cores. *J. Soil Sci.* **42**, 335-349.

Davis W. L., de Pater I. and McKay C. P. (2010) Rain infiltration and crust formation in the extreme arid zone of the Atacama Desert, Chile. *Planet. Space Sci.* **58**, 616-622.

DGA (the Dirección General de Aguas) (2011) Informe Hidrológico Proyecto Antakena: http://seia.sea.gob.cl/ (accessed June 2012).

Didyk B. M., Simoneit B. R., Alvaro Pezoa L., Luis Riveros M. and Anselmo Flores A. (2000) Urban aerosol particles of Santiago, Chile: Organic content and molecular characterization. *Atmos. Environ.* **34**, 1167-1179.

Dirección General de Aguas (DGA) (2010) Actualización de la Evaluación de la Disponibilidad de Recursos Hídricos para Constituir Derechos de Aprovechamiento en las Subcuencas Afluentes al Salar de Atacama. II region, Santiago, Chile (in Spanish).

Dong Z., Qu J., Wang X., Qian G., Luo W. and Wei Z. (2008) Pseudo-feathery dunes in the Kumtagh Desert. *Geomorphology* **100**, 328-334.

Duce R., Liss P., Merrill J., Atlas E., Buat-Menard P., Hicks B., Miller J., Prospero J., Arimoto R. and T. Church (1991) The atmospheric input of trace species to the world ocean. *Global Biogeochem. Cy.* **5**, 193-259.

Dunai T. J., Löpez G. A. G. and Juez-Larré J. (2005) Oligocene-Miocene age of aridity in the Atacama Desert revealed by exposure dating of erosion-sensitive landforms. *Geology* **33**, 321-324.

Elliott E., Kendall C., Wankel S., Burns D., Boyer E., Harlin K., Bain D. and Butler T. (2007) Nitrogen isotopes as indicators of NO_x source contributions to atmospheric nitrate deposition across the midwestern and northeastern United States. *Environ. Sci. Tech.* **41**, 7661-7667.

Ericksen G. (1961) Rhyolite tuff, a source of the salts of northern Chile. US Geol. Surv. Prof. Pap. **424**, 224-225.

Ericksen G. (1981) Geology and origin of the Chilean nitrate deposits. US Geol. Surv. Prof. Paper 1188.

Evans M. C., Campbell S. W., Bhethanabotla V. and Poor N. D. (2004) Effect of sea salt and calcium carbonate interactions with nitric acid on the direct dry deposition of nitrogen to Tampa Bay, Florida. *Atmos. Environ.* **38**, 4847-4858.

Ewing S., Michalski G., Thiemens M., Quinn R., Macalady J., Kohl S., Wankel S., Kendall C., McKay C. and Amundson R. (2007) Rainfall limit of the N cycle on Earth. *Global Biogeochem. Cy.* **21**, GB3009.

Ewing S., Sutter B., Owen J., Nishiizumi K., Sharp W., Cliff S., Perry K., Dietrich W., McKay C. and Amundson R. (2006) A threshold in soil formation at Earth's arid-hyperarid transition. *Geochim. Cosmochim. Acta* **70**, 5293-5322.

Ewing S., Yang W., DePaolo D.J., Michalski G., Kendall C., Stewart B.W., Thiemens M. and Amundson R. (2008) Non-biological fractionation of stable Ca isotopes in soils of the Atacama Desert, Chile. *Geochim. Cosmochim. Acta* **72**, 1096-1110.

Farías L., Chuecas L. A. and Salamanca M. A. (1996) Effect of coastal upwelling on nitrogen regeneration from sediments and ammonium supply to the water column in Concepcion Bay, Chile. *Est. Coast. Shelf Sci.* **43**, 137-155.

Farquhar J., Bao H. and Thiemens M. (2000) Atmospheric influence of Earth's earliest sulfur cycle. *Science* **289**, 756-758.

Felix J. D., Elliott E. M. and Shaw S. L. (2012) Nitrogen isotopic composition of coal-fired power plant NO_x: Influence of emission controls and implications for global emission inventories. *Environ. Sci. Tech.* **46**, 3528-3535.

Fenn M. E., Haeuber R., Tonnesen G. S., Baron J. S., Grossman-Clarke S., Hope D., Jaffe D. A., Copeland S., Geiser L. and Rueth H. M. (2003) Nitrogen emissions, deposition, and monitoring in the western United States. *BioScience* **53**, 391-403.

Ferek R., Chatfield R. and Andreae M. (1986) Vertical distribution of dimethylsulphide in the marine atmosphere. Nature **320**, 514-516.

Ferm M. (1998) Atmospheric ammonia and ammonium transport in Europe and critical loads: a review. *Nutr. Cycl. Agroecosys.* **51**, 5-17.

Feth J. H., Rogers S. M. and Roberson C. E. (1964) Chemical composition of snows in the northern Sierra Nevada and other areas. US Geol. Surv. Water Supply Pap. 1535.

Field C. V., Schmidt G. A., Koch D. and Salyk C. (2006) Modeling production and climate-related impacts on ^{10}Be concentration in ice cores. *J. Geophys. Res.* **111**, D15107.

Fisher R. L. and Raitt R. W. (1962) Topography and structure of the Peru-Chile trench. *Deep-Sea Res. Pt. 1* **9**, 423-443.

Fitzgerald J. W. (1991) Marine aerosols: A review. *Atmos. Environ.* **25**, 533-545.

Francis J. E. and Hill R. S. (1996) Fossil plants from the Pliocene Sirius Group, Transantarctic Mountains: Evidence for climate from growth rings and fossil leaves. *Palaios* **11**, 389-396.

Freyer H. (1991) Seasonal variation of $^{15}N/^{14}N$ ratios in atmospheric nitrate species. *Tellus B* **43**, 30-44.

Fuzzi S., Orsi G., and Mariotti M. (1985) Wet deposition due to fog in the Po Valley, Italy. *J. Atmos. Chem.*, **3**, 289-296.

Gaffney J. S., Marley N. A. and Cunningham M. M. (2004) Natural radionuclides in fine aerosols in the Pittsburgh area. *Atmos. Environ.* **38**, 3191-3200.

Galli-Olivier C. (1967) Pediplain in northern Chile and the Andean uplift. *Science* **158**, 653-655.

Galloway J. N. (1998) The global nitrogen cycle: changes and consequences. *Environ. Pollut.* **102**, 15-24.

Galloway J. N., Dentener F. J., Capone D. G., Boyer E. W., Howarth R. W., Seitzinger S. P., Asner G. P., Cleveland C., Green P. and Holland E. (2004) Nitrogen cycles: Past, present, and future. *Biogeochemistry* **70**, 153-226.

Galloway J. N., Keene W. C. and Likens G.E. (1996) Processes controlling the composition of precipitation at a remote southern hemispheric location: Torres del Paine National Park, Chile. *J. Geophys. Res.* **101**, 6883-6897.

Gao Y. Q. and Marcus R. (2001) Strange and unconventional isotope effects in ozone formation. *Science* **293**, 259-263.

Garreaud R. and Muñoz R. C. (2005) The low-level jet off the west coast of subtropical South America: Structure and variability. *Mon. Wea. Rev.* **133**, 2246-2261.

Garreaud R., Vuille M. and Clement A. C. (2003) The climate of the Altiplano: observed current conditions and mechanisms of past changes. *Palaeogeogr. Palaeoclimatol. Palaeoecol.* **194**, 5-22.

Gattuso J. P. and Buddemeier R.W. (2000) Ocean biogeochemistry: Calcification and CO_2. *Nature* **407**, 311-313.

Gerson R. and Amit R. (1987) Rates and modes of dust accretion and deposition in an arid region-the Negev, Israel. *Geol. Soc. London Spec. Publ.* **35**, 157-169.

Ginot P., Kull C., Schwikowski M., Schotterer U. and Gäggeler H. W. (2001) Effects of postdepositional processes on snow composition of a subtropical glacier (Cerro Tapado, Chilean Andes). *J. Geophys. Res.* **106**, 32375-32386.

Gleeson D. B., Herrmann A. M., Liuesley S. J. and Murphy D. V. (2008) Influence of water potential on nitrification and structure of nitrifying bacterial communities in semiarid soils. *Appl. Soil Ecol.* **40**, 189-194.

Goldewijk K. K. and van Drecht G. (2006) HYDE 3: Current and historical population and land cover. In: *Integrated Modelling of Global Environmental Change. An Overview of IMAGE 2.4* (eds. Bouwman A. F., Kram T. and Goldewijk K. K.). The Netherlands Environmental Assessment Agency (MNP), Bilthoven, pp 93-112.

Gosse J. C. and Phillips F. M. (2001) Terrestrial in situ cosmogenic nuclides: Theory and application. *Quatern. Sci. Rev.* **20**, 1475-1560.

Goudie A. S. and Middleton N. (2006) Desert Dust in the Global System. Springer, Heidelberg.

Goudie A. S., Wright E. and Viles H. A. (2002) The roles of salt (sodium nitrate) and fog in weathering: A laboratory simulation of conditions in the northern Atacama Desert, Chile. *Catena* **48**, 255-266.

Graham I., Ditchburn R. and Whitehead N. (2001) Be isotope analysis of a 0–500ka loess–paleosol sequence from Rangitatau East, New Zealand. *Quatern. Int.* **76**, 29-42.

Graham R. C., Hirmas D. R., Wood Y. A. and Amrhein C. (2008) Large near-surface nitrate pools in soils capped by desert pavement in the Mojave Desert, California. *Geology* **36**, 259-262.

Gregory-Wodzicki K. M. (2000) Uplift history of the Central and Northern Andes: A review. *Geol. Soc. Am. Bull.* **112**, 1091-1105.

Grimm N. B. and Fisher S. G. (1986) Nitrogen limitation in a Sonoran Desert stream. *J. N. Am. Benthol. Soc.* **5**, 1-15.

Grosjean M., Geyh M. A., Messerli B. and Schotterer U. (1995) Late-glacial and early Holocene lake sediments, ground-water formation and climate in the Atacama Altiplano 22-24 S. *J. Paleolimnol.* **14**, 241-252.

Gu Z. Y., Lal D., Liu T. S., Southon J., Caffee M. W., Guo Z. T. and Chen M. Y. (1996) Five million year ^{10}Be record in Chinese loess and red-clay: Climate and weathering relationships. *Earth Planet. Sci. Lett.* **144**, 273-287.

Hardy J. T. (1982) The sea surface microlayer: Biology, chemistry and anthropogenic enrichment. *Prog. Oceanogr.* **11**, 307-328.

Harkel M. T. (1997) The effects of particle-size distribution and chloride depletion of sea-salt aerosols on estimating atmospheric deposition at a coastal site. *Atmos. Environ.* **31**, 417-427.

Hart S. and Gunther A. (1989) In situ estimates of annual net nitrogen mineralization and nitrification in a subarctic watershed. *Oecologia* **80**, 284-288.

Hartley A. (2003) Andean uplift and climate change. *J. Geol. Soc. London* **160**, 7-10.

Hartley A. and Chong G. (2002) Late Pliocene age for the Atacama Desert: Implications for the desertification of western South America. *Geology* **30**, 43-46.

Hartley A. J. and May G. (1998). Miocene gypcretes from the Calama Basin, northern Chile. *Sedimentology* **45**, 351-364.

Hartley A. J., Chong G., Houston J. and Mather A. E. (2005) 150 million years of climatic stability: Evidence from the Atacama Desert, northern Chile. *J. Geol. Soc. London* **162**, 421-424.

Hastings M., Jarvis J. and Steig E. (2009) Anthropogenic impacts on nitrogen isotopes of ice-core nitrate. *Science* **324**, 1288-1288.

Haug E. W., Kraal E. R., Sewall J. O., Van Dijk M. and Diaz G. C. (2010) Climatic and geomorphic interactions on alluvial fans in the Atacama Desert, Chile. *Geomorphology* **121**, 184-196.

Hayes D. E. (1966) A geophysical investigation of the Peru-Chile trench. *Mar. Geol.* **4**, 309-351.

Heaton T. (1986) Isotopic studies of nitrogen pollution in the hydrosphere and atmosphere: A review. *Chem. Geol.* **59**, 87-102.

Heaton T. (1990) $^{15}N/^{14}N$ ratios of NO_x from vehicle engines and coal-fired power stations. *Tellus B* **42**, 304-307.

Heikkilä U., Beer J., Feichter J., Alfimov V., Synal H., Schotterer U., Eichler A., Schwikowski M. and Thompson L. (2009) ^{36}Cl bomb peak: comparison of modeled and measured data. *Atmos. Chem. Phys.* **9**, 4145-4156.

Hereford R., Webb R. and Longpré C. (2006) Precipitation history and ecosystem response to multidecadal precipitation variability in the Mojave Desert region, 1893–2001. *J. Arid Environ.* **67**, 13-34.

Herreros J., Moreno I. Taupin J. D., Ginot P., Patris N., Angelis M. D., Ledru M. P., Delachaux F. and Schotterer U. (2009) Environmental records from temperate glacier ice on Nevado Coropuna saddle, southern Peru. *Adv. Geosci.* **22**, 27-34.

Herzschuh U., Tarasov P., Wünnemann B. and Hartmann K. (2004) Holocene vegetation and climate of the Alashan Plateau, NW China, reconstructed from pollen data. *Palaeogeogr. Palaeoclimatol. Palaeoecol.* **211**, 1-17.

Hesse P. P. and McTainsh G. H. (1999) Last glacial maximum to early Holocene wind strength in the mid-latitudes of the Southern Hemisphere from aeolian dust in the Tasman Sea. *Quatern. Res.* **52**, 343-349.

Hewitson B. and Crane R. (2006) Consensus between GCM climate change projections with empirical downscaling: precipitation downscaling over South Africa. *Int. J. Climatol.* **26**, 1315-1337.

Hicks B., Meyers T. and Baldocchi D. (1988) Aerometric measurement requirements for quantifying dry deposition. In: *Principles of environmental sampling* (ed. Keith L. H.). American Chemical Society Professional Reference Book Washington, DC, USA, pp. 297-315.

Hillel D. and Rosenzweig C. (2002) Desertification in relation to climate variability and change. *Adv. Agron.* **77**, 1-38.

Hoering T. (1957) The isotopic composition of the ammonia and the nitrate ion in rain. *Geochim. Cosmochim. Acta* 12, 97-102.

Hoffman E., Hoffman G. and Duce R. (1974) Chemical fractionation of alkali and alkaline earth metals in atmospheric particulate matter over the North Atlantic. *J. Rech. Atmos.* **8**, 675-688.

Holland E. A., Dentener F. J., Braswell B. H. and Sulzman J. M. (1999) Contemporary and pre-industrial global reactive nitrogen budgets. *Biogeochemistry* **46**, 7-43.

Houston J. (2006) Variability of precipitation in the Atacama Desert: Its causes and hydrological impact. *Int. J. Climatol.* **26**, 2181-2198.

Houston J. (2007) Recharge to groundwater in the Turi Basin, northern Chile: An evaluation based on tritium and chloride mass balance techniques. *J. Hydrol.* **334**, 534-544.

Houston J. and Hartley A. J. (2003) The central Andean west-slope rainshadow and its potential contribution to the origin of hyper-aridity in the Atacama Desert, *Int. J. Climatol.* **23**, 1453-1464.

Hoyle F. C., Murphy D. V. and Fillery I. R. P. (2006) Temperature and stubble management influence microbial CO_2-C evolution and gross N transformation rates. *Soil Biol. Biochem.* **38**, 71-80.

Hulme M., Doherty R., Ngara T., New M. and Lister D. (2001) African climate change: 1900-2100. *Climate Res.* **17**, 145-168.

Huneeus N., Gallardo L. and Rutllant J. (2006) Offshore transport episodes of anthropogenic sulfur in northern Chile: Potential impact on the stratocumulus cloud deck. *Geophys. Res. Lett.* **33**, L19819.

Hwang H. and Ro C. U. (2006) Direct observation of nitrate and sulfate formations from mineral dust and sea-salts using low-Z particle electron probe X-ray microanalysis. *Atmos. Environ.* **40**, 3869-3880.

Isbell R. (2002) The Australian soil classification. CSIRO publishing, Collingwood, Australia.

Jaenicke R. (1993) Tropospheric aerosols. In: *Aerosol-cloud-climate interactions* (ed. Hobbs P. V.). Academic Press, San Diego, USA, pp. 1-31.

Jannik N., Phillips F., Smith G. and Elmore D. (1991) A ^{36}Cl chronology of lacustrine sedimentation in the Pleistocene Owens River system. *Geol. Soc. Am. Bull.* **103**, 1146-1159.

Jenny H. (1941) Factors of soil formation: A system of quantitative pedology. McGraw-Hill Book Company, New York.

Jesinkey C., Forsythe R. D., Mpodozis C. and Davidson J. (1987) Concordant late Paleozoic paleomagnetizations from the Atacama Desert: Implications for tectonic models of the Chilean Andes. *Earth Planet. Sci. Lett.* **85**, 461-472.

Johnson S. L., Neuer S. and Garcia-Pichel F. (2007) Export of nitrogenous compounds due to incomplete cycling within biological soil crusts of arid lands. *Environ. Microbiol.* **9**, 680-689.

Johnston J. C. and Thiemens M. H. (1997) The isotopic composition of tropospheric ozone in three environments, *J. Geophys. Res.* **102**, 25395-25404.

Jordan T. E., Isacks B. L., Allmendinger R. W., Brewer J. A., Ramos V. A. and Ando C. J. (1983) Andean tectonics related to geometry of subducted Nazca plate. *Geol. Soc. Am. Bull.* **94**, 341-361.

Jordan T. E., Kirk-Lawlor N. E. and Rech J. (2011) Rates of landscape modification in response to paleoclimate variability since ~12 Ma, Atacama Desert, Pampa del Tamarugal, Chile. *GSA Abstr. with Programs* **43**, 274.

Jorquera H. (2009) Source apportionment of PM10 and PM2.5 at Tocopilla, Chile (22°05'S, 70°12'W). *Environ. Monitor Assess.* **153**, 235-251.

Joubert A. and Hewitson B. (1997) Simulating present and future climates of southern Africa using general circulation models. *Prog. in Phys. Geogr.* **21**, 51-78.

Junge C. E. and Gustafson P. (1957) On the distribution of sea salt over the United States and its removal by precipitation. *Tellus* **9**, 164-173.

Kaiser J., Hastings M. G., Houlton B. Z., Röckmann T. and Sigman D. M. (2007) Triple oxygen isotope analysis of nitrate using the denitrifier method and thermal decomposition of N_2O. *Anal. Chem.* **79**, 599-607.

Keene W. C., Pszenny A. A., Galloway J. N. and Hawley M.E. (1986) Sea-salt corrections and interpretation of constituent ratios in marine precipitation. *J. Geophys. Res.* **91**, 6647-6658.

Keene W. C., Sander R., Pszenny A. A. P., Vogt R., Crutzen P. J. and Galloway J. N. (1998) Aerosol pH in the marine boundary layer: A review and model evaluation. *J. Aerosol Sci.* **29**, 339-356.

Keller G., Adatte T., Hollis C., Ordóñez M., Zambrano I., Jiménez N., Stinnesbeck W., Aleman A. and Hale-Erlich W. (1997) The Cretaceous/Tertiary boundary event in Ecuador: Reduced biotic effects due to eastern boundary current setting. *Mar. Micropaleontol.* **31**, 97-133.

Kendall C., Campbell D. H., Burns D. A., Shanley J. B., Silva S. R. and Chang C. C. Y. (1995) Tracing sources of nitrate in snowmelt runoff using the oxygen and nitrogen isotopic compositions of nitrate. *IAHS Publ. Ser. Proc. Rep. Int. Assoc. Hydrol. Sci.* **228**, 339-348.

Kessler E. (1969) On the distribution and continuity of water substance in atmospheric circulations. In: *Meteorological Monographs* **10**. American meteorological society, Boston, USA.

Khoder M. (2002) Atmospheric conversion of sulfur dioxide to particulate sulfate and nitrogen dioxide to particulate nitrate and gaseous nitric acid in an urban area. *Chemosphere* **49**, 675-684.

Kidron G. J. (1999) Altitude dependent dew and fog in the Negev Desert, Israel. *Agr. Forest Meteorol.* **96**, 1-8.

Kirchman D. L. (2000) Uptake and regeneration of organic nutrients by marine heterotrophic bacteria. In: *Microbial Ecology of the Oceans* (ed. Kirchman D. L.). John Wiley & Sons, New York. pp. 261-289.

Klaveness D. and Paasche E. (1979) Physiology of coccolithophorids. In: *Biochemistry and Physiology of Protozoa volume 1* (eds. Levandowsky M. and Hutner S. H.). Academic Press, New York. pp. 191-213.

Kovaltsov G. A. and Usoskin I. G. (2010) A new 3D numerical model of cosmogenic nuclide ^{10}Be production in the atmosphere. *Earth Planet. Sci. Lett.* **291**, 182-188.

Krankowsky D., Lammerzahl P. and Mauersberger K. (2000) Isotopic measurements of stratospheric ozone. *Geophys. Res. Lett.* **27**, 2593-2595.

Kunasek S., Alexander B., Steig E., Hastings M., Gleason D. and Jarvis J. (2008) Measurements and modeling of Δ^{17}O of nitrate in snowpits from Summit, Greenland. *J. Geophys. Res.* **113**, D24302.

Kuroiwa M., Koba K., Isobe K., Tateno R., Nakanishi A., Inagaki Y., Toda H., Otsuka S., Senoo K., Suwa Y., Yoh M., Urakawa R. and Shibata H. (2011) Gross nitrification rates in four Japanese forest soils: Heterotrophic versus autotrophic and the regulation factors for the nitrification. *J. For. Res.* **16**, 363-373.

Lagos G. and E. Blanco (2010) Mining and development in the region of Antofagasta. *Resour. Pol.* **35**, 265-275.

Lal D., Malhotra P., and Peters B. (1958) On the production of radioisotopes in the atmosphere by cosmic radiation and their application to meteorology. *J. Atmos. Terres. Phys.* **12**, 306-328.

Lal, D. (1987) ^{10}Be in polar ice: Data reflect changes in cosmic ray flux or polar meteorology. *Geophys. Res. Lett.* **14**, 785-788.

Lalley J., Viles H., Henschel J. and Lalley V. (2006) Lichen-dominated soil crusts as arthropod habitat in warm deserts. *J. Arid Environ.* **67**, 579-593.

Lamb S. and Davis P. (2003) Cenozoic climate change as a possible cause for the rise of the Andes. *Nature* **425**, 792-797.

Larrain H., Velasquez F., Cereceda P., Espejo R., Pinto R., Osses P. and Schemenauer R. (2002) Fog measurements at the site "Falda Verde" north of Chañaral compared with other fog stations of Chile. *Atmos. Res.* **64**, 273-284.

Lee Y. Y., Kao W. C. and Lee Y. P. (1990) Kinetics of the reaction hydroxyl + sulfur dioxide in helium, nitrogen, and oxygen at low pressure. *J. Phys. Chem.* **94**, 4535-4540.

Legrand M. and Kirchner S. (1990) Origins and variations of nitrate in South Polar precipitation. *J. Geophys. Res.* **95** (D4), 3493-3507, 1990.

Lester E. D., Satomi M., and Ponce A. (2007) Microflora of extreme arid Atacama Desert soils, *Soil Biol. Biochem.* **39**, 704-708.

Levine S. and Schwartz S. (1982) In-cloud and below-cloud scavenging of nitric acid vapor. *Atmos. Environ.* **16**, 1725-1734.

Lewis R. and Schwartz E. (2004) Sea salt aerosol production: mechanisms, methods, measurements and models—A critical review. American Geophysical Union, Washington DC.

Leys J. F., and Eldridge D. J. (1998) Influence of cryptogamic crust disturbance to wind erosion on sand and loam rangeland soils. *Earth Surf. Proc. Land.* **23**, 963-974.

Li D. and Wang X. (2008) Nitrogen isotopic signature of soil-released nitric oxide (NO) after fertilizer application. *Atmos. Environ.* **42**, 4747-4754.

Li W. H., Ren T. R. and Zhou Z. B. (2005) Study on the soil physicochemical characteristics of biological crust on sand dune surface in Gurbantünggtüt Desert, Xinjiang Region. *J. Glaciol. Geocryol.* **27**, 619-627.

Li X., Jiang F., Li L. and Wang G. (2011) Spatial and temporal variability of precipitation concentration index, concentration degree and concentration period in Xinjiang, China. *Int. J. Climatol.* **31**, 1679-1693.

Liao H. and Seinfeld J. H. (2005) Global impacts of gas-phase chemistry-aerosol interactions on direct radiative forcing by anthropogenic aerosols and ozone. *J. Geophys. Res.* **110**, D18208.

Lifton N., Smar D. and Shea M. (2008) Scaling time-integrated in situ cosmogenic nuclide production rates using a continuous geomagnetic model. *Earth Planet. Sci. Lett.* **268**, 190-201.

Liss P. S. and Galloway J. N. (1993) Air-sea exchange of sulphur and nitrogen and their interaction in the marine atmosphere. In: *Interations of C, N, P and S Biogeochemical Cycles and Global Change* (eds. Wollast R., Mackenzie F. T. and Chou L.). Springer, Berlin, pp. 259-281.

Liu B., Phillips F. M., Fabryka-Martin J. T., Fowler M. M. and Stone W.D. (1994) Cosmogenic ^{36}Cl accumulation in unstable landforms: 1. Effects of the thermal neutron distribution. *Water Resour. Res.* **30**, 3115-3125.

Liu B., Phillips F. M., Fabryka-Martin J. T., Fowler M. M. and Stone W. D. (1994) Cosmogenic ^{36}Cl accumulation in unstable landforms: 1. Effects of the thermal neutron distribution. *Water Resour. Res.* **30**, 3115-3125.

Lowenstein T. K. and Hardie L. A. (1985) Criteria for the recognition of salt-pan evaporites. *Sedimentology* **32**, 627-644.

Lowenstein T. K., Hein M. C., Bobst A. L., Jordan T. E., Ku T. L. and Luo S. (2003) An assessment of stratigraphic completeness in climate-sensitive closed-basin lake sediments: Salar de Atacama, Chile. J. Sediment. Res. **73**, 91-104.

Luz B. and Barkan E. (2005) The isotopic ratios $^{17}O/^{16}O$ and $^{18}O/^{16}O$ in molecular oxygen and their significance in biogeochemistry. *Geochim. Cosmochim. Acta* **69**, 1099-1110.

Lybrand R. A., Michalski G., Graham R. C. and Parker D. R. (2012) The geochemical associations of nitrate and naturally formed perchlorate in the Mojave Desert, California, USA. *Geochim. Cosmochim. Acta* **104**, 136.

Lyons J. R. (2001) Transfer of mass-independent fractionation in ozone to other oxygen-containing radicals in the atmosphere. *Geophys. Res. Lett.* **28**, 3231-3234.

MacIntyre F. (1974) Chemical fractionation and sea-surface microlayer processes. In: *The Sea* (ed. Goldberg E. D.). John Wiley & Sons, New York. pp. 245-299.

Magaritz M., Aravena R., Pena H., Suzuki O. and Grilli A. (1990) Source of ground water in the deserts of northern Chile: Evidence of deep circulation of ground water from the Andes. *Ground Water* **28**, 513-517.

Mahowald N. M., Lamarque J. F., Tie X.X. and Wolff E. (2006) Sea-salt aerosol response to climate change: Last Glacial Maximum, preindustrial, and doubled carbon dioxide climates. *J. Geophys. Res.* **111**, D0530.

Maier R., Drees K., Neilson J., Henderson D., Quade J. and Betancourt J. (2004) Microbial life in the Atacama Desert. *Science* **306**, 1289.

Mamane Y. and Gottlieb J. (1992) Nitrate formation on sea-salt and mineral particles—A single particle approach. *Atmos. Environ.* **26**, 1763-1769.

Marandino C., De Bruyn W., Miller S. and Saltzman E. (2009) Open ocean DMS air/sea fluxes over the eastern South Pacific Ocean. *Atmos. Chem. Phys.* **9**, 345-356.

Marlon J., Bartlein P., Carcaillet C., Gavin D., Harrison S., Higuera P., Joos F., Power M. and Prentice I. (2008) Climate and human influences on global biomass burning over the past two millennia. *Nat. Geosci.* **1**, 697-702.

Masarik J. and Beer J. (2009) An updated simulation of particle fluxes and cosmogenic nuclide production in the Earth's atmosphere. *J. Geophys. Res.* **114**, D11103.

Mather T., Tsanev V., Pyle D., McGonigle A., Oppenheimer C. and Allen A. (2004) Characterization and evolution of tropospheric plumes from Lascar and Villarrica volcanoes, Chile. *J. Geophys. Res.* **109**, D21303.

Matson P., Lohse K. A. and Hall S. J. (2002) The globalization of nitrogen deposition: consequences for terrestrial ecosystems. *AMBIO* **31**, 113-119.

Mauersberger K. (1981) Measurement of heavy ozone in the stratosphere. *Geophys. Res. Lett.* **8**, 935-937.

Mayer B., Bollwerk S. M., Mansfeldt T., Hütter B. and Veizer J. (2001) The oxygen isotope composition of nitrate generated by nitrification in acid forest floors. *Geochim. Cosmochim. Acta* **65**, 2743-2756.

McCabe J. R., Thiemens M. H. and Savarino J. (2007) A record of ozone variability in South Pole Antarctic snow: Role of nitrate oxygen isotopes. *J. Geophys. Res.* **112**, D12303.

McClaugherty C. A., Pastor J., Aber J. D. and Melillo J. M. (1985) Forest litter decomposition in relation to soil nitrogen dynamics and litter quality. *Ecology* **66**, 266-275.

McCracken K., Dreschhoff G., Zeller E., Smart D. and Shea M. (2001) Solar cosmic ray events for the period 1561–1994: 1. Identification in polar ice, 1561–1950. *J. Geophys. Res.* **106**, 21585-21598.

McDonald R., Unni C. and Duce R. (1982) Estimation of atmospheric sea salt dry deposition: Wind speed and particle size dependence. *J. Geophys. Res.* **87**, 1246-1250.

McFadden L. D., Wells S. G. and Jercinovich M. J. (1987) Influences of eolian and pedogenic processes on the origin and evolution of desert pavements. *Geology* **15**, 504-508.

McKay C. P., Friedmann E. I., Gómez-Silva B., Cáceres-Villanueva L., Andersen D. T. and Landheim R. (2003) Temperature and moisture conditions for life in the extreme arid region of the Atacama Desert: Four years of observations including the El Niño of 1997-1998. *Astrobiology* **3**, 393-406.

Meijer H. and Li W. (1998) The use of electrolysis for accurate $\delta^{17}O$ and $\delta^{18}O$ isotope measurements in water. *Isot. Environ. Health Stud.* **34**, 349-369.

Michalski G. and Bhattacharya S. (2009) The role of symmetry in the mass independent isotope effect in ozone. *PNAS* **106**, 5493-5496.

Michalski G., Bhattacharya S. K., and Mase D. F. (2011) Oxygen isotope dynamics of atmospheric nitrate and its precursor molecules. In: *Handbook of Environmental Isotope Geochemistry: Advances in Isotope Geochemistry* (ed. Baskaran M.). Springer-Verlag, Berlin Heidelberg. pp. 613-635.

Michalski G., Böhlke J. and Thiemens M. (2004) Long term atmospheric deposition as the source of nitrate and other salts in the Atacama Desert, Chile: New evidence from mass-independent oxygen isotopic compositions. *Geochim. Cosmochim. Acta* **68**, 4023-4038.

Michalski G., Scott Z., Kabiling M. and Thiemens M. (2003) First measurements and modeling of ^{17}O in atmospheric nitrate. *Geophys. Res. Lett.* **30**, 1870.

Middleton N. and Thomas D. (1997) World atlas of desertification (2nd edition). Oxford University Press for the United Nations Environmental Program, Oxford, UK, pp. 82.

Miller M. (2002) Isotopic fractionation and the quantification of ^{17}O anomalies in the oxygen three-isotope system: An appraisal and geochemical significance. *Geochim. Cosmochim. Acta* **66**, 1881-1889.

Millero F. J. (1974) Seawater as a multicomponent electrolyte solution. In: *The Sea* (ed. by Goldberg E. D.). John Wiley & Sons, New York. pp. 3-80.

Ministerio del Medio Ambiente (MMA) (2011) Reporte 2005-2009 del Registro de Emissions y Transferencias de Contaminantes, Gabierno de Chile, Chile (in Spanish).

Moore H. (1977) The isotopic composition of ammonia, nitrogen dioxide and nitrate in the atmosphere. *Atmos. Environ.* **11**, 1239-1243.

Moreno T. and Gibbons W. (2007) The geology of Chile. The Geological Society Publishing House, London, UK.

Morin S., Savarino J., Frey M. M., Yan N., Bekki S., Bottenheim J. W. and Martins J. M. (2008) Tracing the origin and fate of NO_x in the Arctic atmosphere using stable isotopes in nitrate. *Science* **322**, 730-732.

Morin S., Savarino J., Frey M.M., Domine F., Jacobi H.W., Kaleschke L. and Martins J.M. (2009) Comprehensive isotopic composition of atmospheric nitrate in the Atlantic Ocean boundary layer from 65°S to 79°N. *J. Geophys. Res.* **114**, D05303.

Mortimer C., Farrar E. and Saric N. (1974) K-Ar ages from Tertiary lavas of the northernmost Chilean Andes. *Geol. Rundsch.* **63**, 484-490.

Moysey S., Davis S. N., Zreda M. and Cecil L. D. W. (2003) The distribution of meteoric $^{36}Cl/Cl$ in the United States: A comparison of models. *Hydrogeol. J.* **11**, 615-627.

Muñoz R. (2008) Diurnal cycle of surface winds over the subtropical southeast Pacific. *J. Geophys. Res.* **113**, D13107.

Murphy D., Recous S., Stockdale E., Fillery I., Jensen L., Hatch D. and Goulding K. (2003) Gross nitrogen fluxes in soil: theory, measurement and application of ^{15}N pool dilution techniques. *Adv. Agron.* **79**, 69-118.

Nalpas T., Dabard M., Ruffet G., Vernon A., Mpodozis C., Loi A. and Hérail G. (2008) Sedimentation and preservation of the Miocene Atacama Gravels in the Pedernales-Chañaral Area, Northern Chile: Climatic or Tectonic Control? *Tectonophysics* **459**, 161-173.

Navarro-Gonzalez R., Rainey F., Molina P., Bagaley D., Hollen B., de la Rosa J., Small A., Quinn R., Grunthaner F. and Caceres L. (2003) Mars-like soils in the Atacama Desert, Chile, and the dry limit of microbial life. *Science* **302**, 1018.

Nejidat A. (2005) Nitrification and occurrence of salt-tolerant nitrifying bacteria in the Negev desert soils. FEMS Microbiol. Ecol. **52**, 21-29.

Newberg J. T., Matthew B.M. and Anastasio C. (2005) Chloride and bromide depletions in sea-salt particles over the northeastern Pacific Ocean. *J. Geophys. Res.* **110**, D06209.

Nickovic S., Kallos G., Papadopoulos A. and Kakaliagou O. (2001) A model for prediction of desert dust cycle in the atmosphere. *J. Geophys. Res.* **106**, 18113-18118,18129.

Nishiizumi K., Caffee M., Finkel R., Brimhall G. and Mote T. (2005) Remnants of a fossil alluvial fan landscape of Miocene age in the Atacama Desert of northern Chile using cosmogenic nuclide exposure age dating. *Earth Planet. Sci. Lett.* **237**, 499-507.

Noone K. J., Ogren J. A., Hallberg A., Heintzenberg J., Ström J., Hansson H. C., Svenningsson B., Wiedensohler A., Fuzzi S. and Facchini M. C. (1992) Changes in aerosol size-and phase distributions due to physical and chemical processes in fog. *Tellus B* **44**, 489-504.

O'Dowd C. D. and de Leeuw G. (2007) Marine aerosol production: A review of the current knowledge. *Philos. T. Roy. Soc. A* **365**, 1753-1774.

O'Dowd C. D., Geever M., Hill M. K., Smith M. H. and Jennings S. G. (1998) New particle formation: Nucleation rates and spatial scales in the clean marine coastal environment. *Geophys. Res. Lett.* **25**, 1661-1664.

Oyarzun J. and Oyarzun R. (2007) Massive volcanism in the Altiplano-Puna Volcanic Plateau and formation of the huge Atacama Desert nitrate deposits: A case for thermal and electric fixation of atmospheric nitrogen. *Int. Geol. Rev.* **49**, 962-968.

Pachur H. J., Wünnemann B. and Zhang H. (1995) Lake evolution in the Tengger Desert, Northwestern China, during the last 40,000 years. *Quatern. Res.* **44**, 171-180.

Papastefanou C. (2010) Paths of air pollutants containing radioactive nuclides in the suburban area of Thessaloniki, Northern Greece. *Aerosol Air Qual. Res.* **10**, 354-359.

Parmanik S. K. (1952) Hydrology of Rajasthan desert --Rainfall, humidity and evaporation. *Bullet. Nat. Inst. Sci. India* **1**, 193–197.

Parungo F. P., Nagamoto C. T., Madel R., Rosinski J. and Haagenson P. L. (1987) Marine aerosols in pacific upwelling regions, *J. Aerosol Sci.* **18**, 277-290.

Pearson J., Wells D., Seller K., Bennett A., Soares A., Woodall J. and Ingrouille M. (2000) Traffic exposure increases natural ^{15}N and heavy metal concentrations in mosses. *New Phytolog.* **147**, 317-326.

Pechony O. and Shindell D. (2010) Driving forces of global wildfires over the past millennium and the forthcoming century. *PNAS* **107**, 19167-19170.

Phillips F. M., Bentley H. W., Davis S. N., Elmore D. and Swanick G. B. (1986) Chlorine 36 dating of very old groundwater: 2. Milk River aquifer, Alberta, Canada. *Water Resour. Res.* **22**, 2003-2016.

Pike W., Staufer U., Hecht M., Goetz W., Parrat D., Sykulska-Lawrence H., Vijendran S., and Madsen M. B. (2011) Quantification of the dry history of the Martian soil inferred from in situ microscopy, *Geophys. Res. Lett.* **38**, L24201.

Pilger R. H. (1984) Cenozoic plate kinematics, subduction and magmatism: South American Andes. *J. Geol. Soc. London* **141**, 793-802.

Placzek C., Matmon A., Granger D., Quade J. and Niedermann S. (2010) Evidence for active landscape evolution in the hyperarid Atacama from multiple terrestrial cosmogenic nuclides. *Earth Planet. Sci. Lett.* **295**, 12-20.

Placzek C., Quade J., Rech J. A., Patchett P. and Pérez de Arce C. (2009) Geochemistry, chronology and stratigraphy of Neogene tuffs of the Central Andean region. *Quatern. Geochron.* **4**, p. 22-36.

Potter C. S., Matson P. A., Vitousek P. M., Davidson E. A. (1996) Process modeling of controls on nitrogen trace gas emissions from soils worldwide. *J. Geophys. Res.* **101**, 1361-1377.

Probyn T. A. (1987) Ammonium regeneration by microplankton in an upwelling environment. *Mar. Ecol. Prog. Ser* **37**, 64.

Prochnow S. J., Nordt L. C., Atchley S. C. and Hudec M. R. (2006) Multi-proxy paleosol evidence for middle and late Triassic climate trends in eastern Utah. *Palaeogeogr. Palaeoclimatol. Palaeoecol.* **232**, 53-72.

Qin Y., Li Y., Bao H., Liu F., Hou K., Wan D. and Zhang C. (2012) Massive atmospheric nitrate accumulation in a continental interior desert, northwestern China. *Geology* **40**, 623-626.

Qu J., Huang N., Dong G. and Zhang W. (2001) The role and significance of the Gobi Desert pavement in controlling sand movement on the cliff top near the Dunhuang Magao Grottoes. *J. Arid Environ.* **48**, 357-371.

Quade J., Chivas A. and McCulloch M. (1995) Strontium and carbon isotope tracers and the origins of soil carbonate in South Australia and Victoria. *Palaeogeogr. Palaeoclimatol., Palaeoecol.* **113**, 103-117.

Quinn P. K., Bates T. S., Johnson J. E., Covert D. S., Charlson R. J. (1990) Interactions between the sulfur and reduced nitrogen cycles over the central Pacific Ocean. *J. Geophys. Res.* **95**, 16405-16416.

Quinn P. K., Charlson R. J. and Bates T. S. (1988) Simultaneous observations of ammonia in the atmosphere and ocean. *Nature* **335**, 336-338.

Quinn P., Barrett K., Dentener F., Lipschultz F. and Six K. (1996) Estimation of the air/sea exchange of ammonia for the North Atlantic Basin. *Biogeochemistry* **35**: 275-304.

Quinn R., Zent A., Grunthaner F., Ehrenfreund P., Taylor C. and Garry J. (2005) Detection and characterization of oxidizing acids in the Atacama Desert using the Mars Oxidation Instrument. *Planet. Space Sci.* **53**, 1376-1388.

Radke L. F., Hobbs P. V., Eltgroth M. W. (1980) Scavenging of aerosol particles by precipitation. *J. Appl. Meteorol.* **19**, 715-722.

Rech J. A., Currie B. S., Michalski G. and Cowan A. M. (2006) Neogene climate change and uplift in the Atacama Desert, Chile. *Geology* **34**, 761-764.

Rech J. A., Currie B. S., Shullenberger E. D., Dunagan S. P., Jordan T. E., Blanco N., Tomlinson A. J., Rowe H. D. and Houston J. (2010) Evidence for the development of the Andean rain shadow from a Neogene isotopic record in the Atacama Desert, Chile. *Earth Planet. Sci. Lett.* **292**, 371-382.

Rech J. A., Quade J. and Hart W. S. (2003) Isotopic evidence for the source of Ca and S in soil gypsum, anhydrite and calcite in the Atacama Desert, Chile. *Geochim. Cosmochim. Acta* **67**, 575-586.

Reheis M. C. and Kihl R. (1995) Dust deposition in southern Nevada and California, 1984–1989: Relations to climate, source area, and source lithology. *J. Geophys. Res.* **100**, 8893-8918.

Reheis M. C., Goodmacher J. C., Harden J. W., McFadden L. D., Rockwell T. K., Shroba, R. R., Sowers J. M. and Taylor E. M. (1995) Quaternary soils and dust deposition in southern Nevada and California. *Geol. Soc. Am. Bull.* **107**, 1003.

Renard J. J., Calidonna S. E. and Henley M. V. (2004) Fate of ammonia in the atmosphere—a review for applicability to hazardous releases. *J. Hazard. Mater.* **108**, 29-60.

Retallack G. J. and Huang C. (2010) Depth to gypsic horizon as a proxy for paleoprecipitation in paleosols of sedimentary environments. *Geology* **38**, 403-406.

Reynolds J. F., Kemp P. R. and Tenhunen J. D. (2000) Effects of long-term rainfall variability on evapotranspiration and soil water distribution in the Chihuahuan Desert: A modeling analysis. *Plant Ecol.* **150**, 145-159.

Riha K., King M. Z. and Michalski G. (submitted) Standardization of $\Delta^{17}O$ and $\delta^{15}N$ using the denitrifier method and gold tube thermal decomposition: in review.

Royer D. L. (1999) Depth to pedogenic carbonate horizon as a paleoprecipitation indicator? *Geology* **27**, 1123-1126.

Rutllant J., Muñoz R. and Garreaud R. (2013) Meteorological observations on the northern Chilean coast during VOCALS-REx. *Atmos. Chem. Phys.* **13**, 3409-3422.

Ryerson T., Buhr M., Frost G., Goldan P., Holloway J., Hübler G., Jobson B., Kuster W., McKeen S. and Parrish D. (1998) Emissions lifetimes and ozone formation in power plant plumes. *J. Geophys. Res.* **103**, 22569-22583.

Saavedra-Pellitero M., Flores J. A., Baumann K. H. and Sierro F. J. (2010) Coccolith distribution patterns in surface sediments of Equatorial and Southeastern Pacific Ocean. *Geobios* **43**, 131-149.

Savarino J., Bhattacharya S., Morin S., Baroni M. and Doussin J. F. (2008) The NO+O reaction: A triple oxygen isotope perspective on the reaction dynamics and atmospheric implications for the transfer of the ozone isotope anomaly. *J. Chem. Phys.* **128**, 194303.

Savarino J., Kaiser J., Morin S., Sigman D. and Thiemens M. (2007) Nitrogen and oxygen isotopic constraints on the origin of atmospheric nitrate in coastal Antarctica. *Atmos. Chem. Phys.* **7**, 1925-1945.

Savarino J., Kaiser J., Morin S., Sigman D. and Thiemens M. (2007) Nitrogen and oxygen isotopic constraints on the origin of atmospheric nitrate in coastal Antarctica. *Atmos. Chem. Phys.* **7**, 1925-1945.

Schaeffer S., Billings S. and Evans R. (2003) Responses of soil nitrogen dynamics in a Mojave Desert ecosystem to manipulations in soil carbon and nitrogen availability: *Oecologia* **134**, 547-553.

Schemenauer R. S. and Cereceda P. (1994) A proposed standard fog collector for use in high-elevation regions. *J. Appl. Meteorol.* **33**, 1313-1322.

Schemenauer R. S. and Isaac G. (1984) The Importance of cloud top lifetime in the description of natural cloud characteristics. *J. Appl. Meteorol.* **23**, 267-279.

Schemenauer R. S. and Joe P. I. (1989) The collection efficiency of a massive fog collector. *Atmos. Res.* **24**, 53-69.

Schemenauer R. S., Fuenzalida H. and Cereceda P. (1988) A neglected water resource: The Camanchaca of South America. *Bull. Am. Meteorol. Soc.* **69**, 138-147.

Schemenauer, R. S. and Cereceda P. (1992) The quality of fog water collected for domestic and agricultural use in Chile. *J. Appl. Meteorol.* **31**, 275-290.

Schlesinger W. H. and Jones C. S. (1984) The comparative importance of overland runoff and mean annual rainfall to shrub communities of the Mojave Desert. *Bot. Gaz.* **145** 116-124.

Schlesinger W. H. and Pilmanis A. M. (1998) Plant-soil interactions in deserts. *Biogeochemistry* **42**, 169-187.

Schlunegger F., Kober F., Zeilinger G. and von Rotz R. (2010) Sedimentology-based reconstructions of paleoclimate changes in the Central Andes in response to the uplift of the Andes, Arica region between 19 and 21° S latitude, northern Chile. *Int. J. Earth Sci.* **99 (Suppl 1)**, S123-S137.

Schmidt E. L. (1982) Nitrification in soil. In: *Nitrogen in agricultural soils (Agron. Monograph 22)*, Am. Soc. Agron., Madison, USA, pp. 253-288.

Schumann T. (1991) Aerosol and hydrometeor concentrations and their chemical composition during winter precipitation along a mountain slope-III. Size-differentiated in-cloud scavenging efficiencies. *Atmos. Environ. A*. **25**, 809-824.

Schwartzman D. W. and Volk T. (1989) Biotic enhancement of weathering and the habitability of Earth. *Nature* **340**, 457-460.

Seinfeld J. H. and Pandis S. N. (2006) Atmospheric Chemistry and Physics: From air Pollution to Climate Change. John Wiley & Sons, New York.

Servicio Nacional de Geologíay Minería (SERNAGEOMIN) (2003) Mapa Geológico de Chile: versión digital. *Servicio Nacional de Geologíay Minería, Publicación Geológica Digital,* No. 4 (CD-ROM, versión1.0, 2003). Santiago.

Sharp Z. (2007) Principles of stable isotope geochemistry, Pearson Education Upper Saddle River, USA.

Shaw G. E. (1991) Aerosol chemical components in Alaska air masses: 2. Sea salt and marine product. *J. Geophy. Res.* **96**, 22369-22372.

Sievering H., Cainey J., Harvey M., McGregor J., Nichol S. and Quinn P. (2004) Aerosol non-sea-salt sulfate in the remote marine boundary layer under clear-sky and normal cloudiness conditions: Ocean-derived biogenic alkalinity enhances sea-salt sulfate production by ozone oxidation. *J. Geophys. Res.* **109**, D19317.

Sievering H., Ennis G., Gorman E. and Nagamoto C. (1990) Size distributions and statistical analysis of nitrate, excess sulfate, and chloride deficit in the marine boundary layer during GCE/CASE/WATOX. *Global Biogeochem. Cy.* **4**, 395-405.

Sillitoe R. and McKee E. (1996) Age of supergene oxidation and enrichment in the Chilean porphyry copper province. *Econ. Geol.* **91**, 164-179.

Sillitoe R., Mortimer C. and Clark A. (1968) A chronology of landform evolution and supergene mineral alteration, southern Atacama Desert, Chile. *Inst.. Min. Metall. Trans. Sect. B* **77**, B166-169.

Simonson R. W. (1959) Outline of a generalized theory of soil genesis. *Soil Sci. Soc. Am. J.* **23**, 152-156.

Simpson H. J. and Herczeg A. L. (1994) Delivery of marine chloride in precipitation and removal by rivers in the Murray-Darling Basin, Australia. *J. Hydrol.* **154**, 323-350.

Slinn W., Radke L. and Katen P. (1982) Inland transport, mixing and dry deposition of sea-salt particles. In: *Precipitation Scavenging, Dry Deposition and Resuspension, vol 1: Precipitation Scavenging* (eds. Pruppacher H. R., Semonin R. G. and Slinn W. G. N.). Elsevier, Santa Monica. pp. 1037-1046.

Soil Survey Staff (1975) Soil Taxonomy: A basic system of soil classification for making and interpreting soil surveys. Soil Conservation Service, US Department of Agriculture, Washington, DC.

Song C. H. and Carmichael G. R. (2001) A three-dimensional modeling investigation of the evolution processes of dust and sea-salt particles in east Asia. *J. Geophys. Res.* **106**, 18131-18154.

Stark J. M. and Firestone M. K. (1995) Mechanisms for soil moisture effects on activity of nitrifying bacteria. *Appl. Environ. Microbiol.* **61**, 218-221.

Stiles C. A., Mora C. I. and Driese S. G. (2001) Pedogenic iron-manganese nodules in Vertisols: A new proxy for paleoprecipitation? *Geology* **29**, 943-946.

Stoertz G. E. and Ericksen G. E. (1974) Geology of salars in northern Chile. US Geol. Surv. Prof. Pap. 811.

Stuut J. B. W., Kasten S., Lamy F. and Hebbeln D. (2007) Sources and modes of terrigenous sediment input to the Chilean continental slope. *Quatern. Intern.* **161**, 67-76.

Sumner M. E. (2000) Handbook of soil science. CRC Press, Loundon, UK, p. C-171.

Sutter B., Dalton J., Ewing S., Amundson R. and McKay C. (2007) Terrestrial analogs for interpretation of infrared spectra from the Martian surface and subsurface: Sulfate, nitrate, carbonate, and phyllosilicate-bearing Atacama Desert soils. *J. Geophys. Res.* **112**, G04S10.

Talbot M., Allen P. and Reading H. (1996) Sedimentary Environments: Processes, facies and stratigraphy. Blackwell Science, Oxford, UK.

Tamm C. O. (1991) Introduction: Geochemical Occurrence of Nitrogen. In: Natural Nitrogen Cycling and Anthropogenic Nitrogen Emissions. Springer, Berlin Heidelberg.

Tanaka T. Y. and Chiba M. (2006) A numerical study of the contributions of dust source regions to the global dust budget. *Global Planet. Change* **52**, 88-104.

Tang I. N. (1980) On the equilibrium partial pressures of nitric acid and ammonia in the atmosphere. *Atmos. Environ.* **14**, 819-828.

Thiemens M. and Heidenreich J. (1983) The mass-independent fractionation of oxygen: A novel isotope effect and its possible cosmochemical implications. *Science* **219**, 1073.

Thiemens M. H. (1999) Mass-independent isotope effects in planetary atmospheres and the early solar system. *Science* **283**, 341.

Thiemens M. H. (2006) History and applications of mass-independent isotope effects. *Annu. Rev. Earth Planet. Sci.* **34**, 217-262.

Thompson A. M. (1992) The oxidizing capacity of the Earth's atmosphere: Probable past and future changes. *Science* **256**, 1157-1165.

Thompson L. G., Mosley-Thompson E., Davis M. E., Lin P. N., Henderson K. and Mashiotta T. A. (2003) Tropical glacier and ice core evidence of climate change on annual to millennial time scales. *Clim. Chang.* **59**, 137-155.

Titley S. and Marozas D. (1995) Processes and products of supergene copper enrichment. Southwestern North America. In: *Porphyry Copper Deposits of the American Cordillera* (eds. Pierce F. W. and Bolm J. G.). Tucson, Arizona Geological Society Digest 20, 156-168.

Tosdal R., Clark A. and Farrar E. (1984) Cenozoic polyphase landscape and tectonic evolution of the Cordillera Occidental, southernmost Peru. *Geol. Soc. Am. Bull.* **95**, 1318.

Tsunogai S. (1971) Ammonia in the oceanic atmosphere and the cycle of nitrogen compounds through the atmosphere and the hydrosphere. *Geochem. J.* **5**, 57-67.

Tyler S., Chapman J., Conrad S., Hammermeister D., Blout D., Miller J., Sully M. and Ginanni J. (1996) Soil-water flux in the Southern Great Basin, United States: Temporal and spatial variations over the last 120,000 years. *Water Resour. Res.* **32**, 1481-1499.

Tyler S., Chapman J., Conrad S., Hammermeister D., Blout D., Miller J., Sully M. and Ginanni J. (1996) Soil-water flux in the southern Great Basin, United States: Temporal and spatial variations over the last 120,000 years. *Water Resour. Res.* **32**, 1481-1499.

Tzedakis P. (1994) Vegetation change through glacial-interglacial cycles: A long pollen sequence perspective. *Philos. Trans. R. Soc. Lond., B* **345**, 403-432.

Usoskin I. G., Solanki S. K. and Kovaltsov G. A. (2007) Grand minima and maxima of solar activity: New observational constraints. *Astron. Astrophys.* **471**, 301-309.

Van Moort J. C. (1985) Natural enrichment processes of nitrate, sulphate, chloride, iodate, borate, perchlorate, and chromate in the caliches of northern Chile. *Congreso Chileno.* **4**, 674-702.

Vargas G, Ortlieb L and Rutllant J. (2000) Aluviones históricos en Antofagasta y su relación con eventos El Niño/Oscilación del Sur. Revista Geológica de Chile **27**: 157-176.

Verchot L. V., Groffman P. M. and Frank D. A. (2002) Landscape versus ungulate control of gross mineralization and gross nitrification in semi-arid grasslands of Yellowstone National Park. *Soil Biol. Biochem.* **34**, 1691-1699.

Veron S., Paruelo J. and Oesterheld M. (2006) Assessing desertification. *J. Arid Environ.* **66**, 751-763.

Vogt R. (1996) A mechanism for halogen release from sea-salt. *Nature* **383**, 26.

Wagner G., Masarik J., Beer J., Baumgartner S., Imboden D., Kubik P. and Synal H. A. (2000) Reconstruction of the geomagnetic field between 20 and 60 kyr BP from cosmogenic radionuclides in the GRIP ice core. *Nucl. Instrum. Methods Phys. Res.* B **172**, 597-604.

Wall S. M., John W. and Ondo J. L. (1988) Measurement of aerosol size distributions for nitrate and major ionic species. *Atmos. Environ.* **22**, 1649-1656.

Walvoord M. A., Phillips F. M., Stonestrom D. A., Evans R. D., Hartsough P. C., Newman B. D. and Striegl R. G. (2003) A reservoir of nitrate beneath desert soils. *Science* **302**, 1021-1024.

Wang Y., Zhang X., Arimoto R., Cao J. and Shen Z. (2005) Characteristics of carbonate content and carbon and oxygen isotopic composition of northern China soil and dust aerosol and its application to tracing dust sources. *Atmos. Environ.* **39**, 2631-2642.

Warneck P. (1988) Chemistry of the natural atmosphere. Academic Press, London.

Warneck P. (2000) Chemistry of the natural atmosphere. Academic Press, San Diego, pp. 927.

Watson A. (1985) Structure, chemistry and origins of gypsum crusts in southern Tunisia and the central Namib Desert. *Sedimentology* **32**, 855-875.

Wells P. V. and Jorgensen C. D. (1964) Pleistocene Wood Rat Middens and Climatic Change in Mohave Desert: A Record of Juniper Woodlands. *Science* **143**, 1171.

West N. E. and Skujins J. J. (1978) Nitrogen in desert ecosystems, Dowden, Hutchinson and Ross, Stroudsberg, PA, USA.

Westbeld A., Klemm O., Grießbaum F., Sträter E., Larrain H., Osses P. and Cereceda P. (2009) Fog deposition to a Tillandsia carpet in the Atacama Desert. *Ann. Geophys.* **27**, 3571-3576.

Whitney F. and Freeland H. (1999) Variability in upper-ocean water properties in the NE Pacific Ocean. *Deep Sea Res. II* **46**, 2351-2370.

Wieler R., Beer J. and Leya I. (2011) The galactic cosmic ray intensity over the past 10^6-10^9 Years as recorded by cosmogenic nuclides in meteorites and terrestrial samples. *Space Sci. Rev.* doi: 10.1007/s11214-011-9769-9.

Willenbring J. K. and von Blanckenburg F. (2010) Meteoric cosmogenic Beryllium-10 adsorbed to river sediment and soil: Applications for Earth-surface dynamics. *Earth Sci. Rev.* **98**, 105-122.

Williams E. R. (2005) Lightning and climate: A review. *Atmos. Res.* **76**, 272-287.

Williams J., Dobrowolski J., West N. and Gillette D. (1995) Microphytic crust influence on wind erosion. *Trans. ASAE* **38**, 131-137.

Wolfe S. A. and Nickling W. G. (1993) The protective role of sparse vegetation in wind erosion. *Prog. Phys. Geogr.* **17**, 50-68.

Wolff E. W. (1995) Nitrate in polar ice. In: Ice core studies of global biogeochemical cycles NATO ASI Set. I 30 (ed. Delmas R.), Springer-Verlag, New York, pp. 195-224.

Wolff G. T. (1984) On the nature of nitrate in coarse continental aerosols. *Atmos. Environ.* **18**, 977-981.

Wood J. R. (1975) Thermodynamics of brine-salt equilibria—I. The systems NaCl-KCl-$MgCl_2$-$CaCl_2$-H_2O and NaCl-$MgSO_4$-H_2O at 25° C. *Geochim. Cosmochim. Acta* **39**, 1147-1163.

Yamamoto N., Nishiura H., Honjo T., Ishikawa Y. and Suzuki K. (1995) A long-term study of atmospheric ammonia and particulate ammonium concentrations in Yokohama, Japan. *Atmos. Environ.* **29**, 97-103.

Yang M., Huebert B., Blomquist B., Howell S., Shank L., McNaughton C., Clarke A., Hawkins L., Russell L., and Covert D. (2011) Atmospheric sulfur cycling in the southeastern Pacific–longitudinal distribution, vertical profile, and diel variability observed during VOCALS-REx, *Atmos. Chem. Phys.* **11**, 5079-5097.

You C. F., Lee T. and Li Y. H. (1989) The partition of Be between soil and water. *Chem. Geol.* **77**, 105-118.

Young J., Ellis E. and Hidy G. (1988) Deposition of air-borne acidifiers in the western environment. *J. Environ. Qual.* **17**, 1-26.

Zeller E. J. and Dreschhoff G. A. (1995) Anomalous nitrate concentrations in polar ice cores—Do they result from solar particle injections into the polar atmosphere? *Geophys. Res. Lett.* **22**, 2521-2524.

Zeller E. J., Dreschhoff G.A. and Laird C. M. (1986) Nitrate flux on the Ross Ice Shelf, Antarctica and its relation to solar cosmic rays. *Geophys. Res. Lett.* **13**, 1264-1267.

Zhang X. Y., Arimoto R. and An Z. S. (1997) Dust emission from Chinese desert sources linked to variations in atmospheric circulation. *J. Geophys. Res.* **102**, 28028-28047.

Zhang X. Y., Arimoto R., Zhu G., Chen T. and Zhang G. (1998) Concentration, size-distribution and deposition of mineral aerosol over Chinese desert regions. Tellus B 50, 317-330.

Zhang Y., Zheng L., Liu X., Jickells T., Neil Cape J., Goulding K., Fangmeier A. and Zhang F. (2008) Evidence for organic N deposition and its anthropogenic sources in China. *Atmos. Environ.* **42**, 1035-1041.

Zhao H. L., Guo Y. R., Zhou R. L. and Drake S. (2010) Biological soil crust and surface soil properties in different vegetation types of Horqin Sand Land, China. *Catena* **82**, 70-76.

Zhuang H., Chan C. K., Fang M. and Wexler A. S. (1999) Formation of nitrate and non-sea-salt sulfate on coarse particles. *Atmos. Environ.* **33**, 4223-4233.

Ziegler, L., Constable C., Johnson C. and Tauxe L. (2011) PADM2M: A penalized maximum likelihood model of the 0-2 Ma palaeomagnetic axial dipole moment: *Geophys. J. Int.* **184**, 1069-1089.

Ziereis H. and Arnold F. (1986) Gaseous ammonia and ammonium ions in the free troposphere. *Nature* **321**, 503-505.

APPENDICES

Appendix A Matlab Codes for Salt Accumulation Simulation

A.1 Chloride and $^{36}Cl/Cl$ Depth Profile under a Gradual Drying Climatic Scheme

```
clc
clear all
%initial soil condition when t=1
 duration=90000;      % the duration of the runtime
 depth=601;
 Cl=zeros(depth,duration);
 RCl=zeros(depth,duration);

 Cl(1,1)=1.3*1*1;
 %Meteoric Cl- deposition rate (mol):1.3 mmol/(m2 yr)*0.001 mol/mmol×1 m2×1 yr
 RCl(1,1)=350;                %36Cl/Cl ratio in atmospheric deposition:350×10-15

 for i=2:depth
 % The number of soil layers (depth=layer-1, layer 1→surface, layer 2→0-1 cm...)
   Density=1.4;       % Soil density(g/cm3)
   Thickness=1;       % Soil layer thickness (cm): 1
   Ksp=37.7;          % Ksp for NaCl at 20 celsius degree (35.9g/100g water)
   S(1)=0;            % Surface layer mass
   S(i)=Density*Thickness*10000;   % Soil layer mass(g) by assuming 1 m2 area
   Cl(i,1)=0;         % Original chloride amount in each layer(mol)
   RCl(i,1)=0;        % Original 36Cl in each layer
 end

%rainfall regime
for t=2:duration
 if (t>=2)&(t<=10000)
   R(t)=50+1*randn;     %Normal distribution of rainfall amount with the mean of 50 mm
 else if t<=20000
   R(t)=40+1*randn;
 else if t<=30000
   R(t)=30+1*randn;
 else if t<=40000
   R(t)=20+1*randn;
 else if t<=50000
   R(t)=10+1*randn;
 else if t<=60000
   R(t)=9+1*randn;
 else if t<=70000
   R(t)=8+1*randn;
```

```
 else if t<=80000
    R(t)=7+1*randn;
 else if t<=90000
    R(t)=6+1*randn;
 else
    R(t)=5+1*randn;
     end
     end
     end
     end
     end
     end
     end
     end
 end

% The influence of a wet event
 w=round(R(t)*10);                % Wetting depth (cm): 10R(t)
 TCl=Cl(1,1);

 for j=w:-1:2;
    V(1,t)=2*R(t)/(w+1);          %  Linear decrease of water volume with depth (0-w)
    V(j,t)=V(1,t)*(1-(j-1)/w);
    DCl(j)=V(j,t)*sqrt(Ksp);
   if DCl(j)<TCl
    WASH=DCl(j);
   else
    WASH=TCl;
   end
   TCl=TCl-WASH;
   Cl(j,t)=Cl(j,t-1)+WASH;  %the linear decrease of rainwater (i.e. Cl amount)with depth
   if Cl(j,t)~=0
   RCl(j,t)=(RCl(j,t-1)*Cl(j,t-1)*exp(-2.25/1000000*1)+WASH*350)/Cl(j,t);
   else
      RCl(j,t)=0;
   end
 end
 for m=(w+1):depth;
   Cl(m,t)=Cl(m,t-1);
   RCl(m,t)=RCl(m,t-1)*exp(-2.25/1000000*1);
 end
end

p=0:1:(depth-1);
plot(Cl(p+1,duration),p);
```

```
xlabel('chloride amount in each soil layer, mmol'),ylabel('Depth, cm');
set(gca, 'ydir', 'reverse');
figure;
plot(RCl(p+1,duration),p);
xlabel('36Cl/Cl ratio,x1E-15'),ylabel('Depth, cm');
set(gca, 'ydir', 'reverse');
```

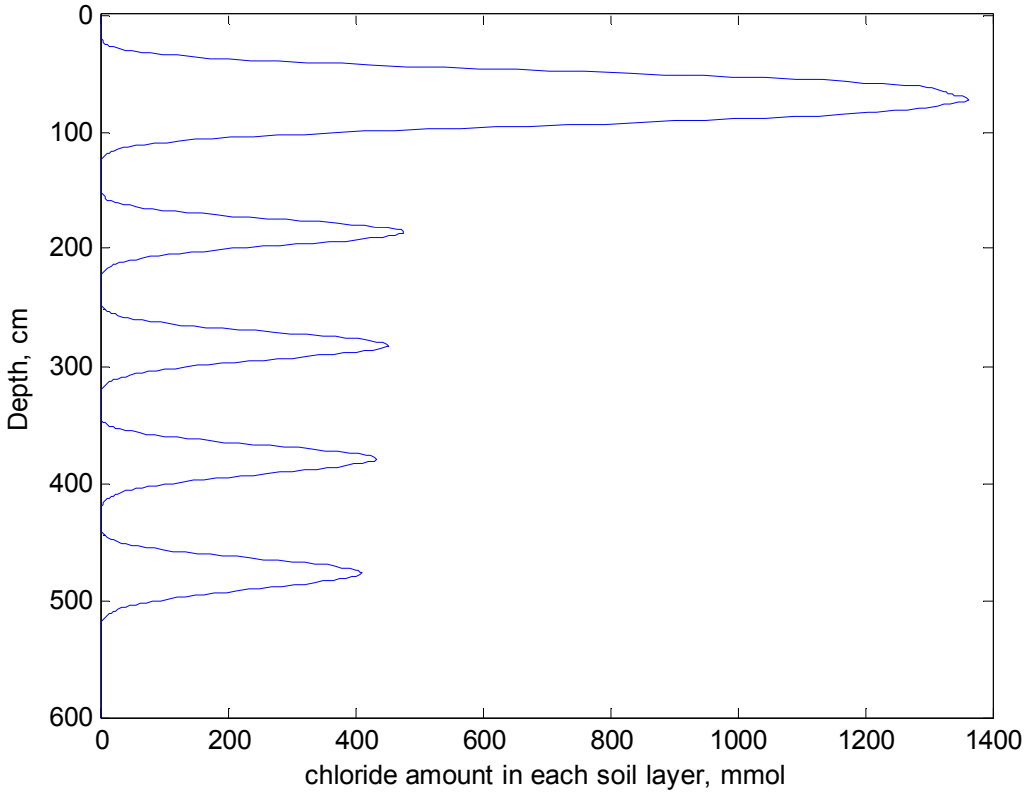

Figure A1 The matlab output-chloride depth profile

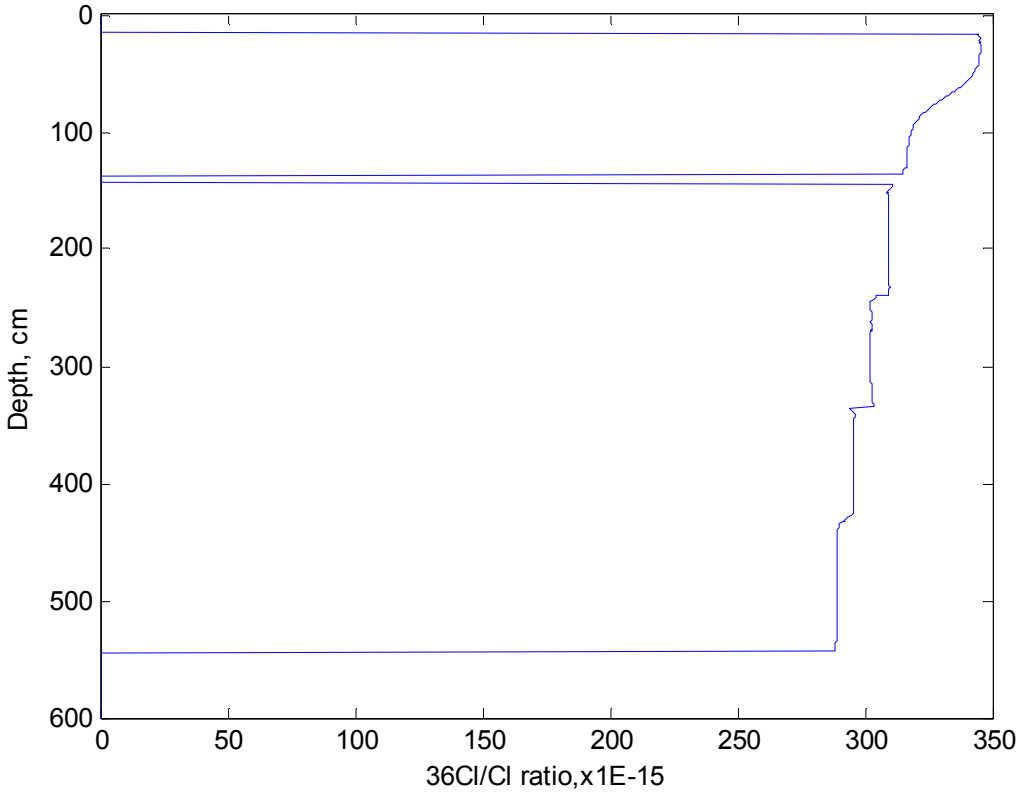

Figure A2 The matlab output-^{36}Cl/Cl ratio depth profile

Appendix B *In situ* ^{36}Cl production calculation for the Baquedano soil profile

The production rate of *in situ* ^{36}Cl in the soil samples is mainly dependent on the soil calcium, potassium and chlorine contents and can be expressed as follows:

$$P(Z) = \Psi_{Ca}([Ca], Z) + \Psi_{K}([K], Z) + \Psi_{n}((\sigma_{th})_{35}N_{35}/\Sigma(\sigma_{th})_{i}N_{i}, Z) \quad \text{Eq. B1}$$

where Ψ_{Ca}, Ψ_{K} and Ψ_{n} are the production rates of ^{36}Cl due to spallation of calcium (Ca) and potassium (K) and thermal neutron absorption, respectively; [Ca] and [K] are elemental concentrations for Ca and K, respectively; Z is the cumulative mass density length, g cm^{-2}; σ_{th} is the thermal neutron absorption cross section; N is the atomic concentration.

B.1 Spallation of Ca and K

$$\Psi_{Ca}([Ca], Z) = K_{EL}(P_{Ca})_{0}[Ca]\exp(-Z/\Lambda_{f}) \quad \text{Eq. B2}$$

$$\Psi_{K}([K], Z) = K_{EL}(P_{K})_{0}[K]\exp(-Z/\Lambda_{f}) \quad \text{Eq. B3}$$

$(P_{Ca})_{0}$ and $(P_{K})_{0}$ are the surface production rates from Ca and K normalized to sea level and geomagnetic latitude ≥60° (66.8 atoms (g Ca)$^{-1}$ yr^{-1} and 137 atoms (g K)$^{-1}$ yr^{-1}) (Phillips et al., 2001)

i. K_{EL} is the scaling factor for $(P_{Ca})_{0}$ and $(P_{K})_{0}$ for the effects of elevation and latitude (2.182 for my sampling site, 22.88°S, 69.64°W, 1500 m a.s.l) (Stone, 2000)

ii. [Ca] and [K] denote elemental concentrations, g Ca/K (g soil)$^{-1}$ (see Table B1)

iii. Z is the cumulative mass density length, g cm^{-2}: $Z = \rho h$, where ρ is the soil density of 1.4 g cm^{-3} and h is the soil depth (cm); Z equals to 0 at land surface elevation, and is positive downward and negative upward

iv. Λ_f is the effective fast neutron attenuation length (170 g cm^{-2} based on the Cd-shielded neutron counting data) (Liu et al., 1994)

The resulted ^{36}Cl production rates from Ca and K spallation with depth are shown in Figure B1.

B.2 Thermal neutron absorption

Neutron flux in the subsurface (ss) can be calculated as follows (Liu et al., 1994):

$$\phi_{ss} = p(E_{th})_a K_{EL} P_f(0)[R\Lambda_{th,ss} \exp(-Z/\Lambda_f) + (L_a^{-1} + \Lambda_f^{-1})/((L_a^{-1} + L_{ss}^{-1})(\Lambda_{th,a} - R\Lambda_{th,ss}) \exp(-Z/L_{ss})] \quad \text{Eq. B4}$$

i. $p(E_{th})_a$ is resonance escape probability that a neutron will reach thermal energies without capture of the atmosphere (0.56) (Liu et al., 1994)

ii. K_{EL} is 2.182 as mentioned above

iii. $P_f(0)$ is the production rate of secondary cosmogenic neutrons at the land-atmospheric surface normalized to sea level and geomagnetic latitude ≥60° (626 atoms (g air)$^{-1}$ yr^{-1}) (Phillips et al., 2001)

iv. R is the ratio of neutron production and moderation to thermal energies in the subsurface to that in the atmosphere at land surface elevation: $R = p(E_{th})_{ss}/p(E_{th})_a (A_{ss}/A_a)^{1/2}$, where $p(E_{th})_{ss}$ is the resonance escape probability of the subsurface, A is the average atomic weight of the elements composing either air or subsurface. $p(E_{th})_{ss} = \exp(-I_{eff}/(\Sigma\xi_i N_i(\sigma_{sc})_i)$, I_{eff} is the effective resonance integral of the media for absorption of neutrons in the epithermal region and $I_{eff} = \Sigma(I_a)_i N_i$, where I_a is the dilute resonance integral for epithermal neutron absorption by element i (note that the "a" in this term refers to "absorption" rather than "atmosphere"), ξ_i is the average log decrement of energy per collision, N_i is the atomic density of element i,

and $(\sigma_{sc})_i$ is the cross section of element *i* for scattering of neutrons; $A = \Sigma A_i N_i/(\Sigma N_i)$. N_i is derived from Table B1 and the other variables are adopted from Philips et al. (2001), giving R = 0.3618

v. $\Lambda_{th,ss}$ is the effective thermal neutron attenuation length that depends on the soil chemical composition: $\Lambda_{th,ss} = \Sigma_{th,ss}^{-1} = (\Sigma(\sigma_{th})_i N_i)^{-1}$, where $(\sigma_{th})_i$ is the elemental thermal neutron absorption cross section for element *i* adopted from Phillips et al. (2001), giving $\Lambda_{th,ss} = 19.62$ g cm^{-2}

vi. Z is the cumulative mass density length, g cm^{-2}

vii. Λ_f is the effective fast neutron attenuation length (170 g cm^{-2})

viii. L_a is the thermal neutron diffusion length in the atmosphere (3.9 g cm^{-2}) (Liu et al., 1994)

ix. L_{ss} is the thermal neutron diffusion length in the subsurface, equaling to $(D_{ss}/\Sigma_{th,ss})^{1/2}$, where $D_{ss} = (3\Sigma_{sc,i}(1\text{-}2(3A_{ss})^{-1})^{-1}$ and $\Sigma_{sc,i} = \Sigma(\sigma_{sc})_i N_i)$, leading to $L_{ss} = 10.89$ g cm^{-2}

The ^{36}Cl production rate due to thermal neutron activation can then be derived as:

$$\Psi_n((\sigma_{th})_{35}N_{35}/\Sigma(\sigma_{th})_i N_i, Z) = (\sigma_{th})_{35}N_{35}\phi_{ss} \quad \text{Eq. B5}$$

i. $(\sigma_{th})_{35}$ is the thermal neutron absorption cross section of ^{35}Cl (3.35×10^{-23} cm^2 atom^{-1})

ii. N_{35} is the atomic concentration of ^{35}Cl, atoms g^{-1}

The resulted ^{36}Cl production rates from thermal neutron absorption with depth are shown in Figure B2.

B.3 CHOLE model simulation

My calculation above based on Liu et al. (1994) is similar to the CHOLE model (version 98-2.1) estimates (Figure B3) (Phillips and Plummer, 1996).

B.4 ^{36}Cl Input in the soils

$$dN_{36}/dt = P_m + P_s + P_n - \lambda N_{36} \quad \text{Eq. B6}$$

Assume salt is built up over time as layers at a constant depth accumulation rate $a = h/t$ (cm yr^{-1}), then:

$$N_{36} = (P_s(0) + f\,\phi_{ss}^{*}/\Lambda_{th,ss})\,[\exp(-\rho h/\Lambda_f) - \exp(-\lambda h/a)]/(\lambda - \rho a/\Lambda_f)] + (fF\Delta\phi^{*}/\Lambda_{th,ss})/(\lambda - \rho a/\Lambda_f)\,[\exp(-\rho h/L_{ss}) - \exp(-\lambda h/a)] + N_0 \exp(-\lambda h/a) \quad \text{Eq. B7}$$

where N_0 is the meteoric input, $N_0 \exp(-\lambda h/a)$ is the meteoric contribution term ($N_{36\_meteoric}$), and the left terms represent *in situ* contribution ($N_{36\_in\ situ}$);

$P_s(0) = K_{EL}\,(P_{Ca})_0[\mathrm{Ca}] + K_{EL}\,(P_K)_0[\mathrm{K}] = 9.66$ atoms (g soil)$^{-1}$ yr^{-1}

$\phi_{ss}^{*} = p(E_{th})_a K_{EL} P_f(0) R\Lambda_{th,ss} = 5.43 \times 10^3$ atoms cm^{-2} yr^{-1}

$\Delta\phi^{*} = p(E_{th})_a\, K_{EL} P_f(0)(\Lambda_{th,a} - R\Lambda_{th,ss}) = 7.28 \times 10^3$ atoms cm^{-2} yr^{-1}

$F = (L_a^{-1} + \Lambda_f^{-1})/(L_a^{-1} + L_{ss}^{-1}) = 0.75$

$f = (\sigma_{th})_{35} N_{35}/\Sigma_{th,ss} = 0.10$

$N_0 = (^{36}\mathrm{Cl}/\mathrm{Cl})_0 \times [\mathrm{Cl}]_{avg} \times 6.02 \times 10^{23} = 350 \times 10^{-15} \times 0.35 \times 10^{-3}$ mol (g soil)$^{-1}$ $\times$ 6.02×10^{23} atoms mol^{-1} $= 7.37 \times 10^7$ atoms (g soil)$^{-1}$.

With the chloride depth accumulation rate varied from 2.5×10^{-4} to 5×10^{-4} cm yr^{-1}, the N_{36} estimates including both the meteoric and *in situ* input (N_{36_total}) based on Eq. B7 are close to the observation, and the N_{36} estimates from only *in situ* input ($N_{36\_in\ situ}$) range from 1.4-6.7 $\times 10^6$ atoms (g soil)$^{-1}$ (Figure B4). Especially, when $a = 3.3 \times 10^{-4}$ cm yr^{-1}, the N_{36_total} remarkably well reproduces the observed data: $N_{36} = (^{36}\mathrm{Cl}/\mathrm{Cl})_{obs} \times [\mathrm{Cl}]_{avg} \times$

6.02×10^{23} atoms (g soil)$^{-1}$ (note that using average [Cl] is to eliminate [Cl] variations impacted by chloride migration) (Figure B5); the $N_{36\_in\ situ}$ to the total N_{36} is negligible near the surface, but becomes increasingly important with depth accounting for ~30 % of the total ^{36}Cl. In view of the significant *in situ* net input over my salt accumulation timescale in the lower sections of my profile, there may be an underestimation in soil chloride age and an overestimation of chloride depth accumulation rate. To solve the chloride age and chloride depth accumulation rate by integrating the variations of *in situ* ^{36}Cl input with depth/time is too complicated, and for the sake of simplicity, we assume the *in situ* ^{36}Cl net input ($N_{36\_in\ situ}$) with depth is constant, considering meteoric net input is one order of magnitude higher at most depths. Therefore, a constant *in situ* ^{36}Cl input of 5×10^{6} atoms (g soil)$^{-1}$, close to the estimates in the bottom profile, is assumed that causes an offset of 23.7×10^{-15} between meteoric and observed ^{36}Cl/Cl ratios. This ^{36}Cl/Cl ratio offset is subtracted from the measurement to isolate the meteoric influence to explore the salt accumulation chronology in the manuscript.

REFERENCES CITED

Ericksen G. E. (1981) Geology and origin of the Chilean nitrate deposits: U.S. Geological Survey Professional Paper 1188, 37 p.

Liu B., Phillips F. M., Fabryka-Martin J. T., Fowler M. M. and Stone W. D. (1994) Cosmogenic ^{36}Cl accumulation in unstable landforms: 1. Effects of the thermal neutron distribution. *Water Resour. Res.* **30**, 3115-3125.

Phillips F. M., Stone W. D. and Fabryka-Martin J. T. (2001) An improved approach to calculating low-energy cosmic-ray neutron fluxes near the land/atmosphere interface. *Chemical Geology* **175**, 689-701.

Phillips F. M. and Plummer M. A. (1996) CHLOE: A program for interpreting in-situ cosmogenic nuclide data for surface exposure dating and erosion studies. Radiocarbon, 7th International Conference on Accelerator Mass Spectrometry, Tucson, Arizona, Abstracts, v. 38, p. 98-99.

Stone J. O. (2000) Air pressure and cosmogenic isotope production. *J. Geophys. Res.* **105**, 23753-23759.

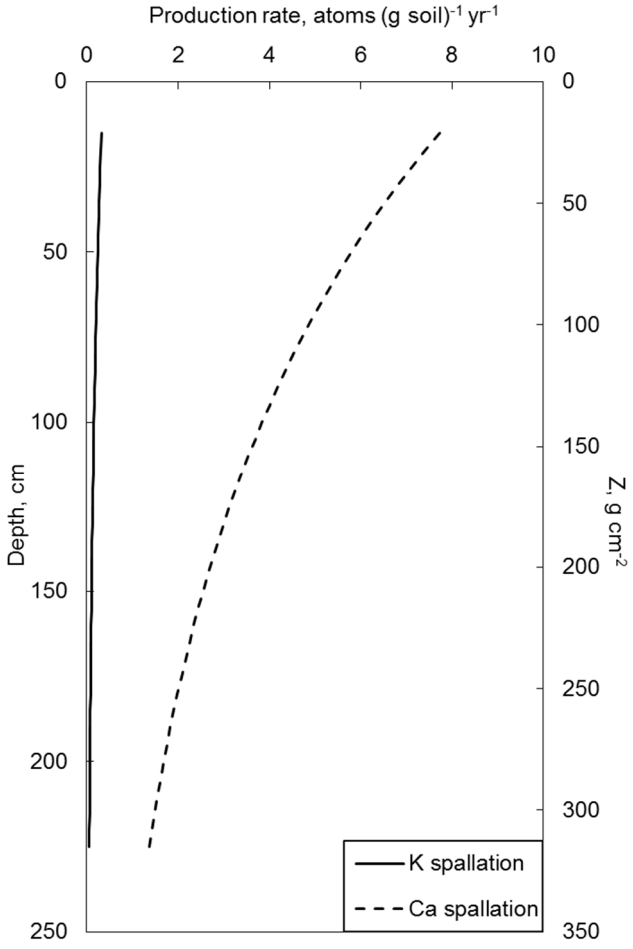

Figure B1. The production rates of ^{36}Cl from Ca and K spallation

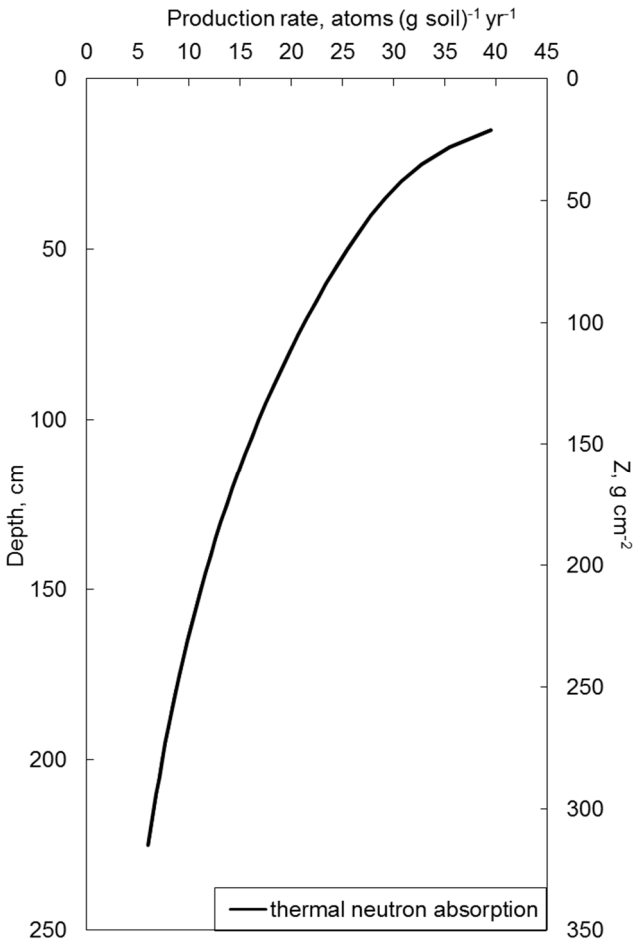

Figure B2. The production rate of ^{36}Cl due to thermal neutron absorption

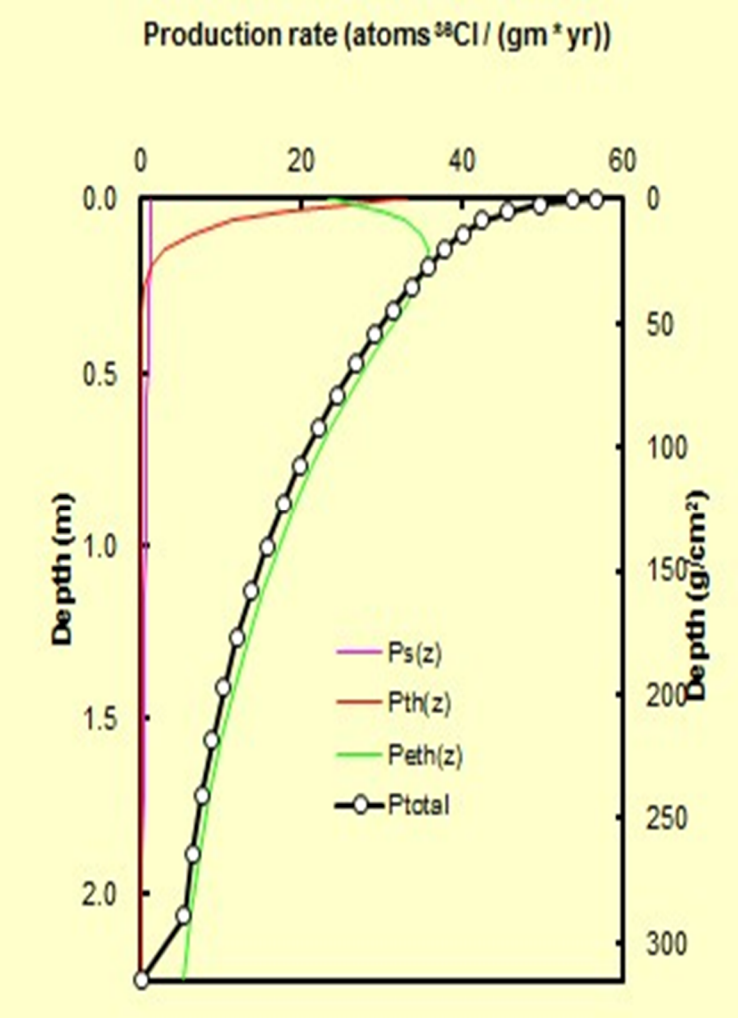

Figure B3. Estimates of *in situ* ^{36}Cl production rate through CHOLE model (version 98-2.1) (Phillips and Plummer, 1996)

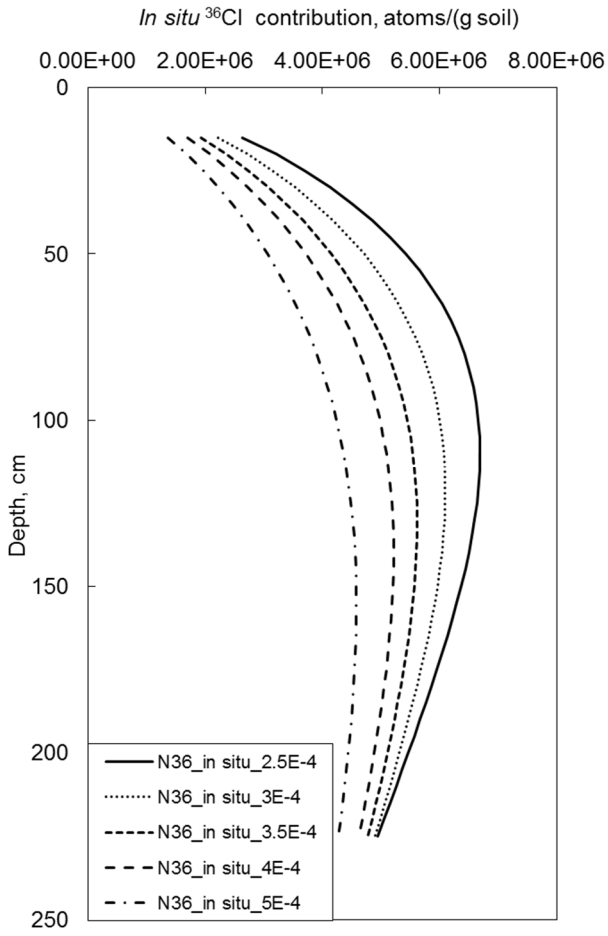

Figure B4. *In situ* ^{36}Cl input ($N_{36\ in\ situ}$) with the chloride depth accumulation rate varying from 2.5×10^{-4} to 5×10^{-4} cm yr^{-1} as a function of depth based on Eq. B7

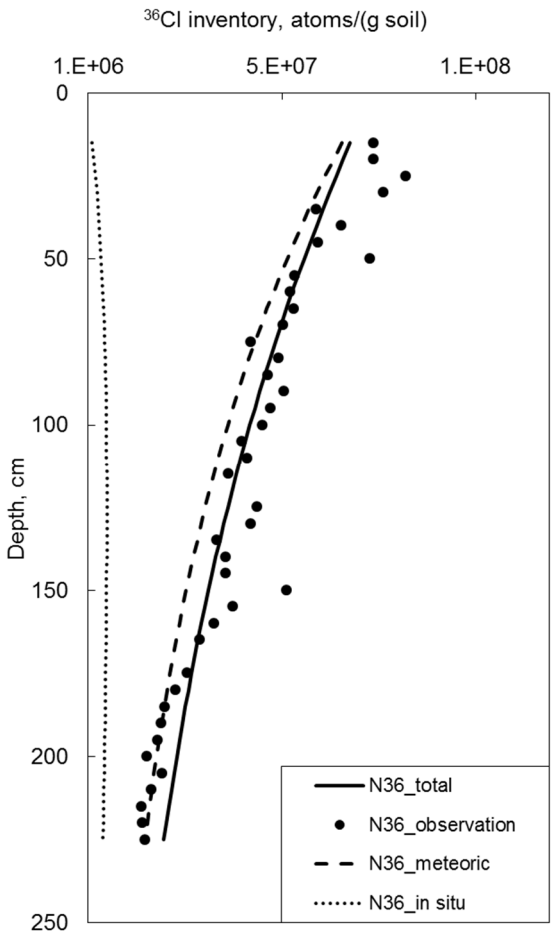

Figure B5. *In situ* ^{36}Cl input ($N_{36\_in\ situ}$), meteoric ^{36}Cl input ($N_{36\_meteoric}$) and the total estimated ^{36}Cl inventory (N_{36_total}) with the chloride depth accumulation rate of 3.3×10^{-4} cm yr^{-1} based on Eq. B7 are compared to the observed ^{36}Cl inventory ($N_{36\_observation}$)

Table B1. The major-element composition of the Atacama soils, %

O[†]	Na[§]	Mg[§]	Si[†]	K[§]	Ca[#]	Cl[††]	B[§§]
48.00	1.45	0.11	42.00	0.12	6.38	1.24	0.10

[†]Insoluble matter accounts for ~ 90% of the Atacama soils in the major form of silicate that is identified by X-ray diffraction analysis. Hereby, 90% of soil mass is assumed in the form of SiO_2

[§]Measured by inductively coupled plasma-optical emission spectroscopy (ICP-OES Thermo Scientific iCAP 6500) on the soil extract. Mg content not including insoluble fractions may have been underestimated

[#]Ca content was estimated to account for the remaining fraction of soil, which is significantly higher than the measured soluble Ca content of 0.89% by ICP-OES on soil extract

[††]Measured using Ion chromatography as stated in the manuscript

[§§]Estimated from the measurement for Ofcina Maria Elena that is 31 km due north of my sampling site by Ericksen (1981)

VITA

VITA

Fan Wang
Graduate School, Purdue University

Education

B.S., Engineering, 2006, Beijing Normal University, Beijing, China
M.S., Engineering, 2009, Beijing Normal University, Beijing, China
Ph.D., Science, 2013, Purdue University, West Lafayette, Indiana

Research Interests

Stable isotope geochemistry; Paleoclimatology; Cosmogenic nuclide dating; Global nitrogen cycling; Martian surface evolution; Hyperspectral remote sensing; Environmental quality monitoring and assessment.

Recent Academic Activities

A new regional paleo-precipitation proxy: Oxygen isotopes in desert nitrate (US National Science Foundation Grant)

- Developed and calibrated a new paleo-precipitation proxy (^{17}O anomalies in soil nitrate)
- Established chronologies of soil and salt accumulation using cosmogenic nuclide dating
- Reconstructed the regional paleo-precipitation history
- Explored desert soil formation mechanisms

The Origin of the Nitrate Deposits in Turfan-Hami Basin, China (US National Geographic Society Exploration Grant)

- Delineated the origin of nitrate deposits by using ^{17}O anomalies in soil nitrate
- Constrained the nitrogen cycle in Turfan-Hami Basin

Salt mineralogy of the Atacama Desert, Chile: A terrestrial analog for aqueous derived mineral formation on Mars (the Mineralogical Society of America Grant)

- Distinguished the water-related salt mineralogy evolution
- Investigated the origins of the salt minerals

Nitrogen Cycling and Crypto-Biotic Crust (CBC) in the Atacama Desert (the Geological Society of America grant)

- Explored and explained the occurrence of Crypto-Biotic Crusts

- Identified the alteration of nitrogen cycling and soil formation by crypto-biotic crusts

Publication

Wang, F., Bu, Q., Xia, X., Shen, M., 2011, "Contrasting effects of black carbon amendments on PAH bioaccumulation by *Chironomus plumosus* larvae in two distinct sediments: Role of water absorption and particle ingestion", *Environmental Pollution*, 159: 1905.

Wang, F., Xia, X., Sha, Y., 2008, "Distribution of phthalic acid esters in Wuhan section of the Yangtze River, China", *Journal of Hazardous Materials*, 154: 317.

Wang, F., Han, X., Wang, C., Wang, Y., Xia, X., 2007, "Mechanism and causes of high concentration nitrite nitrogen in hot water boilers of Beijing Normal University", *Modern Preventive Medicine* (in Chinese), 34: 2488.

Shen, M., Xia, X., **Wang, F.**, Zhang, P., Zhao, X., 2011, "Influences of multi-walled carbon nanotubes and plant residue chars on bioaccumulation of polycyclic aromatic hydrocarbons by *Chironomus plumosus* larvae in sediment", *Environmental Toxicology and Chemistry*, doi: 10.1002/etc.722.

Chen, X., Xia, X., Wu, S., **Wang, F.**, Guo, X., 2010, "Mercury in urban soils with various types of land use in Beijing, China", *Environmental Pollution*, 158: 48.

Manuscripts Submitted & in Preparation

Wang, F., Michalski, G., Seo J. H., Ge W. S., "Geochemical, isotopic and mineralogical constraints on the role of atmospheric deposition in soil development in the hyper-arid Atacama desert, Chile", *Geochimica et Cosmochimica Acta* (in review).

Wang, F., Michalski, G., Seo, J. H., Granger, D. E., Lifton N. Caffee, M. W., 2012, "Berrylium-10 dating of the hyper-arid soils in the Atacama Desert, Chile: Implications for soil formation mechanism and climatic change", *Geochimica et Cosmochimica Acta* (in review).

Wang, F., Michalski, G., Luo, H., Seo J. H., "Oxygen isotopes in soil nitrate: Evaluating nitrification potentials in desert soils and a new paleo-precipitation proxy in arid landscapes", *Journal of Geophysical Research* (in review).

Liu, T., **Wang, F.**, Michalski, G., Xia, X., Liu, S., "Using ^{15}N, ^{17}O, ^{18}O to Determine Nitrate Sources in the Yellow River, China", *Environmental Science & Technology* (in review).

Wang, F., Michalski, G., Granger, D. E., Caffee, M., 2012, "A ^{36}Cl chronology of salt accumulation in the hyper-arid Atacama Desert, Chile", in preparation.

Wang, F., Michalski, G., "The distribution of meteoric $^{36}Cl/Cl$ ratio in the Atacama Desert, Chile", in preparation.

Wang, F., Michalski, G., Seo J.H., Choudhury, R., "The surface evolution under hyper-arid settings" (in preparation).

Published Abstracts and Presentation

Wang, F., Michalski, G., Granger, D. E., Caffee, M. W., A ^{36}Cl chronology of hyper-arid soil accumulation in the Atacama Desert, Chile, Abstract for GSA Annual Meeting, Minnenapolis, USA, October 9-12, 2011 (Oral Presentation).

Wang, F., Seo, J. H., Bowen, B. B., Ochoa, R., Michalski, G., The tale of hyper-arid pedogenesis – Two comparing sites in the Atacama Desert, Chile, Abstract for AGU Fall Meeting, San Francisco, USA, December 13-17, 2010 (Poster).

Wang, F., Ge, W. S., Michalski, G., Role of water availability in source partitioning for desert nitrate: New evidence from mass-independent oxygen isotopic compositions, Abstract for Goldschmidt Conference, Knoxville, USA, June 13-18, 2010 (Poster).

Michalski, G., **Wang, F.**, Seo, J. H., Oxygen isotopes in soil nitrate: A new proxy for paleo-precipitation in arid environments, Abstract for GSA Annual Meeting, Minnenapolis, USA, October 9-12, 2011 (Oral Presentation).

Seo, J.H., Michalski, G., **Wang, F.**, Caffee, M. W., Isochron dating using ^{36}Cl and ^{10}Be of hyper-arid soils in the Atacama Desert, Chile, Abstract for GSA Annual Meeting, Minnenapolis, USA, October 9-12, 2011 (Poster).

Teaching Experience

Mentor Purdue University, West Lafayette, IN 8/2009-12/2012

- Supervised and motivated five undergraduate students to conduct undergraduate research (One mentee won the Vice-Provost best article award in the university's inaugural *Journal of Purdue Undergraduate Research*)

Teaching Assistant Beijing Normal University, Beijing, China 9-12/2006

- Developed and taught water quality monitoring lab courses (Named to Teaching Honor Roll)

Practice Teacher Beijing No. 166 Middle School, Beijing, China 9-12/2005

- Lectured to Grade 9 students in Math club

Recent Field Work Experience

Lichen field and salt lake mapping in the Atacama Desert, Chile 12/2011
Salt lake investigation in Turfan-Hami Basin, China 8/2011
Nitrate deposits mapping in Turfan-Hami Basin, China 4/2010
Nitrate deposits mapping in Atacama Desert, Chile 12/2009
Water pollution investigation in Wuhan Section of the Yangtze River, China 10/2006

Honors & Awards

Purdue Bilsland Dissertation Fellowship 2012-2013
Purdue Research Foundation Fellowship 2011-2012
Geological Society of America Graduate Student Research Grant (Outstanding Award) 2011
Mineralogical Society of America Student Award in Mineralogy and Petrology 2011
Purdue P. F. Low AGU Travel Grant 2010
Purdue Climate Change Research Center Ross Fellowship 2009-2010

Beijing Normal University Outstanding Master's Thesis	2009
Beijing Normal University Excellent Graduate	2008-2009
Beijing Normal University Excellent Studying Scholarship	2006-2007

Professional Memberships

American Geophysical Union
Geological Society of America
Geochemical Society